Photoproduction of Gluonic Excitations and Unusual Mesons

The Hall D Collaboration

R. Clark, P. Eugenio, G. Franklin, C. A. Meyer (Acting Co-Spokesperson), B. Quinn, R. Schumacher
Carnegie Mellon University (Pittsburgh,PA)

H.Crannell, D.Sober
Catholic University of America (Washington, D. C.

D. Doughty, D. Heddle
Christopher Newport University (Newport News, VA)

R. Jones
University of Connecticut (Storrs, CT)

W. Boeglin, L. Kramer, P. Markowitz, B. Raue, J. Reinhold
Florida International University (Miami,FL)

L. Dennis, P. Dragovitch, G. Riccardi
Florida State University (Tallahassee,FL)

A. Dzierba (Spokesperson), M. Pichowsky, E. Scott, P. Smith, T. Sulanke, A. Szczepaniak, S. Teige
Indiana University (Bloomington,IN)

S. Denisov, N. Fedyakin, A. Gorokhov, V. Samoilenko, A. Schukin
Institute for High Energy Physics (Protvino, Russia)

D. Abbott, I. Bird, R. Carlini, H. Fenker, A. Freyberger, G. Heyes, R. Macleod, J. Manak, C. Sinclair, E. Smith (Hall D Group Leader), D. Weygand, E. Wolin
Jefferson Lab (Newport News,VA)

R. Mischke, A. Palounek, J. C. Peng
** Los Alamos National Lab (Los Alamos,NM)*

V. A. Bodyagin, A. M. Gribushin, N. A. Kruglov, V. L. Korotkikh, M. A. Kostin,
A. I. Demianov, O. L. Kodolova, L. I. Sarycheva, A. A. Yershov
Nuclear Physics Institute, Moscow State University, Moscow, Russia

M. Khandaker, V. Punjabi, C. Salgado
Norfolk State University (Norfolk,VA)

E. Solodov
Budker Institute of Nuclear Physics (Novosibirsk, Russia)

A. Klein
Old Dominion University (Newport News,VA)

D. Carman, K. Hicks
Ohio University (Athens,OH)

S. Dytman, J. Mueller
University of Pittsburgh (Pittsburgh, PA)

E. J. Brash, G. M. Huber, G. J. Lolos, Z. Papandreou
University of Regina (Regina, Saskatchewan,Canada)

G. Adams, J. Cummings, R. Davidson, A. Empl, N. Mukhopadhyay, J. Napolitano,
P. Stoler
Rensselaer Polytechnic Institute (Troy,NY)

J. M. Laget, M. Garçon
** Saclay (France)*

Theory Group

S. Godfrey
Carleton University (Ottawa, Ontario,Canada)

R. Kaminski, L. Lesniak
** Institute for Nuclear Theory (Cracow, Poland)*

J. Goity
Hampton University (Hampton,VA)

M. Pichowsky, A. Szczepaniak
Indiana University (Bloomington,IN)

P. Page
Los Alamos National Lab (Los Alamos, NM)

A. Afanasev
North Carolina Central University (Durham, NC)

E. Swanson
North Carolina State University (Raleigh, NC)

T. Barnes
University of Tennessee (Knoxville, TN)
Oak Ridge National Lab (Oak Ridge, TN)

R. Davidson,N. Mukhopadhyay
Rensselaer Polytechnic Institute (Troy,NY)

(*) Insitutions not yet committed but involved in workshops and planning

Contents

Chapter 1

Introduction

This is a revised Design Report from the HALL D collaboration to build a 4π hermetic detector with the purpose of studying the photoproduction of unusual mesons and gluonic excitations at Jefferson Lab. This HALL D project also includes a beamline and an above-ground tagger building and detector building to be located off the stub at the east end of the north linac of the CEBAF accelerator. This project assumes that the energy of CEBAF will be increased to 12 GeV by the early part of the next decade.

1.1 Preliminary Design Report and PAC-15

A Preliminary Design Report appeared in January, 1999 and was presented to the JLab Program Advisory Committee (PAC-15) at its meeting in January, 1999 as a Letter of Intent (LOI).

The summary PAC-15 report had this to say about the LOI:

> A letter-of-intent was presented by a large collaboration that is interested in greatly extending the meson spectroscopy program at JLab. This letter focussed on the opportunities in this field that would be made possible with a 12-GeV beam and a hermetic detector to be located in a new Hall (Hall D) at Jlab. The PAC was asked to begin the process of evaluating the scientific opportunities and experimental feasibility of such a program. We have recommended the establishment of a PAC sub-committee that includes PAC members and outside experts in order to begin the review process of this ambitious project.

The more detailed report included these statements:

> This letter of intent represents one of the key physics motivations of the energy upgrade of CEBAF. The existence and nature of gluonic excitations in low energy spectroscopy is one of the most important open questions in the standard model. The collaboration proposes to use linearly polarized photons to study the production of mesonic states with masses in the 1-3 GeV region with unparalleled statistical precision. Photon beams have unique properties that complement meson beams, and the existing data are quite limited. Meson spectroscopy is one sector that is not optimally addressed with the existing experimental equipment.

> The proposed approach is extremely promising. The collaboration has made an impressive start in assembling a talented team of physicists, exploring the required detector capabilities and developing concepts of how this program can be carried out at JLab. The PAC is quite encouraged by the parallel efforts of members of this group in E-99-005 to begin mining JLab data for this physics.
>
> This program sets much of the scale for the energy upgrade, both in the choice of the target energy and in proposing to consume the largest single fraction of resources for new experimental equipment. It appears likely that the physics justifies this focus. It is essential that the collaboration present a concise statement of the physics impact that the physics community can support enthusiastically. At the same time, we encourage the collaboration to seek out other physics opportunities to broaden the scientific case.
>
> The PAC enthusiastically supports this effort. Given its significance to the future of the laboratory, we believe it is appropriate to appoint a PAC subcommittee to more carefully assess this initiative.

The JLab management has appointed a review committee and the HALL D project review will take place in early September, 1999.

1.2 History

The HALL D plans have evolved over the last 24 months, starting with a workshop held in July, 1997 at Indiana University and the formation of a working group (HALL D collaboration or *Eightplus* working group). There then followed workshops at North Carolina State University (November, 1997), Carnegie Mellon University (March, 1998), Florida State University (October, 1998) and at Rensselaer Polytechnic Institute (March, 1999).

The Jefferson Lab Users Community was given a status report at the Users Meetings in June, 1998 and June, 1999. During 1998 and 1999, there also were a number meetings involving principals of the HALL D collaboration with the management, accelerator division and personnel from the civil construction group. Negotiations with Los Alamos National Lab and Fermilab indicate that we will be able to transfer the MEGA superconducting solenoid (also used in the LASS spectrometer at SLAC) and a dipole magnet to Jefferson Lab for use in the proposed detector.

The HALL D collaboration activities and workshops are summarized here:
http://dustbunny.physics.indiana.edu/~dzierba/Eightplus/.

Chapter 2

Executive Summary

2.1 Overview

A remarkable prediction of Quantum Chromodynamics (QCD) is that the force carriers, the gluons, which bind quarks to form hadrons, should also bind to each other to form quarkless hadrons or *glueballs*. These glueballs should appear in the spectrum of mesons, along with conventional $q\bar{q}$ mesons. QCD further predicts that the collection of gluons in mesons - the *glue* - should also manifest itself in *hybrid mesons*, some of which can have J^{PC} quantum numbers not allowed for conventional $q\bar{q}$ states. A picture of such states is emerging, supported by recent advances in lattice gauge theories (LGT), in which the gluons binding quarks in hadrons are confined to flux tubes. In hybrid mesons, the flux tube is in an excited state. We refer to glueballs and hybrids collectively as *gluonic excitations*. The flux-tube and LGT predictions of the spectrum of gluonic excitations agree that the low-lying states are in the mass region between 1.5 and 2.5 GeV/c^2. Understanding the spectrum of these states, their production and decays, goes to the very heart of QCD in the soft regime and the nature of confinement.

Despite 25 years of searches in hadron-induced fixed target experiments, in $\bar{p}p$ annihilations, e^+e^- and $\gamma\gamma$ collisions, and decays of the J/ψ and Υ, evidence for gluonic excitations has been hard to find - although there are tantalizing candidates. An unexplored search area is the photoproduction of states in the 1.5 to 2.5 GeV/c^2 regime. There are good reasons to expect that photons are a particularly good probe in searching for the glue - these gluonic excitations.

This Design Report describes a plan, the so-called HALL D project at Jefferson Lab (JLab), to build a coherent bremsstrahlung photon beam and a hermetic, 4π detector to search for unusual mesons in the 1.5 to 2.5 GeV/c^2 mass range. The optimal photon energy for these searches is in the range from 8 to 10 GeV, assuming 12 GeV electrons from an energy-upgraded CEBAF. The unprecendented quality of photon beams possible at JLab, with respect to intensity, energy resolution, spot size and duty factor, make this facility unique for carrying out this search. The plans call for extracting the electron beam through the stub at the east end of the north linac of CEBAF and to deliver this beam to an above-ground photon tagger building and a new experimental hall, HALL D.

This Design Report is submitted by a collaboration of over 80 physicists from 25 institutions – a collaboration which will grow as the plans for the HALL D project mature. A key feature of this collaboration is the close cooperation of theorists and experimentalists to define the goals within the context of the progress of the field of light quark spectroscopy. This collaboration will also develop and refine analysis techniques, especially with regard to extracting information on the quantum numbers of observed mesons.

This chapter provides an overview and highlights some of what appears in this Design Report.

2.2 Scientific goals

The evidence that QCD mesons outside the naive quark model ($q\bar{q}$) have been found is tantalizing. The light quark meson spectrum (below charm threshold) has more states than can be accommodated within the $q\bar{q}$ model. Furthermore, there seems to be evidence for at least one glueball state and at least one state with so-called exotic J^{PC} quantum numbers, that is, quantum numbers which cannot be formed in a $q\bar{q}$ system. In parallel, lattice gauge calculations and QCD-inspired models (e.g. flux-tube model, bag model) are starting to converge on the prediction of the masses of unconventional mesons.

The challenge for theorists and experimentalists in the next decade will be to carefully map out the spectrum of these gluonic excitations and the $q\bar{q}$ mesons with which they mix, gathering information about their quantum numbers and their decay modes, and using this, to gain an understanding of the nature of the effective low energy degrees of freedom of QCD. The ultimate goals are to test QCD and to gain insight into the nature of confinement in QCD.

The photon probe is distinct from hadronic probes (π, K, p) which have been used to date. In contrast to the $q\bar{q}$ system of the π or K, with quark spins anti-aligned, the photon is a virtual vector meson, a $q\bar{q}$ system with quark spins aligned. Within the flux tube model, before the interaction, this spin-1 $q\bar{q}$ has its flux tube in the ground state. After interaction with the target, the flux tube can be excited to its first excited state giving rise to states which include those with exotic J^{PC} : 0^{+-}, 1^{-+} and 2^{+-}. These exotic states are expected to be produced with cross sections comparable to those of ordinary mesons. Since the photon can also be viewed as an $s\bar{s}$ structure, photoproduction will also yield important new information on $s\bar{s}$ spectroscopy. The $s\bar{s}$ content of the photon at the energies of the proposed upgrade is also relevant to providing the bridge between the light quark (u and d) sector and the heavy quark (c and b) sector. Another important aspect of the nature of the photon beam is polarization, which will be used as an important new tool for identifying gluonic excitations.

The vector photon is very efficient at producing massive vectors, ρ, ω and ϕ via diffractive scattering with relatively high cross sections in the forward direction. We can view CEBAF as a factory for these mesons to study their rare decays. Of particular interest is the ϕ meson, whose decays are relevant for studies of the nature of the mesons into which the ϕ can radiatively decay. The boost of these ϕ's in the lab frame offers some important advantages over producing them at rest.

2.3 Beam

The goal of the HALL D project is a study of the photoproduction of mesons (X) in the reaction $\gamma p \rightarrow Xp$ for masses, m_X, in the range from the lightest mass up to $\approx$ 2.5 GeV/c^2. This requires photon energies in the range 8 to 10 GeV and in turn, 12 GeV electrons.

The production of X is characterized by the dependence of the cross-section on the square of momentum transferred, t, between the incident γ and the outgoing meson, X. There are a number of considerations in determining the optimal parameters of the incident photon beam.

For a given m_X, there is a minimum photon energy required (e.g. E_γ of 5.8 GeV for m_X of 2.5 GeV/c^2). Of course, it is desirable to produce X with sufficient boost so that the decay products of X can be detected with good efficiency and resolution. The determination of the J^{PC} quantum numbers of X depends on a partial wave analysis (PWA) which in turn depends on measuring decay angles. The PWA must be carried out in fine enough bins in m_X and t with large enough statistics in these bins. Since production is characterized by t, and since for a given E_γ there is a minimum momentum-transfer-squared, $|t_{min}|$ for a given m_X, it is essential that E_γ be large enough so that the variation in $|t_{min}|$ across the width of X be minimized.

Another requirement is to kinematically identify the exclusive reaction producing X. This requires measuring the four-vectors of the reaction products and the incident photon energy with sufficient accuracy.

Understanding the mechanism for producing X with a photon beam requires linearly polarized photons. This is discussed in more detail in Chapter 3 where we consider, for example, the production of a vector meson by exchange of a scalar (natural parity) or psuedoscalar (unnatural parity). Using circularly polarized photons, we cannot distinguish between the two mechanisms. The distinction is possible, however, using linearly polarized photons. The determination of exchange mechanisms will be important in determining the substructure of produced mesons. In Chapter 4 we show that the only practical way to achieve linear polarization with sufficient flux and energy is to use the coherent bremsstrahlung technique.

As discussed in Chapter 4, the photon flux in the coherent peak falls as the energy of the photons approaches the endpoint (electron) energy. The degree of polarization also falls as one approaches the endpoint energy. For example, with 12 GeV electrons, the flux of photons in the coherent peak falls by a factor of 12 as E_γ increases from 8 to 11 GeV while the peak polarization falls from 0.54 at the lower energy to 0.11 at the higher energy. This dependence of flux and polarization as a function of photon beam energy is shown in Fig. 2.1.

The desire to operate at higher photon energies to reach higher masses and lower $|t_{min}|$ is balanced by the desire to maximize flux and degree of polarization. We attempt to define a figure-of-merit for choosing the optimal energy. First, the flux of mesons is determined by the cross-section dependence on E_γ and t, the latter typically given by an exponential such as $e^{-\alpha|t|}$ where α can range from 2 to 8 $(GeV/c)^{-2}$. In Fig. 2.2, the plot on the left shows the rate of mesons of different masses as a function of E_γ where we assume the mesons are produced with equal cross sections and the rates are given by integrating $e^{-\alpha|t|}$ from $|t_{min}|$ to $|t_{max}|$. No other explicit energy dependence is assumed and we chose α equal to 4 $(GeV/c)^{-2}$. In the plot on the right we show the result of convolving the dependence shown in the plot on

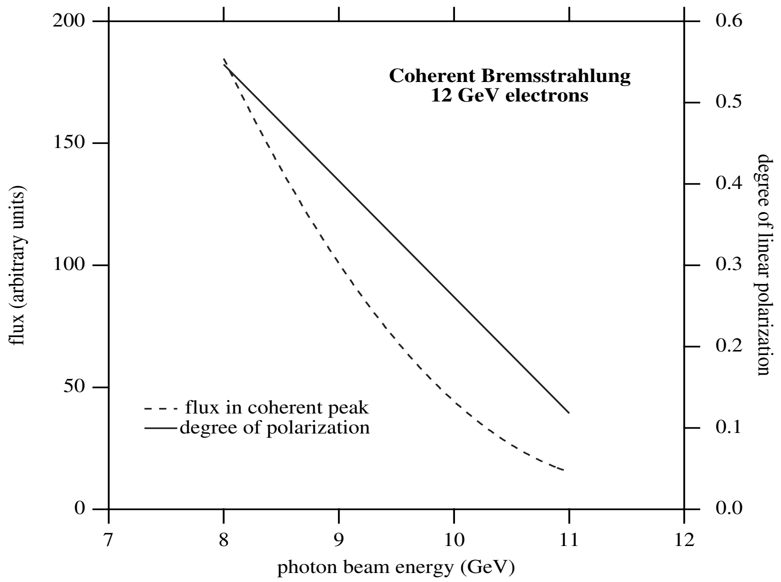

Figure 2.1: Variation of flux in the coherent peak and degree of linear polarization as a function of photon beam energy using 12 GeV electrons.

the left with the energy dependence of the flux of photons in the coherent peak and degree of polarization (see Table 4.5 in Chapter 4).

Another consideration is the variation of $|t_{min}|$ across the width of the resonance. In Fig. 2.3 we show the variation in $|t_{min}|$ relative to the value at m_X at 2.6 GeV/c^2 as we move across the width of the resonance, assumed here to be 0.10 $GeV/c^2$for E_γ of 7, 8 and 11 GeV. At $m_X = 2.6\ GeV/c^2$ we are at the extreme of the mass range we wish to study but for $E_\gamma = 7\ GeV$, the variation in $|t_{min}|$ is severe. The optimal energy range for the photon beam is from 8 to 10 GeV.

The coherent bremsstrahlung technique describe in Chapter 4 will allow us to achieve sufficient energy resolution ($\sigma/E \approx 0.001$) for kinematic identification of exclusive reactions. With initial photon fluxes of 10^7 photons/sec, in one year of running we will exceed the extant data collected with incident π beams by a factor of 10. Eventually we plan to run with fluxes of 10^8 photons/sec.

2.4 Detector

The physics goals of the HALL D project require a full partial wave analysis of kinematically identified exclusive reactions producing mesons. The decay products of produced mesons must be identified and measured with good resolution and with full acceptance in decay angles. In many cases, the decays of mesons involve a chain of particle decays. The HALL D detector must therefore be hermetic with 4π coverage with the capability of measuring energies of neutral particles (γ, π^0, η) and momenta of charged particles with good resolution. Particle identification is also required.

The HALL D detector described in Chapter 5 is optimized for photon beam energies between 8 and 10 GeV. The detector consists of a large aperture superconducting solenoid

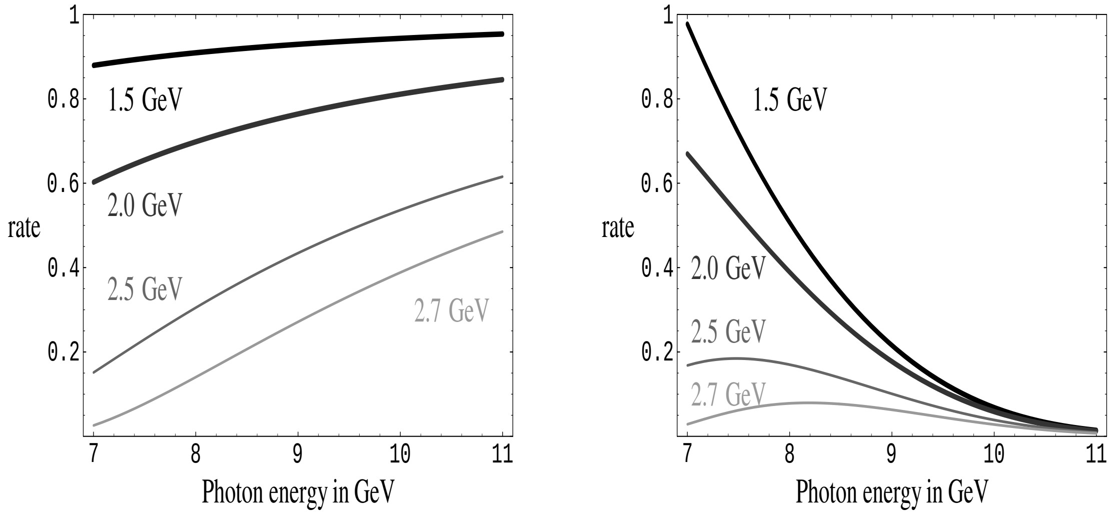

Figure 2.2: Rate of meson production vs incident photon energy. (left) Rate of meson production as a function of beam energy for various values of m_X. Assumptions are given in the text. (right) The same dependence now convolved with the dependence on photon flux in the coherent peak and degree of linear polarization as a function of energy.

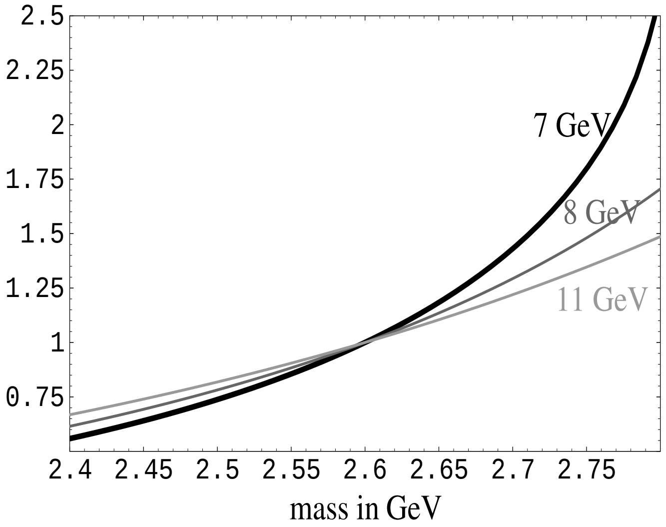

Figure 2.3: Relative variation of $|t_{min}|$ across the width of a resonance centered at $m_X = 2.6$ GeV/c^2 for various incident photon energies.

filled with a target, tracking chambers and calorimetry. The calorimetry will also provide time-of-flight information for particle identification. The solenoid will be followed with a threshold Čerenkov counter, particle tracking and a lead glass electromagnetic calorimeter.

The superconducting solenoidal magnet is the LASS/MEGA magnet. This magnet was built for the Large Aperture Superconducting Solenoid Spectrometer (LASS) and SLAC and later transferred to LANL for use in the MEGA experiment. It will be transferred to JLab for use in HALL D. The forward electromagnetic calorimeter will be constructed using lead glass and electronics originally used in the E852 experiment at Brookhaven Lab.

2.5 Civil construction

The plan is to site the meson spectrometer in a new experimental hall (HALL D) to be located at the end of a new beamline which would come off the stub at the east end of the north linac of CEBAF. The civil construction includes work associated with breaking through the stub, delivering beam above ground to a tagger, a tagger building, HALL D, the counting house, roads, and a parking area. Members of the HALL D collaboration have been meeting with members the JLab civil construction team to arrive at a cost estimate and milestones for civil construction. Details are given in Chapter 6.

2.6 Rates,trigger and DAQ

Initially the HALL D detector will run with tagged photon fluxes of 10^7 photons/sec and data archive rates of 1,500 events/sec. Estimates of the hadronic and electromagnetic tagged and untagged rates have been made along with estimates of accidental rates. These rate estimate calculations are backed by measurements made in Hall B and while technically challenging, are within the capabilities of a state-of-the art electronics system.

The trigger system will be implemented from the outset in a pipeline fashion to provide maximum flexibility for sophisticated triggers. This will allow us to gradually increase the incident flux to 10^8 photons/sec – greatly opening the scope of physics, in meson spectroscopy and rare decays.

The proposed data acquisition (DAQ) system system is based on an upgrade of the existing CODA-based DAQ system already in use at Jefferson Lab. Details about rates, the trigger and DAQ are given in Chapter 7.

2.7 Costs

The total cost for the HALL D project is $\approx$ \$30.9 M (not including contingencies). The cost of the detector is $\approx$ \$18.4 M The civil and beamline costs total $\approx$ \$10.9 M and include the tunnel from the accelerator to the HALL D tagger, beamline elements, the HALL D building, control room, parking and roads. The cost of the photon tagger is $\approx$ \$1.7 M. Further details of the costs for the various subsystems of the detector, the civil construction, beamline and tagger are given in Chapter 12 and Appendix A.

Not included in the HALL D cost estimate is the cost of the additional arc in the CEBAF accelerator which would allow 5.5 passes for the electron beam in HALL D. The cost of the extra arc is $\approx$ \$2.9 M and is assumed to be part of the overall accelerator upgrade.

Chapter 3

Scientific Goals

3.1 Introduction

The scientific goal of the HALL D project is a high–statistics study of the photoproduction of mesons with masses below $c\bar{c}$ threshold, using a hermetic 4π detector with sensitivity to a wide variety of decay modes of these mesons. Photoproduction of these light mesons is expected to yield important new information on the spectrum of mesons beyond the naive quark model. The discussion below will show how this study impacts on our understanding of Quantum Chromodynamics (QCD), especially on the issues of mesons with unusual quantum numbers, and non-perturbative QCD. The HALL D spectrometer also has the physics potentials associated with the high statistics production of the light vector mesons ρ, ω and ϕ. These physics topics include rare decays and symmetry tests.

3.1.1 QCD: mesons and strong QCD

QCD is the theory of the strong interaction, expressed in terms of the fundamental quark and gluon constituents of hadrons. QCD has successfully met experimental tests in the perturbative regime, where calculational techniques have made possible comparisons with collider experiments and fixed-target experiments at high energy and large momentum transfer. The same situation does not yet hold in the non-perturbative regime, but important progress is being made on both theoretical and experimental fronts. Comparison between theory and experiment in this non-perturbative regime may improve our understanding of QCD in the strongly interacting regime, particularly in the areas of the spectroscopy of exotics and non-$q\bar{q}$ mesons and the nature of confinement. Much of the recent progress in understanding strong QCD has related to the spectrum of unconventional mesons. Theoretical advances are being made in two general areas, lattice gauge theories (LGT) and QCD-inspired models, both of which lead to predictions of the spectrum of mesons and their decays. Experimental studies using π and K beams, $\bar{p}p$ annihilations, e^+e^- collisions and J/ψ, Υ, τ and Z^o decays indicate that the meson spectrum is rich indeed and has more states than the naive quark model suggests, but the experimental picture is very incomplete. High statistics data on the photoproduction of mesons promises to be an extremely valuable contribution to our understanding of the experimental spectrum.

QCD predicts that the spectrum of light mesons consists not only the *conventional* mesons dominated by valence $q\bar{q}$ degrees of freedom, but also of other mesons as well. The novel types of mesons include (1) *glueballs* – states composed mainly of pure glue basis states (for example gg and ggg), (2) *hybrids* – which carry valence glue in addition to quarks ($q\bar{q}g$) and (3) *molecular* or *four quark* states. The four-quark states might include novel nuclear species such as the deuteron–like $K\bar{K}$ molecules, as well as and combinations of diquark and anti-diquark ($qq\bar{q}\bar{q}$). Categories (1) and (2) are referred to as *gluonic mesons*, and and are predicted by most models of QCD, (see section 3.2.2 for an overview of many of these models). Of course physical mesons will be linear superpositions of these idealized basis states, but the success of the naive $q\bar{q}$ quark model suggests that this configuration mixing may be small in most cases.

Figure 3.1 shows a level diagram giving the range of masses for the conventional $q\bar{q}$ nonets and estimates of the masses of the lightest glueballs and hybrids, and thresholds which might have nearby associated molecular meson-meson bound states.

There are a number of detailed reviews of light quark mesons. Two of the more recent ones [1, 2] also give references to earlier review articles.

3.1.2 Conventional and non-conventional mesons

Conventional $q\bar{q}$ mesons, made of u, d and s quarks are grouped in nonets, each characterized by a given J^{PC}. The rules for allowed values of J^{PC} follow from the requirements of a fermion–antifermion system: the quark spins can be parallel ($S=1$) or antiparallel ($S=0$) with relative orbital angular momentum (L), $\vec{J}=\vec{L}+\vec{S}$, $P=(-1)^{L+1}$ and $C=(-1)^{L+S}$. For a $q\bar{q}$ meson, $J^{PC}=0^{--}$, 0^{+-}, 1^{-+}, 2^{+-}, $\cdots$ are not allowed and are referred to as *exotic* quantum numbers. In addition to the ground state nonets, radial excitations are expected and observed as well. Figure 3.2 shows our current knowledge of these $q\bar{q}$ states. The exact association of an observed meson with a particular $q\bar{q}$ state within a nonet often depends on a good understanding of the various decay modes of the meson as well as its mass, width and production characteristics.

There is also now clear evidence that the observed meson spectrum includes states which cannot be accommodated within the naive quark model. For example, there are at least five scalar states reported with masses below 2 GeV/c^2 suggesting that among these may be a scalar glueball. Lattice Gauge Theory calculations indicate that the lightest scalar glueball should have a mass in the range from 1.5 to 1.7 GeV/c^2, which is consistent with two of the observed states. There exists strong evidence for states with exotic quantum numbers, (the $q\bar{q}$ quantum number restrictions do not apply to gluonic mesons or molecules), although their exact interpretation is unclear. Finally, we have possible evidence for molecular states in the $f_0(980)$ and $a_0(980)$.

3.1.3 Photoproduction of mesons

Photon beams at Jefferson Lab are and will be of unprecedented quality with regard to intensity, emittance and duty factor. New physics will be uncovered starting with initial photon energies of about 5 GeV, culminating in energies of 12 GeV, which will allow examination of the meson spectrum up to masses of ≈ 3 GeV/c^2.

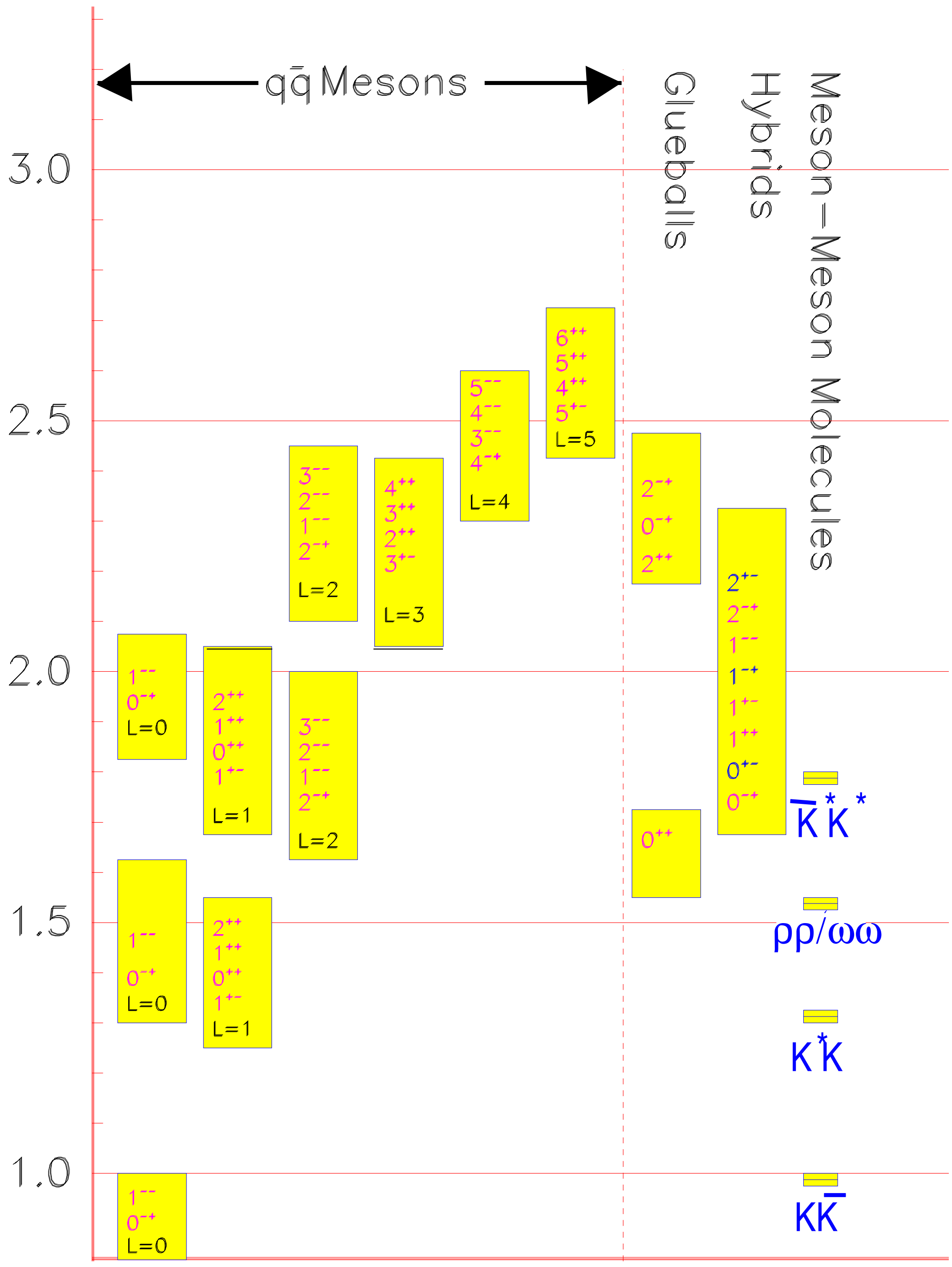

Figure 3.1: A level diagram showing conventional nonets and expected masses of glueballs, hybrids and molecular thresholds.

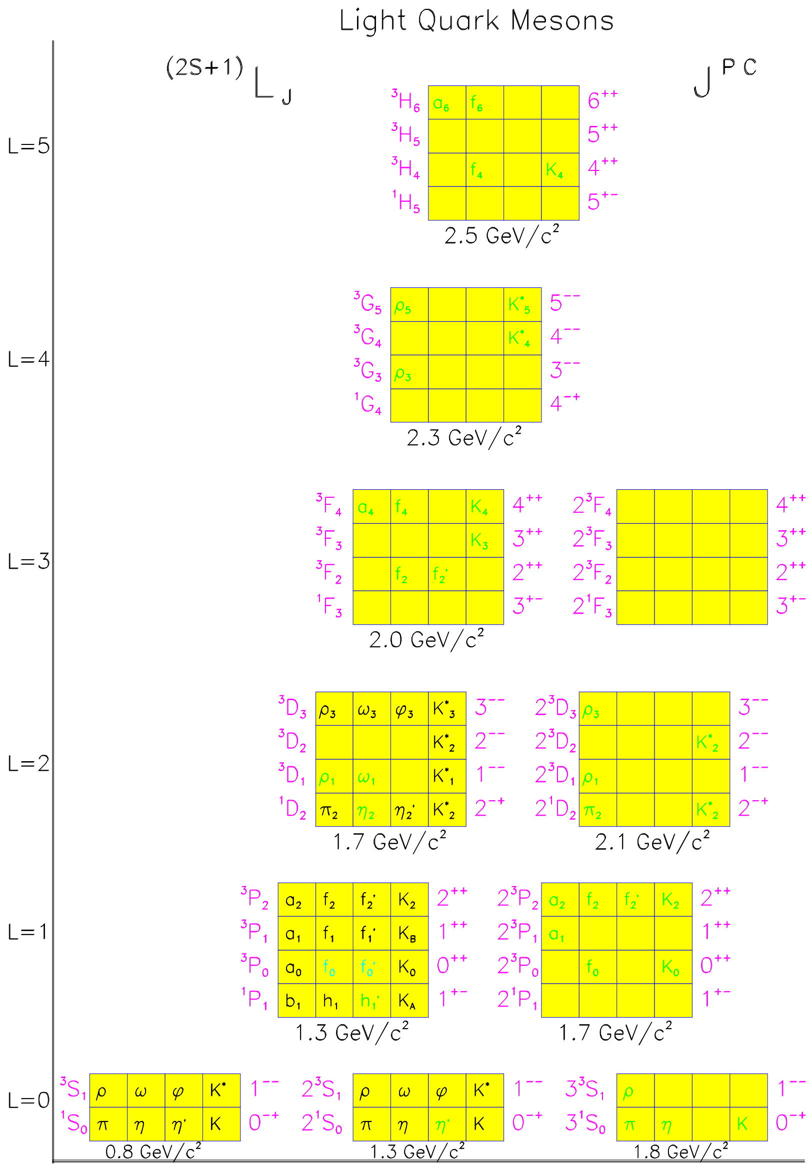

Figure 3.2: The $q\bar{q}$ spectrum of states. The assignments of the light colored states are speculative, while the empty boxes are missing states. The orbital angular momentum of the nonet is plotted on the vertical axis, while the towers of radial excitations are shown along the horizontal axis.

Production of mesons using beams of photons is expected to add much to our knowledge of light quark mesons. For reasons which are partly technical and partly historical, there is little known about the photoproduction of light mesons. In contrast, there is a wealth of data from fixed target experiments using π and K beams, $\bar{p}p$ annihilations, central production, two–photon fusion and from J/ψ decays. Experience has shown that information from new probes leads to an increased understanding of the meson spectrum and that is expected to be especially true of the photon.

The photon is a very different probe compared to the π or K. The valence quark content of these pseudoscalar beams consists of a q and $\bar{q}$ with spins antiparallel ($S = 0$) whereas the photon, via vector dominance, can be viewed as a vector $q\bar{q}$ with spins aligned ($S = 1$). Model calculations within the flux tube picture view the incident probe as a spins aligned $q\bar{q}$ system with its flux tube in its ground state. If, after scattering the flux tube is excited to its first excited state and the quark spins remain aligned, the resulting system can have J^{PC} quantum numbers of: $\underline{0^{+-}}$, 0^{-+}, 1^{+-}, $\underline{1^{-+}}$, $\underline{2^{+-}}$ and 2^{-+}. The underlined three possibilities are exotic combinations of J^{PC}. Another recent flux tube calculation [3] indicates that the photoproduction cross section for the 1^{-+} exotic may be as large $0.8\,\mu$b, which is comparable in size to typical meson production.

Since the photon can also be viewed as a valence $s\bar{s}$ system, the photon is expected to be a rich source of meson states with an $s\bar{s}$ component. The identification of $s\bar{s}$ members of the nonets has been and will continue to be important in the assignment of mesons to the nonets. The mixing in nonets has played an important role in identifying scalar glueball candidates, and non–ideal mixing in other sectors would help establish other unusual mesons. The $s\bar{s}$ component of the photon provides us with an important bridge between the very light quark sector of u and d quarks and the heavy quark sector starting with the c quark.

Photons can be polarized and this polarization will be a powerful tool in the spin analysis of the produced meson systems and may lead to an additional method for distinguishing hybrid states from conventional mesons.

At energies of several GeV and above, meson photoproduction proceeds dominantly through t–channel exchange mechanisms, while at lower energies there is a large contribution from s–channel baryon processes. The t–channel exchanges, or peripheral production, is usually broken into two classes based on the exchanged object. Simple t–channel meson exchange where a $q\bar{q}$ meson is exchanged, and *diffractive production*, or *pomeron* exchange. It is useful to distinguish them because they can be separated to a large extent kinematically, and in some reactions they populate different meson sectors. For our purposes, these two forms of t–channel exchange are much more interesting than the s–channel processes.

Also at energies of several GeV and above the incident photon, through vector dominance, behaves like a vector meson and diffractively scatters off the target nucleon. The intermediate vectors $\rho : \phi : \omega$ are theoretically produced in the intensity ratios 9:2:1, due to their constituent quark charges. Although diffractive scattering is poorly understood in terms of elementary QCD interactions, it is well known that it can be treated as the exchange of neither flavor nor charge in the t–channel. This leads to the production of $C = (-)$ neutral hadronic states with all possible J^P. Since the nature of the pomeron is not well understood, it is difficult to anticipate which $C = (-)$ states will be produced with large amplitudes, and what the relative amplitudes will be. Indeed, a systematic survey of the diffractive photoproduction amplitudes may give us interesting new information about the nature of the pomeron.

At lower energies, nondiffractive mechanisms with nonvacuum t–channel exchanges become important and even dominant. One-pion exchange is especially interesting, because it can be isolated by cuts in t and by choice of final state flavor, and this provides a filter for $G = (-)$ and (for neutrals) $C = (-)$ states. States which couple strongly to $\rho\pi$, $\omega\pi$ and $\phi\pi$ should then be produced profusely. Of course, other meson exchanges will also occur, and will allow us to photoproduce most of the light–quark mesons. Pomeron exchanges are expected to have nearly constant energy dependence sufficiently high above the meson threshold, while the meson exchanges will be produced with cross sections that fall like E^{-2}. The energies available at HALL D are chosen to be in the transition region between the two mechanisms.

3.1.4 Experimental situation

The current experimental situation in photoproduction is sparse at best and a unique opportunity now exists using high intensity polarized photon beams available at a 12 GeV CEBAF to radically change this. With tagged photon intensities between 10^7 and 10^8 per second, it will be possible to generate data samples comparable or larger than all other meson production reactions. This will allow a full partial wave analysis, which in turn will allow us to identify both normal $q\bar{q}$ mesons, as well as non–$q\bar{q}$ states. The addition of linear polarization will both simplfy the partial wave analysis, and improve our understanding of the production mechanisms.

Current photoproduction data

Table 3.1 is a partial compilation of known photoproduction cross sections and the numbers of events from the existing experiments. The typical cross sections range from of order 0.1 μb up to of order 10 μb, with most measurements involving rather small numbers of events, typically on the order of a few thousand. These experiments were able to perform careful spin analyses, from which much was learned. However, the statistics were insufficient for a full partial wave analysis. This situation can be radically improved in photoproduction experiments at CEBAF, where a full partial wave analysis involving both production and many decay channels will be possible. Typically, these analyses divide the photoproduction data into bins of *invariant mass* and $|\, t \,|$. A reasonable grid might be 5 bins in $|\, t \,|$ between 0.0 and 1.0 $(GeV/c^2)^2$, and 0.01 GeV/c^2 wide bins in mass. Making the following conservative assumptions allow one to estimate a typical year's worth of data.

- The tagged photon flux is $\Phi = 10^7 s^{-1}$. The tagger sees a 3 GeV energy bite which tops out at 95% of the electron beam energy, E_e. (Hall B can currently tag five times this rate.)
- The total photoproduction cross section for a reaction $\gamma p \to NX$ is $\sigma = 1.0\,\mu$b. This is independent of the photon energy, and distributed over the m_x vs t plane using a t–dependent weight, $e^{-8|t|}$. It should be noted that the slope parameter of 8 $(GeV/c^2)^{-2}$ is at the high end of expected slopes, which range from 4 to 8 $(GeV/c^2)^{-2}$.

Reaction	E_γ *GeV*	σ (μb)	*Events*	*Ref.*
$\gamma p \to p\pi^+\pi^-$	9.3		3500	[4]
$\gamma p \to p\pi^+\pi^-$	19.3		20908	[5]
$\gamma p \to p\pi^+\pi^-\pi^\circ$	2.8		2159	[4]
$\gamma p \to p\pi^+\pi^-\pi^\circ$	4.7		1606	[4]
$\gamma p \to p\pi^+\pi^-\pi^\circ$	9.3		1195	[4]
$\gamma p \to p\pi^+\pi^-\pi^\circ$	4.7–5.8	$13.5 \pm 1.5\,\mu b$	3001	[6]
$\gamma p \to p\pi^+\pi^-\pi^\circ$	6.8–8.2	$11.8 \pm 1.2\,\mu b$	7297	[6]
$\gamma p \to n\pi^+\pi^+\pi^-$	4.7–5.8	$4.6 \pm 1.4\,\mu b$	1723	[6]
$\gamma p \to n\pi^+\pi^+\pi^-$	6.8–8.2	$4.0 \pm 1.2\,\mu b$	4401	[6]
$\gamma p \to n\pi^+\pi^+\pi^-$	16.5–20		3781	[7]
$\gamma p \to p\pi^+\pi^-\pi^\circ$	20–70		14236	[8]
$\gamma p \to p\pi^+\pi^-\pi^+\pi^-$	4–6	$4.0 \pm 0.5\,\mu b$	~ 330	[9]
$\gamma p \to p\pi^+\pi^-\pi^+\pi^-$	6–8	$4.8 \pm 0.5\,\mu b$	~ 470	[9]
$\gamma p \to p\pi^+\pi^-\pi^+\pi^-$	8–12	$4.5 \pm 0.6\,\mu b$	~ 470	[9]
$\gamma p \to p\pi^+\pi^-\pi^+\pi^-$	12–18	$4.4 \pm 0.6\,\mu b$	~ 380	[9]
$\gamma p \to p\pi^+\pi^-\pi^+\pi^-$	15–20		6468	[10]
$\gamma p \to p\pi^+\pi^-\pi^\circ\pi^\circ$	20–70		8100	[11]
$\gamma p \to p\pi^+\pi^+\pi^-\pi^-\pi^\circ$	19.5		2553	[12]
$\gamma p \to \Delta^{++}\pi^-\pi^+\pi^-$	4–6	$1.65 \pm 0.2\,\mu b$	~ 200	[9]
$\gamma p \to \Delta^{++}\pi^-\pi^+\pi^-$	6–8	$1.8 \pm 0.2\,\mu b$	~ 200	[9]
$\gamma p \to \Delta^{++}\pi^-\pi^+\pi^-$	8–12	$1.1 \pm 0.2\,\mu b$	~ 200	[9]
$\gamma p \to \Delta^{++}\pi^-\pi^+\pi^-$	12–18	$1.15 \pm 0.2\,\mu b$	~ 200	[9]
$\gamma p \to p\omega$	4.7–5.8	$2.3 \pm 0.4\,\mu b$	< 1600	[6]
$\gamma p \to p\omega$	6.8–8.2	$2.0 \pm 0.3\,\mu b$	< 1200	[6]
$\gamma p \to p\omega$	4.7	$3.0 \pm 0.3\,\mu b$	1354	[4]
$\gamma p \to p\omega$	9.3	$1.9 \pm 0.3\,\mu b$	1377	[4]
$\gamma p \to p\phi$	4.7	$0.41 \pm 0.09\,\mu b$	136	[4]
$\gamma p \to p\phi$	9.3	$0.55 \pm 0.07\,\mu b$	224	[4]
$\gamma p \to na_2^+$	4.7–5.8	$1.7 \pm 0.9\,\mu b$		[6]
$\gamma p \to na_2^+$	6.8–8.2	$0.9 \pm 0.9\,\mu b$		[6]
$\gamma p \to na_2^+$	19.5	$0.29 \pm 0.06\,\mu b$	~ 100	[7]

Table 3.1: A sample of measured photoproduction cross sections from several references. Note the small numbers of events in any given channel.

- The experiment runs for 300 days per year with 33% live time.
- The overall reconstruction efficiency is 10%

In Fig. 3.3 are shown the expected number of events collected under the above assumptions for E_e=6.0, 8.0, 10.0 and 12.0 GeV. Fig. 3.3(a) is a sum over all $\mid t \mid$ between 0 and 1.0 $(GeV/c^2)^2$ and shows on order of 100000 events per mass bin. Fig. 3.3(b) through (f) show the events binned in $\mid t \mid$. Due to the $e^{-8|t|}$ dependence of the cross section, the number of events per t–bin falls off rapidly for the higher t bins. However, even in the highest t bin, there are still several hundred events per mass bin, which is quite sufficient to perform a full partial wave analysis.

The photon beam energy

The range of meson masses, from the lightest mesons up to ≈ 3 GeV/c^2, is expected to be rich in non-conventional mesons. This includes glueball and exotic hybrid masses, as predicted by lattice gauge calculations and various models such as flux tube models and bag models. Figure 3.4 shows the maximum mass of particle X, in the reaction $\gamma p \to Xp$ as a function of incident photon energy. As can be seen from this plot, the desired mass range could be achieved with photon energies below ≈ 8 GeV. However, other factors are equally important.

An important consideration in the choice of energy is the effect of the minimum square of the momentum transfer, $\mid t_{min} \mid$, from incoming photon to outgoing nucleon required in the reaction $\gamma p \to Xp$. The dependence of $|t_{min}|$ on the mass of X is shown in Figure 3.4 for various incident photon energies. Cross sections for t–channel meson production are known to scale like $e^{-b|t|}$, where the slope parameter b had values between 4 and 8 $(GeV/c^2)^{-2}$. As such, it is clear that energies higher than 8 GeV are needed in order to produce mesons in the desired mass range with adequate statistics.

The effect of $|t_{min}|$ can be illustrated in the production rate of mesons in peripheral processes. Figure 3.5 shows the mass spectrum of the meson system X in the reaction $\gamma p \to Xp$. Resonances with equal cross-sections are assumed but weighted by $dN/dt = e^{-8\cdot|t|}$. Resonance widths were all chosen to be 0.10 GeV/c^2 with masses of 1.0, 1.5, 2.0 and 2.5 GeV/c^2 for incident photon energies of 6, 8, 10, and 12 GeV. Clearly, photon beam energies of $\approx$ 10.5 GeV are required if the mass region up to 3 GeV/c^2 is to be studied.

The final state mesons can be produced as decay products of low $- \mid t \mid$ production of both meson and baryon resonances. As the beam energy is increased, the kinematical overlap between these two processes is reduced due to the expansion of the available phase space for production. This is illustrated by the Dalitz plot boundaries of Figure 3.6 for the reactions $\gamma p \to \pi\pi p$ and $\gamma p \to \eta\eta p$ for various incident photon energies. As the incident energy is increased from 4 to 8 to 12 GeV, the effect of overlap of produced mesons with produced baryon resonances (N^* or Δ) becomes less important. In addition, the cross section for s–channel baryon production falls away rapidly as one goes to higher photon energies.

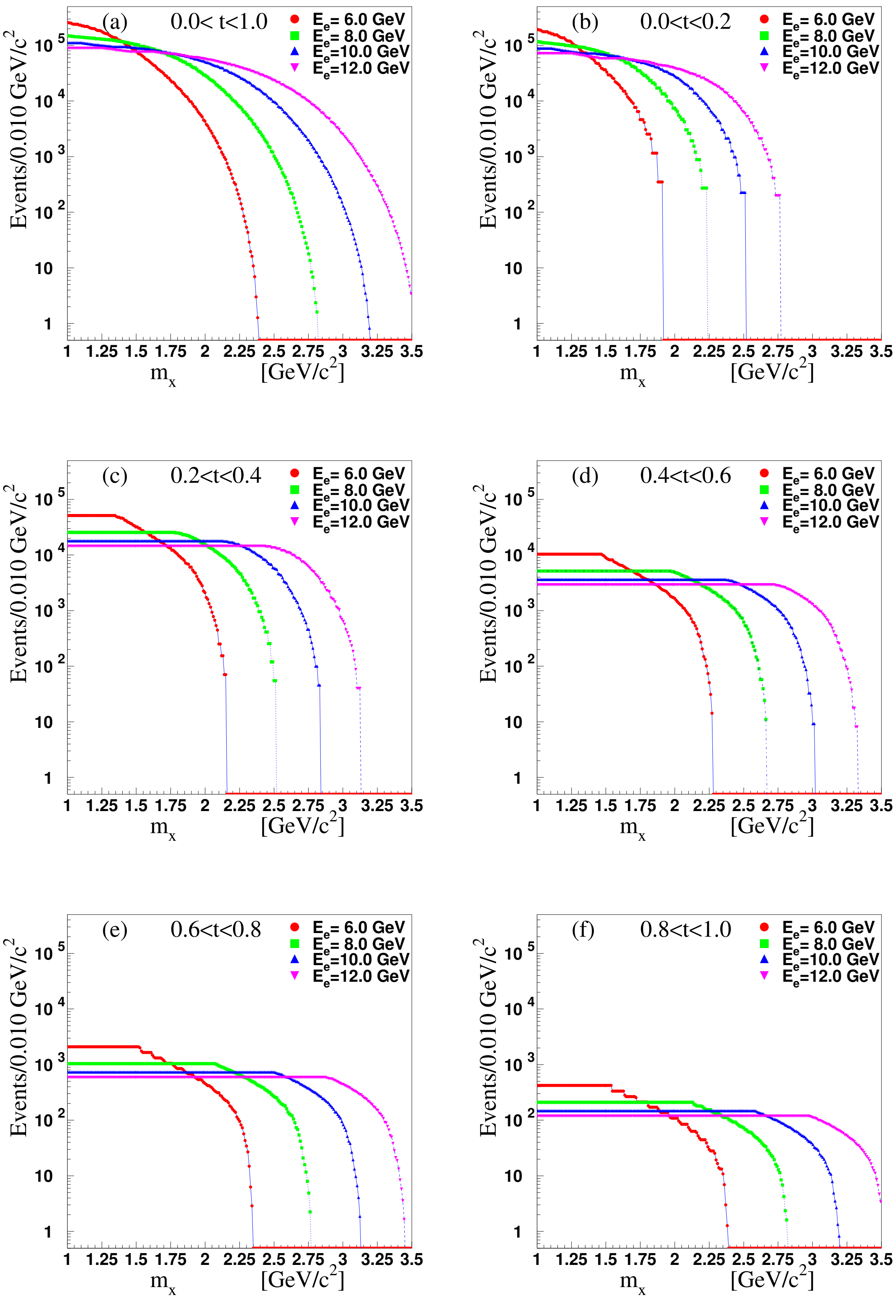

Figure 3.3: Expected numbers of events from the reaction $\gamma p \to Xp$ for $0.010\ GeV$ wide bins in m_x.The data assume an energy independent total cross section of $\sigma = 1.00 \mu b$. The four curves are from top to bottom for $E_e = 6\ GeV$, E_e=8 GeV, E_e=10 GeV and E_e=12 GeV.

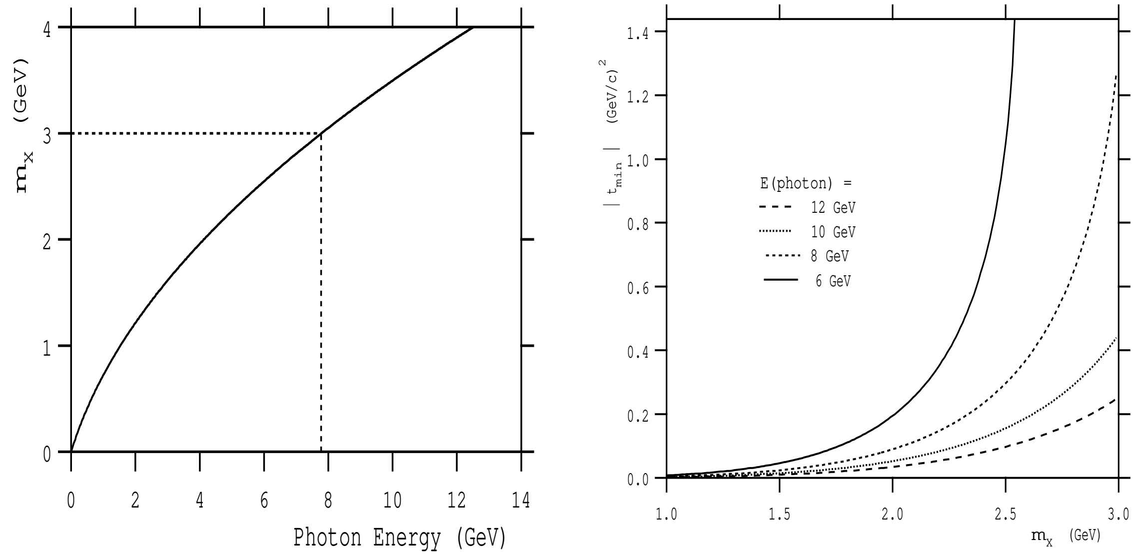

Figure 3.4: Kinematic limits on production properties for several choices of beam energy. (left) Maximum mass for particle X as a function of incident photon energy in the reaction $\gamma p \to Xp$. (right) The minimum value of $\mid t \mid$ as a function of the mass of particle X in the reaction $\gamma p \to Xp$ for various values of incident photon energies.

3.1.5 Photon linear polarization

For processes dominated by t–channel exchanges, as expected at HALL D energies, linear polarization is very important since it enables one to separate natural from unnatural parity exchanges. Measurement of the naturality of the exchanged particle together with its t–dependence is crucial for extracting photocouplings of hybrids and therefore discriminating between models of hybrid structure.

To illustrate how linear polarization is crucial in determining the naturality of the exchanged particle we will consider the following simple example. We assume that the exchanged particle has either $J^P = 0^+$ or 0^-, (natural or unnatural respectively), and we refer to these two amplitudes as A^N and A^U. We will also assume that the produced mesonic system is a $J^P = 1^-$ state, (natural parity). Parity invariance imposes relations between amplitudes with opposite spin projections which are summarized in Table 3.2.

t–channel exchange	Amplitude relations
$J^P = 0^-$	$A^U_{++} = -A^U_{--} \quad A^U_{+-} = A^U_{-+} = 0$
$J^P = 0^+$	$A^N_{++} = +A^N_{--} \quad A^N_{+-} = A^N_{-+} = 0$

Table 3.2: Relations between vector meson photoproduction amplitudes $A_{\lambda_\gamma,\lambda_V}$ in the Gottfried–Jackson frame. Dependence on target and recoiling baryon spins is implicit.

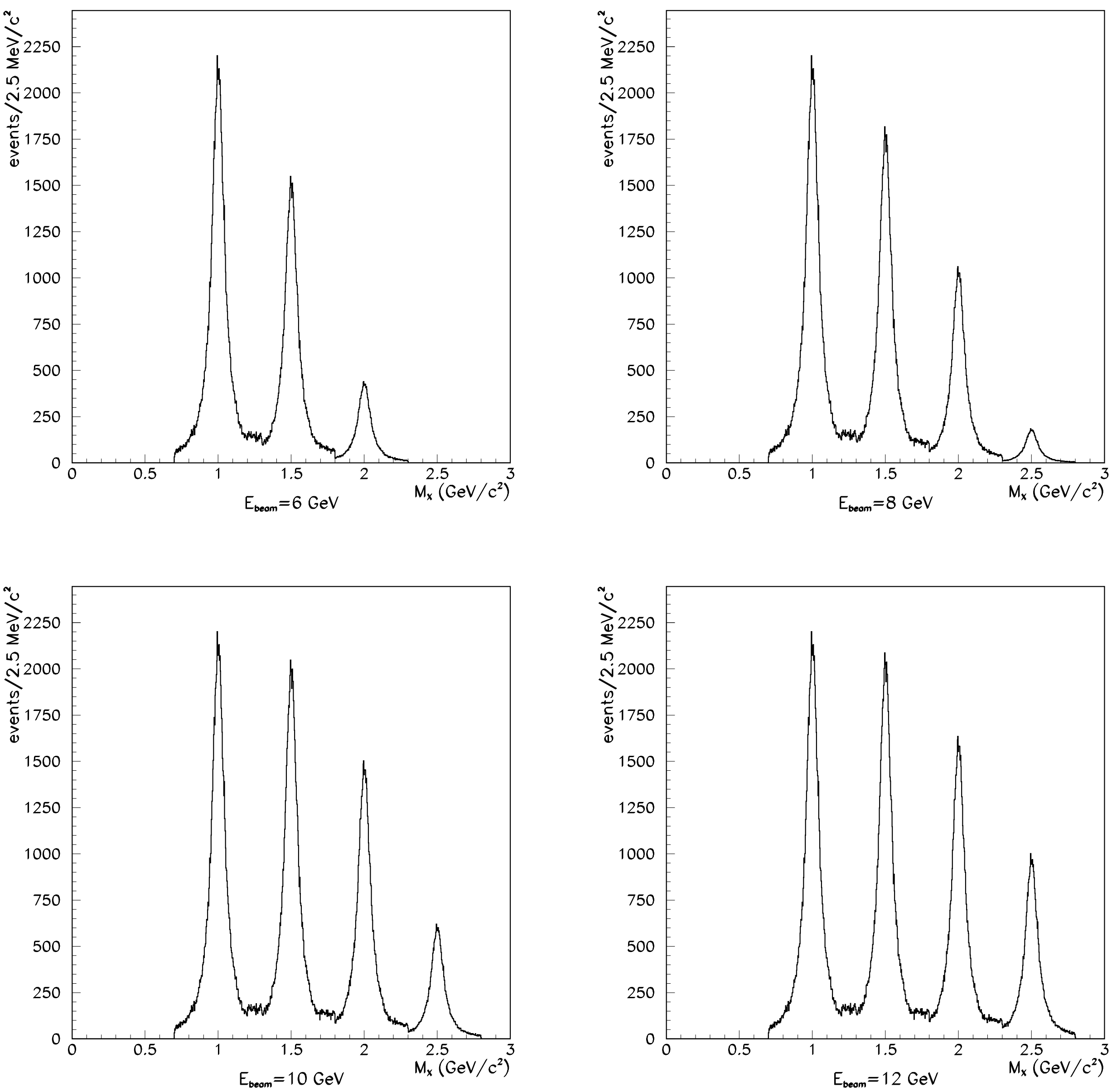

Figure 3.5: Plots of the mass distribution of 4 produced resonances in the reaction $\gamma p \rightarrow Xp$ taking into account the t_{min} effect for an incident photon energy of 6 GeV (upper left), 8 GeV (upper right), 10 GeV (lower left) and 12 GeV (lower right).

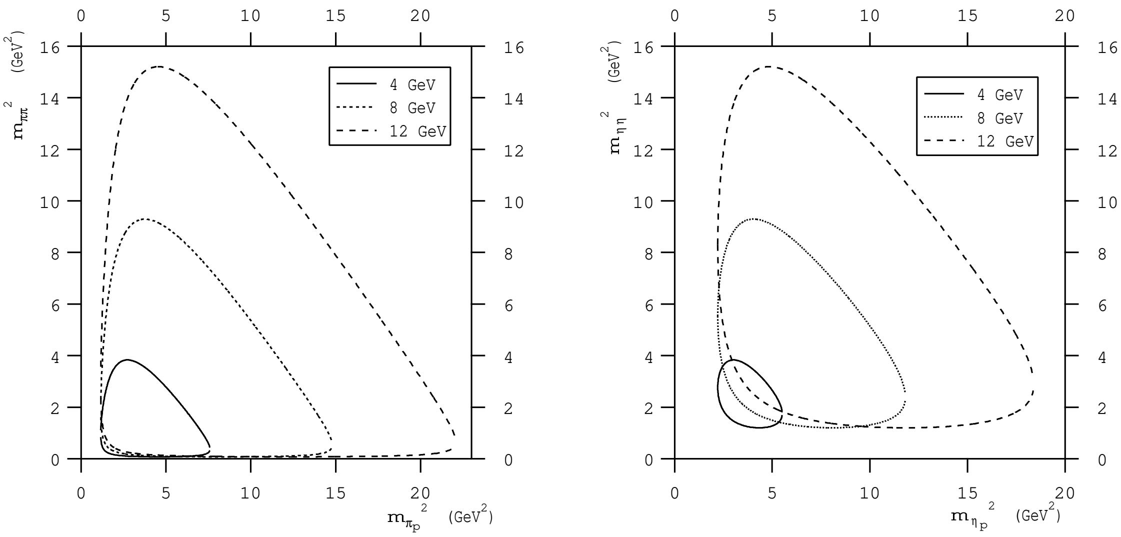

Figure 3.6: Dalitz plot boundaries for the reaction $\gamma p \to \pi\pi p$ (left) and $\gamma p \to \eta\eta p$ (right) for incident photon energies of 4, 8 and 12 GeV.

These relations can be derived by considering the production process in the Gottfried–Jackson frame. In this frame, the produced vector meson is at rest and the 3–momentum of the photon is along the positive z axis. The z axis is also used to define spin projections. We use the photon helicity, $\lambda_\gamma = \pm 1$, to define the polarization state of the photon. In the Gottfried–Jackson frame, the photon helicity and photon spin projection along the z axis become equal. Parity invariance places restrictions on the orbital angular momentum, L, between photon and the exchanged particle. In the Gottfreid–Jackson frame, (vector meson at rest), L is even, $(L = 0, 2)$ if the exchanged particle is natural and L is odd, $(L = 1)$, if it is unnatural. In addition, the orbital angular momentum does not contribute to the total spin along the z axis. Therefore the spin projection, λ_V, of the produced vector meson becomes equal to the helicity of the photon, $\lambda_V = \lambda_\gamma \equiv \lambda$. This means that all amplitudes involving a helicity flip are zero. Furthermore, the coupling between the photon, the produced vector meson, and the exchanged particle is proportional to the Clebsch-Gordan coefficient, $\langle\, 1\,\lambda_\gamma, L\,0 \mid 1\,\lambda_V \,\rangle$. These coefficients satisfy the relationship:

$$\langle\, 1\,-\lambda_\gamma, L\,0 \mid 1\,-\lambda_V \,\rangle \;=\; (-1)^L \langle\, 1\,\lambda_\gamma, L\,0 \mid 1\,\lambda_V \,\rangle\,,$$

which allows us to arrive at the results given in Table 3.2.

If the two exchanges take place simultaneously, the total amplitude is given by a sum of A^U and A^N and the production rate is proportional to

$$R \propto \sum_{\lambda',\lambda=\pm} \rho_{\lambda\lambda'} (A^U_{\lambda\lambda} + A^N_{\lambda\lambda})(A^U_{\lambda'\lambda'} + A^N_{\lambda'\lambda'})^*. \tag{3.1}$$

The spin density matrix, $\rho_{\lambda'\lambda}$, of the photon is given as $\rho_{\lambda'\lambda} = a_{\lambda'} a^*_\lambda$. Here, a_λ is the probability amplitude for finding a photon in the initial state with helicity λ. The photon spin density matrices are listed in Table 3.3. For circularly polarized beams, $a_\lambda = \delta_{\lambda +}$ for right–handed polarization, and $a_\lambda = \delta_{\lambda-}$ for left–handed polarization states, (the δ represents the Kronecker symbol). From these, the rates for the right–handed polarization are given in 3.2.

$$R \propto \mid A^U_{++} + A^N_{++} \mid^2 \tag{3.2}$$

This mixes contributions from both natural and unnatural exchanges. Similarly, for unpolarized beams the rate is given in 3.3 which also involves contributions from both naturalities.

$$R \propto \mid A^U_{++} + A^N_{++} \mid^2 + \mid A^U_{--} + A^N_{--} \mid^2 \tag{3.3}$$

On the other hand, linearly polarized photons are able to separate the naturalities. For linearly polarized light, (polarization perpendicular to the production plane), the a_λ are given as follows:

$$\begin{array}{ll} x \text{ Direction} & a_\lambda = \dfrac{1}{\sqrt{2}}\left[\delta_{\lambda\,-} - \delta_{\lambda\,+}\right] \text{ and} \\ y \text{ Direction} & a_\lambda = \dfrac{i}{\sqrt{2}}\left[\delta_{\lambda\,-} + \delta_{\lambda\,+}\right]. \end{array}$$

From these, we arrive at the rates for the polarization in the x (equation 3.4) and y (equation 3.5) directions. The natural and unnatural exchanges have been separated based on the polarization of the photon, x or y respectively.

$$x \text{ Direction} \qquad R \propto \mid A^N_{++} \mid^2 + \mid A^N_{--} \mid^2 \tag{3.4}$$

$$y \text{ Direction} \qquad R \propto \mid A^U_{++} \mid^2 + \mid A^U_{--} \mid^2 \tag{3.5}$$

The above relations between R and the different photon polarization states are summarized in Table 3.3.

Photon Pol.	Density matrix	Rate	
None	$\frac{1}{2}\begin{pmatrix} 1 & 0 \\ 0 & 1 \end{pmatrix}$	$\frac{1}{2}\sum_\lambda(\mid A^N_{\lambda\lambda} + A^U_{\lambda\lambda} \mid^2)$	$\frac{1}{2}(\lvert A_{++}\rvert^2 + \lvert A_{--}\rvert^2)$
Right handed	$\begin{pmatrix} 1 & 0 \\ 0 & 0 \end{pmatrix}$	$\lvert A^N_{++} + A^U_{++}\rvert^2$	$\lvert A_{++}\rvert^2$
Left handed	$\begin{pmatrix} 0 & 0 \\ 0 & 1 \end{pmatrix}$	$\lvert A^N_{--} + A^U_{--}\rvert^2$	$\lvert A_{--}\rvert^2$
Linear-y	$\frac{1}{2}\begin{pmatrix} 1 & 1 \\ 1 & 1 \end{pmatrix}$	$\sum_{\lambda=\pm} \lvert A^N_{\lambda\lambda}\rvert^2$	$\frac{1}{2}\{\mid A_{++} \mid^2 + \mid A_{--} \mid^2$ $+2\mathrm{Re}(A_{++}A^*_{--})\}$
Linear-x	$\frac{1}{2}\begin{pmatrix} 1 & -1 \\ -1 & 1 \end{pmatrix}$	$\sum_{\lambda=\pm} \lvert A^U_{\lambda\lambda}\rvert^2$	$\frac{1}{2}\{\mid A_{++} \mid^2 + \mid A_{--} \mid^2$ $-2\mathrm{Re}(A_{++}A^*_{--})\}$

Table 3.3: Spin density matrix elements for various photon polarizations and the corresponding vector meson production rates in terms of t-channel amplitudes, $A_{\lambda\lambda} = A^N_{\lambda\lambda} + A^U_{\lambda\lambda}$ assuming a combination of a natural (N) and unnatural (U), spin–0 exchanges in the t–channel.

Inspecting the results from Table 3.3 it becomes clear that to distinguish between the different naturalities in the t-channel requires measuring the relative phase between amplitudes with opposite spin projections of the beam and of the produced meson. This can only happen if the measured rate depends on the interference between amplitudes with opposite spin projections. Since unlike a spin–0 particle, the photon can have more than one polarization state, the necessary condition is to use a *coherent* superposition of the two possible photon polarization states. As seen from the last column in Table 3.3, this is the case if photons are polarized linearly, (or more generally, elliptically). It is however not the case for unpolarized photons when contributions from the two polarization add *incoherently* nor for circularly polarized photons when only one of the two amplitudes contributes to the rate. Finally, being able to separate the natural and unnatural exchanges reduces the number of free parameters in the partial wave analysis by a factor of two. This provides a significant simplification in the overall analysis.

In the case of a spin-less exchange discussed above, in the Gottfried–Jackson frame the spin projection of the produced mesonic system becomes equal to photon helicity and therefore linear polarization is sufficient to determine the naturality of the exchanged particle, *i.e.* no measurement of the outgoing meson polarization is necessary (this is true even if the produced meson has $J > 1$ since orbital angular momentum has a projection of 0 along the z axis in the Gottfried-Jackson). In a more general case when spin of the t-channel exchange is non-vanishing, the relation $A^{N,U}_{\lambda_\gamma,\lambda_M} = \tau_M A^{N,U}_{-\lambda_\gamma,-\lambda_M}$ still holds, here λ_M and τ_M are the spin projection along the z axis and naturality of the produced meson respectively, but in general $\lambda_\gamma \neq \lambda_M$ and it is also possible for the mesonic system to be produced with vanishing spin projection along the z axis. In this case, linear polarization alone is not sufficient. It becomes necessary to have information on the polarization of the produced meson which can be done by measuring angular distribution its decay products [13]. However, it is still true that the two amplitudes do not interfere, and the simplification in the partial wave analysis is still valid.

As mentioned above, pion beams have no initial state polarization and therefore measurement of the polarization of the produced meson is sufficient to discriminate between naturalities of the t–channel exchanges. However the vector nature of the photon gives us access to a larger number of observables. For example, photoproduction of vector mesons can be described in terms of 17 independent real spin–density matrix elements. For comparison, the analogous reaction with pion beams, $\pi p \to VN$ has only 4 independent real parameters. Out of the 17 parameters in photoproduction, 11 can be measured from the angular distributions of the vector meson decays products. Sensitivity to the dynamics of the production process in photoproduction is clearly much larger. The crucial point is how many of the spin–density matrix elements can actually be measured in a single experiment. In general this number also depends on the type of photon polarization. For example, in vector meson photoproduction the vector meson is analyzed via its two body, (pseudo)scalar decay, (*e.g.* $V = \rho \to 2\pi$ or $V = \phi \to K\bar{K}$). Linearly, circularly, and unpolarized photons access 9, 5, and 3 out of the 17 spin matrix elements respectively [13]. It is also true that in general linear polarization enables one to extract the largest number of the spin–density matrix elements.

A promising reaction for producing an exotic state is a charge exchange $\gamma p \to \pi_1^+ n \to (\rho\pi)^+ n$ [14]. The advantages of the charged $(\rho\pi)^\pm$ channel is that it has $G = (-)$, $I > 0$ thus in the absence of an $I = 2$ meson multiplet, the P-wave would correspond to an $I = 1$, 1^{-+} exotic state. If the t–channel of this reaction is dominated by a one–pion exchange, OPE, then one can use the arguments given above to relate the polarization with naturalities of the produced particles [14]. Thus, for example the unnatural and natural parity states will be polarized parallel and perpendicular to the production plane, respectively. For a *natural* exotic, 1^{-+} state with mass around 1.5 to 1.6 GeV/c^2, as seen in the E852 data [15], the dominant backgrounds are expected from the *unnatural* $a_1(1260)$ and $\pi_2(1670)$. Thus, the direction of the linear polarization of the exotic signal is expected to be at 90° with respect to the backgrounds. Linear polarization could act as a filter on the naturality, by which backgrounds could be suppressed and the partial wave analysis greatly simplified.

3.2 Theoretical considerations

3.2.1 Overview

Strongly-interacting QCD is the most poorly understood regime of the standard model. Whereas conventional perturbation theory can be applied to the physics of high energies, strong QCD is essentially nonperturbative, and the study of this field has required the use of models and the development of new theoretical techniques.

The crucial feature of QCD that dominates the physics of this regime is the phenomenon of confinement. This is a nonperturbative result of gluon self-interactions, which, for example, leads to an interquark potential that grows approximately linearly with distance. Confinement implies that the isolated states we see in the spectrum are color-singlet hadrons rather than individual quarks and gluons, and the masses, interactions and decays of hadrons are for the most part problems in nonperturbative quantum field theory.

The challenge of describing strong QCD has led to the development of LGT, which continues to see wide application in QCD and in many other field theory and condensed matter contexts. The presence of confinement in pure-glue QCD is easily observed in LGT. Similarly, the spectrum of low-lying $q\bar{q}$ mesons and qqq baryons in the stable-hadron "quenched" approximation is relatively easily determined, and after about two decades of improved statistics and computer capabilities the agreement is quite good. LGT is also the preferred theoretical method for investigating strong QCD at finite temperatures (which will be studied at RHIC) and the interplay between finite temperatures and chiral symmetry breaking.

LGT makes some rather dramatic predictions for the spectrum of states that arise as a result of confinement. One prediction is that there should be a spectrum of glueballs, flavor-singlet states composed only of gluons. (An as yet unknown amount of configuration mixing with $q\bar{q}$ will take place in the physical states.) LGT methods are now sufficiently advanced for the predictions of the spectrum of glueballs to be rather precise. The lightest glueball is expected to be a scalar near 1.6 GeV/c^2, followed by a pseudoscalar and tensor at about 2.3 GeV/c^2, and many additional states at higher masses. There should also be a spectrum of quark-and-gluon hybrid states, which are more attractive experimentally because of their quantum numbers. LGT has only very recently been applied to these states, and confirms that the lightest of these ($J^{PC} = 1^{-+}$ exotic) hybrid mesons should be found at about 2.0 GeV/c^2.

Theorists have also developed various models of these hadrons. In the conventional $q\bar{q}$ and qqq sectors, Coulomb plus linear potential models have proven to be the most useful. These give very good descriptions of the spectrum of conventional hadrons and their couplings and decays, and for $q\bar{q}$ and qqq are more accurate and of wider applicability than LGT. There are several models of hybrids, which we shall discuss subsequently. The flux tube model is the best known, and gives detailed predictions of the spectroscopy and decay modes of hybrids; the unusual decay modes predicted by this model have motivated several experimental studies of $f_1\pi$ and $b_1\pi$ channels in particular. In this proposal we favor a more conservative approach, and plan to search all accessible two body modes, in addition to those suggested by the flux tube model.

How can experiment improve our theoretical understanding of the physics of strong QCD? Determination of the spectrum of exotic states will be the most important new contribution; the LGT results assume stable hybrids, and this *may* lead to an important bias in mass predictions. Similarly, the various models of hybrids differ in the details of the spectrum of states, and identification of several exotics will be crucial in determining which model describes the physics of hybrids most accurately.

The experimental determination of the exotic spectrum is already in progress. At present there are two candidate exotics, the $\pi_1(1400)$ and $\pi_1(1600)$; note that the reported masses are rather far from the LGT and flux-tube predictions of about 1.8-2.0 GeV/c^2. One pion exchange photoproduction (through $\rho\pi$) is a straightforward method for producing states with these quantum numbers, and since the $\pi_1(1600)$ was first reported in $\rho\pi$, photoproduction is an ideal way to search for this state.

Finally, to date there have been no LGT predictions of hybrid decay widths, although these are expected to be determined in future work. Hybrid decay predictions have come exclusively from models, and the unusual branching fractions predicted by the models will require experimental measurements of branching fractions and relative amplitudes for comparison. Since LGT cannot easily treat decays or radial excitations, models will continue to be important in describing the physics of exotics.

Progress in understanding the gluonic degree of freedom in strong QCD should therefore follow from experimental studies of the conventional and exotic spectrum, improved LGT studies, and improved models of these states.

3.2.2 Strong QCD and the role of glue

Eliminating quark degrees of freedom in principle allows one to focus on gluon dynamics. To date, the main source of information about confinement are the phenomenology and lattice analysis of heavy (static) quark systems. However, the light quark systems are particularly useful for studies of strong QCD. The enormous success of the quark model indicates that after dynamical chiral symmetry breaking, the effective constituent quarks behave as heavy, nonrelativistic particles. Spectroscopy and data on the residual interactions of ordinary, and in particular light gluonic mesons, will therefore provide us with crucial information about the connection between the two main features of low energy QCD.

In this section, we briefly summarize the current models of strong QCD. These models present very different concepts of the behavior of soft glue, and an extensive and high quality experimental effort will be needed to clarify this situation.

Flux tube model

The flux tube model is an explicit realization of the string picture of glue [16]. The model is based on the strong coupling expansion of the lattice QCD Hamiltonian. One works with the basis of gauge invariant states and organizes the strong coupling eigenstates into sectors of differing *topologies*. By assuming that the inter–sector couplings are weak, one is able to restrict considerations of the dynamics to the $q\bar{q}$ valence sector. The next step was to model the dynamics of the links as N point-like spinless *beads* of mass ba, where a is the lattice spacing. Finally, adiabatic and small oscillation approximations of the flux tube dynamics are made to arrive at an N–body discrete string–like model Hamiltonian for gluonic degrees of freedom. This was meant to be operative at intermediate scales $a \sim b^{-1/2}$ where the strong coupling is order unity.

It is widely believed that at large distances glue must behave as a sort of string, so that the model is probably reasonably accurate at large scales [17]. However, the authors have relied strongly on intuition to derive the final form of the string Hamiltonian and the efficacy of their approximations is largely unknown. Nevertheless, the validity of the adiabatic and small oscillation approximations have been checked in a simple (one-bead) version of the flux tube mode [18]. It was found that neither approximation is accurate; however, the errors tend to cancel and the final hybrid mass estimates do not shift a great deal. Light hybrids are found to have a mass of roughly 1.9 GeV/c^2.

Lattice gauge theory

At present, LGT offers the greatest hope for determining the low energy properties of QCD. In principle, LGT is an exact representation of the QCD path integral which employs a lattice regulator. This is achieved by explicitly writing the path integral on a discrete four dimensional space-time lattice. The path integral is then numerically evaluated using sophisticated Monte Carlo techniques.

Unfortunately, the lattice must be Euclidean to ensure the tractability of the numerical computations leading to problems with the definition of some quantities. Furthermore, it is very difficult to include all of the physical effects due to quarks and these are often truncated (the *quenched approximation*). Two prominent effects of this truncation are a distortion of the chiral nature of the theory and shifts in the properties of hadrons due to the neglect of coupled channel effects.

Very successful computations have been made in spite of these uncertainties. For example, the nucleon and delta masses are computed within 10% of their experimental values. Great strides in computational power and algorithm efficiency have been made in recent years. As a result reliable quenched low lying glueball masses are available. Estimates of the strengths of the scalar glueball decay modes have also been made. Finally, the masses of heavier hybrids have been determined and light hybrid masses are being calculated. Present estimates for light hybrid masses are 2.0 GeV/c^2 with an error of several hundred MeV [19]. There have also been measurements of several of the lowest lying adiabatic hybrid glue potentials [20] which are useful for heavy hybrid mass estimates and for comparison to analytic models.

Instanton models

An instanton is a specific topological vacuum gauge field configuration which is thought to dominate the QCD vacuum. Instantons were originally introduced to resolve the *U(1) problem* of QCD (based on chiral symmetry, the η' should have a lighter mass than the η – in contradiction with experiment). However, they have since been widely employed to explain many properties of strong QCD. For example, instantons induce an effective interaction between quarks which may account for chiral symmetry breaking. Calculations of hadronic masses proceed in much the same way as with lattice gauge theory – the correlation function of interpolating fields is evaluated in the instanton vacuum ensemble and the leading behavior is extracted to obtain the mass. While technical problems remain in the application of these ideas to instanton physics, initial results for the scalar glueball are in approximate agreement with lattice calculations [21]. Light hybrid masses have also been estimated with a result of roughly 1.3 GeV/c^2.

Schwinger–Dyson models

The Schwinger–Dyson equations are a set of infinitely many coupled functional equations which are equivalent to the quantum field theory from which they were derived. They are of interest in modeling strong QCD because they may be truncated in a non-perturbative manner and they are easy to organize in a way which provides information about bound states. In particular, one typically truncates the equations, assumes a confining form for the gluon propagator, solves the resulting gap equation for the quark propagator, and solves the Bethe-Salpeter for the properties of the bound state in question [22].

This approach has the benefits of being covariant, of being close to the underlying field theory, and of being capable of describing spontaneous chiral symmetry breaking. Many successful calculations of light hadron (in particular, pion) properties are extant. The methodology may also be easily extended to finite temperatures. Unfortunately, the Schwinger-Dyson program must be considered a model of QCD because of the truncations made and assumptions about the gluon propagator. Furthermore, it is technically difficult to obtain information on heavy states. Recently Schwinger-Dyson calculations of hybrid masses have appeared. The study employs a separable model for the nonperturbative gluon propagator which provides a algebraic relation between the quark and gluon propagators, the forms of which are fit to pion and kaon observables. A numerical solution of the Bethe-Salpeter equation with these propagators reproduces the pseudoscalar, vector and axialvector meson spectra to within 9% of accepted values and yields two exotic-1^{-+} mesons with masses of 1.44 and 1.50 GeV/c^2 [23].

Potential models

Potential models of hadrons date to the 1960's when they were introduced in an attempt to place Gell–Mann/Zweig's quark model on firm phenomenological ground. The introduction of QCD was crucial to providing the modern framework upon which modern quark potential models are built. These models are in large part non-relativistic or semi-relativistic and incorporate a phenomenological quark-quark interaction – usually with a linear confinement term, a short range one gluon exchange term, and perhaps terms reflecting meson loop effects (pion exchange terms). Potential models are well known for correlating vast amounts of hadronic data, from meson and baryon masses, to baryon magnetic moments, to radiative decays, to transition form factors.

Among the more severe flaws with potential models are their lack of covariance, their phenomenological character, and the lack of glue as a dynamical degree of freedom. The latter problem implies that potential models must be extended in order to describe hybrids. Several approaches have been taken in this regard. The earliest is due to Horn and Mandula [24] who postulated a massless gluon interacting with quarks via a linear potential. Other models assume massive gluons, incorporate glue-glue interactions, or abandon the idea of a glue-quark potential altogether.

Because these models rely heavily on a nonexistent phenomenology, there are relatively few predictions regarding hybrid properties. One group finds non-exotic light hybrids in the 1.3 – 1.8 GeV/c^2 range and 1.8 – 2.2 GeV/c^2 for light exotic hybrids [25]. A more recent calculation is based on a relativistic, many-body, Coulomb gauge, QCD-based model which generates an effective gluon mass by assuming a BCS–like QCD vacuum and solving the resulting gap equation. Linear confinement is assumed between color current densities which allows one to write and solve a relatively simple Salpeter equation [26]. This approach is in modest agreement with lattice results for heavy hybrids [20]. It has not yet been applied to light hybrids.

Bag models

The simplest bag models assume that colored partons are confined in a spatial region of varying (typically spherical) shape [27]. Calculating hadronic masses then becomes similar to calculating electromagnetic resonance modes in a cavity. A great advantage of this approach is that it may be formulated relativistically and hence the model is of particular use in providing qualitative information on such quantities as the nuclear equation of state. However, it does not appear to provide as consistent a picture of hadronic masses as, for example, potential models. Bag models also suffer from parameter uncertainties and theoretical problems such as spurious center of mass degrees of freedom and gluon self energies.

Hybrid calculations typically place a noninteracting quark, antiquark, and gluon in the confining region. Spin splittings may be incorporated by allowing the quarks and gluon to interact perturbatively. Because of the problems developing a consistent picture of the low mass spectrum, most bag calculations date from the early 1980's; typical masses for light hybrids are in the 1.3 – 1.8 GeV/c^2 range [28, 29, 30, 31]. More recent calculations have used the adiabatic bag model of Ref. [32] to calculate gluonic potential surfaces in heavy hybrids [33], with quite good results.

QCD sum rules

QCD sum rules are an analytical method for determining nonperturbative properties of QCD. The formalism involves equating the perturbative expression for a correlation function (say) to a spectral representation of the same function [34]. Nonperturbative information on the perturbative side of the equation is contained in unknown condensates. One may obtain the condensates by equating to well known spectra. These may then be used to predict spectral properties in other channels, such as hybrid masses and couplings. Unfortunately, this approach is not robust and a consensus on hybrid masses has not been achieved. Estimates for lightest hybrid masses are in the 2.1 – 2.5 GeV/c^2 region [35, 36, 37], however, older results and one current group [38] predict a light hybrid mass of roughly 1.5 GeV/c^2.

3.2.3 Phenomenology

With a few exceptions, such as spin splitting of quarkonia, and the phenomenology of strong two body decays, we have had to rely on lattice calculations to provide information on confinement. Most notable are predictions for hybrid masses [19, 20, 39, 40, 41], convergence in the low lying glueball spectrum [42, 43, 44, 45], and the calculation of the potential surfaces for excited glue configurations with static quarks[20]. The latter is especially useful for comparison with model predictions. For example it has recently been compared to the bag model [46], the flux tube model [17], Nambu-Goto inspired models [47], and to a relativistic constituent glue model[26].

Several interesting features have emerged. Although it is believed that glue must behave in a string-like fashion at large quark separation, this behavior is not being seen on the lattice (there are now indications that it may be occurring at very large distances[17]). Alternatively, constituent models have been shown to either contain the wrong degrees of freedom (and so are unable to describe all of the possible gluonic excitations seen on the lattice) or to approach the linear confining regime too quickly[26]. The latter is interesting because it implies that more degrees of freedom than a single constituent gluon are required to describe hybrids at moderate to large interquark separation.

Although the lattice is useful for obtaining static information about hadrons, it is very difficult to calculate hadronic decays or interactions numerically. Thus the experimental explication of this important area of hadronic physics is crucial. At present there are very few models of hybrid decays. These comprise older perturbative gluon-based models[48, 49, 50], the well-known flux tube decay model[51, 52], and a new flux tube-based decay model[53, 54]. The importance of understanding this aspect of hybrids cannot be overstated. For example, simply detecting hybrids will be difficult without some guidance as to how they decay. We stress that models of hybrid decays are built upon assumptions of hybrid structure and decay mechanisms. As an example of this point we note that in the flux tube model, vector hybrids contain quarks in a spin singlet. In constituent models; however, the quarks may be in a spin triplet. This simple difference in structure may lead to large differences in the decay characteristics of vector hybrids because it is widely held that states with quarks in a singlet cannot decay to mesons which also have their quarks in spin singlets (the $S = 0 \not\to (S = 0) + (S = 0)$ rule).

Although the prospects of constructing a reliable model of hybrid decay seems daunting without extensive input from experiment, an interesting phenomenon has been observed in all hybrid decay models considered to date: hybrids couple weakly to identical S-wave mesons[1]. Thus for example a hybrid with the quantum numbers of the ρ will not decay to $\pi\pi$ and only weakly to $\omega\pi$ but strongly to πa_1. This expectation can be used to distinguish hybrids from the conventional spectrum. Even though the hierarchy of hybrids decays have

[1]The model of Ref.[53] generalizes this: hybrids couple weakly to all pairs of identical mesons.

been found to be rather insensitive to the details of the underlying dynamics, as illustrated in Table 3.4 if there is more than one wave present in a given decay mode the relative strengths are highly sensitive probes of hybrid structure. It is apparent that a detailed partial wave analysis will be crucial in discriminating between models of hybrids.

Decay Mode	Flux–tube [54]		Constituent Glue		QCD sum rules		
	PSS	IKP	[55]	[48]	[56]	[57]	[58]
$b_1\pi$	24	59	144	3			
$f_1\pi$	5	14		0	100 ± 50		
$\rho\pi$	9	8	36	2	40 ± 20 †	274	600
K^*K	1	0		2		8	300
$\eta'\pi$	0	0		28		3	3
$\eta(1295)\pi$	2	1					
$\eta\pi$	0	0		44			0

Table 3.4: Predicted partial widths (in all partial waves) of the 1^{-+} exotic hybrid in MeV. The hybrid mass is 1.6 GeV/c^2 [54, 48, 56, 58], 1.5 GeV/c^2 [57] or 1.4 GeV/c^2 [55]. $\rho\omega$ and $f_2\pi$ is 0 MeV/c^2 [54]. The D– to S–wave width ratio of $b_1\pi$ and $f_1\pi$ is much smaller in the PSS than in the IKP model [54]. Other constituent gluon models quote ratios of widths [59]. † $10 - 100$ [37].

3.2.4 Conventional light quark mesons - theory

The conventional $q\bar{q}$ light meson spectrum is reasonably well understood theoretically up to masses of about 1.5 GeV/c^2. Electromagnetic transitions, which are clearly relevant to studies of photoproduction, are known for many of the light S-wave mesons and for several P-wave states, and are in good agreement with simple electric and magnetic dipole transition rate formulas. Strong decays are much less well understood, indeed the mechanism of strong decays is one of the most important open questions in the field of conventional light hadron spectroscopy. There is a phenomenological model of light hadron decays, known as the $^3P_0$ model, which assumes that decays take place through pair production of a $q\bar{q}$ pair from the vacuum, with $S = 1$, $L = 1$, $J = 0$ (hence $J^{PC} = 0^{++}$) quantum numbers. Other decay models are generally simple modifications of the spatial strength of pair production that do not change this basic decay mechanism. Although the relationship between this phenomenological decay model and the quark-gluon and gluon-gluon interactions of QCD has not been established, the model can be related to QCD for nonrelativistic quark pair production in the strong coupling limit [60].

This decay model is especially useful in searches for exotica because it gives reasonably accurate predictions for partial widths and relative decay amplitudes of well established $q\bar{q}$ states. An accurate description of decay amplitudes of conventional $q\bar{q}$ mesons is important because we expect the anomalous strong decay amplitudes of non-exotic glueballs and hybrids to distinguish them from non-exotic $q\bar{q}$ states with identical quantum numbers and similar masses. Indeed, strong decay amplitudes and quantum numbers may be the only experimental information we will have for most higher-mass meson resonances.

The spectrum of conventional light $q\bar{q}$ resonances is discussed in detail by Godfrey and Isgur [61] in the most cited and most successful work on meson spectroscopy, which uses a relativised Coulomb-plus-linear potential model. One should note however that there are recent experimental indications that their model has overestimated the masses of radial excitations [62], so an updated theoretical study of higher-mass states may be required. Mukhopadhyay [63, 64] has also given detailed predictions of $q\bar{q}$ spectroscopy, and more recent addenda regarding decays of $s\bar{s}$ states have been given by Godfrey *et al.* [65, 66]. An exhaustive calculation of all allowed quasi-two-body strong decay amplitudes in the $^3\mathrm{P}_0$ model for all $n\bar{n}$ mesons ($n = u$ or d quarks) expected up to 2.1 GeV/c^2 has been published recently by Barnes, Close, Page and Swanson [67]. These theoretical results should suffice to distinguish between plausibly $q\bar{q}$ and non-$q\bar{q}$ mesons in the mass regime of greatest current interest, provided that the $^3\mathrm{P}_0$ model remains accurate for these higher-mass states.

3.2.5 $s\bar{s}$ states - theory

The quark model describes conventional light mesons as bound states of quarks and antiquarks, interacting through perturbative gluon exchange at short distance and a non-perturbative confining interaction at large distances. Four "flavor" types are distinguished according to the type of quark and antiquark in the meson; in the light $q\bar{q}$ mesons we can have any of the three light quarks u, d, s and their antiquarks. If both q and $\bar{q}$ are of u, d type we have a "nonstrange meson", which we refer to generically as $n\bar{n}$. With one chosen from $n = u, d$ and the other s, we have an $n\bar{s}$ or $s\bar{n}$ "kaonic state". The remaining possibility, $s\bar{s}$, is called "strangeonium".

The nonstrange $n\bar{n}$ mesons are fairly well established experimentally at lower masses, *albeit* with notable exceptions such as the scalar states. Taking 2.2 GeV/c^2 as a current frontier of light meson spectroscopy, the quark model anticipates 44 $n\bar{n}$ states up to this mass. (These are the 1S, 2S, 3S, 1P, 2P, 1D, 1F = 22 J^{PC} levels, with a doubling for $I = 0$ and $I = 1$.) About half these mesons have been identified experimentally. Similarly we anticipate 22 kaonic J^{PC} levels ($n\bar{s}$ and $s\bar{n}$), and about 2/3 of these are known. In comparison the $s\bar{s}$ "strangeonium" states are a *terra incognita*; we consider only 5 $s\bar{s}$ states to be well established. These are the $\eta(547)$ and $\eta'(958)$ (counted as one $s\bar{s}$ state), $\phi(1019)$ $f_2'(1525)$, $\phi(1680)$ and the $\phi_3(1854)$. Other more controversial possibilities are $\eta(1295)$, $h_1'(1380)$, $f_1(1420)$ and $\eta(1440)$.

Although sectors such as 2^{++} clearly have almost flavor pure $n\bar{n}$ and $s\bar{s}$ resonances, there are counterexamples such as the famous $\eta-\eta'$ mixing and perhaps evidence for strong $n\bar{n}-s\bar{s}$ mixing in the scalar sector, which has complicated the identification of the scalar glueball. This *Zweig rule violation* is another interesting and poorly understood aspect of QCD, and an experimental search for $s\bar{s}$ states should clarify the level of Zweig violation in other J^{PC} sectors. The various flavor mixing angles could be established experimentally by comparing branching fractions of nominally $n\bar{n}$ and $s\bar{s}$ partners to $(n\bar{n})(n\bar{n})$ $(s\bar{n})(n\bar{s})$ and $(s\bar{s})(s\bar{s})$ final states, for example $\pi\pi$, $K\bar{K}$, $\eta\eta$ and $\eta\eta'$.

Photoproduction is an excellent technique for producing $s\bar{s}$ mesons, because the incident photon is in effect a vector meson beam with a large ϕ-meson component. Much of the photon–hadron interaction takes place through vector dominance, in which the incident photon becomes a vector meson. The relative probability of interacting through the different light meson types ρ°:ω:ϕ is 9:1:2 according to the quark model, and this relative coupling strength is approximately confirmed by the diffractive cross sections for vector meson photoproduction. (There is an additional suppression of the $s\bar{s}$ cross section by about a factor of two that is not well understood.) Thus in photoproduction we have the opportunity to produce mesons with vector meson beams of all diagonal light flavors $u\bar{u}$, $d\bar{d}$ and $s\bar{s}$, with a known relative luminosity between the flavors. In addition to diffractive photoproduction, which produces C=(−) states, other mechanisms such as t–channel vector exchange may lead to significant photoproduction of C=(+) $s\bar{s}$ states. In contrast, hadronic production of $s\bar{s}$ states is suppressed because the initial hadrons provide at most one strange valence quark (for example in KN experiments such as LASS).

The $s\bar{s}$ sector is also attractive because some decay modes should be very *clean.* These include channels such as $\phi\eta$, $\phi\eta'$ and $\phi\phi$, which according to the Zweig rule should only arise from $s\bar{s}$ initial states. One may also study channels such as $\phi\pi$, which are *not* expected as decays of $q\bar{q}$ states. One might find evidence for molecular states or Zweig–rule violation in this channel. Observation of both the $n\bar{n}$ and $s\bar{s}$ partners of a flavor nonet would be useful for establishing the $q\bar{q}$ (and $q\bar{q}g$ hybrid) spectrum, since the relative photoproduction amplitudes can be estimated. This would distinguish a $q\bar{q}$ or hybrid flavor nonet from a meson–meson molecule or a glueball, as molecules and glueballs do not span nonets.

The total widths of $s\bar{s}$ states are predicted on average to be comparable to the widths of $n\bar{n}$ states. Detailed calculations in the ^{3}P$_0$ model [68, 69] do however find some rather narrow states. Four of the $s\bar{s}$ states anticipated in the 1.6-2.2 GeV/c^2 region are predicted to have widths in the 100-200 GeV/c^2 range: These are the ^{3}D$_3$ $\phi_3(1854)$ (predicted total width 104 MeV/c^2, observed $\approx$ 90 MeV/c^2), the ^{3}D$_2$ (predicted 214 MeV/c^2), the ^{1}D$_2$ $\eta_2(1850)$ (predicted 129 MeV/c^2) and the ^{3}F$_4$ $f_4(2200)$ (predicted 154 MeV/c^2, possibly observed by LASS [70] with a total width of roughly 100 MeV/c^2.) Since the $\rho_3(1690)$ has been reported in diffractive photoproduction, the $\phi_3(1850)$ should also be observed, with a known cross section. Comparison of photoproduction amplitudes of the various ϕ_J states will be interesting as a test of the quantum number dependence of the photoproduction mechanism. It might also be produced through $\phi\eta$ collisions in η exchange (a strong coupling to $\phi\eta$ is predicted), and could be observed in the $\phi\eta$ final state. Studies of these narrower states, especially the as yet unknown levels, will be useful as tests of our decay models, photoproduction mechanisms, and mixing with non-$s\bar{s}$ components.

The vector sector provides an example of the paucity of information on $s\bar{s}$ spectroscopy. As in the $n\bar{n}$ case one expects both $L = 0$ and $L = 2$ vectors, a 2^3S$_1$ and a ^{3}D$_1$. In the $I = 1$ $n\bar{n}$ sector there has been progress recently in separating these states [71, 72]. Experimentally there are somewhat overlapping $\rho(1450)$ and $\rho(1700)$ states, which both appear to be present in diffractive photoproduction. Usually the 1450 state is assumed to be 2^3S$_1$ and the 1700 is ^{3}D$_1$, since the nonrelativistic quark model anticipates approximately this mass splitting between spectroscopically pure $n\bar{n}$ levels. The ^{3}P$_0$ decay model predicts that these states should have very different couplings to the S+P modes πh_1 and πa_1; these should couple very strongly to ^{3}D$_1$ but quite weakly to 2^3S$_1$. A recent study of 4π modes by the Crystal Barrel has confirmed this result. In the $s\bar{s}$ sector only one higher-mass vector state has been reported, the $\phi(1680)$. This is seen in e^+e^- annihilation and in photoproduction, and

	KK	K^*K	K^*K^*	$K_1(1273)K$	$\phi\eta$
expt.(1680 region)	seen	dominant	-	-	-
theor. $2^3\mathrm{S}_1$(1680 assumed)	89	245	0	0	44
theor. $^3\mathrm{D}_1$(1850 assumed)	65	75	5	465	29

Table 3.5: Predicted and observed partial widths (in MeV/c^2) of the two 1^{--} $s\bar{s}$ states $2^3\mathrm{S}_1(1680)$ and $^3\mathrm{D}_1(1850)$.

apparently decays to KK but dominantly to K^*K. Can one similarly confirm that this state is the $2^3\mathrm{S}_1$ level as the mass suggests? If so, should the unknown higher-mass $^3\mathrm{D}_1$ be observable in any particular final states? The experimental situation is summarized in Table 3.2.5 ; it is consistent with the $2^3\mathrm{S}_1$ $\phi(1680)$ identification, but only qualitative information on branching fractions is available, and the crucial $K_1(1273)K$ mode has not been investigated. Both states should appear in the clean $\phi\eta$ mode, but again this has not been studied. Thus we have the beginnings of $s\bar{s}$ spectroscopy, but quantitative studies of interesting and characteristic modes such as $\phi\eta$ and the "$s\bar{s}$ workhorse" modes KK, K^*K, K^*K^* and K_1K simply have not been carried out. We may find many surprises in the $s\bar{s}$ sector, especially as regards mixing with non-$s\bar{s}$ states.

If these $s\bar{s}$ states were expected to be simple copies of the $n\bar{n}$ states, with a mass higher by ca. 250 MeV/c^2, establishing the $s\bar{s}$ spectrum might be considered a mundane exercise. However even the lightest $s\bar{s}$ system, the η and η', show a remarkable and poorly understood strong mixing with $n\bar{n}$; the physical states are close to the maximally mixed $(|n\bar{n}\rangle \pm |s\bar{s}\rangle)/\sqrt{2}$ combinations. This is due to a large $q\bar{q}$ annihilation amplitude in the 0^{-+} channel, which has been attributed to various perturbative and nonperturbative QCD mechanisms but has never been convincingly explained. This large mixing is presumably due to annihilation through the gluonic sector, but why 0^{-+} shows such a large annihilation amplitude, whereas others such as vector and tensor are relatively unmixed, remains a mystery. The discovery of the CERN glueball candidate has added more information to this puzzle [43, 44, 73, 74, 75, 76, 77]. The observed decays of the $f_0(1500)$ are far from the flavor–symmetric pattern of $\pi\pi : KK : \eta\eta : \eta\eta' = 3 : 4 : 1 : 0$ (for branching fraction divided by phase space) that one would expect from a simple model of glueball decay, and instead strongly favor $\pi\pi$. This may be due to an intrinsic quark mass dependence of these couplings (as suggested by the LGT results of Weingarten et al), or (as suggested by Close and Amsler) it may be due to a large $n\bar{n} \leftrightarrow G \leftrightarrow s\bar{s}$ mixing similar to the $n\bar{n} \leftrightarrow s\bar{s}$ mixing in the η–η' system. While all J^{PC} channels will provide important information regarding $n\bar{n} \leftrightarrow s\bar{s}$ mixing, the most likely *a priori* to show a significant effect are the radial pseudoscalars (perhaps the $\eta(1295)$ and the $\eta(1440)$) and the 2^{-+} pseudotensors. The 2^{-+} states are interesting because some models predict this to be one of the lighter glueball channels In addition, there are η_2 states at about 1.65 and 1.87 GeV/c^2 (reported by Crystal Barrel [78]) both of which couple strongly to modes forbidden to $s\bar{s}$ by the Zweig rule.

3.2.6 Hybrids - theory

The area of greatest interest in recent studies of meson spectroscopy has been the subject of hybrids. Hybrids are formally defined as mesons that have both $q\bar{q}$ and glue in their dominant *valence* basis state; clearly this is a working definition, and complications such as large levels of $q\bar{q} \leftrightarrow q\bar{q}g$ mixing in physical resonances might require a more careful classification. One can at least be confident that there will be more states than expected by the naive quark model, since the presence of both $q\bar{q}$ and $q\bar{q}g$ basis states will lead to more physical resonances than would follow given only $q\bar{q}$ basis states. As with glueballs, confirmation of this "overpopulation" of the spectrum is one of the strategies used in searching for hybrids.

There is a much more striking signature for hybrids, (which is a principal reason they are so attractive experimentally, in that they can have exotic quantum numbers (forbidden to $q\bar{q}$). The discovery of a resonance with exotic J^{PC} would be convincing evidence of a non–$q\bar{q}$ meson. The search for exotic hybrids is the most exciting topic in modern meson spectroscopy, as no such states have been universally accepted as confirmed, although there are now two candidates. The $J^{PC} = 1^{-+}$ channel, especially $I = 1$, is of greatest current interest since this is expected theoretically to contain one of lightest and most stable of the light–quark hybrids.

Theorists have given detailed predictions of the spectrum of hybrids and their strong couplings. Many techniques have been used in these calculations, beginning with the bag model and constituent gluon models, and continuing with QCD sum rules and the flux tube model. Common conclusions of these studies were that there should be a relatively light $J^{PC} = 1^{-+}$ exotic in the lowest multiplet (where determined), with a mass in the 1.5 to 2.0 GeV/c^2 region. These estimates have been improved on recently by lattice gauge theory, which presumably lacks most of the systematic uncertainty of the models. Recent LGT calculations [19, 79] find that the $J^{PC} = 1^{-+}$ is indeed the lightest hybrid exotic, with a mass close to 2.0 GeV/c^2. Although this appears to vindicate the flux tube model of Isgur, Kokoski and Paton [51], which estimated the mass of the $J^{PC} = 1^{-+}$ exotic to be 1.9 GeV/c^2, one should note that the $J^{PC} = 0^{+-}$ exotic which the flux tube predicts to be degenerate with 1^{-+}, is found by the MILC LGT collaboration to be about 0.7 GeV/c^2 higher in mass! Evidently we still have much to learn about the spectrum of hybrids.

Calculations of strong decay modes of hybrids are of great interest, since these should help us to distinguish between non-exotic hybrids and quarkonia, and also because they may indicate which hybrids are most accessible in photoproduction (for example those with large $\rho^o\pi$ couplings). The more recent decay calculations have relied exclusively on the flux tube model, which may or may not be accurate for these novel states. The first detailed study of hybrid decays in the flux tube model was that of Isgur, Paton and Kokoski [51], who found the now famous hybrid selection rule that the lightest hybrids should decay dominantly to S+P meson pairs rather than the simpler S+S modes. This implies for example that a search for an $I = 1$ $J^{PC} = 1^{-+}$ hybrid should concentrate on unfamiliar quasi-two-body modes such as $\pi f_1(1285)$ and $\pi b_1(1235)$ rather than the more easily accessible $\pi\eta$ and $\pi\rho$. This paper found that the total widths of several hybrids should be relatively narrow ($\Gamma_{tot} \approx$ 150 MeV/c^2, notably including the $I = 1$ $J^{PC} = 1^{-+}$.

The Isgur *et al.* reference considered only the exotic hybrids, whereas the flux tube predicts 5 non-exotic J^{PC} nonets, 0^{-+}, 1^{+-}, 1^{++}, 1^{--} and 2^{-+}, at the same mass as the 3 exotics 0^{+-}, 1^{-+} and 2^{+-}. With this many states, overpopulation could be apparent if any of the non-exotic hybrids is narrow. The calculation of decays of these non-exotic hybrids in the flux tube model was carried out by Close and Page [52], who found that several of these hybrids are indeed predicted to be quite narrow. Especially attractive non-exotic hybrids are relatively narrow 2^{-+} states in both $I = 0$ and $I = 1$, and a remarkably narrow $I = 0$ 1^{--}, with a total width of 100 MeV/c^2. Close and Page anticipate that the dominant mode of the $I = 1$ 2^{+-} exotic should be $a_2\pi$; a comparative study of photoproduction of the $a_2^{\pm}\pi^{\mp}$ and $a_2^o\pi^o$ channels should especially interesting, since production by exchange of different C-parities in t-channel can be separated in this manner. Finally, perturbative QCD signatures of hybrids have been theoretically investigated by Carlson and Mukhopadhyay [80].

3.2.7 Glueballs - theory

There has been tremendous interest in finding glueballs, as they are conceptually the furthest removed from the conventional $q\bar{q}$ of all the mesons expected in QCD. Although many anticipated properties of glueballs may be strongly model dependent, there are reliable LGT predictions [42, 43, 44, 45] of a lightest scalar glueball mass of 1.5 to 1.7 GeV/c^2. The next glueballs found above this scalar in LGT studies are 0^{-+} and 2^{++}, both expected at a mass of about 2.2 to 2.3 GeV/c^2, with all other J^{PC} found at higher masses.

Since these lighter glueballs are non-exotic, one can hope to identify them through *overpopulation*, as anomalous extra states in the background of conventional $I = 0$ $q\bar{q}$ mesons. Here we are unfortunate, since $I = 0$ 0^{++} is probably the most obscure sector in the entire light meson spectrum, with broad states $f_0(1300)$ and $f_0(1700)$, the narrow $K\bar{K}$ candidate $f_0(980)$, and the relatively narrow CERN glueball candidate $f_0(1500)$. Conventional $I = 0$ $n\bar{n}$ and $s\bar{s}$ states are expected at about 1.3 and 1.5 GeV/c^2 in the quark model; these are likely to be rather broad, although the $^3P_0$ model predictions for their width are quite sensitive to their radial wave functions.

Several experiments at the LEAR $p\bar{p}$ facility at CERN have found the rather narrow $f_0(1500)$ scalar [81, 82], with a total width of 112 ± 10 MeV/c^2; this has been widely cited as a scalar glueball candidate. There are complications with this identification, however. The reduced decay couplings to pseudoscalar pairs do not follow the naive 3:4:1 $\pi\pi$:$K\bar{K}$:$\eta\eta$ ratio expected for a flavor singlet, instead the $K\bar{K}$ mode appears quite weak. Recent LGT studies of the $\mid k \mid$ dependence of glueball–Ps–Ps couplings finds the opposite result [44], that heavier mesons should be produced preferentially from scalar glueball decay, and for this reason the $f_0(1700)$ might instead be the scalar glueball. In either case these are rather narrow states, so one might also hope to find the 0^{-+} and 2^{++} glueballs as unusually narrow states. Of course the spectrum around 2.2 and 2.3 GeV/c^2 is poorly known, so this cannot be investigated without higher statistics high–mass data.

3.2.8 Multiquark systems - theory

The best known *multiquarks* are nuclei, which are weakly bound associations of largely unmodified color-singlet nucleons. Similarly we know of many examples of hypernuclei, in which a nucleon has been replaced by a Λ, and the famous $\Lambda(1405)$ appears plausible as a weakly bound $\bar{K} - N$ meson-baryon nucleus. The $f_0(980)$ and $a_0(980)$ are likely cases of weakly bound meson pairs, and if so are our first examples of mesonic nuclei. There are many arguments in favor of this interpretation (see Weinstein and Isgur [83, 84]), most obviously that they are just below $K\bar{K}$ threshold, have S-wave $K\bar{K}$ quantum numbers, are 0.2 to 0.3 GeV/c^2 lighter than expectations for 0^{++} nnbar states, and are very narrow compared to expectations for scalar quarkonia at this mass.

Although the $f_0(980)$ and $a_0(980)$ can be explained as dominantly $K\bar{K}$ molecules, earlier predictions of four-quark states with these quantum numbers at light masses has resulted in persistent speculations that these might actually be $q^2\bar{q}^2$ clusters, once known as *baryonia* [85, 86]. These issues can be tested through photoproduction of an initial $\phi(1020)$ and a measurement of radiative transition rates. Preliminary experimental results from Novosibirsk [87] are closer to the theoretical $q^2\bar{q}^2$ branching fraction, although they may include important non-980 backgrounds.

There is likely to be a rich spectrum of meson-meson molecules in other sectors, such as vector-vector, so confirmation (or disproof) of the $K\bar{K}$ molecule hypothesis would be a very important step in the study of multiquark systems.

3.3 Other photoproduction physics

3.3.1 $K\bar{K}$ threshold physics and the a_0/f_0

In strong QCD, besides the possibility of mixed quark–gluon states, it is expected that multi-quark states and/or meson–meson molecules will show up in the hadronic spectrum below 2 GeV/c^2. To date the best candidates for such states are the scalar–isoscalar $f_0(980)$ and –isovector $a_0(980)$ mesons. Their masses are too low as compared to quark model expectations. In addition, their decay modes, in particular their strong coupling to the $K\bar{K}$ channel and weak coupling to the $\gamma\gamma$ channel, are at odds with the quark model predictions for $q\bar{q}$ states [88]. There are many theoretical models which address the properties of these states beyond the valence approximation [83, 89, 90, 91, 92, 93, 94, 95, 96]. In particular it has been recognized that the proximity of the $K\bar{K}$ threshold should play an important role in these states, and therefore the structure of these states should ultimately be related to the properties of the residual meson–meson forces. This provides an opportunity for addressing one of the fundamental issues of strong QCD *i.e.* the nature of transition between short range, color exchange forces, and long range meson exchange interactions. Furthermore, with only a few nearby channels, they play an important role in constraining methods of *unquenching* the quark model and studying the role of open channels in meson spectroscopy. The situation is similar to that encountered in the NN system, where from the low energy scattering phase shifts it is possible to determine properties of the NN force and in particular determine the existence and describe the properties of the deuteron. In fact, several models predict the $f_0(980)$ to be mesonic analog of the deuteron, being a $K\bar{K}$ bound state without a major $q\bar{q}$ component, moving to the continuum due to the open $\pi\pi$ channel.

The low energy data on $K\bar{K}$ interactions is very imprecise [97, 98]. In terms of parameters entering the effective range expansion, fits to the existing data on $K\bar{K}$ scattering have determined the scattering length, $a_{K\bar{K}}$, to approximately 30%. The data are however too poor to get even an order of magnitude estimate of the effective range parameter, $r_{K\bar{K}}$ and the volume parameter, $v_{K\bar{K}}$. The presence of the open $\pi\pi$ channel modifies the simple threshold expansion; *e.g.* the threshold parameters in the effective range expansion become complex and a complete analysis requires measurements of all of the open channels simultaneously. Table 3.6 summarizes results of a recent analysis [95].

Data	a_K (fm)	r_K (fm)	v_K (fm^3)
Ref.[97]	$-1.73 + i\,0.59$	$-0.057 + i\,0.032$	$0.016 - i\,0.0044$
Ref.[98]	$-1.58 + i\,0.61$	$-0.352 + i\,0.043$	$0.028 - i\,0.0057$

Table 3.6: Parameters of low energy $K\bar{K}$ scattering phase shifts from Ref. [95]. The fits are to the two data sets of Ref. [97], and Ref. [98].

At present, existing uncertainties do not permit making a definite characterization of the effective $K\bar{K}$ interactions, nor to establish the bound state nature of these scalar mesons. Furthermore these uncertainties lead to large theoretical errors in determining the scalar meson's wave functions and ultimately in predicting rates for decay processes involving them.

Photoproduction of kaon pairs near threshold offers unique opportunities for measuring the S wave interactions. The near–threshold photoproduction is dominated by the P–wave from the decay of the ϕ meson and it is possible to use this P–wave as a *magnifying glass* for extracting the near threshold behavior of the S-wave. In the K^+K^- channel, this is given by the interference between the ϕ and the two scalars $f_0(980)$ and $a_0(980)$. To completely isolate the isoscalar and isovector channels would, in principle, require measurement of the two neutral modes, K_SK_S and K_SK_L. However, even without the later it should be possible to isolate the dominant P–wave from its characteristic angular dependence. Furthermore, with the measurement of the $\pi\pi$ and $\pi\eta$ channels, it will be possible to obtain a complete set of phase shifts and inelasticities describing the scalar channel.

The existing, very limited, data on charged kaon pair production with invariant mass near 1 GeV/c^2 comes form DESY [99] and Daresbury [100] and clearly identifies a strong S–wave signal under the P–wave ϕ peak. The data are however too imprecise to distinguish between resonant and non-resonant production. Under the same rate assumptions as in section 3.1.3, the 3500 total events collected as DESY are to be compared with 14000 reconstructed ϕ events per day expected in the first stage of Hall D operations. These high statistics will enable one to analyze the t–dependence of individual partial waves which is very important in isolating the different production mechanisms, and thus for identification of the produced resonances. This will be further enhanced by the use of linear polarization of the photon, enabling one to discriminate between the naturalities of the t–channel exchanges. The ability to measure the various photoproduction amplitudes is another important aspect of S/P interferometry. In the forward direction, angular momentum conservation requires the S–wave to be produced via a nucleon helicity flip, and therefore S/P interference occurs with the $\gamma - \phi$ helicity flip amplitude. Since ϕ production is dominated by the $\gamma - \phi$ helicity non–flip amplitude, analysis of t dependence of the S/P interference will permit the isolating of the two amplitudes.

Several model have been used to describe diffractive vector meson photoproduction. Although each of these models successfully describes the energy W, t, and low–q^2 behavior of diffractive photoproduction cross sections, their predictions for spin observables vary significantly. This suggests that the measurement of such spin observables can be used to distinguish between competing theoretical descriptions of Pomeron exchange, thereby providing a sensitive probe of the QCD dynamics underlying Pomeron exchange.

In particular, Fig. 3.7 depicts one of the spin–polarization density matrices for ϕ–meson photoproduction on a nucleon. The data are from Ref. [100], and are shown for photon energies in the range $E_{LAB} = 2.8 - 4.8\ GeV$. The three curves illustrate the sensitivity of spin observables to the dynamical mechanisms underlying Pomeron exchange under different assumptions on the underlying quark mechanisms for γ–Pomeron–ϕ coupling.

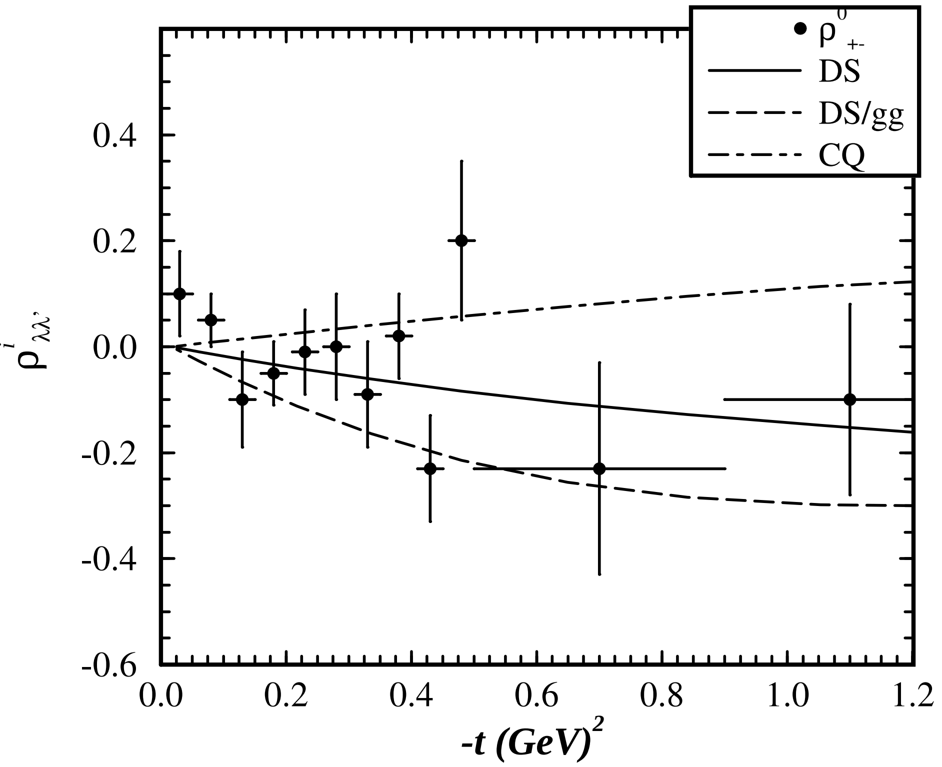

Figure 3.7: The solid curve is a calculation using the Dyson–Schwinger–based model described in Ref. [101]. The dashed curve is calculated using a model similar to that of Pichowsky and Lee, but with the Pomeron interaction replaced with an effective two–gluon–exchange interaction. The dot–dashed curve is calculated using the usual Pomeron–exchange interaction, but with constituent quarks, a bare photon–quark coupling, and a modeled ultra–soft ϕ–meson Bethe–Salpeter amplitude.

3.3.2 Rare decays

The copious production of the vector mesons ρ, ω and ϕ, the pseudoscalars η and η', and the strange mesons $K^{\pm}$, K_S and K_L will allow measurements of various rare meson decay modes at HALL D. Table 3.7 estimates the numbers of these mesons expected per year at HALL D. These rates are based on 10^7 seconds of running per year with a 30 cm-liquid hydrogen target. Rates are quoted for both $10^7\,\gamma/s$ and $10^8\,\gamma/s$. The Ks are assumed to come exclusively from ϕ decays, whereas the cross sections for η and η' are estimates from existing data.

Reaction	Cross Section	Events/s per γ	Events/s $10^7\gamma/s$	Events/s $10^8\gamma/s$	Events/yr $10^7\gamma/s$	Events/yr $10^8\gamma/s$
$\gamma p \to \eta p$	200 nb	$2.5\times10^{-7}/\gamma$	2.5	25.	2.5×10^{7}	2.5×10^{8}
$\gamma p \to \omega p$	2 μb	$25.\times10^{-7}/\gamma$	25.	250.	2.5×10^{8}	2.5×10^{9}
$\gamma p \to \eta' p$	50 nb	$6.3\times10^{-8}/\gamma$	0.63	6.3	6.3×10^{6}	6.3×10^{7}
$\gamma p \to \phi p$	400 nb	$5.0\times10^{-7}/\gamma$	5.0	50.	5.0×10^{7}	5.0×10^{8}

Table 3.7: Expected rates of meson photoproduction based on 10^7 seconds per year. The cross sections for η and η' production are estimates based on existing data.

Operating at the ϕ peak with $1\times10^8\,\gamma/s$, HALL D will produce approximately $50\,\phi$'s per second. This is a factor of 12 smaller than what is expected at the dedicated ϕ-factory DAΦNE, operating at a luminosity of $5\times10^{32}cm^{-2}s^{-1}$. Hadronic photoproduction however has additional features which will compensate for the lower luminosity. These are the boost factor, which enhances detection of low-energy photons, photon polarization, and the existence of a strong S-wave under the ϕ-peak. All these will help to isolate a rare signal from various backgrounds. Even with only $10^7\,\gamma/s$, the 5.0×10^7 ϕ's produced per year at HALL D will allow us to study several interesting rare decays with good statistics.

The largest ϕ radiative decay is $\eta\gamma$, which has a branching fraction of, BR$(\phi\to\eta\gamma)=(1.29\pm0.07)\times10^{-2}$. There are several allowed radiative decay channels which are important for spectroscopy. These include $\phi\to\gamma f_0(a_0), \phi\to\pi\pi\gamma, \phi\to K\bar{K}\gamma, \phi\to\pi\eta\gamma$ and $\phi\to\eta'\gamma$ [102].

Recently the CMD-2 and SND collaboration reported observation of a total of about 30 events for $\phi\to\eta'\gamma\to\pi^+\pi^-\eta\gamma\to\pi^+\pi^-3\gamma$, corresponding to a branching fraction of BR$(\phi\to\eta'\gamma)$=$(0.8\pm0.2)\times10^{-4}$. This sample of events was extracted from about 3×10^7 ϕ decays [103, 104]. The precise measurement of this branching ratio, relative to $\phi\to\eta\gamma$, is important as a constraint on the gluonic component of the η'. During one year of running, with a flux of 10^8 photons/sec, we expect a total of about 5,000 such decays; this would increase the world's data sample by two orders of magnitude.

The C-parity violating decays $\phi\to\rho\gamma$, $\phi\to\omega\gamma$ and $\phi\to\eta\pi^0$ have not been observed. At present these modes have experimental upper limits of $10^{-2}-10^{-5}$. (A recent VEPP-2M experiment has set a limit for $\phi\to\rho\gamma$ of 1.2×10^{-5} [105].) The hadronic modes $\phi\to3\pi$ and $\phi\to\rho\pi$ break the OZI rule and are sensitive to the $\phi-\omega$ mixing. (Historically, the OZI rule was first suggested by the weakness of $\phi\to\rho\pi$. It has since been generalized to the rule that $q\bar{q}$ annihilation in a meson is suppressed in strong decays and transitions.) Both the OZI rule and isospin are violated in $\phi\to\pi^+\pi^-$, $\phi\to\omega\pi^0$ and $\phi\to\pi^+\pi^-\eta$, which are sensitive to the amount of $\phi-\rho^o$ mixing. The decays $\phi\to\pi^+\pi^-$ and $\phi\to\omega\pi^0$ have recently been reported by the CMD-2 and SND collaborations [104, 103]; these measurements made use of interference with the nonresonant background processes $e^+e^-\to\pi^+\pi^-$ and $e^+e^-\to\omega\pi^0$.

Direct photoproduction of the ϕ should allow one to observe these ϕ decays without relying on interference. Since the OZI rule remains poorly understood, measurement of these transitions should provide important information on the amount of (OZI-violating) flavor mixing present in the vectors.

Measurements of the transitions $\phi \to \gamma K\bar{K}$ and $\phi \to \gamma\pi\eta$ are very important as tests of models of the scalars $f_0(980)$ and $a_0(980)$. These branching fractions can differentiate between $q\bar{q}$, $K\bar{K}$-molecule and four-quark models of these states. Close, Isgur and Kumano found the ratios of branching fractions $BR(\phi \to a_0\gamma)/BR(\phi \to f_0\gamma) = 0, 1, 9$ respectively for the three assignments [86].

The CMD-2 and SND collaborations have recently reported observation of the radiative decays $\phi \to \pi^0\pi^0\gamma$, $\phi \to \pi^+\pi^-\gamma$, and $\phi \to \pi\eta\gamma$ [106, 107, 105]. The branching fractions were determined to about 10% accuracy; $\phi \to \pi^0\pi^0\gamma$ was found to be 1.1×10^{-4}, and $\phi \to \pi\eta\gamma$ is 0.9×10^{-4}. One should note that the interpretation of the observed final hadron spectrum is controversial. The $a_0(980)$ and $f_0(980)$ are observed in the detected spectra, but one the presence of other resonances (such as $f_0(400-1200)$) and interference with nonresonant background such as $e^+e^- \to \omega\pi^0$ has not yet been modelled with precision. This admixture can *a priori* be as high as 60% of the observed number of events. The HALL D photoproduction experiment will have different backgrounds and systematics, and with an expected 10^2 - 10^4 events per year should be able to make a very important contribution to this radiative test of the nature of the $a_0(980)$ and $f_0(980)$ mesons.

Another possibility is to measure direct S-wave production through S/P interference, as discussed in section 3.3.1. This could be used to determine the radiative decay rates $S \to \gamma\pi\pi(\eta\pi)$ $(S = f_0, (a_0))$, which are also very sensitive to the model assumed for the scalars. The large boost factor $\gamma_\phi = E_\phi/m_\phi \sim E_\gamma$ will be especially useful experimentally in this case, as it implies an enhanced photon acceptance.

3.3.3 Tests of chiral dynamics

Much of the preceding discussion of the physics which can be addressed at HALL D has described hadrons in terms of their quark and gluon constituents. One may alternatively discuss hadronic interactions using an "effective lagrangian" constructed from hadron fields and spatial momenta. This approach, which has seen considerable application in recent years, is most highly developed for low-energy processes involving pseudoscalars, although generalizations to baryons and to other mesons are currently being considered. Since effective lagrangians are typically nonrenormalizable, they are treated at successive orders in a loop expansion, and a minimal set of couplings at each order must be taken from data. Once these parameters are fixed, all the physical amplitudes at that order are determined. This approach is attractive in part because it describes hadronic processes using well-established Feynman diagram techniques. The symmetries of QCD such as isospin and chiral symmetry can be incorporated automatically through constraints on the terms allowed in the effective lagrangian. Single meson production and meson pair production near threshold are typical processes in which HALL D can be used to test the predictions of effective hadron lagrangians.

Tests of chiral anomalies are especially interesting for HALL D, since these are feasible experimentally and have important physical implications, for example in the two-photon widths of the light pseudoscalars. Primakoff production of π^0, η and η' provide tests of chiral anomalies involving two electromagnetic currents. There are plans to measure the π^0 lifetime at Jefferson Lab's Hall B in the near future [108], using Primakoff production with a photon beam of up to 2 GeV; it is expected that this measurement will be sensitive to corrections due to the u and d quark masses. At HALL D energies, Primakoff production of the η and η' mesons will be possible [109]. The two-photon widths of the η and η' are predicted by the chiral anomaly, and are also sensitive to the $\eta - \eta'$ mixing angle [109].

It is also possible to measure the slope of the π^0, η, and η' $\gamma\gamma^*$ form factors; these are of interest because they involve higher-order corrections in chiral perturbation theory. A study of photoproduction possibilities at JLab [110] shows that with an electron beam of 12 GeV, a photon flux of 7×10^7 γ/s, and a ^{12}C target of 1 cm thickness (5% of a radiation length), using photon energies of 10 and 11.5 GeV, one can produce $20,000$ η mesons in a five day run. This will permit a test of the $\eta \to \gamma\gamma^*$ amplitude to better than 5%, which is the level of sensitivity required to observe corrections due to the s-quark mass. Determination of their branching fractions of η and η' to other decay modes can also provide very useful tests of chiral dynamics. For example, rare decays such as $\eta' \to \pi^+\pi^-\gamma$ [111] have not yet been accurately measured.

Double pion production in the photoproduction process $\gamma p \to p(n)\pi\pi$ at small t can be used to determine the anomalous vertex $\gamma\pi^+\pi^-\pi^0$, because this process is dominated by one pion exchange in t-channel. This provides a further test of chiral anomalies. An experiment (PR-94-015) was previously carried out in Hall B at Jefferson Lab [112, 113] using a photon beam with energies ranging from 0.5 to 2.0 GeV; the reduction of t_{min} at higher photon energies will enable one to improve this measurement and study other related processes, such as low-t production of $\pi\eta$. Another interesting process is the strange analogue reaction $\gamma p \to \Lambda(\Sigma)K\pi$, in which a virtual K meson is exchanged in t-channel. Measurement of these near-threshold amplitudes at HALL D will allow novel tests of the SU(3) flavor dependence of these anomalous vertices.

Finally, one can measure pion Compton scattering amplitudes by studying peripheral pion production in the process $\gamma p \to \gamma\pi p$ at small t, where one pion exchange dominates. By restricting the kinematics to small photon energies in the final pion rest frame, one can determine the first nontrivial corrections to pointlike Compton scattering, which involve the pion polarizabilities [114, 115, 116, 117]. These are predicted in chiral perturbation theory (and in other models of hadron electromagnetic interactions), but at present are poorly known experimentally.

HALL D will be an intense source of η mesons; we anticipate an eventual rate of 2.5×10^8 η's per year. The known η decays modes are radiative transitions, two-photon processes, or 3π processes that violate isospin, and hence are formally classified as electromagnetic as well. Since the final hadron kinetic energy released in η decays is small ($m_\eta = 550$ MeV/c^2), these decays include excellent opportunities for the study of low-energy effective hadronic theories. Three-body decays are of particular interest in tests of effective lagrangians. Several theoretical approaches are in approximate agreement on the absolute decay rate for $\eta \to 3\pi$, although discrepancies still exist in the description of the Dalitz plots. The process $\eta \to \pi^+\pi^-\gamma$ has also been studied using effective lagrangians [118], and accurate data on this process will also be useful as tests of these models.

HALL D is eventually expected to produce 10^9 kaons/year from ϕ decays. These will contribute to the measurement of weak-radiative kaon decays. These rates are sensitive tests of effective lagrangians, since decays to pions and photons involve the higher $O(p^4)$ terms of the chiral lagrangian [119]. Although the statistics at HALL D are not expected to exceed DAΦNE, the boosted kinematics will provide an important complementary analysis with very different systematics, especially in multiphoton final states.

Chapter 4

Photon Beam

One of the unique opportunities presented by a CEBAF upgrade to energies of 8 GeV and beyond is the possibility of generating high-intensity c.w. photon beams for high energy photoproduction experiments. In this regime, photon beams represent an interesting extension to the meson spectroscopy program that has been actively pursued using beams of pseudoscalar mesons at hadron accelerator laboratories: with high energy photons one has essentially a beam of *vector* mesons. It is difficult, in fact, to conceive of any other way to obtain such a vector beam.

The requirements for photon beam energy and polarization were described in chapter 3. This chapter describes a design for a real photon facility that meets these requirements. Starting with a beam of monochromatic electrons, it provides an intense beam of high-energy photons with an energy spectrum that is dominated by a single peak. Nearly half of the total power in the beam is concentrated inside this peak, which has a width of less than 10% f.w.h.m. At a fixed electron beam energy E_0, the peak energy of the photon beam can be varied anywhere from below 50% up to 90% E_0 simply by rotating a crystal. The photon spectrum inside the intensity peak has a large degree of plane polarization. The precise energy of an individual photon inside the peak is determined ("tagged") from the momentum of the recoil electron measured in a dedicated "tagging" spectrometer. The design is formed around the expected parameters for the CEBAF beam following the energy upgrade to 12 GeV, although nothing prevents its operation at lower energies before the time that 12 GeV beams are available. The design of the tagging spectrometer makes allowance for operation at energies up to 20 GeV, in the event of a further energy upgrade in the future.

This chapter begins with a survey of the techniques for producing high-energy photons that were considered in the development of this design, and the reasons for the choice of coherent bremsstrahlung. The coherent bremsstrahlung source is then described in greater detail, followed by a discussion of the requirements that the design places on the electron beam that feeds the source. The tagging spectrometer design is described next, and the chapter concludes with a discussion of the considerations that govern the choice of beam intensity for particular measurements.

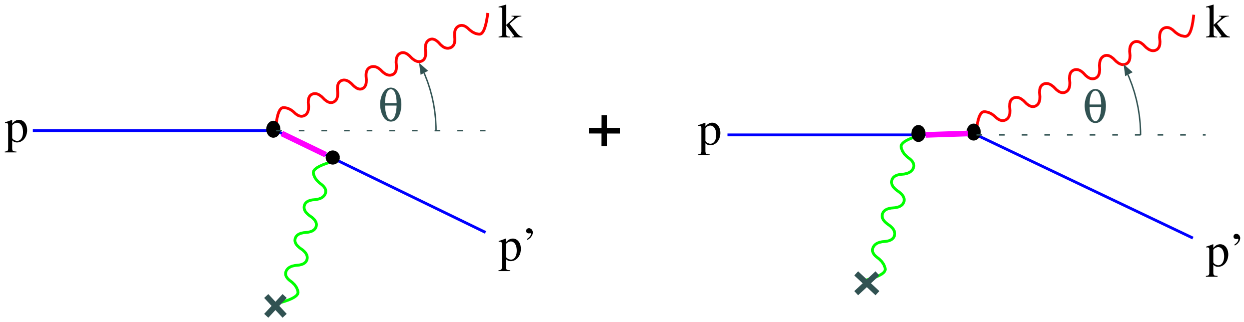

Figure 4.1: Generic diagrams for hard photon production from a high energy electron beam. The symbol × represents either a static charge distribution, in the case of virtual photons in the initial state (i.e. bremsstrahlung), or an optical cavity, in the case of real photons in the initial state (i.e. Compton scattering).

4.1 Choice of technique

Two basic methods have been considered for producing photons of the highest possible energy, flux and polarization from electrons of 12 GeV. The methods are bremsstrahlung and Compton scattering of light. Both are well-established methods of producing photon beams. Both techniques are actually described by the same Feynman diagrams, shown in Fig. 4.1. In the case of Compton scattering the incoming photon is real, whereas it is virtual for the case of bremsstrahlung.

Each of these techniques has its own limitations and advantages. In order to be suitable for HALL D, the photon source must be capable of producing photons of energy at least 80% E_0. The photon beam should have linear polarization. The energy resolution for individual photons in the beam should be as good as possible, *i.e.* on the order of the energy spread of the electron beam itself. It should be capable of producing fluxes up to 10^8/s. The contamination of the beam with photons outside the desired energy band should be as low as possible. It is also important that the source should be reliable and require a minimum of down-time for maintenance. The suitability of each approach is discussed below in the light of these criteria.

4.1.1 Compton back-scatter

A Compton source begins with a beam of visible or ultraviolet light, typically from a laser, that is aligned to intersect the incident electron beam at close to 180°. Some of the photons undergo Compton scattering with the beam electrons. In the lab frame, the scattered photons come out in a narrow cone about the incident electron direction, and carry a significant fraction of the electron energy.

The basic design of the Compton back-scatter source for this study was put forward by from C. Keppel and R. Ent [120]. The design entails the use of a four-mirror high-gain cavity pumped by a 10kW argon-ion laser putting out 2 ps pulses at a frequency of 100 MHz. The pulses in the cavity are synchronized so that the light pulses intercept an electron bucket each time they pass through the beam. The total length of the cavity is 2 m with a crossing angle of 1°. Both cavity and electron beam are focused to a tiny spot of 10 μm r.m.s. radius at the crossing point. A small spot size is necessary in order to get as high a scattering rate as possible. The gain of the cavity is 10^4, which is conservative in view of recent advances in mirror technology. The wavelength of the light is 514 nm. The rate spectrum of the back-scattered beam from this source is shown in Fig 4.2a for a 1μA electron beam at 12 GeV.

From the point of view of flux, this source is marginal. With a few μA of beam and mirror improvements, it might produce 10^8 photons/s in the upper 1/3 of its energy spectrum. However, its maximum photon energy of 3.7 GeV is far short of the 80% E_0 needed for HALL D. To remedy this one must decrease the wavelength of the laser beam. This can be done by the use of a frequency-doubling crystal that absorbs the green light from the laser and produces ultraviolet light at 257 nm. Storing this light in a cavity of similar design to that described above yields the back-scatter rate spectrum shown in Fig. 4.2b. The major reason for the drop in rate is the decrease in the cavity gain from 10000 to 250. This is imposed by the diminished reflectivities of mirrors in the UV. Other factors are the inefficiency of the doubling crystal, a factor of two in rate from the doubling itself, and the decreasing Compton cross section with energy. The maximum photon energy is still under 50% E_0 and the flux is three orders of magnitude below the desired rate.

In order to reach photon energies of 80% E_0, initial photons of 20eV are needed. The brightest sources of these would be a synchrotron light source or a free electron laser (FEL). Mirrors that operate at these wavelengths typically have reflectivities around 70%. With these one could conceive of a scheme that uses a wiggler to extract energy from the 12 GeV beam before it enters the dump. This light would have the same time structure as incident beam, and so it could be reflected back and made to cross the incident beam at a small angle, for a Compton back-scatter source. An indication of the level of flux that could be achieved with such a source can be obtained by using the laser cavity model described above, setting the gain to 1, the wavelength to 62 nm, and assuming 1kW peak (1W average) of synchrotron light. The back-scatter rate is shown in Fig 4.2c. This plot shows that even if the full power of a 1μA 12 GeV beam were converted into 20eV photons and backscattered from the incoming beam, the rate would still fall far short of the requirements for HALL D.

From the point of view of polarization, the Compton back-scatter source would be ideal. The polarization of the back-scattered beam is controlled by that of the laser, and can be essentially 100%. This source is also virtually background-free because the spectrum below any desired cutoff can be eliminated by collimation. The energy of the remaining beam can be measured to within the resolution of the electron beam by tagging. However the the combination of sufficient energy and sufficient flux for the purposes of HALL D cannot be achieved using this source.

4.1.2 Tagged bremsstrahlung

A bremsstrahlung source consists of a thin piece of material (the radiator) that is placed in the electron beam and converts part of the energy of the beam into bremsstrahlung radiation. Bremsstrahlung offers the only practical way, starting with an electron beam at CEBAF energies, to produce a photon beam with a significant flux in the vicinity of the end point. It produces a naturally collimated photon beam with a characteristic angular spread

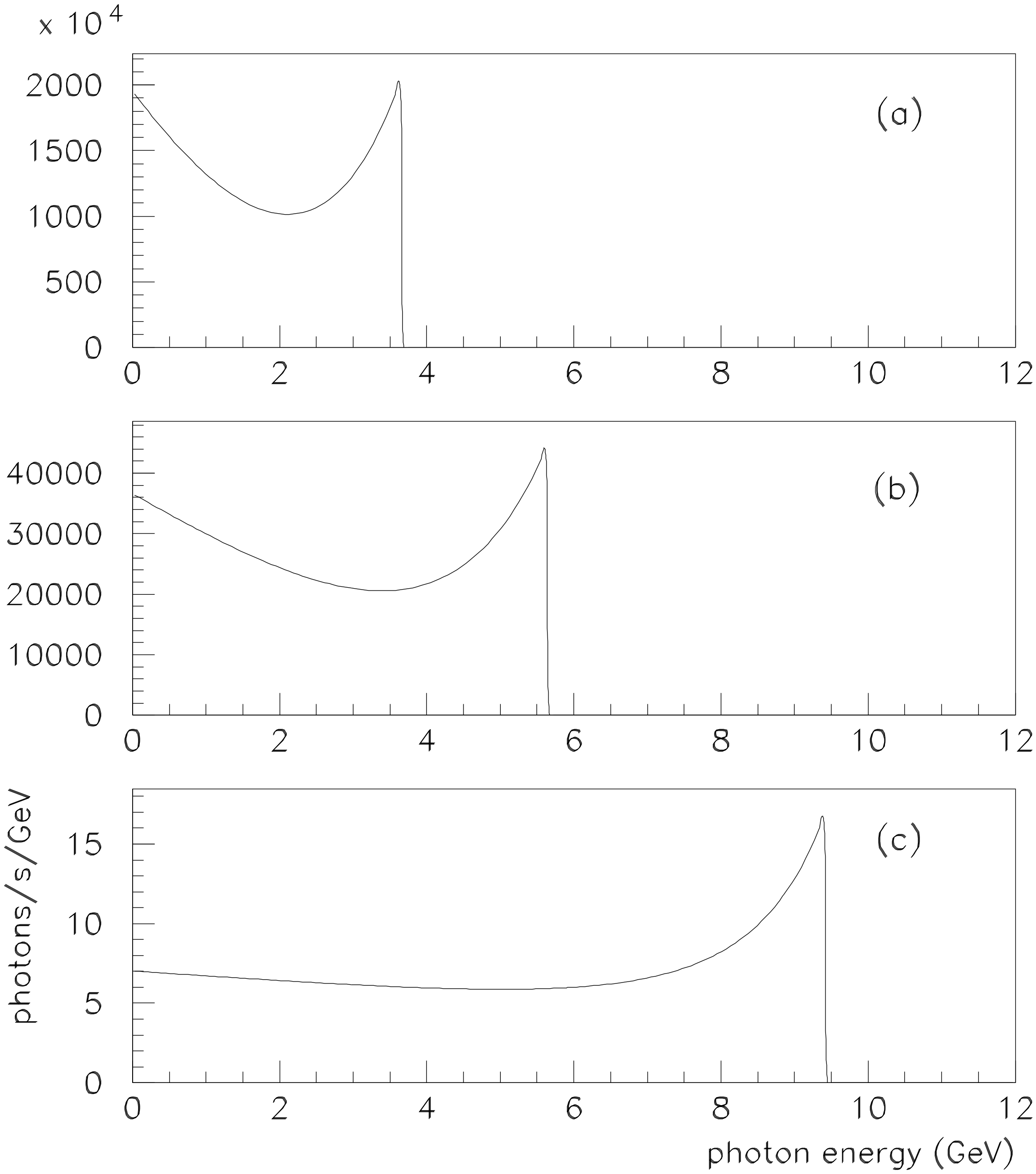

Figure 4.2: Photon energy spectrum from the Compton back-scatter source described in the text and a 12 GeV electron beam at 1μA. (a) cavity of gain 10000 driven by a 10kW Argon-ion laser (514 nm) pulsed at 100 MHz. (b) cavity of gain 250 driven by 3kW frequency-doubler (257nm) pulsed at 100 MHz. (c) cavity of gain 1 driven by a hypothetical FEL source operating at 20eV with same structure as CEBAF beam, peak power 1kW.

of m/E_0. This allows the low emittance of the CEBAF beam to be effectively transfered into the secondary photon beam.

Bremsstrahlung does not suffer from the kind of flux limitations that were encountered in the examination of Compton back-scatter sources. The radiator thickness must be kept below 1% of a radiation length in order to maintain good energy resolution in the tagger. Keeping the thickness below 10^{-3} radiation lengths ensures that multiple scattering in the radiator does not significantly broaden the divergence angle of the photon beam. A 10^{-3} radiator and 1μA of electrons would produce much more than sufficient flux for HALL D.

A bremsstrahlung source is, however, deficient in some other respects. Averaged over the bremsstrahlung cone, the photon beam has zero plane polarization. Circular polarization can be achieved by polarization transfer from a circularly polarized electron beam, but for the purposes of HALL D it is plane polarization that is desired. A bremsstrahlung source also suffers from a large low-energy flux in the beam. The power spectrum of a bremsstrahlung beam is approximately uniform from zero up to the energy of the incident electrons. This means that an experiment that uses the high-energy part of the beam must operate in a background of low-energy photons that are many times more frequent. The tagger is helpful in eliminating many of the false starts in the detector that arise from the background, but this technique becomes ineffective at rates above a few 10^7 tagged photons/s. For the typical experiment using tagged bremsstrahlung and open detector geometry, background from low-energy beam particles limits the rate at which the experiment can run to less than $5 \cdot 10^7$ tagged photons/s. The goal for HALL D pushes that limit to 10^8/s.

4.1.3 Coherent bremsstrahlung

The source described in the previous section meets most of the requirements for HALL D, but is deficient in the areas of polarization and backgrounds. Both of these deficiencies can be remedied by replacing the conventional amorphous or polycrystalline radiator with a thin mono-crystalline wafer. At special settings for the orientation of the crystal, the atoms in the radiator can be made to recoil together from the radiating electron. When they do this they produce a coherent enhancement at particular energies in the radiation spectrum, which correspond to the reciprocal lattice vectors of the crystal. The kinematics are such that a randomly oriented lattice vector would make a tiny peak located up at the end point of the energy spectrum, where the coherent gain factor is negligible. By careful orientation of the crystal, however, one of the lattice vectors can be aligned with the favored kinematics for bremsstrahlung, at which point its coherent peak appears well below the end point, and its coherent gain can be large enough that it contributes a large fraction of the total radiated power.

This is illustrated in Fig. 4.3. This plot shows the intensity (EdN/dE) or power spectrum of the coherent bremsstrahlung beam after collimation. The sequence of secondary peaks above the primary correspond to integral multiples of the primary reciprocal lattice vector and so they are always present. By careful choice of orientation angles it is possible to suppress all other vectors and isolate just one primary peak. By rotating the crystal, the position of the peak can be moved from one end of the spectrum to the other. Note that the coherent peaks appear on top of the incoherent bremsstrahlung continuum.

Unlike the underlying continuum, the photons in the coherent peak have significant net

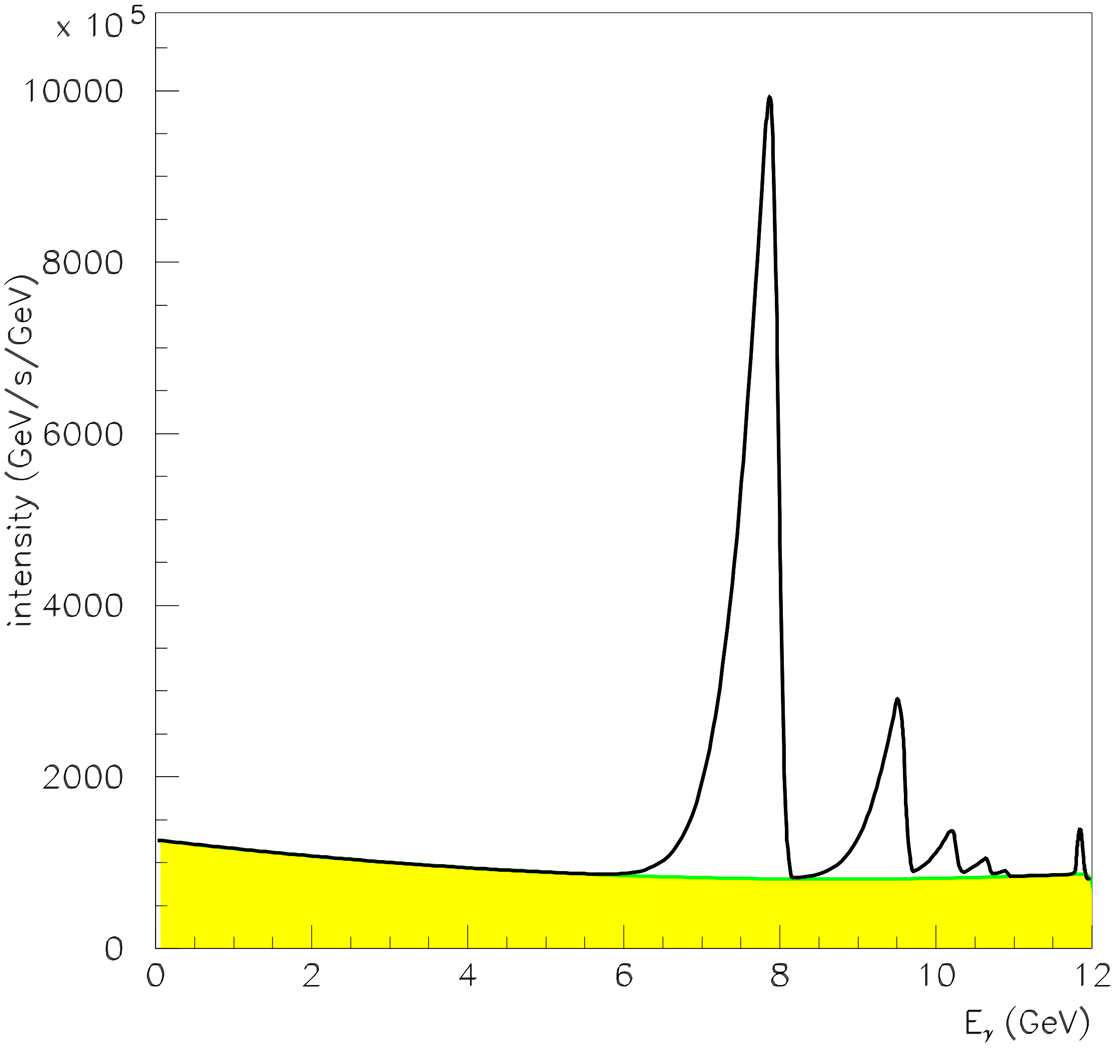

Figure 4.3: Photon power spectrum from an oriented diamond radiator. The y axis is dP/dE with power P expressed in GeV/s and E in GeV. The radiator thickness is 10^{-4} radiation lengths and the electron beam current is 1μA. Shown is what emerges after the photon beam passes through a collimator 3.4 mm in diameter located 80 m downstream from the radiator.

linear polarization in the plane given by the beam direction and the crystal lattice vector. This polarization is enhanced by collimating the photon beam beyond its intrinsic angular spread, as discussed in the next section. The loss in flux from collimation can be recovered by increasing the crystal thickness or the electron beam current. As will be shown in the following section, even in the case of very thin crystals and severe collimation, only modest electron beam currents are needed to produce the required photon flux.

The use of coherent bremsstrahlung improves the background conditions by increasing the ratio of hard to soft photons in the beam. For measurements that do not require polarization, a crystal radiator can be used without collimation to reduce the amount of low-energy background for a given rate of tagged photons. Where polarization is required, coherent bremsstrahlung is indispensable.

4.2 Photon Source

A horizontal plan view of the photon beam line is shown in Fig. 4.4 with the major components labeled. The electron beam enters the figure from below ground at the left and is bent into the horizontal plane to enter the tagger building. There it passes through two small dipoles to impinge upon the bremsstrahlung radiator. After its exit from the radiator, the electron beam passes into the tagger magnet where the primary beam is bent in the direction of the electron beam dump. The radiator crystal is thin enough that most of the electrons lose less energy in traversing the radiator than the intrinsic energy spread of the incident beam. Those electrons which lose a significant fraction of their initial energy inside the radiator do so by emitting a single bremsstrahlung photon. These degraded electrons are bent out of the primary beam inside the tagger magnet and exit the vacuum through a thin window, passing through air for a short distance to strike the focal plane of the spectrometer. The primary electron beam is contained inside vacuum all the way to the dump. The two dipole magnets shown in the figure downstream of the tagger may not be necessary if the deflection angle of the primary beam inside the tagger magnet is deemed to be sufficient.

The photons that are produced in the radiator pass through a small hole bored in the return yoke of the tagger magnet to exit the vacuum through a thin window in the forward direction. They then pass into a transfer pipe, which may either be evacuated or filled with helium to reduce photon beam degradation due to interactions, and travel to the experimental hall. Just before entering the hall the photon beam passes through a system of collimators and sweeping magnets. In the figure they are shown in a separate enclosure for shielding purposes. The primary collimator is first. It defines the part of the photon beam that is allowed to reach the target. Debris from interactions along the inside surface of the collimator bore forms a halo around the photon beam that exits the collimator. The charged component of the halo is deflected away from the beam axis by a dipole "sweeping" magnet just downstream of the collimator. A secondary collimator follows the sweeping magnet to stop the deflected shower particles and block the halo of secondary photons generated by the first collimator. The secondary collimator is of a larger diameter than the primary and so sees a reduced rate of secondary interactions on the inner surface of the hole. What new showers are generated there are cleaned up by a second sweeping magnet. The beam then passes through a final collimating aperture into the experimental hall. This triple-collimation

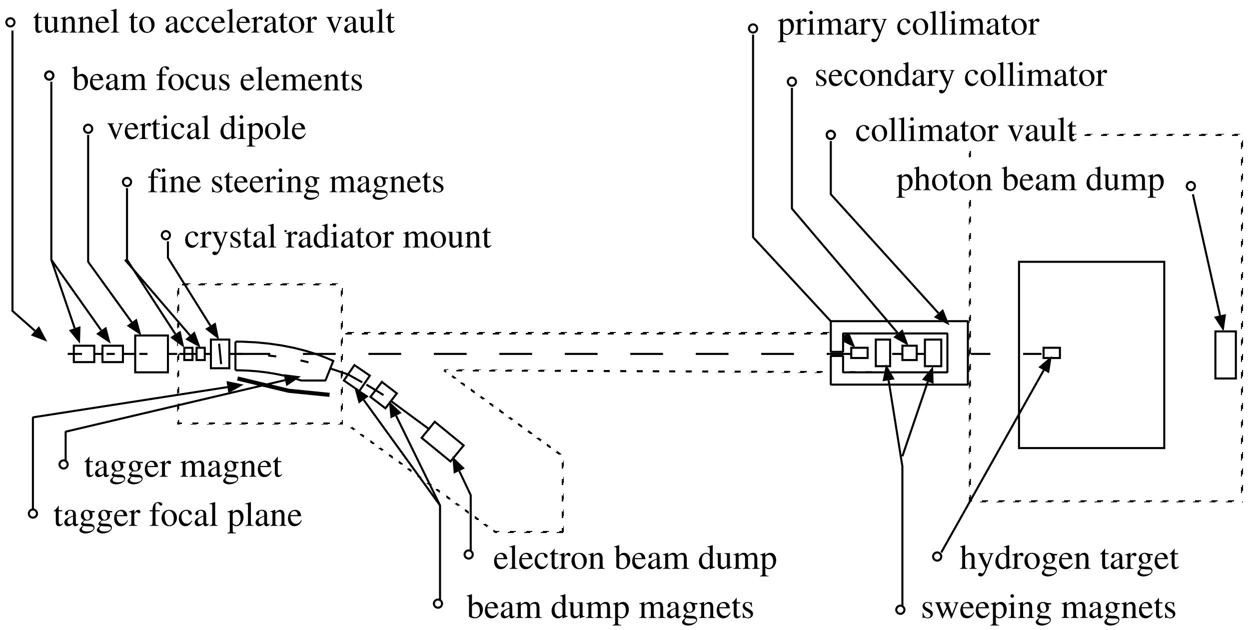

Figure 4.4: Schematic plan view of the photon beam line, shown in the horizontal plane as viewed from above. The objects in this figure are not drawn to scale.

system was copied from the setup developed at SLAC [121].

The collimated photon beam, now only a few mm in diameter, is delivered to the experimental target. After passing through of order 3% radiation lengths of target, the photon beam passes through the detector and into the photon beam dump at the back of the hall. Based upon a design upper limit of 60kW (5μA at 12 GeV) being delivered to the electron beam dump, the total power in the photon beam is at most 1.5W in the experimental hall and at most 15W in the collimator enclosure.

4.2.1 Essential features

The adjective 'coherent' in coherent bremsstrahlung does not indicate that the photons in the beam are in a coherent state, as is light from a laser. Rather it refers to the coherent effect of multiple atoms in a crystal lattice in absorbing the recoil momentum from a high energy electron when it radiates a bremsstrahlung photon. In X-ray spectroscopy one encounters the same thing in the Mössbauer effect, except in that case the chief physical consequence is the disappearance of the recoil Doppler shift from the photoabsorption/emission spectrum. Here the chief consequence is the enhancement of bremsstrahlung at those particular kinematics for which the recoil momentum matches one of the reciprocal lattice vectors of the crystal.

Another useful way to view the process of coherent bremsstrahlung is as virtual Compton scattering. To the high energy electron, the atoms in the radiator appear as clouds of virtual photons. For a disoriented radiator material, the virtual photon spectrum is given simply by the atomic form factor, averaged over the different species in the material. If the radiator is a single crystal, however, the atomic form factor gets multiplied by the form factor of the crystal, which in the ideal case looks like a series of delta-functions located at the sites of the reciprocal lattice. In effect, the crystal provides a set of virtual laser beams, each one a standing wave tuned to a specific reciprocal lattice vector. In this view the process of hard bremsstrahlung is seen to be the same as Compton back-scattering of laser light. For a more detailed discussion of the physics of coherent bremsstrahlung there are a number of good references [121, 122, 123, 124].

The use of Compton back-scattering of laser light as a photon source was earlier noted as ruled out by the limitation of high-power lasers and cavities to wavelengths above 100 μm. The characteristic wavelength of the crystal photons is a few Angstroms, three orders of magnitude shorter. In this case, 180° scattering would result in essentially 100% of the electron beam momentum being transfered to the photon in the lab frame. However, the Compton cross section contains a factor of $1/(\vec{q}\cdot\vec{p})^2$ where $\vec{q}$ is the virtual photon momentum and $\vec{p}$ is that of the electron, which strongly favors incident photons with $\vec{q}$ nearly orthogonal to $\vec{p}$. With reciprocal lattice vectors pointing in almost every direction, only those nearly perpendicular to the beam contribute appreciably to the scattering rate. This fact applies equally to ordinary bremsstrahlung; in fact, to a first approximation the bremsstrahlung spectrum from a single crystal is the same as from a disoriented radiator. The reason is that, if the sum over crystal momenta were replaced with a continuous integral, one would recover the ordinary bremsstrahlung result for isolated atoms. Beyond a few unit cells from the origin in reciprocal lattice space, the atomic form factor and kinematic factors become slowly varying on the scale of the lattice spacing, and the sum becomes indistinguishable from the integral. Besides that, the uncertainty principle requires that atoms localized at the sites in a crystal undergo fluctuations about their mean position. This has the effect of attenuating the discrete peaks in the crystal form factor at progressively higher-order crystal momenta, eventually washing them out and filling in the gaps between them, so that the sum deforms smoothly into the integral at high momentum transfer. Hence, the sum over crystal indices that yields the final photon spectrum can be separated into two parts: a discrete sum over a limited set of small crystal indices and an integral over the continuum of momentum transfer values beyond. The latter appears in the coherent bremsstrahlung beam as an ordinary $1/k$ bremsstrahlung spectrum, while the former appears as a set of peak structures superimposed upon it. The $1/k$ continuum, referred to as the incoherent component, is invariant as the crystal is rotated, whereas the coherent peaks change in position and intensity, depending on crystal orientation.

A typical coherent bremsstrahlung spectrum is shown in Fig. 4.5. The distinction between incoherent and coherent components in the figure is artificial; it is there to show the part of the spectrum that shifts as the crystal is rotated. The vertical scale in the figure gives the photon rate for the given beam current and crystal thickness. Note that the intensity of the incoherent background is less than what would be obtained with an amorphous carbon radiator of the same thickness, because a part of the momentum transfer integral in the Bethe-Heitler formula has been moved into the discrete sum and contributes to the coherent part. The radiation length of diamond is actually an average over all orientations of the crystal. In the calculation for Fig. 4.5 the leading 400 lattice sites were included in the discrete part of the calculation, although it can be seen that only two or three of them contribute with sufficient intensity to be individually visible in the spectrum.

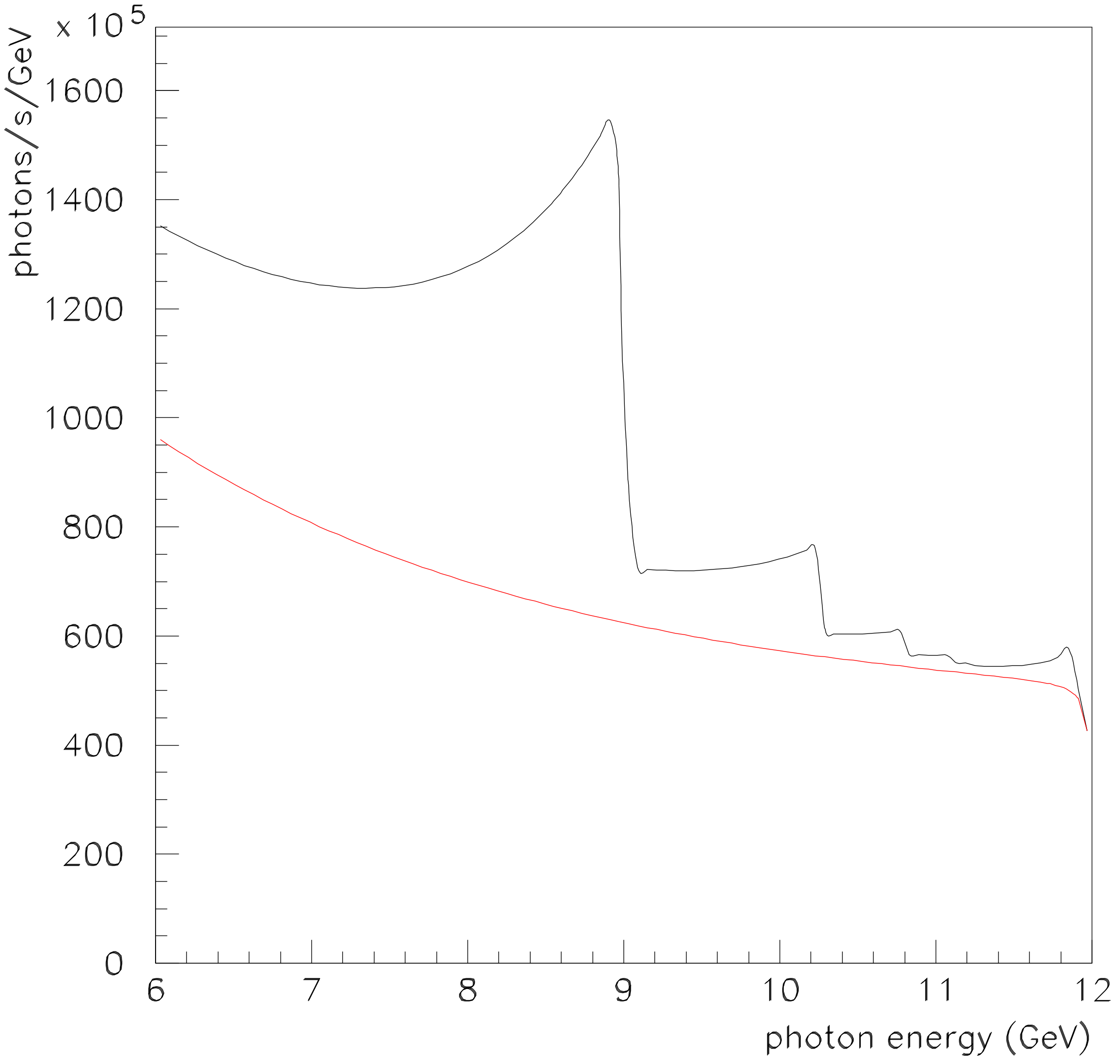

Figure 4.5: Coherent bremsstrahlung spectrum, calculated for a diamond crystal radiator 15μm thick and a 1μA electron beam of 12 GeV energy. Typical values were used for beam emittance and crystal mosaic spread.

4.2.2 Use of collimation

The presence of the large incoherent flux in Fig. 4.5 presents a significant handicap to a photoproduction experiment. Not only do the low energy photons produce background in the detector, but they diminish the polarization of the beam. The entire beam polarization appears in the coherent component; the underlying incoherent flux only serves to dilute the polarization. There is another difference between the two components that allows them to be separated to some extent. The kinematics of bremsstrahlung confines most of the intensity of the photon beam to forward angles within m/E radians of the incident electron direction. In the lab this is a small angle, but in the rest frame of the electron-photon system it subtends all angles in the forward hemisphere. A peak in the coherent component that corresponds to a single reciprocal lattice vector has two-body kinematics, so there is a well-defined relation between the emission angle and the energy of the emitted photon in the lab: emission at 0° yields a maximum energy photon, with energy decreasing with increasing angle. This accounts for the shape of the coherent peaks in Fig. 4.5, with the sharp right-hand edge corresponding to 0° emission and the tail to lower energies corresponding to scattering into higher angles.

The incoherent component, because it comes from a sum over momentum transfers at all angles, has essentially no correlation between photon energy and emission angle. This means that collimating away all photons beyond some angle $\theta_{max} < m/E$ uniformly attenuates the incoherent spectrum at all energies, whereas it preserves all of the coherent photons from the maximum energy for the given peak down to some cutoff. The kinematic relations for coherent bremsstrahlung are as follows,

$$\theta^2 + 1 = \left(\frac{1-x}{x}\right)\left(\frac{x_{max}}{1-x_{max}}\right) \tag{4.1}$$

$$x_{max} = \frac{2\vec{p}\cdot\vec{q}}{2\vec{p}\cdot\vec{q} - m_e^2} \tag{4.2}$$

where x is the photon energy in units of the incident electron energy and θ is the lab emission angle of the photon relative to the incident electron momentum axis, in units of m/E .

The effects of collimation are demonstrated in the calculated spectra shown in Fig. 4.6. First, note that the collimation angles are very small, which requires a long flight path of order $100\,m$ in order that the collimator can be larger than the intrinsic beam spot size, otherwise the collimator is cutting in transverse coordinate instead of in angle. This distance is, in fact, a sensitive function of the electron beam emittance from the machine, and must be increased in inverse proportion to the beam emittance if the effectiveness of collimation is to be maintained. This issue, along with the associated demands placed on beam alignment and position stability, are taken up in more detail in the following section on the electron beam line.

Second, note that the cut imposed on the coherent peak by collimation does not produce a perfectly sharp edge as would be expected from two-body kinematics. This is because a collimator cuts on radius at some fixed position which translates into a cut on emission angle only in an approximate way, and is why the curves in Fig. 4.6 are labeled by their collimator size and distance individually rather than their ratio which is the nominal collimation angle. Multiple scattering by the electron in the radiator prior to emission and beam spot size

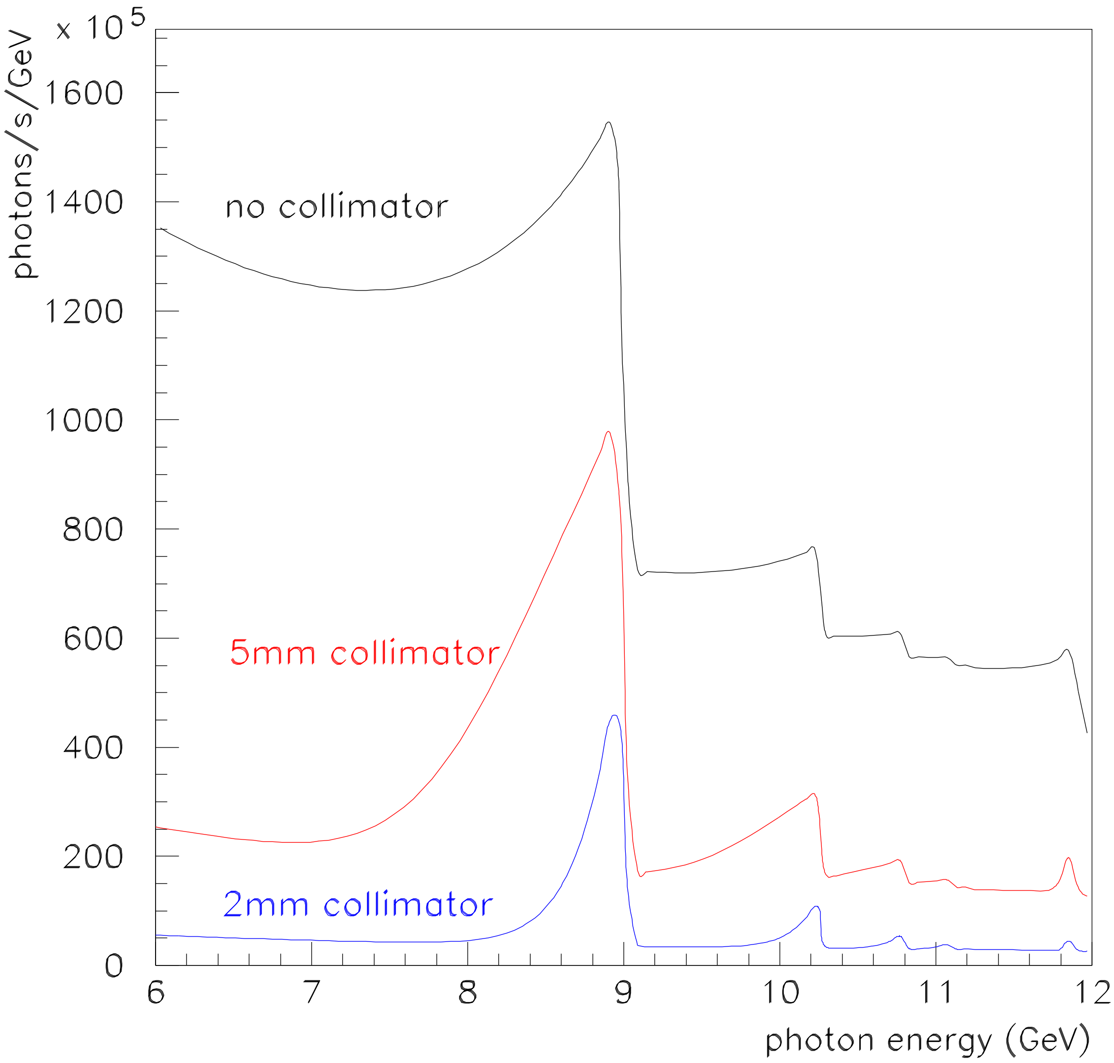

Figure 4.6: Coherent bremsstrahlung spectrum, calculated under the same conditions as in Fig. 4.5 , after collimation. The upper curve is the uncollimated spectrum from Fig. 4.5. The middle curve corresponds to a 5mm diameter collimator placed 80m downstream of the radiator, or approximately 0.75 m/E in collimator half-angle. The lower curve corresponds to a 2mm collimator in the same position, approximately 0.30 m/E

and divergence are the major contributors to the error involved in interpreting a collimator as a cut in emission angle. All of these effects have been incorporated into the analytical calculation of the yields from a collimated coherent bremsstrahlung source that has been used in preparing this report. Crystal imperfections, which amount to an intrinsic spread in the direction of the incoming virtual photon, are also accounted for in the calculation.

Third, note that the relatively weak collimation at $5\,mm$ reduces the incoherent background without significantly affecting the coherent flux near the maximum, and thereby almost doubling the polarization of the beam at the peak relative to the uncollimated case. Further reducing the collimator diameter continues to narrow the peak and reduce the incoherent flux relative to the peak, albeit at some cost in peak intensity. In the case of the $2\,mm$ collimator, the peak polarization is essentially that of the coherent component alone. For this collimator diameter most of the photon beam energy is being absorbed at the collimator. However the necessary flux in the collimated beam can be made up by increasing the electron beam current. provided there is adequate shielding around the collimator. The peak in Fig. 4.6 for a $2\,mm$ collimator contains 20M photons/s for an electron beam current of 1μA, which could be increased by a factor of up to 3 in the facility being planned for HALL D.

Fourth, note that the rate seen in the focal plane of the tagging spectrometer corresponds to the upper curve in Fig. 4.6, regardless of the collimation. This means that collimating the bremsstrahlung beam increases the rate in the tagger focal plane relative to what is seen at the detector. For example, running with the 2mm collimator and 10^7 photons/s in the main coherent peak implies according to Fig. 4.6 a rate of $70\,MHz$ per GeV in the focal plane. Under these conditions, only a small part of the focal plane is in coincidence with the events of interest, which limits the rate of accidental tags to a reasonable level.

The net polarization of the beam under different collimation conditions is shown in Fig. 4.7. The dashed curves show how the maximum polarization in the peak varies as the peak energy is changed by rotating the crystal. The polarization in all cases is zero at the endpoint. Without collimation it rises as $(k - E)^2$, one power coming from the intensity of the coherent peak relative to the incoherent component going to zero linearly at the endpoint, and the other from the intrinsic polarization of the coherent photons also behaving like $(k - E)$ near the endpoint. Collimation allows one to essentially isolate the coherent component, so that the polarization available to the experiment rises from zero at the endpoint in a linear fashion. The dashed curves in Fig. 4.7 demonstrate this point.

In order to obtain the full polarization enhancement from collimation, it is necessary to have a distance between the radiator and collimator on the order of $100\,m$. This distance scale is set by the requirement that the collimator aperture must be large compared to the virtual electron beam spot on the collimator but small compared to the actual photon spot size. Fig. 4.8 shows the maximum polarization as a function of radiator-collimator distance for a coherent peak at $9\,GeV$. The collimator diameter is adjusted in this calculation to keep the collimation half-angle at $0.5\ m/E$. At zero distance the collimator has no effect except to attenuate the beam, and so the uncollimated polarization from coherent bremsstrahlung is obtained. At 100m separation distance the polarization enhancement has saturated. The design for HALL D calls for a radiator-collimator distance of $80\,m$.

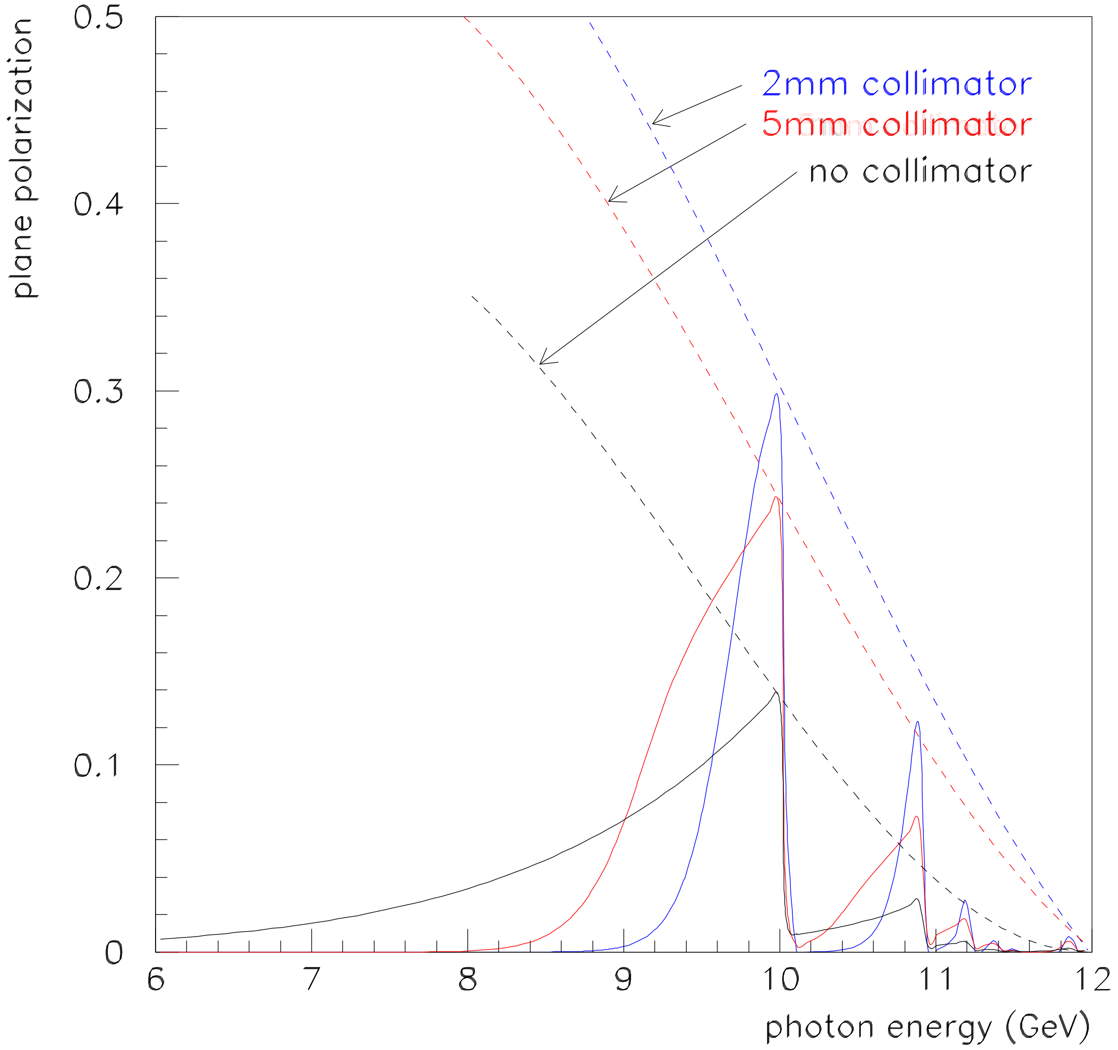

Figure 4.7: Plane polarization of the coherent bremsstrahlung beam, calculated under the same conditions as in Fig. 4.6. The dashed lines indicate the trajectory of the peak polarization as the peak energy is swept across the focal plane by rotating the crystal.

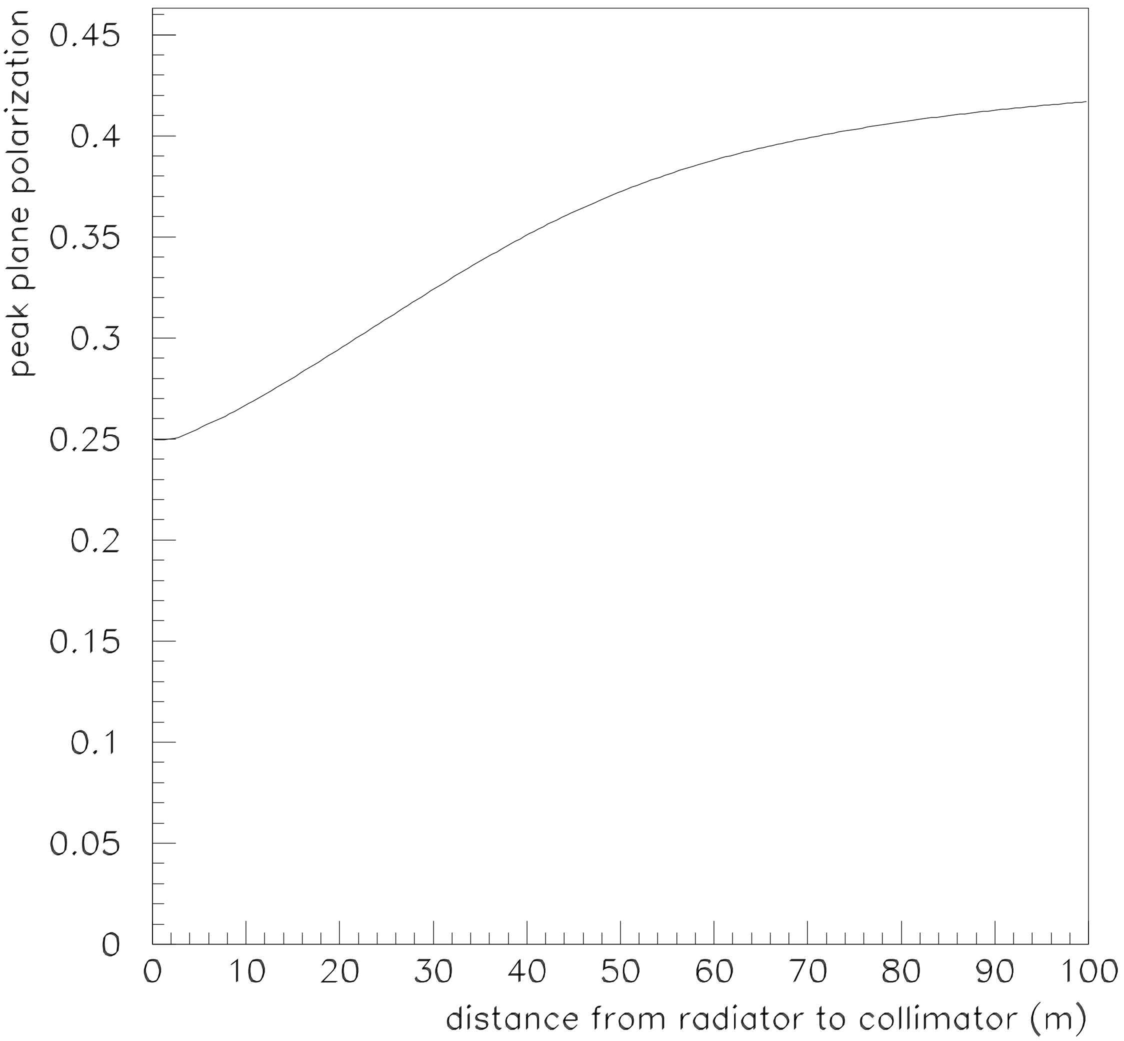

Figure 4.8: Maximum polarization *vs* radiator-collimator distance for a coherent peak at 9 GeV. The collimator diameter is varied in this calculation to keep the collimation half-angle at 0.5 m/E.

crystal	best reciprocal vector	$P/P_{diamond}$
diamond	2,-2,0	1.00
beryllium	0,0,2	0.86
boron	2,0,8	0.38
silicon	2,-2,0	0.19
Be_2C	2,2,0	1.10

Table 4.1: Figure of merit of various materials that might be used as a coherent bremsstrahlung radiator. This table is reproduced from Table 2 in H. Bilokon *et al.*

4.2.3 Choice of radiator

The ideal radiator would be a layered structure with a strong transverse fields that alternate between layers spaced about 50 nm apart, thus simulating the standing wave in a cavity driven by a 15 eV laser. While it is possible to construct ordered materials with unit cells as large as this, the self-shielding of atoms means that beyond the atomic length scale the residual fields are comparatively weak. Hence heterogeneous structures are not viable for use as a coherent radiator. Since the strong fields inside a solid are revealed at the atomic scale, the first requirement for a good radiator is that the unit cell be compact and closely packed. The best radiators are those with the smallest unit cells because these provide the best match between the atomic and the crystal form factors. This match is best for the light elements, and essentially prohibits the effectiveness of any materials heavier than carbon. An extensive survey of possible radiator materials is presented in Ref. [122]. In Table 4.1 is shown the figure of merit that those authors report for favored crystalline materials. The figure of merit is the product of the atomic times the crystal form factor evaluated at the leading peak, normalized to the value for diamond.

Table 4.1 shows that the list of viable materials for a crystal radiator is relatively short. Silicon would be an excellent choice from the point of view of price and fabrication, but unfortunately it is far inferior in terms of performance. Beryllium carbide is not a material that is familiar to the crystal growth industry, and nothing is known at present concerning its suitability for the growth of single crystals of large area. In general compound materials are more susceptible to radiation damage than are pure elements, which would argue in favor of diamond and beryllium metal. These two materials are comparable in terms of their performance.

Most of the experience to date with coherent bremsstrahlung has been with diamond radiators. Extensive expertise for handling large diamond crystals exists within the gem industry. High quality monocrystals of $6\,mm \times 6\,mm$ area were obtained by SLAC [121] some time ago from a jeweller, who was able to cleave a thin wafer from the face of a large high-quality gem. Those wafers that passed quality checks were then milled down to less than 100 μm using chemical erosion in an atomic oxygen discharge. Now three decades later, it is not clear whether this same route can be travelled again, as it owed its success in a large measure to a friendly contact within the gem business at that time. The cost of the entire gems from which the shavings were taken would have been prohibitive. Today other methods exist for growing single crystals which might be capable of producing diamonds of sufficient size and quality for this application. A variety of potential sources for single crystals are being pursued.

Beryllium is another material that might be used as a crystal radiator. Beryllium metal is widely used in industry, being preferred for its high strength-to-weight ratio and robustness, in addition to its transparency to X-rays. Thin films of high-purity beryllium are routinely produced for vacuum window applications, which use some of the same vacuum deposition techniques that would be used for the growth of single crystals. As a radiator material, beryllium is distinguished as the metal with the highest Debye temperature, around 1400°K . The Debye temperature measures the temperature at which the thermal motion of the atoms in the lattice reaches the level of the zero-point motion due to their confinement in the lattice, as dictated by the uncertainty principle. A high Debye temperature indicates a stiff crystal lattice, in which the atoms have little liberty to move and so have large momentum fluctuations, as dictated by the uncertainty principle.

A high Debye temperature is important for a bremsstrahlung radiator material for three reasons. First, the cross section for coherent bremsstrahlung from a discrete crystal momentum vector $\vec{q}$ contains a factor $e^{-q^2/4M\theta_D}$ which reflects the fact that position fluctuations of atoms in the lattice diminish the coherent effect. This factor is near unity for the low-order crystal momenta provided that θ is sufficiently large. Second, the Debye temperature is, roughly speaking, a measure of the stability of the crystal structure and hence its readiness to form as a single crystal and to survive significant doses of radiation. Third, the radiator material will inevitably be heated by the beam, and will normally operate in vacuum well above the ambient temperature. A high Debye temperature means that there is a large range of temperatures over which the material may operate without degraded performance as a crystal radiator. The Debye temperature of diamond is about 2200° K. Past experience has shown that diamond meets all of the requirements for a good crystal radiator. There is good reason to believe that beryllium would function almost as well at substantially less cost, but this remains to be proved.

4.2.4 Crystal thickness

The range of permissible thicknesses for a crystal radiator is bounded both from above and below. It is bounded from above by multiple scattering of the electron beam as it passes through the radiator, which causes the divergence of the incident beam to grow, thereby enlarging the photon beam spot on the collimator face and degrading the degree to which collimation discriminates against the incoherent component in favor of the coherent part. It is bounded from below by the fact that the crystal must be of some minimum thickness in order to achieve the full coherent gain. In the calculation of the coherent bremsstrahlung process one begins by assuming an infinite crystal, although practically it is presumed to mean only that the crystal is large compared to the some characteristic scale. It is important to identify what the characteristic scale is in this problem in order to know how thin one can make the crystal without hurting performance. In the analogous case of the Mössbauer effect, one can estimate the number of atoms participating in the collective absorption by looking at the emission time of the photon (lifetime of the radiating transition) and asking how many nuclei lie within the envelope of the photon wave packet. In the coherent bremsstrahlung process, the lifetime of the radiating system is given in the lab system by the uncertainty principle and by how far the electron energy deviates from its on-shell value between absorbing the virtual photon and emitting the real one. The latter quantity is almost exactly given by q_z , the virtual photon momentum component along the incident electron axis, which means that the electron travels a distance $\lambda = \hbar c/q_z$ during the interaction. For a given coherent peak at normalized energy x in the photon spectrum, the coherence length is given by

$$\lambda = \frac{2e(1-x)}{xm^2} \tag{4.3}$$

in units of $\hbar c$. From this simple argument one sees that the coherent gain goes linearly to zero at the endpoint, a result that is borne out by the full QED calculation. One also sees that the lower limit on crystal thickness imposed by the coherence length depends upon both the electron beam energy and the photon energy. For a 12 GeV beam energy and a 6 GeV coherent photon the coherence length is 18 nm, or about 50 unit cells for diamond. This shows that the coherence length does not impose a practical limit on how thin the radiator should be.

The effects of multiple scattering are best presented by showing the calculated spectra for various radiator thicknesses. In Fig. 4.9 is shown the photon spectrum for a 20 μm and a 100 μm radiator to demonstrate the effect. The 100 μm spectrum is scaled down by a factor of 5 to facilitate the comparison. The calculation assumed a 2 mm collimator located 80 m downstream of the radiator. The loss in normalized intensity with the thicker radiator, as well as the broadening of the left edge of the peak, is due to the enlarging of the photon beam spot on the collimator face from multiple scattering of the electron beam in the crystal prior to radiation. A 100 μm diamond crystal is roughly 10^{-3} radiation lengths thick. It is reasonable to run with as thick a radiator as is permitted by multiple scattering considerations, in order to keep the beam current to a minimum and prolong as much as possible the lifetime of the crystal.

4.2.5 Crystal mount

It has already been shown that in order to achieve appreciable coherent gain the crystal must be oriented so that the coherent peaks appear well below the end point. Eqn. 4.2 then implies that the orientation must be such that the crystal momentum dotted with the beam momentum be of order m^2 . Given a p of 12 GeV and q of $10keV$, this requires that the two vectors must be within $100\mu r$ of perpendicular to each other and that, within a range of angles of that order, the coherent peak sweeps out nearly the full range in x from 0 to 1. Hence both the incident beam angle and the angle of the crystal radiator must be stable at the level of a few μr in order to have a stable photon beam for running. At least one of the two must be adjustable in steps that are small compared to $100\mu r$ in order to have the ability to position the coherent peak at the desired energy. These requirements are most simply achieved using a precision two-axis goniometer. Commercial devices of this type exist with step sizes as small as required for this application. With two-axis remote control the crystal can be reoriented in a matter of minutes to produce a coherent beam of any desired energy and in either vertical or horizontal plane polarization modes.

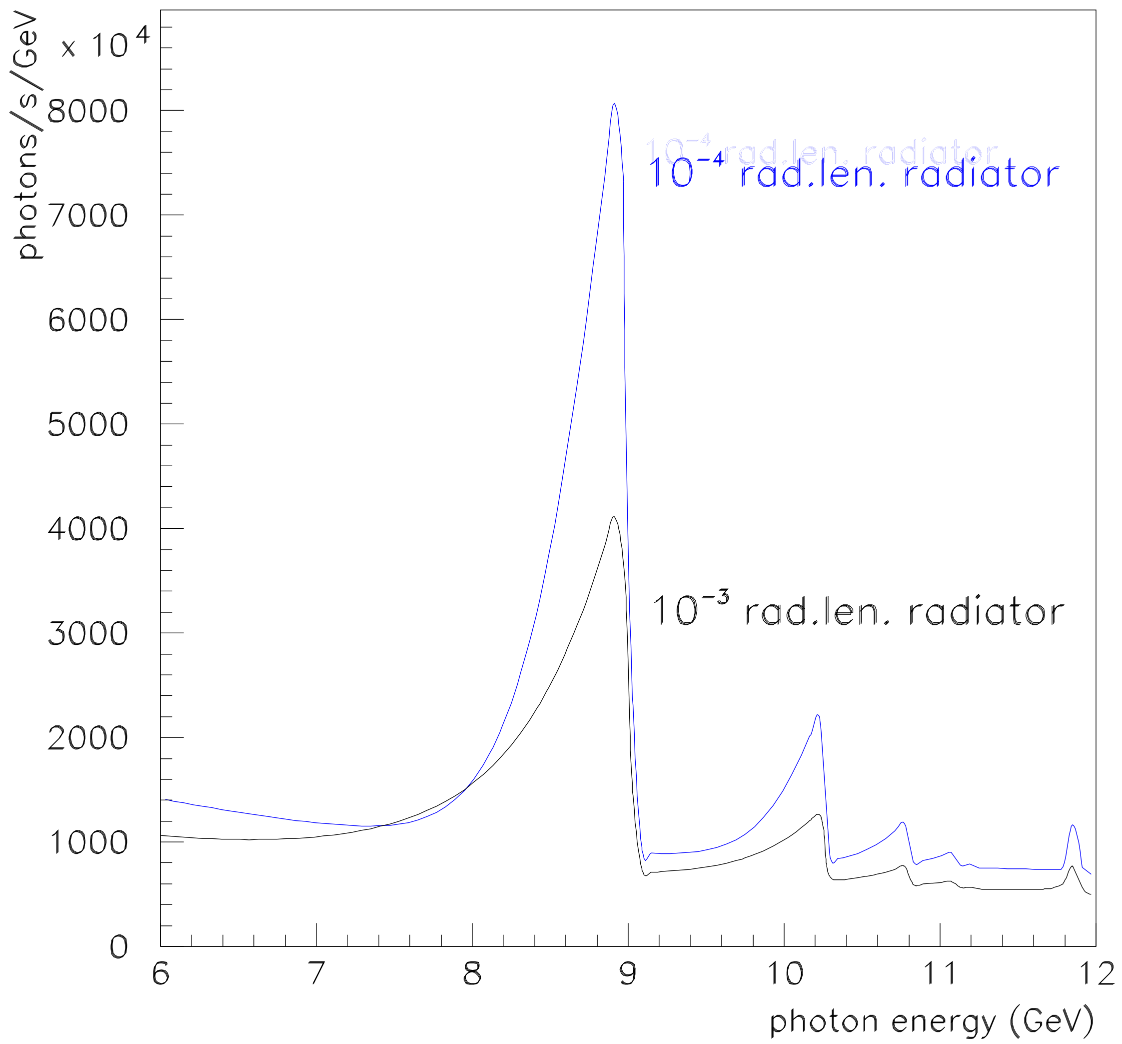

Figure 4.9: Collimated coherent bremsstrahlung spectrum from a 1μA electron beam at 12 GeV using diamond radiators of two different thicknesses. The calculation assumes a $2\,mm$ collimator located $80\,m$ from the radiator, and typical values for beam emittance and crystal quality.

Thermal effects in the crystal mount and small variations in the beam tune from the accelerator make long term stability and reproducibility more difficult to achieve than adequate controls for the initial setup. For this reason it is important that there be sufficient diagnostics present to monitor the crystal orientation relative to the beam. This diagnostic is provided by the rates in the tagger focal plane counters. From Fig. 4.5 it is clear that the critical angle between the beam and the crystal, as well as the quality of the crystal, are accurately reflected in the position and sharpness of the coherent edge in the focal plane rate profile. Better than simply monitoring the critical angle, the tagger profile provides a direct look at the photon beam spectrum prior to collimation. This means that there is no need for an absolute alignment of the crystal and goniometer to this level of precision, because only relative accuracy is required. The second angle is non critical, typically of order a degree, and does not need to be monitored. If conditions require it, a feedback system could be put in place to correct for drifts seen in the tagger focal plane profile by periodically adjusting the goniometer setting within predefined limits. This would involve a slow control system, and does not need to be designed in advance.

4.2.6 Crystal quality and lifetime

There are two considerations that fall under the heading of crystal quality. The first respects the quality of the original crystal, and the second is with regard to degradation from radiation damage. In the calculation of the coherent bremsstrahlung spectrum a perfect single crystal was assumed, but even the very best crystals have some dislocations and other defects. Besides locally disrupting the regularity of the crystal, these defects impose stresses which produce small ripples in the crystal planes. If these ripples were amplified, the surface of a crystal would appear like a mosaic of planar regions with approximately parallel surfaces. The scale of deviations from planarity across the face of a single crystal is termed the *mosaic spread* of the crystal. The mosaic spread contributes in the same way as beam divergence to the smearing in the exact energy-angle relation for coherent photons.

The mosaic spread of a crystal can be measured by means of X-ray diffraction. At the time when the SLAC group was preparing their samples, a laboratory at the National Bureau of Standards had a state-of-the-art facility for these measurements. Their source of high-quality natural diamonds cleaved several samples and sent them to the NBS for rocking-curve measurements. Most of the crystals failed the tests, but among them were a few of sufficiently low mosaic spread to be acceptable. Ref. [121] does not report a value for the mosaic spread of the radiator, but from the sharpness of the coherent peaks in the beam spectra shown in the paper, one can infer that crystals with less than 50 μr mosaic spread were obtained in this way. Other coherent bremsstrahlung facilities that have operated at lower energy are less sensitive to mosaic spread because the characteristic angle scales like m/E. The calculations for this report assumed a mosaic spread of 50 μr for the crystal radiator.

The SLAC group found that the performance of their diamonds had degraded considerably after a total charge of 3 Coulombs had been accumulated over a surface of $6\,mm \times 6\,mm$ in area. They were able to recover a better performance for the damaged crystals by putting them through an annealing process. This translates to five weeks of running, or about two months of real time at 1μA of current, before the crystal would need to be

energy	12 GeV
r.m.s. energy spread	< 10 MeV
transverse x emittance	10 $mm{\cdot}\mu$r
transverse y emittance	2.5 $mm{\cdot}\mu$r
electron polarization	longitudinal when available
minimum useful current	100 pA
maximum useful current	3 μA
x spot size at radiator	1.7 mm r.m.s.
y spot size at radiator	0.7 mm r.m.s.
x spot size at collimator	0.5 mm
y spot size at collimator	0.5 mm
position stability	± 200 μm

Table 4.2: Electron beam properties that were assumed in calculating the properties of the coherent bremsstrahlung source.

removed for treatment. A small set of radiators of different thicknesses would accommodate a run plan that includes some running with maximum polarization, i.e. narrow collimation, a thin radiator and microamps of beam current, and running the rest of the time with a thicker radiator, less beam current and more modest collimation.

4.3 Electron Beam

The performance of the photon source is dependent upon the parameters of the electron beam in several important areas. The assumptions regarding the electron beam that were used in calculating the properties of the coherent bremsstrahlung source reported in this chapter are collected together in Table 4.2. Some of these parameters require further explanation. Only circular polarization can be transfered from the electron to the bremsstrahlung photon beam. In fact, helicity transfer from the electron is the only means available for generating photons with circular polarization in HALL D. Although circular polarization is less interesting than linear polarization from the point of view of meson photoproduction, having access to both kinds makes available a complete set of polarization observables. At the present a concrete design for the optics of the transfer beam line to HALL D does not exist, but when the design is made it would be useful to check that it can deliver circularly polarized photons to the hall.

4.3.1 Beam emittance requirements

The values for the electron beam emittances shown in Table 4.2 are estimates based upon the parameters of the current machine projected to 12 GeV. They were provided by V. Lebedev of the CEBAF accelerator division. The definition of emittance used here is the product of the r.m.s. widths of the beam in transverse position and divergence angle. Because synchrotron radiation occurs mainly in the horizontal plane inside the accelerator, the emittance values in x are generally larger than those for y.

The place where transverse emittance plays a critical role is at the photon collimator. For optimum effectiveness in collimation it is important that the electron beam spot at the collimator position be as small as possible. The electron beam does not actually reach the photon collimator, being bent into the dump shortly after the radiator by the tagger magnet. But considering the optics of the electron beam as if the tagger dipole were switched off, the electron beam at the radiator can be projected forward 80 m to form a virtual image on the collimator entrance plane. The position and size of this spot gives the the definition of the 0° emission angle for the photons. If this spot is small compared to the collimator aperture and is centered then the collimator does its job of removing photons with emission angle beyond the collimator half-angle. However, if the virtual spot is larger than the aperture then the collimator serves only to reduce the intensity of the beam and does not discriminate between coherent and incoherent beam components.

Note that this analysis does not place any specific limits on the size of the beam at the radiator. The beam spot can and should be larger there to avoid burning a hole in the radiator. For the SLAC coherent bremsstrahlung source the beam at the radiator was 6 mm in diameter and focused to image a 2 mm spot at the collimator positioned 91 m downstream of the radiator. The focus ensures that photons emitted near zero degrees, even those far from the beam axis at the radiator, will pass near to the axis at the collimator position and so be seen at the experimental target. The virtual electron beam spot is not the same as the actual photon beam spot on the collimator, which is concentric with the former but larger. The collimator aperture is circular, so the choice was made to make the electron beam come to a virtual focus there with both x and y spot sizes equal there. This is why the beam spot on the radiator is asymmetric.

Figure 4.10 shows how the collimated photon spectrum depends upon the transverse emittance of the electron beam. To generate this plot the increases in emittance were simply translated into an increased virtual spot size on the collimator. This was done because it was assumed that the spot size of the electron beam on the radiator, already close to 2 mm r.m.s., cannot be further inflated and stay contained within the limits of the crystal. When the virtual spot size becomes comparable with the collimator aperture then the collimation is rendered ineffective, and the photon spectrum and polarization revert to their uncollimated values. There is another connection between focal spot size and beam emittance that is connected with the requirement that all electrons enter the radiator at the same incidence angle with respect to the planes of the crystal. Practically, the divergence does not broaden the coherent peak provided that it is kept below the mosaic spread of the crystal. A conservative value for the allowable angular divergence δ in the electron beam at the radiator would then be 20μr . Taken together with a 500 μm r.m.s. spot size at the focus, this leads to an emittance of 10 $mm{\cdot}\mu$r at 12 GeV. This corresponds to the upper curve in Fig. 4.10.

4.3.2 Electron beam line optics

Taking the electron beam out of the machine and focusing it onto a 500 μm spot requires some optics in the beam line leading up to the radiator. Translating the beam emittance into a r.m.s. values for the beam radius and divergence requires the knowledge of the β parameter, defined as the ratio of the r.m.s. beam size to its angular divergence. When it

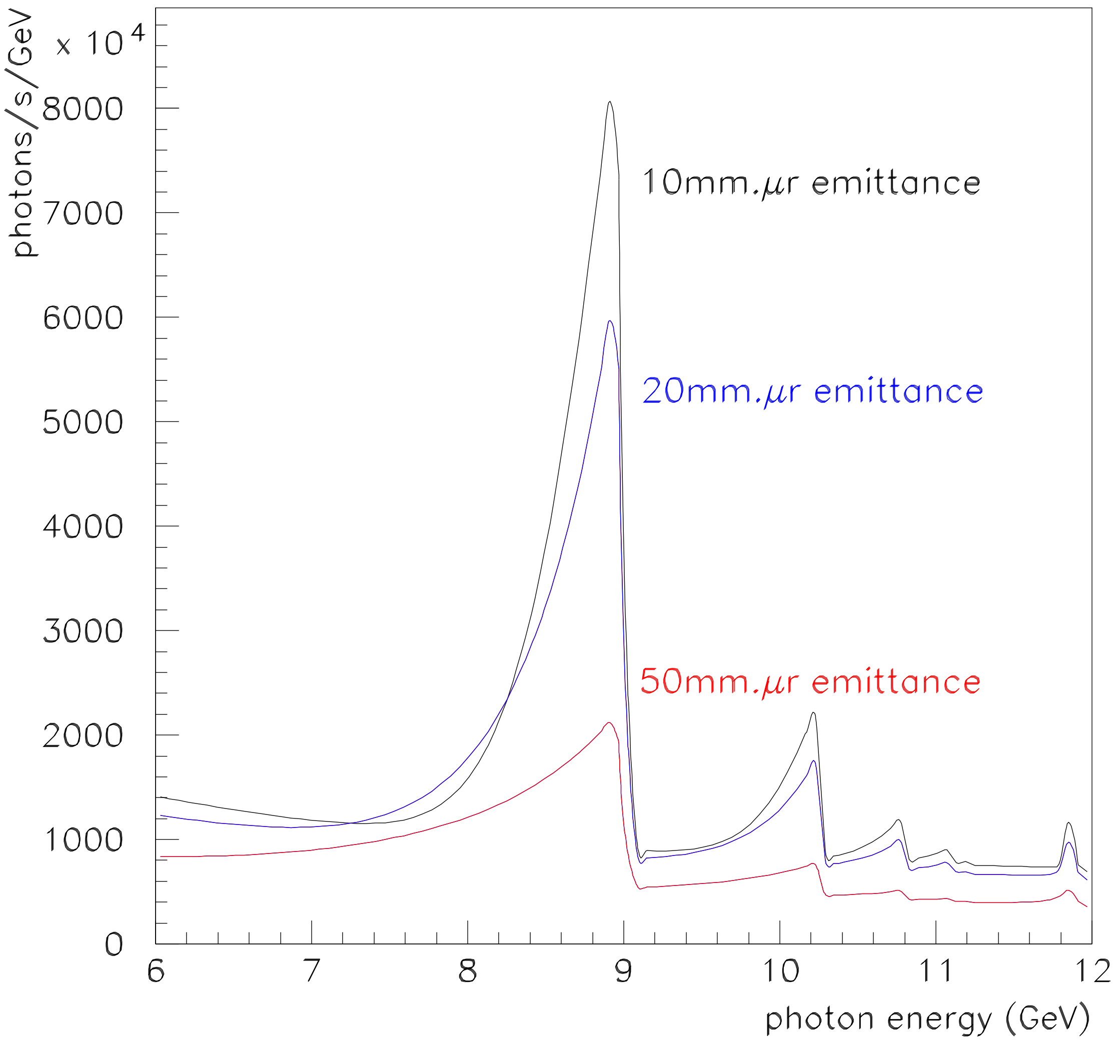

Figure 4.10: Coherent photon spectrum for three different values of the electron beam transverse emittance. The horizontal (shown on the plot) and vertical emittances are assumed to scale together. A 3.4 mm collimator located 80 m from the radiator was used for this calculation.

comes out of the accelerator, β is large, of order 1km, corresponding a very highly parallel beam. In order to focus a beam of emittance $10\,mm{\cdot}\mu$r down to a r.m.s. size of $500\mu r$, the β must be reduced from 1km down to $25\,m$ by the use of focusing elements. The focusing must be done in both x and y axes separately to achieve the desired result, and must be accomplished by elements located along the transfer line from the accelerator vault to the surface. The focusing requirements are very specific for this type of source, and will require careful study in the design of the electron beam line.

Not only must the virtual electron spot be small enough to fit within the collimator aperture, but it must also be centered on the aperture and stable. In order to maintain a stable beam position on the collimator, the SLAC experiment [121] instrumented the collimator with a secondary-emission detector (SEQ). The detector was of the "pin-cushion" design and was installed as a segment of the collimator near the position of the shower maximum. The readout was divided into four quadrants, which read equal currents when the beam was properly aligned on the collimator. The SEQ was connected via a feedback loop to the last steering elements on the electron beam line prior to the radiator. From that distance a bend of only $10\mu r$ results in a shift of $1\,mm$ at the collimator position. Hence the beam alignment feedback system is effectively decoupled from the crystal orientation controls. Small deflections that are necessary to keep the beam centered on the collimator do not produce appreciable walk in the beam-crystal angle, and by using a goniometer to control the latter, the former can be operated in a feedback circuit that operates independent of the photon source energy controls. The experimental program in parity violation at Jefferson Lab has already designed a position stabilization circuit that is able to keep the beam position steady to within $20\mu m$ over a $20\,m$ lever arm. A less sophisticated version of this circuit should be a part of the collimated photon source for HALL D.

4.3.3 Electron beam dump

The electron beam is dumped in the horizontal plane, as shown in figure 4.4. The horizontal bend offers several advantages over dumping the beam into the ground. The tagger magnet is easier to support if it sits in the horizontal position. It is also easier to mount and service the focal plane in this position. The dump itself is also more accessible in case it needs to be serviced. An above-ground dump also affords the possibility of running parasitic beam dump experiments that do not interfere with the operation of the experimental hall.

The primary design requirement for the electron beam dump is that it have a sufficiently high capacity to handle beams of the highest intensities foreseen for HALL D. A 60KW design would provide a a healthy margin for operation of a 12 GeV beam at 3μA and sufficient capacity to handle 3μA at 20 GeV in the case of a further upgrade.

4.4 Tagging Spectrometer

The HALL D tagging system will consist of a dipole magnet spectrometer with a set of plastic scintillation counters in the focal plane to tag photon energies between 50% and 95% of the incident electron energy.

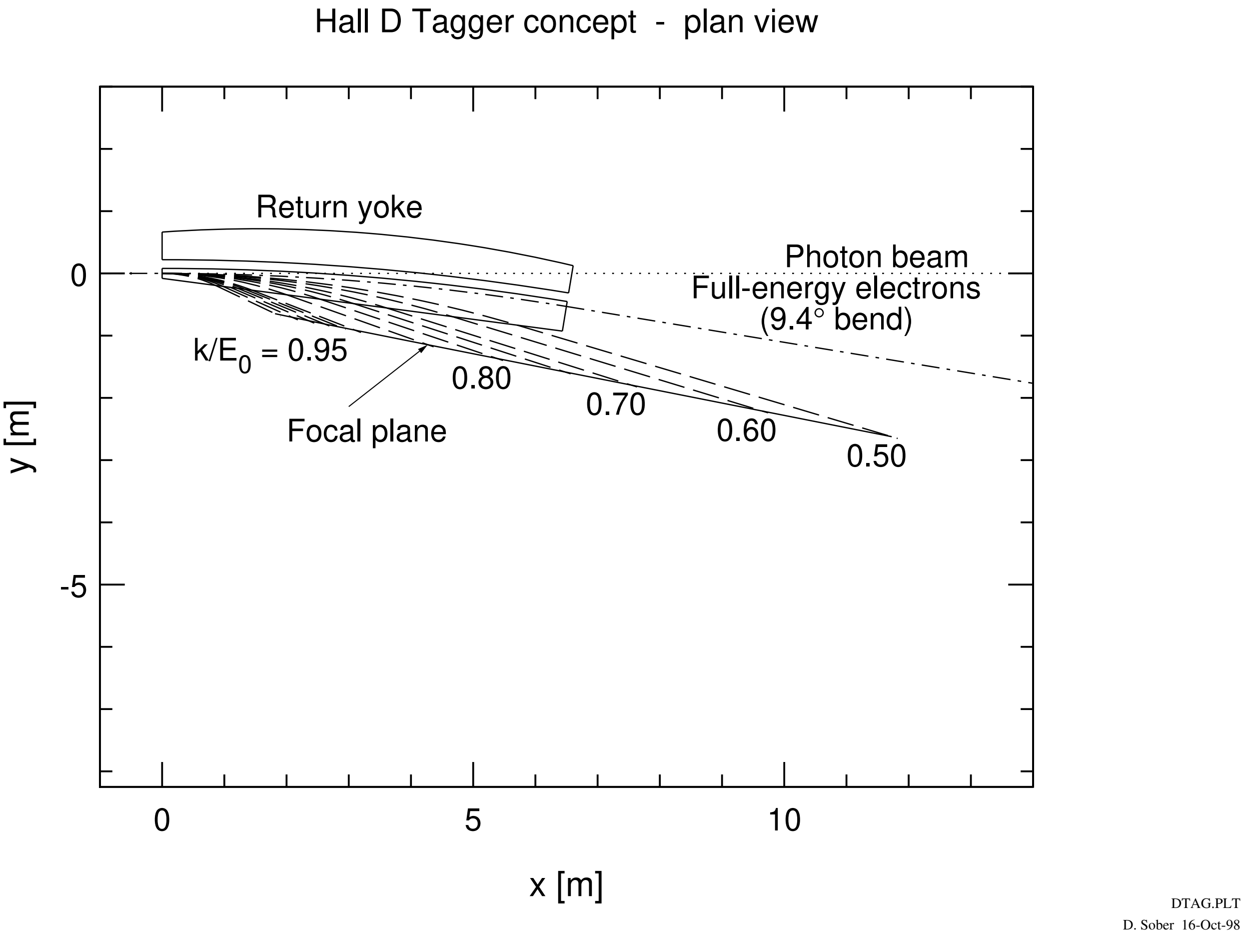

Figure 4.11: A plan view of the tagging spectrometer from above, showing the path of the primary beam and the trajectory of post-bremsstrahlung electrons of various recoil momenta.

4.4.1 Magnet

The tagging spectrometer magnet envisioned for HALL D is modeled closely on the existing tagger magnet in Hall B. Although the HALL D tagger will operate at a much higher energy, the combination of smaller deflection angle and smaller dynamic range (50% to 95% of the incident energy instead of 20% to 95%) result in a device which is comparable to the Hall B tagger in most of its dimensions, allowing the use of existing solutions to many engineering problems.

The tagger magnet will have a length of about 6.5 m and will deflect 12 GeV electrons along a path with radius of curvature 40 m, giving a deflection of about 9.4° (Fig. 4.11). If necessary, additional dipoles may be used downstream to guide the full-energy electron beam to the beam dump. The magnet gap width should be approximately 2.5 cm. A preliminary estimate of power requirements (using a coil configuration like that of the Hall B tagger) gives 500 amperes at 14 volts for 12 GeV operation.

The magnet poles themselves will form part of the vacuum system, and will be welded to a stainless steel vacuum chamber which terminates in a flange for mounting a thin exit window at the focal plane. The exit window, which must be about 10 m long by 10 cm wide, can be built in the same manner as the Hall B tagger window, using aluminized mylar backed by Kevlar cloth [125].

For the above dimensions, the magnetic field at 12 GeV is 1.0 Tesla. If the field is increased to about 1.7 Tesla (the point at which saturation effects become very large), the tagger can operate at a maximum beam energy of about 20.7 GeV. To assure adequate operation at a possible upgraded energy of 24 GeV, the dimensions and cost of the magnet would have to be scaled appropriately.

4.4.2 Spectrometer Optics

The bremsstrahlung electrons are deflected by angles varying from 25.4° to 16.6° over the range of tagged energies. For a radiator position located about 0.5 m upstream of the magnet, a radial focus is obtained along a nearly linear focal surface. Some of the optical properties of the proposed spectrometer are summarized in Table 4.3.

Using the values in Table 4.3, one can calculate the attainable resolution of the tagging spectrometer, which is constrained by the following assumed electron beam sizes:

1. $\Delta p/p_0 = 0.8 \times 10^{-3}$ RMS
2. $\Delta x = 1.7\,mm$ RMS at radiator (horizontal)
3. $\Delta y = 0.7\,mm$ RMS at radiator (vertical)

The horizontal and vertical sizes at the radiator are different because of the different emittances and the need for a symmetric virtual focus at the collimator. For a horizontally-bending tagger magnet, the value x = 1.6 mm would degrade the achievable energy resolution unless the electron beam is rotated to put the smaller emittance in the vertical direction. Table 4.4 indicates the effects of these values at the tagger focal plane, comparing them to the counter width required for an energy channel width of 0.2% E_0.

For a vertical bend, where $y = 0.7\,mm$ applies, the resolution is dominated by the 0.08% momentum width of the beam. If the tagger is built with a horizontal deflection, then the x resolution contribution for $k/E_0 < 0.7$ is comparable to the p contribution, unless the beam is rotated.

4.4.3 Focal-plane hodoscope

Since it is desired to run the experiments at high rate, the tagger detectors will not be incorporated into the trigger logic, but will instead be read out by high-resolution time-to-digital converters (TDCs) for off-line analysis. Assuming that the time correlation with the main detector can be done with a resolution of better than 3 ns, tagged photon rates of up to 100 MHz can be utilized before accidental coincidences become a serious limit.

Electrons will be tagged in energy channels of width 0.002 E_0 (25 MeV at $E_0 = 12\,GeV$). This will result in an RMS energy resolution of about 0.001 E_0, which is consistent with the limits imposed by the beam as discussed in the previous section. As shown in Table 4.4, the width of a counter which defines such a channel varies from 13.2 mm at $k/E_0 = 0.95$ to

k/E_0	Bend (deg)	Drift (m)	Angle (deg)	$cm/\%E_0$ along FP	$cm/\%E_0$ perp.to ray	(x x)	(y y)	(y y') mm/mr
0.95	25.4	1.06	13.3	28.7	6.60	-0.81	3.42	5.8
0.90	21.2	1.78	9.8	24.7	4.19	-0.93	3.49	8.7
0.85	19.5	2.41	8.2	23.2	3.31	-0.97	3.46	11.2
0.80	18.5	3.00	7.3	22.4	2.85	-0.99	3.42	13.5
0.70	17.5	4.12	6.3	21.7	2.37	-1.01	3.34	18.0
0.60	16.9	5.21	5.7	21.3	2.13	-1.01	3.28	22.4
0.50	16.6	6.28	5.4	21.1	1.98	-1.06	3.24	26.2

Table 4.3: Optical parameters of the tagging spectrometer: Bend = deflection angle; Drift = distance from exit edge to focal plane; Angle = angle between electron path and focal plane; cm/%E_0 = dispersion in units of cm per percent of the incident energy; (x x),(y y),(y y') = first-order transport matrix elements where x and y are radial and transverse coordinates respectively; the focal plane is defined by (x x')=0.

k/E_0	Width (mm)	p RMS (mm)	x RMS (mm)	y RMS (mm)
0.95	13.2	5.3	1.4	0.6
0.90	8.4	3.4	1.6	0.7
0.85	6.6	2.6	1.7	0.7
0.80	5.7	2.3	1.7	0.7
0.70	4.7	1.9	1.7	0.7
0.60	4.3	1.7	1.7	0.7
0.50	4.0	1.6	1.7	0.7

Table 4.4: Contributions to tagger energy resolution measured in units of length on the focal plane: Width = physical size of focal plane detector for $\Delta E = 0.002E_0$; p RMS = size due to energy spread of electron beam $p = .0008E_0$; x RMS = size due to horizontal spot size on the radiator $\sigma_x = 1.7\,mm$; y RMS = size due to vertical spot size on the radiator $\sigma_y = 0.7\,mm$.

4.0 mm at $k/E_0 = 0.50$. The spacing of the counters along the focal plane will vary between 4.2 and 5.7 cm according to the data of Table 4.3.

If each detector defines a single energy channel, some overlap with adjacent counters is desirable to avoid gaps in the acceptance and edge effects in the detectors. Because of the close tolerances involved in aligning such narrow counters for small fractional overlap, another solution would be to increase the energy width of the counters and align them so that adjacent counters overlap by 1/3 of their width. In this case, successive energy channels are defined by alternating coincidence and anticoincidence between adjacent counters. The principal disadvantage of this solution is that the counting rate in each scintillator is 3 times the value for the one-counter-per-channel design. For collimated coherent bremsstrahlung running, the coherent peak is confined to a very narrow energy region, especially when the photon energy is close to the endpoint. Under these conditions, individual counters may be required to sustain rates as high as 10 MHz, which will require special bases and electronics, and this rate will probably define the limiting rate for the experiments. Increasing the overlap of the counters would then require a reduction in the total event rate for coherent bremsstrahlung running, and thus is not an attractive solution.

The length of the counters (in the transverse direction) is determined by the desired efficiency for tagging uncollimated incoherent bremsstrahlung events near $k = 0.95E_0$. Counters of length 6 cm will be more than 97% efficient at the endpoint of a 12 GeV beam, and even more efficient at other photon energies. Since the time shifts within a 6 cm-long counter are less than 200 ps, excellent timing can be obtained using a single photomultiplier tube.

Thus the proposed configuration for tagging photons from 50% to 95% of the endpoint energy consists of 225 scintillation counters, each subtending an energy bin of about $0.002E_0$, with minimal (or no) overlap. The dimensions of each counter are approximately as follows: width = 4.0 to 13.2 mm, length = 60 mm, thickness 4 mm. Each counter is read out by a single high-rate photomultiplier tube, permitting rates up to 10 MHz per counter. The counters are at least 4 cm apart along the focal plane, so 2.5 cm PMTs can be used without alternating directions.

4.5 Operating Beam Intensity

Table 4.5 brings together the diverse set of parameters that must be considered in evaluating the optimum beam intensity at which an experiment using the coherent bremsstrahlung beam should operate. All four columns of numbers were obtained for the same beam conditions, except that the crystal orientation was adjusted to align the coherent intensity peak at the energy listed in row one. The second row labeled N_γ gives the integrated rate of beam photons in the coherent peak downstream of the collimator. Note the sharp decrease in the intensity of the coherent peak as the energy approaches the end point. By contrast, the incoherent bremsstrahlung flux is approximately constant over this range of energies. The third and fourth row show the height and width of the peak in the polarization spectrum of the beam. Rows four and five report the height and width of the peak in the tagging efficiency spectrum. The tagging efficiency is defined as the number of beam photons of a particular energy reaching the target divided by the corresponding rate in the tagging focal plane. Large tagging efficiencies are required in order to make effective use of tagging. The

E of peak	8 GeV	9 GeV	10 GeV	11 GeV
N_γ in peak	185 M/s	100 M/s	45 M/s	15 M/s
peak polarization	0.54	0.41	0.27	0.11
(f.w.h.m.)	(1140 MeV)	(900 MeV)	(600 MeV)	(240 MeV)
peak tagging efficiency	0.55	0.50	0.45	0.29
(f.w.h.m.)	(720 MeV)	(600 MeV)	(420 MeV)	(300 MeV)
power on collimator	5.3 W	4.7 W	4.2 W	3.8 W
power on target	810 mW	690 mW	600 mW	540 mW
total hadronic rate	385 K/s	365 K/s	350 K/s	345 K/s
tagged hadronic rate	26 K/s	14 K/s	6.3 K/s	2.1 K/s

Table 4.5: Operating parameters for an experiment using the coherent bremsstrahlung beam. The calculation assumes a 12 GeV electron beam energy and a 3.4 mm collimator 80 m downstream from a radiator of thickness 10^{-4} radiation lengths. The electron beam current is taken to be 3μA. The rates in the detector (last two rows) are calculated for a 30 cm hydrogen target and an open hadronic trigger.

width of the peak in the tagging efficiency spectrum determines the width of the focal plane that would be active when running with collimation. The peak integral reported in row two is summed within the f.w.h.m. tagging efficiency window. Rows seven and eight give the photon beam power that is incident on the experimental target (and photon beam dump) and the photon collimator, respectively.

The last two rows in Table 4.5 give the inclusive and tagged rates for hadronic triggers from a 30 cm liquid hydrogen target placed in the beam following the collimator. Note that the total hadronic rate is dominated by background (*i.e.* non-tagged) events associated with the low-energy component of the beam. This is why the total trigger rate is essentially constant while the flux in the coherent peak varies with peak energy over an order of magnitude. This table illustrates the value of having an electron beam energy well above the photon energy needed for the experiment.

Chapter 5

The Detector

5.1 Overview

The goal of this experiment is to search for gluonic mesons with masses up to 2.5 GeV/c^2. The identification of such states requires knowledge about their production mechanism, the identification of their quantum numbers, J^{PC}, and their decay modes. The production mechanism and J^{PC} determination requires a partial wave analysis which in turn depends on the kinematic identification of exclusive reactions. The decay products of produced mesons must be identified and measured with good resolution and with full acceptance in decay angles. In many cases, the decays of mesons involve a chain of particle decays. The HALL D detector must therefore be hermetic with 4π coverage with the capability of measuring directions and energies of neutral particles (γ, π^0, η) and momenta of charged particles with good resolution. Particle identification is also required.

The partial wave analysis technique also depends on high statistics and in the case of incident photons, also requires linear polarization. As discussed in Chapter 3, the latter is needed to identify the production mechanism. The linear polarization is achieved by the coherent bremmstrahlung technique. The degree of linear polarization and flux of photons in the coherent peak fall dramatically as the photon energy approaches the endpoint energy. On the other hand, it is desirable to have photon energies high enough to produce the required masses with sufficient cross–section and with sufficient forward–boost for good acceptance. For a fixed incident momentum and a fixed resonance mass, it is also desirable to have a fairly constant t_{min} over the natural width of the resonance. This also requires sufficiently high incident photon energy.

An operating photon energy between 8.0 ans 10.0 GeV produced from a 12.0 GeV electron beam represents an optimization of beam flux, cross–section and degree of polarization. The HALL D detector is optimized for this energy range. Figure 5.1 is a schematic representation of the proposed HALL D detector. The individual subsystems are discussed in more detail below.

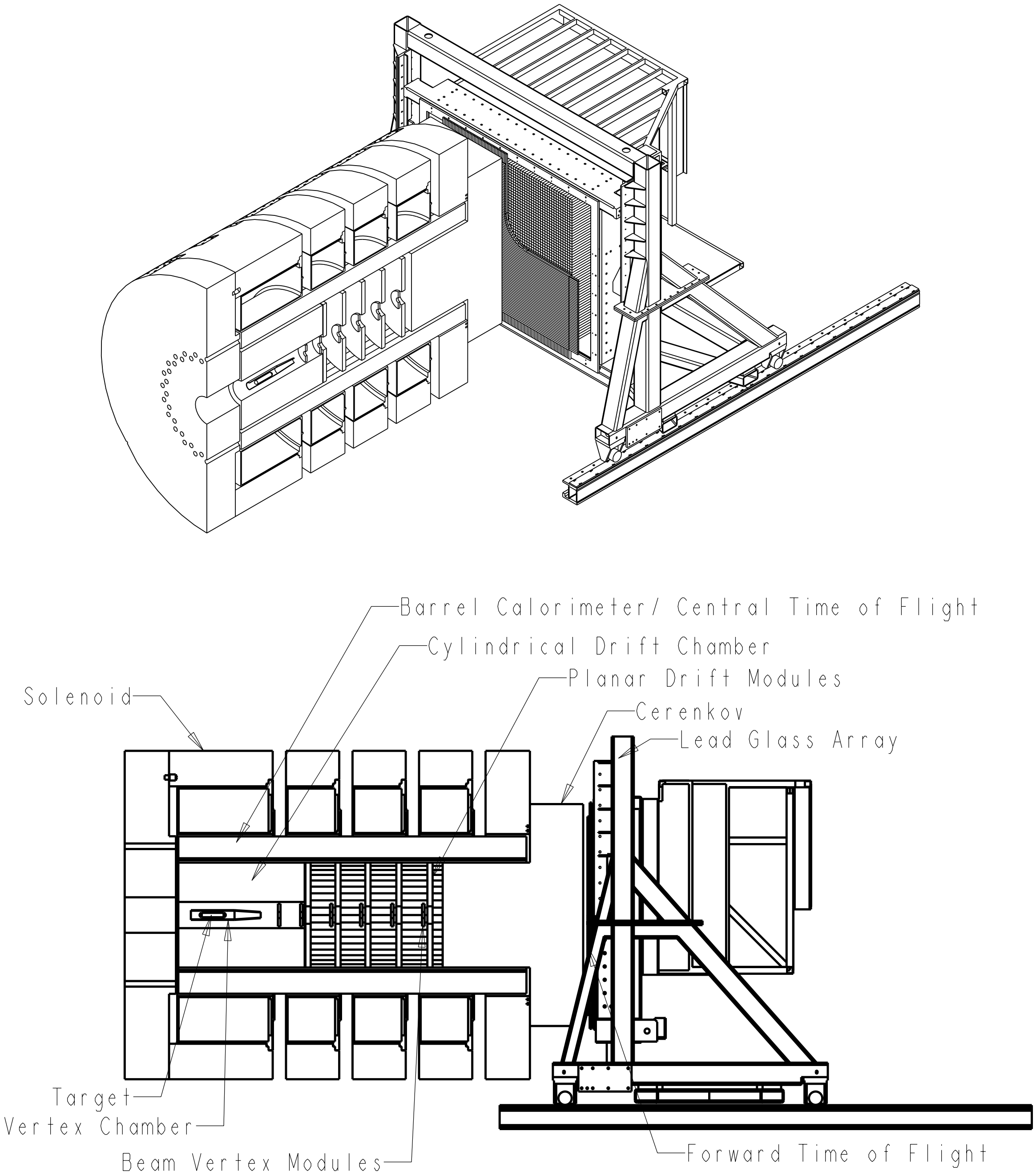

Figure 5.1: An overview of the HALL D detector. The major subsystems are labeled and are discussed individually in the text.

5.2 The solenoid

Momentum analysis of charged particles will be achieved using a superconducting solenoid and tracking chambers. The superconducting solenoid already exists. It was built for the LASS detector at SLAC and later moved to LANL where it was used for the MEGA experiment. The magnet is described in a technical note [126] and some relevant portions of that description are quoted below. Table 5.1 summarizes important magnet parameters. The refrigeration units are not currently available, and alternatives will need to be found.

Inside diameter of coils	80 *inches*
Clear bore diameter	73 *inches*
Overall length (iron)	183 *inches*
Inside iron diameter	116 *inches*
Outside iron diameter	148 *inches*
Coil-to-coil separation	11 *inches*
Total iron weight	200 *tons*
Central field	25 kG
Conductor current	1800 A
Total stored energy	36 MJ
Inductance	22 H
Total helium volume (including reservoir)	5,000 *liters*
Operating heat load (liquid He)	30 *liters/hour*
Operating heat load (liquid nitrogen)	30 *liters/hour*
Cool-down time	2 *weeks*
Copper to superconductor ratio	20:1 (grade A) 28:1 (grade B)
Total conductor length	117,600 *feet*
Total conductor weight	29,000 *lbs*
Turn on time	20 *minutes*
Turn off time (normal)	20 *minutes*
Axial load per coil due to magnetic forces	280 *tons*

Table 5.1: Summary of characteristics of the solenoid in the LASS configuration.

The LASS solenoid magnet provides a 22.4 kG magnetic field parallel to the beam direction. The inside diameter of the magnet is 185 cm and its overall length is 465 cm.

The fiducial region within the bore is 320 cm in length and 75 cm in radius. Within this region the field homogeneity is better than ± 3.1%. Along the beam axis the homogeneity improves to ± 0.9%.

The solenoid is constructed of four separate superconducting toroidal coil-Dewar units [127] in order to permit intercoil placement of planar proportional chambers. A 200 *ton* iron flux return path, similarly split in four places surrounds and supports the coil assemblies. A common liquid helium reservoir is located atop the solenoid providing the gravity feed of the liquid to the coils.

The superconductor used is a stabilized, composite, twisted, multi–filament wire of niobium–titanium. The wire is made by soldering the superconductor composite between two copper strips to form a rectangular cross section 0.763 x 0.533 cm^2. The coil is wound directly on the liquid helium vessel inner cylinder wall. As the coil is wound, a 0.20 *inch* thick stainless steel support band, and a mylar insulating strip are wound along with it for mechanical support and insulation. Cooling by the liquid helium is accomplished from the edges. Each of the four toroidal windings has its own predetermined number of turns, the configuration being selected for optimum central field homogeneity consistent with the requirement of the intercoil gaps and the large downstream end opening.

The liquid helium vessel is surrounded by a liquid nitrogen cooled radiation shield and this assembly centered in the vacuum tank by a circumferential series of tie bolts designed for minimum conductive heat flux to the helium bath. Radial centering and support are achieved by four low conductance hangers arranged in a spiral pattern. Various tie rods and hangers were instrumented with stress bolts to measure the tremendous forces on the assembly caused by the magnetic fields.

The inductance of the coil is 25 *Henries* , and the magnet is run at 1600 *Amperes*. The liquid helium volume is $\approx$ 5000 *liters* and the heat load is $\approx$ 60 $l/hour$. Refrigeration is supplied by two C.T.I. refrigerators, one a nominal 100 *watt* refrigerator, the second nominally 70 *watt*. Either refrigerator alone is capable of supplying the liquid helium required by the magnet while operating under current. However, when operated together at half speed they can handle the magnet and supply additional liquid to a reserve tank. This conservative design, both of the refrigeration system and of a superconductor itself, has produced a stable, reliable and safe superconducting magnet.

5.3 The target

A 30– *cm* liquid hydrogen target will be used. It will be contained in the same vacuum jacket containing the photon tagger radiator and constructed of low mass materials. The collimated photon beam will be contained within 2.5 *cm* from the beam axis. This will allow adequate space between the hydrogen vessel and the innermost detector element for insulation, a vacuum pipe and any plumbing and wiring required to instrument the target. Safety is, of course, a very serious concern for any hydrogen target and we will be consulting with the appropriate lab groups early on in the actual design of the target.

It may be desirable, during some running of the experiment, to use compact, nuclear targets. For this reason it is anticipated that the liquid hydrogen target will be removable from the apparatus. It is assumed that it will be inserted from the upstream end of the solenoid through the hole in the upstream flux return.

5.4 Barrel calorimetry

Electromagnetic (EM) calorimetry in the barrel region of the HALL D detector covers the approximate polar angular range $14° < \theta < 138°$. Exact specifications depend on the final size and location of the liquid hydrogen target, the effective thickness of the calorimeter and its readout scheme on both the upstream and downstream ends of the solenoid. It will be positioned immediately inside the solenoid which constrains the outer radius to be 90 cm. This allows 2 cm for supports and cabling. The outer surface area is approximately 23 m^2. This device is a key component of a hermetic system, and is crucial for fully reconstructing all the photons in many physics reactions. The large size also implies that it will be a challenge to build and instrument at reasonable cost.

The goal of the calorimetry is to detect and measure photons from the decays of π^0's and η's, which, in turn, can come from the decays of an excited baryon (N^* or Δ) and/or from the decays of produced mesons. The positions and energies of the photons must be of sufficient accuracy to allow for a complete kinematic reconstruction of the event. Finally, for events with only charged particles, it is essential to be able to veto on neutral missing energy. Here, nearly hermetic coverage is critical. For selected triggers, neutral energy requirements (or vetoes) are relatively easy to implement.

5.4.1 Design considerations

In order for the tracking elements inside the magnet to perform optimally, the barrel calorimeter must be thin, perhaps no more than 25 cm. The length of the solenoid is 4.5 m. These geometrical constraints lead to a long, narrow tube-like design. In this geometry, readout is easiest at the ends where space exists. However, at the upstream end, a magnetic field-shaping plug complicates the design of the calorimeter. We believe we can overcome these with modifications to the plug. The choice of readout device must bear in mind the considerable magnetic field (22.4 kG) inside the bore and the rapidly varying fringe field at the ends. Conventional photomultiplier tubes (PMTs) will work only outside of the solenoid and even there considerable attention must be paid to shielding.

We have considered a number of candidate calorimeter designs. The leading design utilizes scintillating fibers embedded in a lead matrix to make a relatively high–resolution sampling calorimeter. Advantages include speed, cost, ease of readout, and the fact that it is based on a proven technology. The second, *high–end* option is based on the idea to use the relatively new lead tungstate ($PbWO_4$) crystals which are being developed as the main EM calorimetry for the CMS experiment at the LHC. They offer superior resolution, good light output and the density to make them very compact. Unfortunately, the very large channel count probably makes this option cost–prohibitive. Naturally, a hybrid design, mixing two technologies for different parts of the polar coverage is possible. The very forward angles ($\theta < 14°$) will be covered by an existing lead glass detector (LGD) used in the E852 experiment at BNL and restacked to meet the geometrical acceptance criteria for HALL D. Based mostly on the cost considerations, we are only considering the Pb/SciFi option at the moment.

5.4.2 Pb/SciFi barrel calorimeter

Scintillating fibers embedded in a matrix of lead or other high-Z materials have been used in calorimeter design and operation for more than a decade. The ratio of the active scintillator to the passive high-Z material, as well as the diameter of the fibers can be tuned to enhance resolution, to determine the radiation length, and to achieve uniformity in the electromagnetic to hadronic response (the e/h ratio). For high-resolution EM performance, the Jetset detector developed at Illinois [128] was the first designed specifically to optimize EM resolution. The recipe produced a detector comparable to lead glass at a considerably lower cost and with approximately half the radiation length. It utilizes 1 *mm* fibers spaced uniformly (close packed) on specially grooved plates of lead. The lead is alloyed with $3-6\%$ antimony to provide mechanical stiffness. Tooling was developed in order to groove the plates. A second machine was built to guide spools across stacks of the plates taking care to properly align each fiber spool with a groove in the lead. The assembly of a module consisted of a repeated layering of fibers and plates, all held together with an optical epoxy. A finished module was machined into final shape, polished and outfitted with a plastic lightguide for readout.

The resolution for an array of prototypes subjected to electrons in the range from $0.3-1.5$ *GeV* was represented by the function $\sigma/E = 6.3\%/\sqrt{E}$ with a negligible constant term. In the Jetset Forward Calorimeter, the beam entered nearly parallel to the fiber direction. The energy resolution was also measured with tagged photons below 0.1 *GeV* and improved to $\approx 5\%/\sqrt{E}$; the detector gave a resolvable signal all the way down to 0.02 *GeV*.

In Jetset, a Barrel Gamma Veto detector with thickness $6X_0$ was made in a barrel-like fashion with 24 modules of length 80 *cm* each forming the sides of the barrel. Here, with the interaction point centered in the barrel, gammas entered the modules at normal incidence for polar angles of 90°. For other angles, the detector is effectively thicker. Our design for HALL D follows this concept but would be a full $12.5-15X_0$ thick at normal incidence and considerably longer. Realization of these changes fortunately can be based on the KLOE calorimeter at DAΦNE where they have been building a device of this length with an even larger inner diameter. The KLOE collaboration has taken the development of Pb/SciFi a step further. They have developed better tooling for production of long grooved plates, have pushed the technology for excellent, bright fibers with long attenuation lengths[1] and have produced prototypes with excellent energy and timing characteristics[2].

We intend to follow much of this development and therefore describe some of the aspects below.

Like Jetset, the KLOE design utilizes 1 *mm* scintillating fibers embedded in a lead matrix with a fiber to lead to glue ratio of approximately 48 : 42 : 10. Prototype modules, 2 *m* in length, were produced with PMT readout at both ends. An excellent energy resolution parameterization of $\sigma/E \approx 4.4\%/\sqrt{E}$ was found. In the actual experiment the module length increases to 4.3 *m* (which is similar to HALL D) and therefore special efforts were made to develop and test scintillating fibers with very long attenuation lengths. Tested fibers had attenuation lengths in the range from $2.3 < \lambda < 3.2m$ which is far superior to the average λ of 1 *m* for the Jetset fibers. This aspect of the design is critical because it there exists a significant coupling between the position of impact (essentially the polar angle, θ) and the interpreted energy. Light collected on each end must be corrected for attenuation length before conversion to energy units.

An important feature of these detectors is the signal risetime and overall duration. Because fast plastic scintillator[3] is used, integrated signal time can be kept below 100 *ns* with

[1] A discussion of the properties of the fibers considered for KLOE can be found in [129]. Included are measurements of propagation velocity, attenuation length, light yield and decay time.

[2] Energy, time and position resolutions of a 2.03 meter KLOE prototype calorimeter are discussed in [130].

[3] Decay times are $2.0-2.5$ *ns*

shorter times possible if deemed necessary for rate considerations. At the expected maximum luminosity, no problems are anticipated. With risetimes of a few ns, excellent timing can be expected for each of the PMT's involved in collecting the light from a shower. Time differences from the two ends produces the z coordinate of the hit. Because we will use an array of PMT's on each end (segmented in azimuth and depth), redundant measurements are made of the z coordinate. These measurements of z correspond to different average radii and therefore help to establish the angle of the incoming photon.

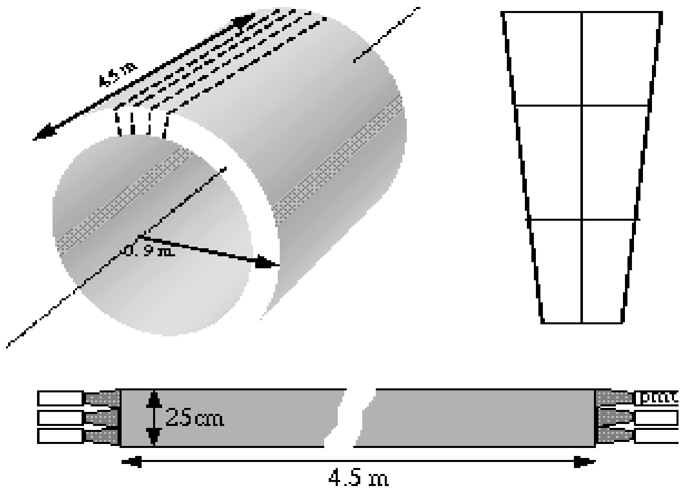

Figure 5.2: Sketch of Barrel Calorimeter made from bars of Pb/SciFi material. (a) perspective view; (b) closeup of end with suggested readout segmentation for one of 48 bars; (c) side view showing approximate locations of PMT's.

The fractional volume of scintillator in the detector naturally makes it efficient for detecting charged hadrons. The mean light collection time of the two readout ends can be used to determine the particle time-of-flight (TOF). TOF coupled with the track length and momentum then yields particle mass. Therefore, this design for a Barrel Calorimeter can be expected to play an important role in the overall barrel PID scheme. In the KLOE design, timing of ≈ 250 ps (RMS) was achieved, and improvements are possible. The same can be expected for HALL D as long as PMT's and discriminator chains are selected carefully.

In order to form grooved plates and construct modules 4.5 m long, we plan to study the KLOE tooling development. We would either replicate or borrow their successful devices. This proof of principle gives us confidence that the daunting mechanical task can be handled. For HALL D we expect to build 48 modules each 4.5 m in length and 20–25 cm deep. Variants on this theme are being considered; in particular, half length modules with intermediate readout will be studied. The readout scheme takes advantage of the fact that all fibers run parallel to the axis of symmetry of the solenoid and therefore all light piped to the ends of the modules retains its azimuthal and radial information. The polished ends of the detectors can be coupled with multiple independent lightguides. In figure 5.2, 6 segments are suggested. This gives a minimum of 96 independent azimuthal slices, each with three dual-ended readouts at varying depths. The transverse size of a module is approximately 4 cm at impact. Because the EM showers spread across these azimuthal boundaries, algorithms for finer positioning of the shower are employed. In Jetset, one finds a typical weighted position resolution of $\delta x \approx 5\,mm\,/\sqrt{E})$. For the HALL D design, this would lead to an azimuthal resolution of $\approx$ 10 mrad. Using the z position resolution of approximately $1\,cm$ obtained from time difference leads to a polar angular resolution at 45° of $\approx$ 8 mrad. As the design of the barrel calorimeter is further refined, it will be important to keep these numbers balanced.

In figure 5.2 several views are shown for the barrel calorimeter including an overall perspective, a side view of one module, and an end view indicating how a single module could be segmented with six independent readouts. In this design, there are $48 \times 6 \times 2 = 576$ PMT's. Each requires ADC, TDC, discriminator, HV and cabling. A calibration system is critical and can be based in part on the use of Nichia blue LED's glued directly to a short lightguide stub at the end of each module. An LED driver system is also required. The choice of ADC and TDC systems depends on the overall readout coordination for HALL D. To estimate costs, we can we can imagine packaging typical of existing Fastbus–based systems with 64 or 96 channels per unit.

5.5 Tracking chambers

The system of tracking chambers in the HALL D detector must cover as close to a 4π solid angle as possible over a wide range of particle momenta and have sufficient momentum resolution to be able to identify missing particles. In the solenoid region, the chambers are inside the barrel calorimeter. This defines a maximum keep–out radius of about $65\,cm$ and for purposes of this report, the active volume has been limited to $60\,cm$ in radius. This provides $5\,cm$ of space for support systems and cables. The chambers also must extend as close to the beam line as possible. Near the target, this will provide very accurate vertex information which will be important in identifying decaying particles (e.g. K_S, Λ, Σ, ...). In the forward region, this is needed to reconstruct very fast small angle particles (down to nearly 0°). Finally, it is necessary that near the target, the tracking be able to separate π's and K's up to momenta of about 0.5 GeV/c — a regime where dE/dx measurements will work.

To satisfy the tracking requirements two configurations of tracking chambers are currently being considered. Both share common elements near the target and beam line, but differ in how the main tracking volume is implemented. One solution is a mixture of a cylindrical drift chamber and forward planar drift chambers, while the second involves a TPC in the solenoid coupled with fewer forward elements. In section 5.5.2 the advantages and disadvantages of both solutions with respect to the tracking requirements outlined in section 5.5.1 are discussed. Sections 5.5.3 through 5.5.7 discuss individual tracking systems.

5.5.1 Design considerations

To satisfy the tracking requirements a starting point based on the LASS detector [126] was examined where we have taken a series of different tracking elements. Each of these elements has been optimized for a particular region in the detector. An example of such a design is shown in Fig. 5.3, where there are four different tracking regions. Just around the target is a *vertex system*, VTX. This is likely to be several layers of scintillating fiber, which would allow it to be used for both track reconstruction and triggering. Around this is either a *cylindrical*

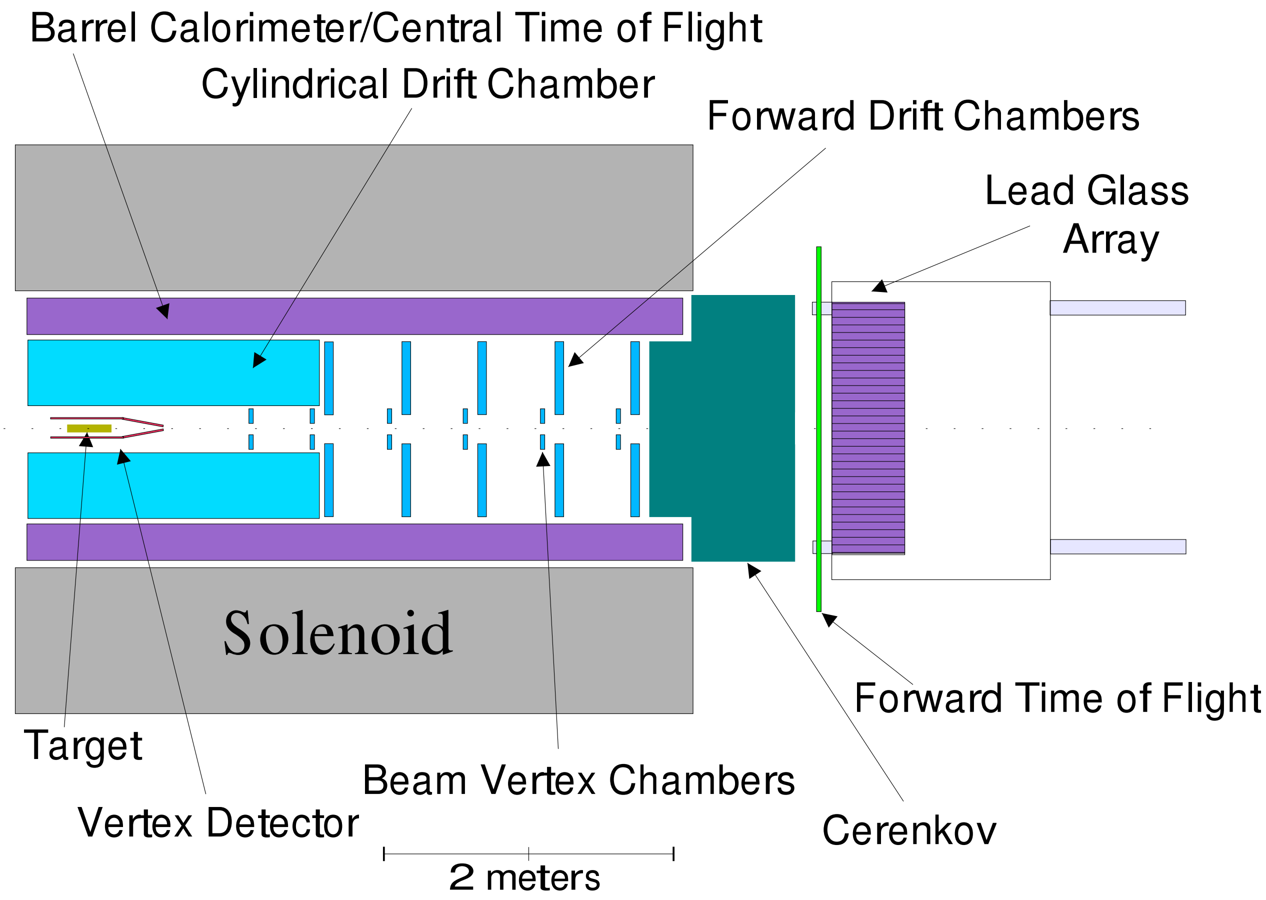

Figure 5.3: The HALL D detector. The tracking elements are the cylindrical drift chamber, CDC, which is a straw tube chamber. The forward drift chambers, FDC, are planar circular shaped planar chambers. The vertex chamber, VTX is a fiber tracking device which doubles as a start counter. The beam vertex chambers, BVT, are low–mass planar drift chambers close to the beam line.

drift chamber, CDC, or a *time projection chamber*, TPC. In either case, this chamber provides very good $r-\phi$ information and moderate to very good z information. This chamber should also provide dE/dx information. In the forward region, at radii larger than about 10 cm, are planar *forward drift chambers*, FDC. Finally, along the beam line in the forward direction, are a series of *beam vertex trackers*, BVT. These BVT chambers must provide good resolution but have as little material as possible to minimize multiple scattering.

System	*Radius*		*Length*		*Resolution*	
	$r_{\min}$	$r_{\max}$	z_{min}	$z_{\max}$	$\sigma_{r-\phi}$	σ_z
VTX	5.0 cm	5.5 cm	10. cm	90. cm	1000 μm	stereo
CDC	15.0 cm	60.0 cm	0. cm	200. cm	200 μm	500 μm
FDC	10.0 cm	60.0 cm	210. cm	450. cm	200 μm	fixed
BVT	3.50 cm	13.0 cm	120. cm	430. cm	200 μm	fixed
VTX	5.0 cm	5.5 cm	10. cm	90. cm	1000 μm	stereo
TPC	15.0 cm	60.0 cm	0. cm	300. cm	200 μm	200 μm
FDC	10.0 cm	60.0 cm	320. cm	450. cm	200 μm	fixed
BVT	3.50 cm	13.0 cm	120. cm	430. cm	200 μm	fixed

Table 5.2: A summary of the tracking chamber parameters. The z values under *Length* give the smallest and largest z of the combined system, (the z measurement starts at the upstream end of the magnet). The z resolution for the CDC comes from cathode strips (500 μm resolution) on the inner and outer shell, and $\pm 6^\circ$ stereo layers. The VTX chamber is expected to measure z resolution using stereo layers. The z resolution of the planar chambers is assumed to be given by their position in space. The upper design involves a straw chamber, while the lower design involves a TPC.

The charged particle system within the solenoid must be optimized for both overall acceptance and momentum resolution. A detailed study using the *HDFast* framework, (see Chapter 9) has been performed to examine this [131]. The results of this study indicate that the above combination of cylindrical drift chambers and planar drift chambers with typical $r-\phi$ position resolutions of 200 μm would satisfy these requirements. The geometrical limits of two such designs are given in table 5.2. In addition, both an earlier study by Mueller [132] and this study [131] found that the transition from the cylindrical chamber to the forward planar chambers introduces a serious discontinuity in the momentum resolution. This is most effectively dealt with by making the cylindrical chamber as long as possible. A plot of resolution as a function of angle is shown in Fig 5.4. This discontinuity can be seen as a spike near about 10° for this design. However, the current Monte Carlo does not fully deal with the degradation in resolution as the tracks become parallel to the CDC wires, so an exact optimization between CDC and FDC has not been performed.

The 22.4 kG solenoid field determines the physically measurable quantities, and hence, the momentum resolution. The transverse momentum, $p_\perp$ and the *dip–angle* λ, ($\lambda = \frac{\pi}{2} - \theta$), are measured from the curvature of the tracks and their initial direction. The total momentum and the longitudinal momentum are then obtained from these as $p_{total} = p_\perp \sec\lambda$ and $p_{||} = p_\perp \tan\lambda$. The accuracy of the $p_\perp$ measurement is completely dominated by the $r-\phi$ resolution of the tracking chambers, while the λ measurement relies on an accurate

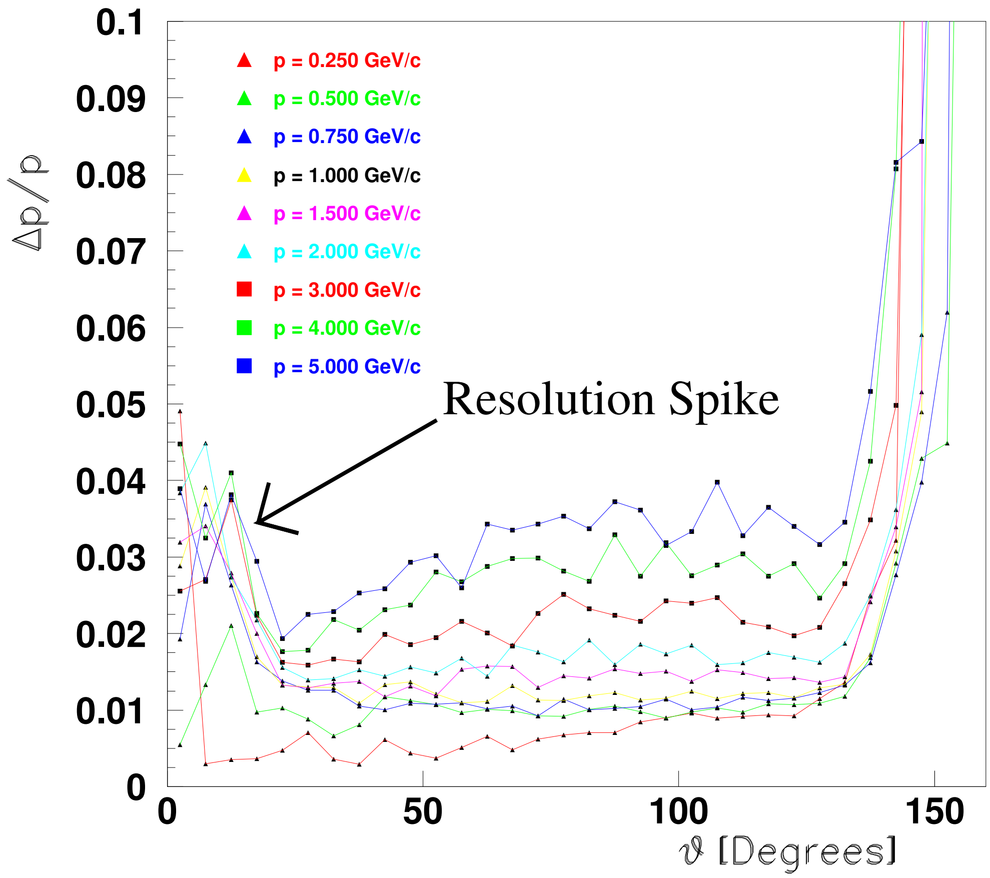

Figure 5.4: The resolution as a function of angle plotted for several total momenta. The plots correspond to the detector design shown in Fig. 5.3. The spike labeled at about 10° corresponds to the transition region between the CDC and the FDC. For polar angles larger than 70°, the maximum detected momentum will be well under $1 GeV/c$ so even though the resolution for high momentum tracks is poor in this large angle region, it will not affect the overall tracking of physics events.

measurement of both z and the distance traveled.

Track reconstruction effects also play a very important role in the design of the system. In particular, track matching between different detectors, and the associated inter–calibration problems often limit the ultimate resolution. In addition, the high magnetic field strength of 22.4 kG means that tracks may spiral significant distances between measurement planes. Ultimately, one would like each measurement along a track to be a full space point, rather than a single coordinate. The magnetic field is known to be nonuniform near the ends of the magnet, particularly due to the lack of a mirror plate at the downstream end. To achieve the ultimate resolution, sufficient space points must be available in the nonuniform region. In addition, particle identification will require projecting charged tracks forward to both the time–of–flight wall and the forward calorimeter, again a requirement for good tracking near the end of the magnets.

As an example, one particular all charged final state is considered. In figure 5.5 is shown the distribution of charged particles in p versus θ space for both $E_\gamma = 6\ GeV$ and $E_\gamma = 10\ GeV$. The events are generated according to reaction 5.1 where the X has masses between 1.7 and 3.2 GeV/c^2.

$$\gamma p \to Xp \to K^+K^-\pi^+\pi^-p \tag{5.1}$$

Table 5.3 summarizes the maximum momentum as a function of angle for both photon energies. From the plots in Fig. 5.5, several important features which drive the design of the detector are observed. In particular, particles that emerge at angles larger than 90° have

θ [°]	$p_{\max}$ [GeV/c]	
	$E_\gamma = 6\ GeV$	$E_\gamma = 10\ GeV$
20°	3.00 GeV/c	5.00 GeV/c
50°	1.00 GeV/c	1.50 GeV/c
70°	0.50 GeV/c	0.50 GeV/c
100°	0.25 GeV/c	0.25 GeV/c

Table 5.3: Maximum total momentum as a function of angle for both E_γ of 6 and 10 GeV for all particles in reaction 5.1.

momenta less than 0.2 GeV/c. To measure these slow particles accurately, good z–resolution will be needed near the target. Additionally, these particles will not make it to any time of flight system. The only particle identification will come from a dE/dx measurement. On the other hand, good tracking resolution for high–momentum particles in the backward angle region is not required.

Next, most events have at least one particle moving in the forward direction at high momentum. In figure 5.5(c) and (d) are shown the momentum versus angle for the most forward particle in each event. Good tracking will be needed as close to the beam line as possible, hopefully extending down to 1°.

Many of the charged particles in HALL D will produce spiraling tracks in the solenoid. Figure 5.6 shows the p versus θ plane for tracks in the solenoid. Tracks which fall above the hyperbolic curve cannot spiral in the 60 cm radius region containing the tracking chambers. Below the hyperbola are a series of approximately horizontal lines. Tracks below these lines spiral the number of times indicated. Based on the p versus θ distributions in figure 5.5, it

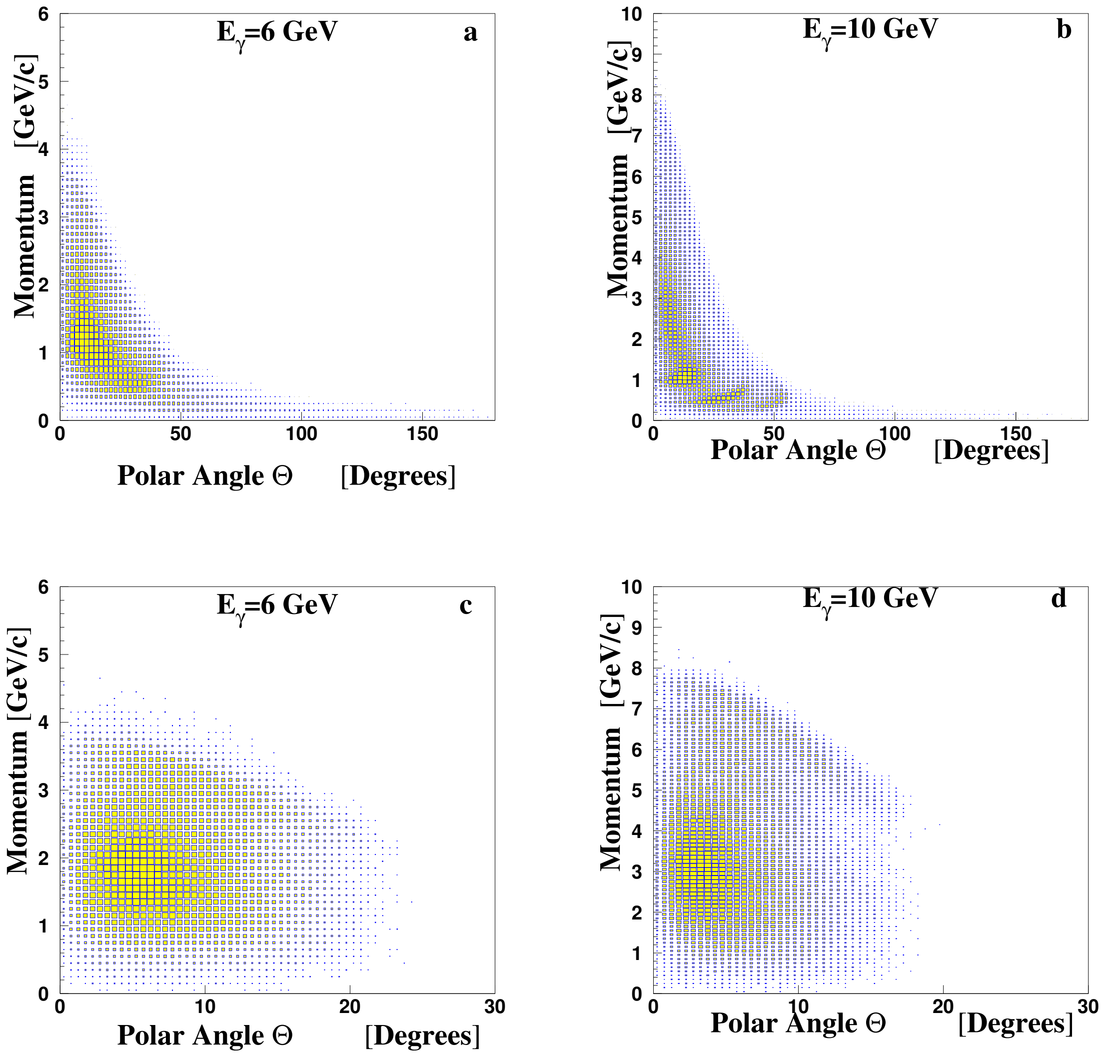

Figure 5.5: Momentum versus polar angle for all charged particles in $\gamma p \rightarrow K^+K^-\pi^+\pi^-p$ data sets. Figures (a) and (b) are the distributions for all particles for $E_\gamma = 6\ GeV$ and E_γ=10 GeV respectively. Plots (c) and (d) show momentum versus angle for the most forward particle in both cases.

can be easily seen that most tracks at angles larger than 50° will always spiral at least once in the detector.

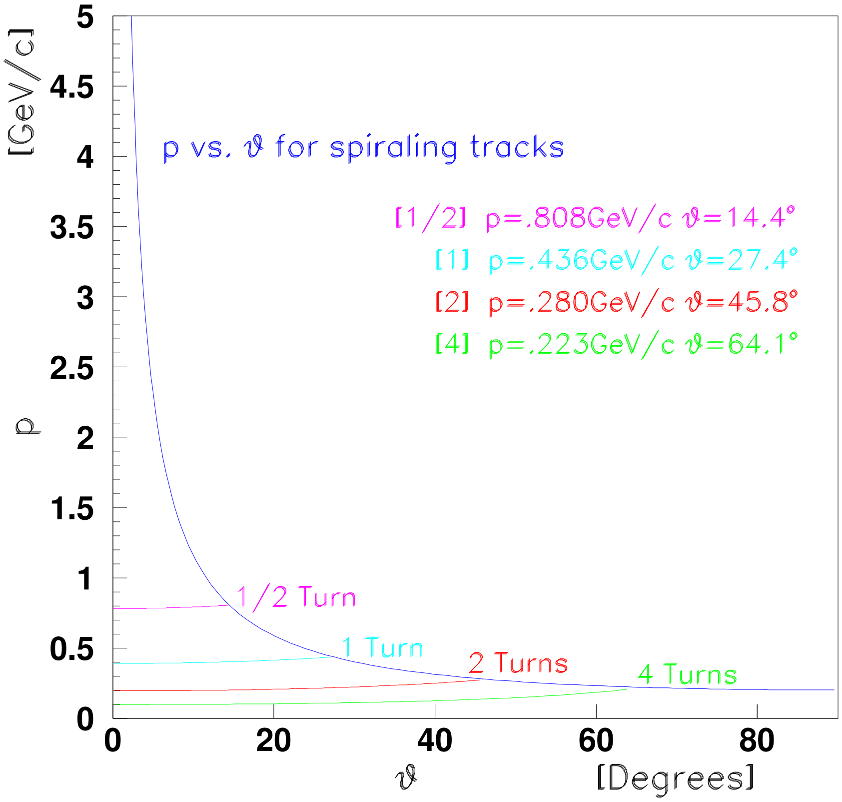

Figure 5.6: This figure shows the number of full circles made by charged particles in the magnetic field. The limit line corresponds to $p_{\perp} = 0.2\ GeV/c$ tracks. The approximately horizontal lines indicate when the particle can make the indicated number of turns without leaving the magnet.

To study the missing mass resolution, reaction 5.2 has been examined.

$$\gamma p \to K^+ K^- \pi^+ \pi^- \pi^0 p \tag{5.2}$$

For this study, the nominal detector as shown in Fig. 5.3 with 200 μm resolutions is assumed. It is also assumed that the π^0 in 5.2 is not detected. Using the reconstructed charged tracks, the known beam energy, and the assumption that the reaction took place on a proton target, the square of the missing mass is computed and shown in Fig. 5.7(a) for a nominal 0.1% beam energy resolution. The distribution is centered at the square of the π mass, but it has a non–negligible width. In Fig. 5.7(b) the width of the peak in (a) is plotted as a function of the beam energy resolution. For this particular reaction with a missing π^0, a beam energy resolution of 0.1 to 0.2% is well matched to the 200 μm resolution of the tracking system.

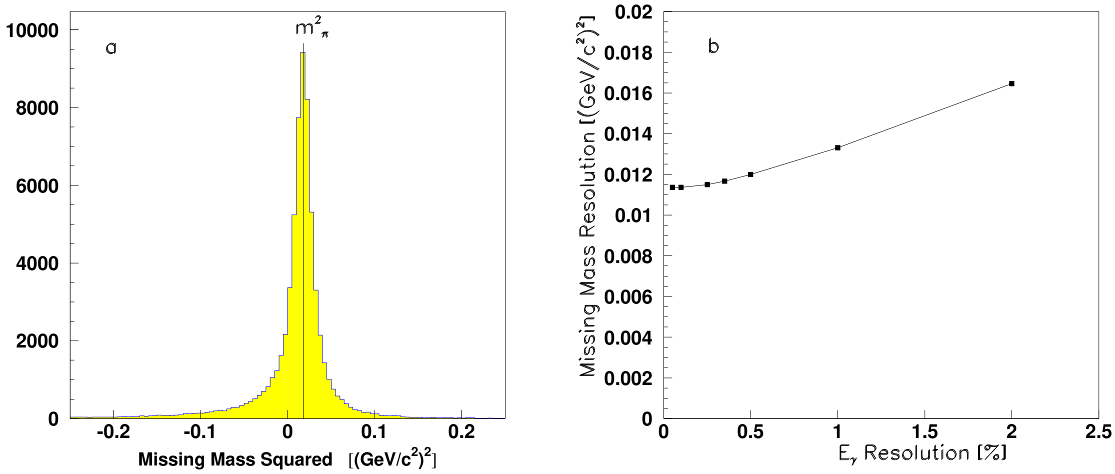

Figure 5.7: Missing mass squared from the reaction 5.2 where the π^0 is assumed missing. (a) is for 0.1% beam energy resolution, while (b) is a plot of the missing mass resolution as a function of the beam energy resolution.

5.5.2 Tracking configurations

Based on the requirements specified in section 5.5.1, two configurations of tracking chambers within the HALL D solenoid are being considered. The first is a combination of chambers as shown in Fig. 5.3 built up of four tracking regions, CDC, FDC, VTX and BVT. The second design involves a TPC as the main chamber, which is then supplemented by a VTX around the target, BVT chambers along the forward beam line, and a smaller number of FDC chambers in the forward region.

The first design with separate CDC and FDC has a large advantage in that it can be designed to read out quickly. Maximum drift times can be kept as short as a few hundred nanoseconds reducing pile–up in the detector to a negligible level. In addition, the signals arrive fast enough to be incorporated into a hardware track multiplicity trigger, which in turn could feed into more sophisticated total event triggers. The major drawback to this design is the material in both the CDC tracking volume and in the end plates of the chamber. This leads to multiple scattering deterioration in the track resolution, as well as preshowering of photons in the tracking volume. Secondly, the hits within the CDC are not true space points, but rather projections.

The second design involving a TPC is intrinsically more appealing, though there are some technical problems that do need to be investigated more carefully. The biggest drawback of this design are the large drift times involved in a TPC. This prevents its use in a hardware multiplicity trigger, but does not preclude using data in a sophisticated software trigger. It also almost guarantees that there will be more than one event in the system at any given time. This requires methods of separating in–time from out–of time tracks. The big advantage of this design is that it provides true space points at every measurement and there is a minimum of material both within the tracking volume and in the end-plates. In addition, the measurement points will be more uniformly spaced throughout the tracking volume, and the dE/dx measurement is an intrinsic part of the system. Finally, because this is a longer chamber, the resolution mismatch which occurs when going from the CDC to the FDC is less severe.

5.5.3 Central drift chamber

The central drift chamber (CDC) is used to accurately track particles between polar angles of 20° back to 170°. To minimize material in the forward end plate of the chamber, one would like a self–supporting chamber. This leads to a straw chamber, where the straw walls support much of the wire tension The disadvantage of this design is the difficulty of making dE/dx measurements in a circular straw tube. It is in principle possible, but additional research would need to be done to determine how to correct for the total path length in a tube. An example of this is shown in Fig. 5.8a where two nominally identical tracks have very different path lengths through the straw.

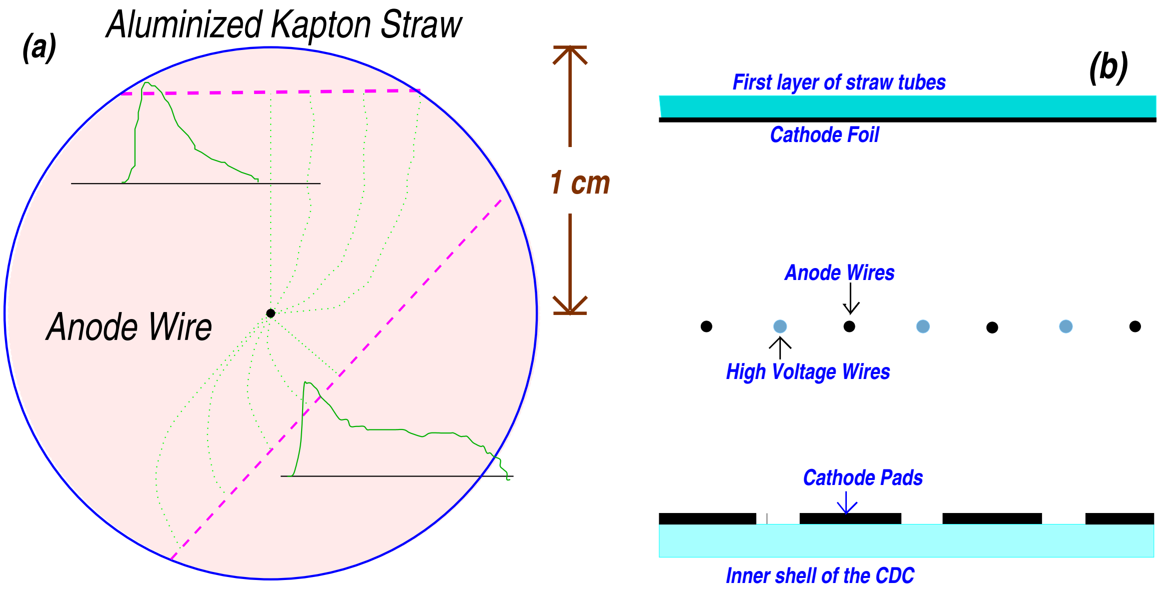

Figure 5.8: A end view of one straw-tube in the the CDC. The two dashed lines indicate charged tracks with quite different path lengths in the tube, which then lead to different electronic pulse shapes as shown. For accurate dE/dx measurements, this path length must be known. (b): A side view sketch showing the cathode pads at the inner shell of the CDC. The first layer of straw tubes starts at the upper side of the figure.

In addition, a chamber filled with straw tubes precludes the simple use of cathode strips on both the inner and outer shells, a technique which gives good z resolution at these surfaces. This could be achieved in a hybrid design where a ring of wires is placed near the inner and outer shells, and these are then coupled with cathode strips or pads. This is sketched schematically in Fig. 5.8b. This also must be investigated. Alternatively, some work has been done on cathode pad readout of straw tubes [133] where $\approx 1.4\,mm$ resolution along the length of a straw has been obtained. Again, this option must be pursued. A possible design has the chamber filled with 5200 1 cm diameter straw tubes arranged in 22 layers as shown in Fig. 5.9. The tubes are assumed to have an $r - \phi$ resolution of $200\,\mu m$, while resolution along the wire length will be obtained by placing about half of the layers at a 6° stereo angle. A typical hydrocarbon drift gas will have v_d on the order of 50 $\mu m/ns$, meaning maximum drift times will be on order of $100\,ns$, in which case a $4\,ns$ drift time corresponds to $200\,\mu m$ of drift. Many of the charged particles will not reach the time–of–flight system in the calorimeter, requiring the use of dE/dx information in the chamber for particle identification. This requires both TDC and ADC readout on the chamber. This is likely to be better accomplished with a flash–ADC system. To achieve the required $200\,\mu m$ resolution, this system will need to run at $250\,MHz$, ($4.0\,ns$ time bins). Time fitting algorithms matched to the pulse shape in the chamber usually yield intrinsic time resolutions around 1/5 of the time bin.

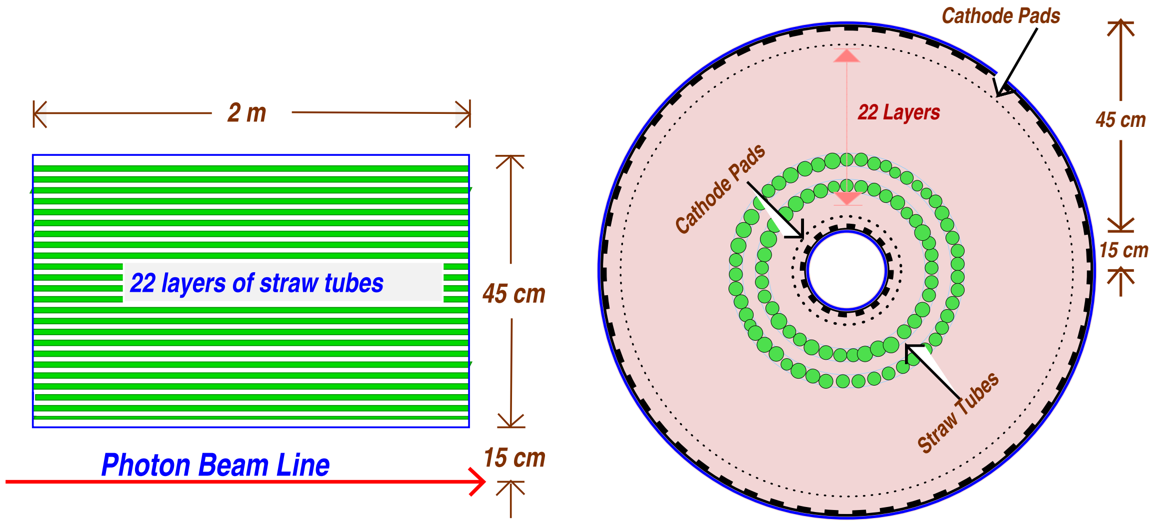

Figure 5.9: (a) A side view sketch of the CDC assuming a straw tube arrangement. (b) An endview picture of the straw tube arrangement. Two of the 22 layers of straw tubes are shown. In addition the cathode pad arrangement is sketched.

In Fig. 5.4 is shown the momentum resolution as a function of angle corresponding to the detector layout in Fig. 5.3. The most striking feature of this plot is the two upward spikes at forward angles. The first is due to very stiff particles at small angles. The second is due to the interface between CDC and FDC. This feature leads us to believe that the CDC chamber should be as long as possible. This is, however, not the complete picture. The current Monte Carlo assumes a CDC position resolution which is independent of the dip–angle. This is not the case; the resolution will deteriorate like $\tan\lambda$. On the other hand, the FDC chamber resolution will be optimum for tracks parallel to the beam axis, and deteriorate for tracks at small values of λ. In any case, intermediate angles have somewhat worse resolution than indicated by this design. Finally, one drawback of this design is the large amount of material in the tracking volume. While this material has been put into the Monte Carlo, it is still worrisome based on the large number of scattering surfaces within this critical tracking volume. Preshowering of photons within the tracking volume is also only partially described by the current Monte Carlo.

The resolution studies in this report are based on such a straw tube chamber. The chamber is built out of 1 *cm* thick aluminum end plates with a 2 *mm* thick carbon fiber shell on the inside, and a 4 *mm* outer carbon fiber shell. The straw tubes are 100 μm thick aluminized kapton, and have 20 μm diameter gold–plated tungsten wires.

5.5.4 Forward drift chambers

The forward drift chambers, FDC, are disk shaped drift chambers. The basic drift package is a plane of wires with 200 μm spatial resolution between two planes of cathode strips. The strips are arranged in a u and v geometry with respect to the wires, allowing the reconstruction of a 3–D space point from each hit. The chambers are arranged in packages of six to provide a small track segment to facilitate later linking of tracks. Given the number of spiraling tracks, it is critical that these chamber packages not only provide good spatial resolution, but also reasonable direction information.

The basic chamber element is an annulus of inner radius 10.0 *cm* and outer radius 60.0 *cm*, the wires strung as chords across the chamber as shown in Fig. 5.10(a). With a 1.0 *cm* wire spacing, each chamber will contain 119 wires. In addition, there will be an equal number of cathode strips on each face. These are arranged in a u–v pattern with respect to the wires as shown. This leads to 357 channels per chamber. Fig. 5.10(b) shows the six chambers in side view forming one FDC package leading to about 2200 channels per package. Adjacent planes will be rotated by 60° with respect to each other to improve the overall resolution.

There is a question about how the gap across the beam line is handled. Assuming no electrical connection across the gap, this increases the number of channels by about 10%. However, it may be possible to connect the wires across the gap by running conducting strips around the cylindrical hub. This requires additional research to determine if it can or needs to be done.

5.5.5 The time projection chamber

An attractive alternative to the configuration of charged tracking devices described above would be to replace the central drift chamber and some of the forward drift chambers with a time projection chamber. This section contains a general description of the relevant features of an appropriate TPC, however, many questions about the optimum design of a TPC for this application will need to be answered by detailed Monte Carlo design studies.

The TPC is a type of detector commonly used in large collider detectors, such as ALEPH [134], DELPHI [135], GEM [136], and STAR [137]. It is a mature technology, dating back to 1974 at SLAC [138]. A typical TPC is a large volume in a solenoidal magnet with an **E** field parallel to the **B** field. When a charged particle traverses the volume, the electrons from ionized atoms along the particles path drift towards the end of the volume due to the **E** field. As the electrons arrive at the end of the detector their time of arrival is recorded. The end cap is divided into pads that give the spatial location of arriving electrons, and the time gives the z location of the particle track. The pulse height can also be recorded, which gives excellent dE/dx information for particle identification.

The TPC has a significant advantage in acceptance over a combination of a cylindrical drift chamber and planar drift chambers because it can fill more of the solenoid with a single

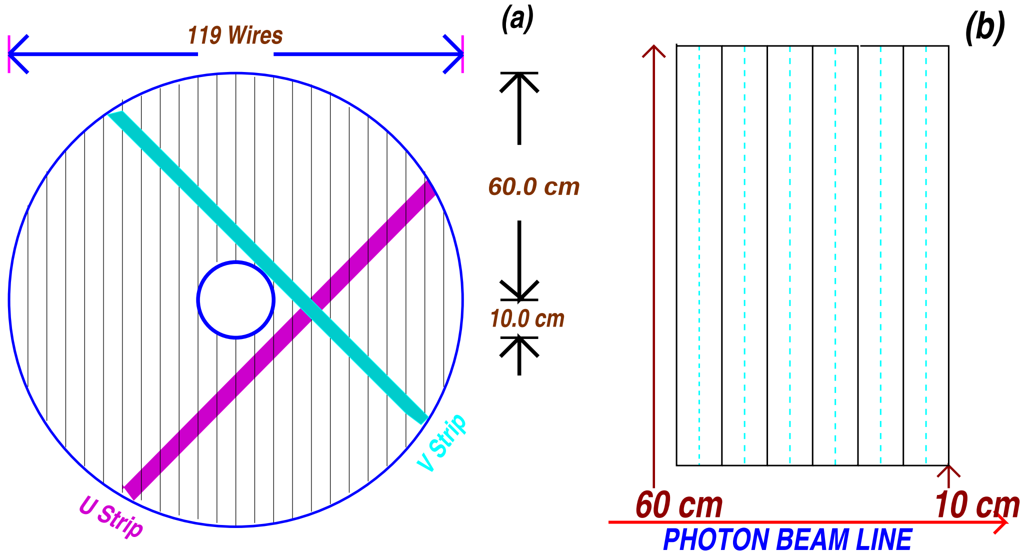

Figure 5.10: A front, (a), and side, (b) sketch of an FDC package. In (a) the wires are schematically indicated as the vertical lines. The u cathode strips are in front of the wires and the v cathode strips are behind the wires. In (b) is shown a side view of the upper half of a six–chamber package. The wire planes are shown as the dashed lines, while the cathode planes are at the boxes. A grounding plane between adjacent chambers is not shown.

tracking volume. This reduces the mismatch between a CDC and the FDC package. Such a TPC would have a cylindrical volume of length $3\,m$ with an inner radius of $15\,cm$ and an outer radius of $60\,cm$. The default option is an axial drift direction and readout only on the upstream end.

The TPC has no structures in the active volume so it has less mass than other types of chambers, which minimizes multiple scattering and energy loss. By putting the readout only on the upstream end, the mass of the downstream end of the detector can be kept to a minimum also.

The rate of interactions, multiplicity of tracks, and the time structure of events are important considerations for the suitability of a TPC. From Chapter 7, the hadronic rate is calculated to be $365\,kHz$ for a tagged rate of 10^8, which is the upper limit of realistically usable flux. At this flux there is an interaction every $3\,\mu$s. If the drift speed is $50\,\mu m/ns$, the clearing time for ionization from a single event is $60\,\mu$s. So on average there will be 20 interactions while an event is clearing. Confusion could result when multiple tracks cross in space–time — either the reference event crossing an earlier track or tracks from a later event crossing the reference tracks before they clear the TPC volume.

To estimate the probability of confusion, three charged tracks per interaction are assumed. Tracks that stay inside the $15\,cm$ radius do not register. Dividing the upstream end plate into pixels that are $1\,cm \times 1\,cm$ yields 14×10^4 pixels and assuming $4\,ns$ time bins gives 10^4 bins in z. We estimate the probability of tracks sharing a pixel as follows: A high–momentum transverse track would fill 45 pixels. A high–momentum longitudinal track would fill 10^4 pixels. A 10 loop track of $50\,cm$ diameter would fill 10^3 pixels. Taking these numbers as representative, the probability of multiple hits in the same pixel is $(3 \times 20 \times 10^3)/10^8 =$

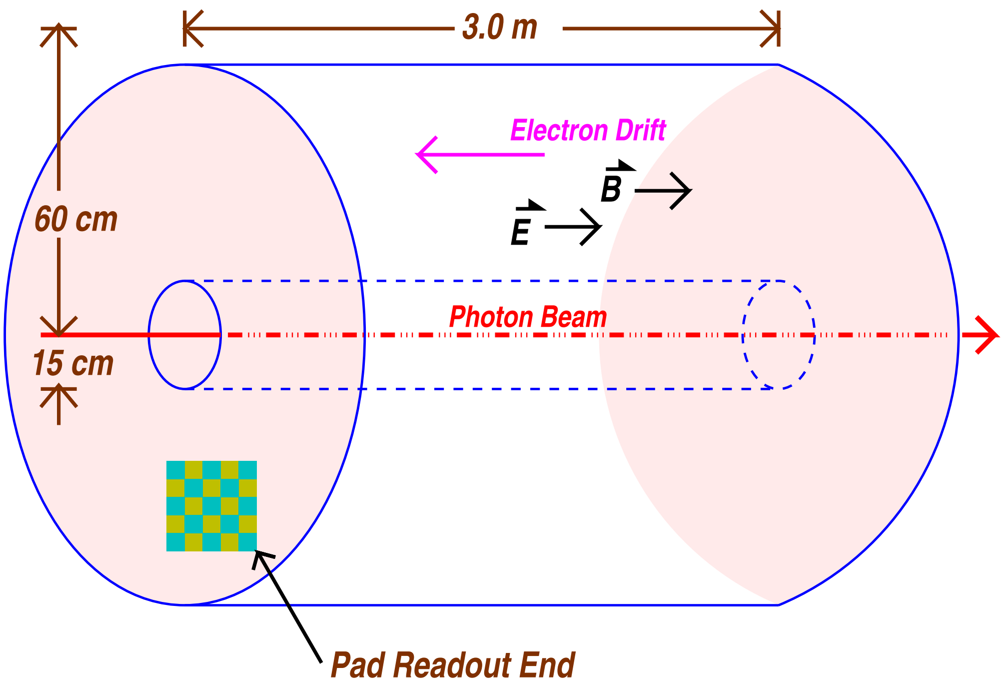

Figure 5.11: A schematic view of an axial drift TPC. The pad readout is shown at the up stream end of the detector.

6×10^{-4}. This estimate is encouraging and hopefully will be validated by a proper simulation.

Similarly, while a typical event has three charged tracks in the TPC, there will be, on average, parts of 60 tracks in each read out event. To identify which ones belong to the event of interest, it will be required that the tracks match a segment in the VTX. The VTX is sufficiently fast that even at the highest rates, the pile–up will be negligible.

Another important consideration is the relative cost of the tracking system options. The cost for the mechanical construction of a TPC is comparable to that for other wire detectors and most likely less, because of the simple structure required. Also the cost for high voltage supplies, installation, and operation should be similar. The potential for a big difference comes with the electronics needed for readout. If the channel count is much higher or the required electronics more sophisticated, the cost goes up.

The cost of the electronics is determined by the number of readout pads, which is driven by the size of the end cap and the spatial resolution desired. A TPC can meet the requirements for the HALL D detector for position resolution of a few hundred microns using electronics similar to that planned for the central straw tube detector.

The area of the TPC end plate is $10^4\ cm^2$. The readout pad size of existing TPCs ranges from $3\,mm$ to $3\,cm$ along a side and so is of order $1\,cm$. Thus if one could achieve 100% coverage, a HALL D TPC could require 10^4 channels. The pad shape is not required to be square, pads longer in the radial direction and smaller in the ϕ direction may reduce the channel count. The coverage will certainly be less than 100% so the number of channels could be approximately the same as that needed for the central drift chamber. For the central drift chamber described earlier, the 5200 channels of the drift chamber electronics require an ADC and TDC for each channel. These ADC/TDC pairs for the CDC can be replaced by flash–ADCs running at 250 MHz. This is exactly what is needed for a TPC, but we may be able to run at somewhat lower frequency. Also, the TPC will replace some of the forward drift chambers, which saves between a third and half of the FDC electronics.

It appears that tiny pads are not needed to achieve adequate resolution. The design resolution is 200 μm in r–ϕ and 500 μm in z for the central drift chamber. Previous TPCs get comparable resolution in $r - \phi$ by taking the centroid of hit pads. The z resolution would be significantly better (200 μm) for a 250 MHz readout. A simulation is needed to see if somewhat worse resolution in $r - \phi$ can be balanced with better resolution in z to meet the needs of the experiment.

There are several options to consider for the choice of technology just in front of the readout electronics. Typically a single layer of (gated) MWPC to amplify the drift electrons and create an image charge on an array of cathode pads is used. It would be nice to consider using the latest technologies such as gas electron multiplier (GEM) or micro-strip structures [139]. To date, these technologies have been applied to high–resolution, small–area applications such as X–ray detectors. To adapt these these technologies to the current application will require study and development. A small prototype TPC would be a good way to evaluate these candidates and determine the optimum readout technology.

Typical TPCs use an Argon–methane mixture, but non–flammable gases are also used. For example, the TPC in ALICE will use a Ne(90%)–CO_2 mixture [140]. Radiation hardness is unlikely to be an issue for any of the detectors under consideration and is mentioned only for completeness.

A TPC can give excellent dE/dx information. Recent technical notes [141], [142] show the limitations of Time of Flight for kaon identification. While dE/dx from a central detector is not a cure–all, it is a critical component of a successful PID system. To first order, the dE/dx information from a TPC will be superior to that of straw tube detector (for the same number of channels). However, the ultimate precision of PID from dE/dx depends on the number of samples and the TPC has the option of increasing the number of samples with the same electronics.

In addition to studies of the optimum physical structure of a TPC, it will be necessary to show that the pattern recognition challenges resulting from overlapping events can be solved. This situation is not unique [143], but is unusual, since in most previous high–rate applications, all tracks originate from a single interaction and the drift electrons clear the TPC before the next interaction.

5.5.6 The vertex chamber and start counter

The central vertex chamber has several purposes. First it will be used to provide accurate tracking information very close to the target. These track elements must be sufficiently well defined to be connected to the other tracking chambers. In the case of a TPC, these elements will also be used to help resolve which tracks came from the event of interest. Secondly, this chamber must provide a fast signal which can be used in the level–1 trigger of the experiment, in particular a start signal for the event. It may also be desirable to trigger on secondary vertices from Λ or K_S decays. In terms of the overall tracking resolution, (Fig. 5.4), the vertex chamber has a non–negligible contribution. In Fig. 5.12 are shown the overall resolutions for 200 μm and 1000 μm $r - \phi$ resolution. Forward of 50° (where the particles have larger momenta) the chamber must have at least 500 μm resolution. In addition, the chamber must have a position resolution along the beam direction, z, on the order of 1 mm to facilitate track matching. This is even more critical in the TPC option where only tracks that match hits in the VTX will be retained as in–time tracks.

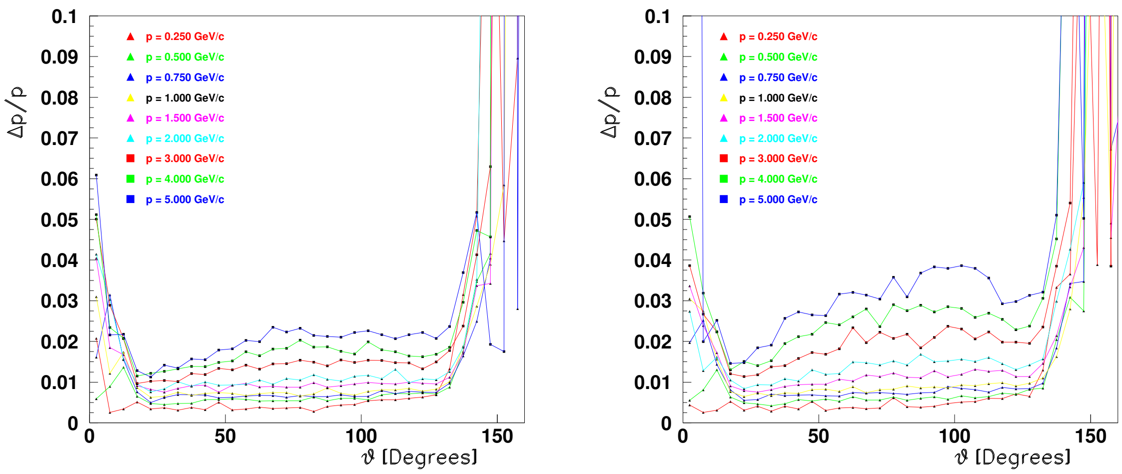

Figure 5.12: Tracking resolution as a function of angle and momentum. The left–hand figure has 200 μm resolution in the VTX, while the right–hand one has 1000 μm resolution.

The vertex detector will consist of two detector packages. One will be optimized for timing purposes and the other one will provide fast tracking information.

The timing detector will consist of a cylindrical array of 10 scintillator paddles. This will allow us to cover scattering angles between 1° and 90° for the full length of the target. The acceptance for large angles could be extended by increasing the length of the detector into the backward area. The scintillators have a thickness of 5 mm which reduces to 2 mm in the forward direction. This will provide a good light output and therefore a good timing signal. The paddles will be coupled to photo tubes at the upstream end via light guides which lead out of the high magnetic field region. Figure 5.13 shows the cross section of the scintillator array parallel and perpendicular to the photon beam. Using Bicron BC-404 scintillating material in combination with fast photo multipliers we expect to achieve better than 120 ps overall timing resolution.

The fast tracking detector will consist of three super–layers of fibers, each containing two layers to minimize dead space. The central layer will be arranged around the target and parallel to the beam. It will determine the azimuthal angle. The z position is deduced from the two outer layers. They will be wound in two opposite helixes around the first layer. Since this detector will be at 5 cm radially outward from the target the conventional solution using position sensitive photo multipliers (PPMT) together with blue scintillating fibers and light guides will not work for the following reasons. PPMTs will not properly function in high magnetic field areas, therefore necessitating long light guide fibers to an area where the field is low enough for the PPMTs to operate successfully. However the absorption length of clear light fibers in the blue area, where the photo cathodes have a maximum in quantum efficiency

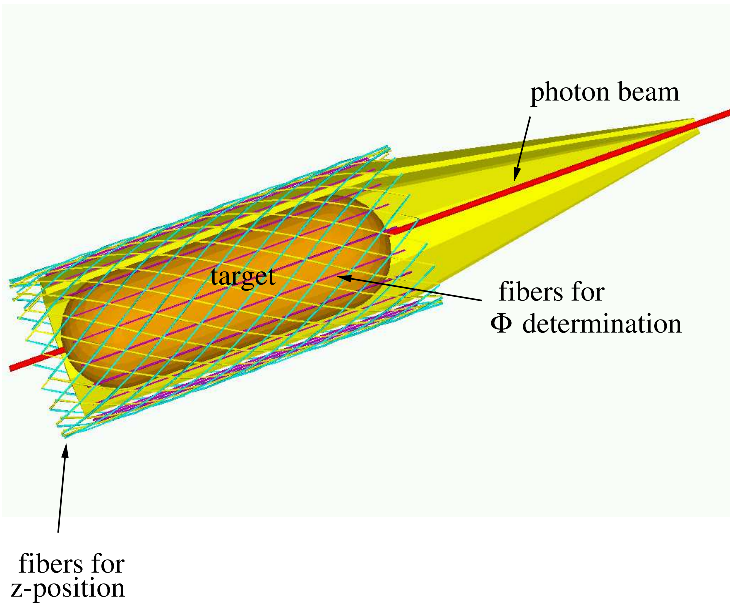

Figure 5.13: Conceptual design of the start detector with the target area surrounded by the cylindrical and conical array of scintillator paddles and the three super-layers of scintillating fibers. Note that the fibers do extend forward over the conical section of the detector.

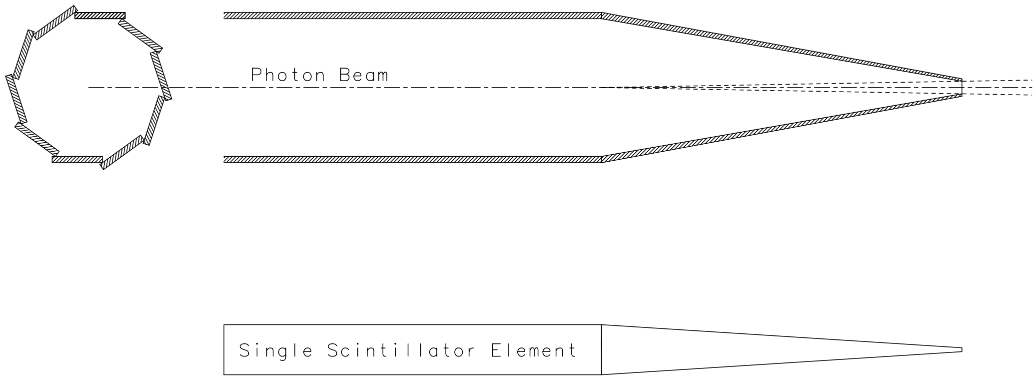

Figure 5.14: Cross sectional view of the scintillator array (timing detector) perpendicular to the beam (left) and parallel to the beam (right) and the top view of a single paddle.

(at best 18 %) is only of the order of 2 meters. As an additional factor one has to consider that blue scintillating fibers are highly susceptible to radiation damage, leading to an additional decrease in photo electrons. These combined effects will result in approximately two to three photoelectrons per minimum ionizing particle (mip) (excluding radiation damage), making a position determination by charge distribution on the PMT anodes impossible. One therefore cannot resolve multiple hits in one PMT.

In order to circumvent the problems mentioned above, we are studying the possibility using Visible Light Photon Counters (VLPC) developed by Rockwell in collaboration with Fermilab [144]. The spectral sensitivity of the VLPCs require us to use SCSF-3HF multi clad scintillating fibers from Kuraray which are also the least susceptible to radiation damage.

One of the main advantages of using VLPCs is their large quantum efficiency of approximately 80% [145] for the light produced by the fibers together with a very high rate capability of 10^8 single photoelectrons per second. Another advantage of using the Kuraray fibers is the long attenuation length of 5.5 m for the scintillating fibers and 10.4 m for the clear ones [146] allowing us to position the readout electronics well outside the region of the magnetic field. The design of the whole detector system will closely follow the prototype system developed [147] by the D0 collaboration at FNAL for the central tracking facility of D0 detector. The expected position resolution will be at least 1 mm.

5.5.7 The beam vertex trackers

The Beam Vertex Trackers, BVT, are small low–mass drift chambers located very close to the beam pipe and are necessary to reconstruct fast, small angle tracks, down to about 1° from the beam axis. The performance of these chambers is dominated by multiple scattering effects, so it is critical to make them as low mass as possible. They are also in a high rate environment, so it is necessary that they have maximum drift times on the order of $100\,ns$. Both of these lead us to believe that some sort of gaseous detector will be the optimum solution. However, further investigation is necessary to settle on a final design.

One possible design involves a traditional drift chamber built around annular shaped rings. These rings would have inner radius $3\,cm$ and outer radius $13\,cm$. With $1\,cm$ wire spacing, each plane will have 23 wires. Each package is assumed to have three planes, with about $1\,cm$ plane to plane spacing. The three planes would be arranged in a u–v–y arrangement as shown in Fig. 5.15. There would be approximately 6 packages in the detector leading to to 414 channels of electronics. With any design there is going to be a technical challenge of getting electronic signals out from the chambers while minimizing the material in the readout cabling.

5.5.8 Chamber infrastructure and alignment

Because the tracking system is built out of several different elements, good reconstruction relies on accurate positioning of the individual detector components. In designing such a system, it is important to build accurate, reproducible positioning of the detectors directly into the system. It is also desirable for cabling and servicing for all the tracking elements within the solenoid to be removable as a single package. This will require some sort of rail structure on the inner surface of the barrel calorimeter and mounting supports on the inner surface of the CDC or the TPC. The current design allocates a 5 cm space between the CDC and the barrel calorimeter. There is also a rather large logistical problem of getting all the cables out from the detector elements. The CDC or TDC will be read out only at the upstream end, and high voltage can be connected there as well. The FDC chambers can be read out at the outer radius, and the cables can pass between the tracking chambers and the barrel calorimeter. The scintillating fiber VTX chamber must be read out using photo tubes. It is possible to extend the fibers outside of the magnet at the upstream end, and attach the photo tubes there. The most difficult readout design problem is presented by the BVT chambers; most obvious readout schemes introduce additional mass in the form of cables directly in the center of the tracking volumes. It will be necessary to do some research to

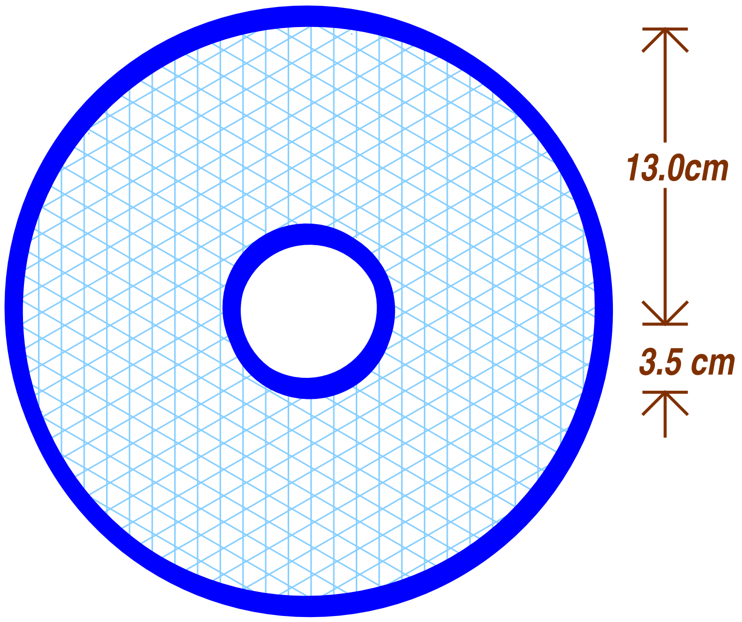

Figure 5.15: A schematic of three planes in the BVT chambers. The wire spacing in a given plane is approximately 1 cm.

try to multiplex, or preprocess the chamber information to minimize cables and high voltage connections.

5.5.9 Electronics

Table 5.4 summarizes the numbers of ADC and TDC channels needed in the basic drift chamber configuration. The only chamber that requires dE/dx information is the CDC, where many of the slow tracks will not reach the time–of–flight systems. Here it would be possible to replace the ADC/TDC pair with flash–ADCs, although a 250 MHz clock speed would be required to provide sufficient spatial resolution in the CDC option. The TPC could use somewhat slower flash–ADCs.

Detector	*Anodes*		*Cathodes*	
	FADC	TDC	FADC	TDC
VTX	0	2000	0	0
CDC	5200	0	1000	0
FDC	0	3570	7140	0
BVT	0	414	0	0
total	5200	5984	8140	0

Table 5.4: A summary of the electronic channels in the detector components for the CDC option.

5.6 Particle identification

Charged particle identification (PID) separates $\pi^\pm$ from $K^\pm$ from p (and the occasional $\bar{p}$). (We do not consider $e^\pm$ or $\mu^\pm$ identification explicitly, but they can be separated from hadrons at some level using the electromagnetic calorimeters.) Two detector systems will be constructed explicitly for this purpose, namely the time of flight hodoscope and the Čerenkov detector. Both of these address PID in the forward region, where velocities are close to c and the separation is most difficult. In the solenoid, we expect to make use of dE/dx in the drift chambers and timing in the barrel calorimeter. Furthermore, constrained fitting is a generally useful tool for identifying the event topology as a whole.

This scheme is modeled after SLAC Experiment E135 [126] which used the LASS solenoid to investigate $K^\pm p$ reactions at 11 GeV/c. They used time-of-flight and two gas Čerenkov detectors, and also relied on kinematic fitting for PID. For example, see their measurements of the reactions $K^-p \to \Lambda K^\star \bar{K}^\star \to \Lambda K^+K^-\pi^+\pi^-$ [148] and $K^-p \to \Lambda\pi^+\pi^-\pi^+\pi^-$ [149]. We expect to use the LASS solenoid as the primary magnetic field for our detector, and it is therefore reasonable to use that facility as a guide for our initial design. A sketch of the apparatus, with particular attention to PID, is shown in Fig. 5.1.

5.6.1 Time-of-flight hodoscope

Time-of-flight is useful for PID in the forward region, if the particle momentum is not too high. A simple calculation gives one an idea of the necessary performance. Assuming a five meter flight path, the time difference between $\pi^\pm$ and $K^\pm$ works out to be the following:

p (GeV/c)	$t_K - t_\pi$ (ps)
2	463
3	207
4	117
5	75

For TOF scintillators that are $\approx 2\,m$ long, RMS time resolutions on the order of 100-120 ps are typically achievable using well established techniques [150, 151]. With improvements in photomultiplier design, however, one can achieve 50 ps RMS for detectors with long, narrow geometry. For example, Ref. [152] describes 2 m long detectors, with $2.5 \times 2.5\,cm^2$ cross section and a 12-stage bialkali PMT on each end, which do this well. Furthermore, these authors demonstrate superior time resolution with mesh PMTs which will work well in a high magnetic field. Of course, it would be important to control temperature and many other factors to routinely get 50 ps resolution on a large bank of counters.

Costs have been estimated based on a hodoscope with 100 counters, each about 1 inch wide and with a photomultiplier on each end. This provides a large enough aperture to cover the forward region, just upstream of the lead glass calorimeter.

Some preliminary tests have been made to determine if a TOF hodoscope with sufficient resolution for this application can be made using inexpensive scintillator and photomultipliers. Recent tests at the Institute for High Energy Physics (IHEP) near Protvino, Russia indicate that this will indeed be possible. Figure 5.16 shows the results of these tests. Strips of Bicron BC-404a measuring 2 $cm\times$ 1.27 $cm\times$ 150 cm read out by FEU-115 photomultipliers at both ends were investigated. Constant fraction discriminators were used in lieu of offline corrections for pulse height slewing. The HALL D detector will use FADCs and pipelined TDCs to allow offline corrections to be made.

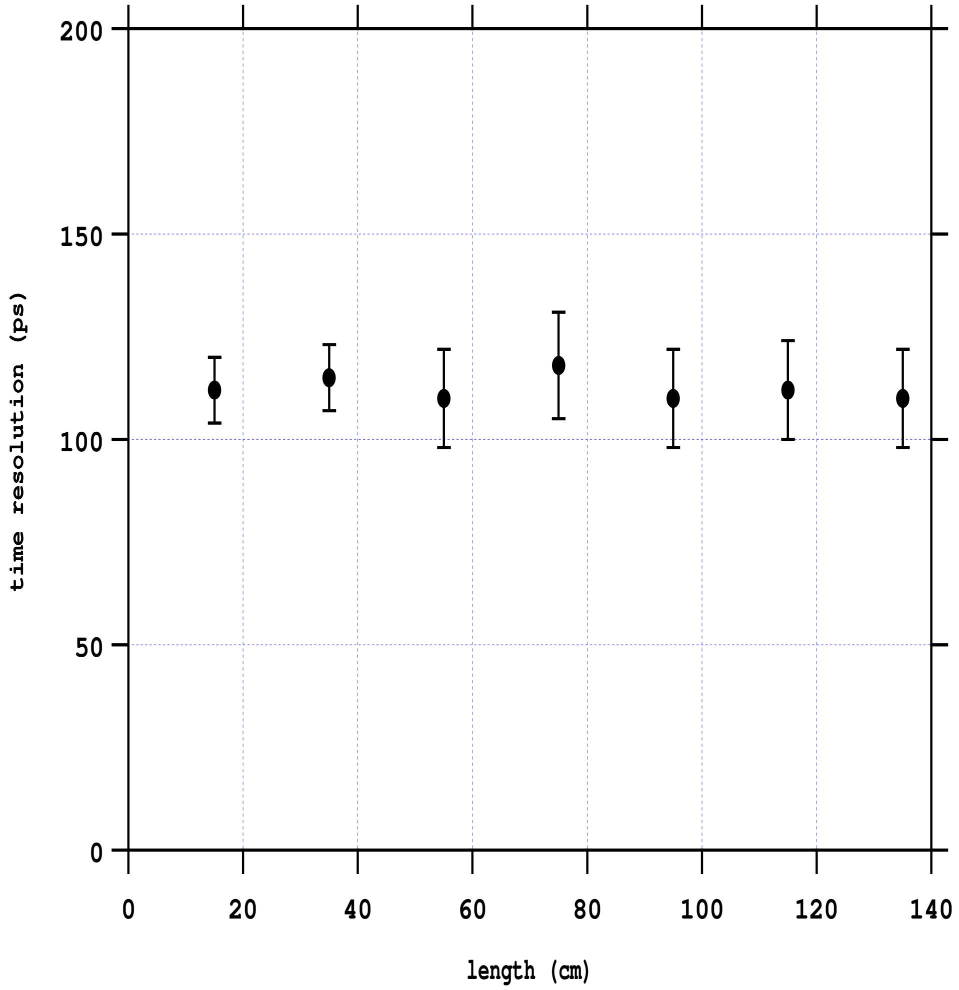

Figure 5.16: The resolution achieved during TOF tests.

5.6.2 Čerenkov detector

As demonstrated above, TOF should be sufficient for momenta up to 3 GeV/c or so. Threshold Čerenkov detection will be used for K/π separation in the forward region for the upper end of the momentum spectrum. E135/LASS employed such a detector, using geometry and energies rather similar to what we consider here. Their detector [126] used a gas volume that filled the downstream end of the solenoid, and used mirrors and guiding optics to focus light onto high gain, single-photon counting PMTs (RCA 8850, now available from Burle Industries). These optics and PMTs separated the detector into 12 equal "pie" slices in azimuthal angle, with each slice divided radially into three segments. There were also two mirror and PMT combinations in the beam region, giving a total of 38 optically separated detectors viewing the same gas volume but for different particle trajectories.

The LASS Čerenkov detector worked rather well. Figure 5.17 shows the efficiency calibration for each of the three radial "rings" of optical segments. For these measurements, the gas volume was filled with Freon-114 ($C_2Cl_2F_4$), with $n-1 = 1.53 \times 10^{-3}$. This translates to a π (K) momentum threshold of 2.51 GeV/c (8.95 GeV/c). (Fluoro-chlorocarbons are not longer produced, but a similar gas, C_4F_{10} is available and has $n-1 = 1.4 \times 10^{-3}$.) [153] The photoelectron yield, based on a simultaneous fit to the efficiency curves of all three rings, which includes a constant background term, gives photoelectron yields of $(4.6 \pm 0.2)/m$, $(4.8 \pm 0.1)/m$, and $(5.3 \pm 0.2)/m$ for rings A, B, and C respectively.

These results suggest a C_4F_{10} filled Čerenkov detector followed immediately by a TOF system, just upstream of the LGD. Certainly, a design closely following E135 is feasible. However, more recent technology may provide solutions that are simpler and more cost effective to implement.

For example, a novel threshold Čerenkov design[154] has been prototyped for the CLEO-III experiment at Cornell. This design is particularly compact and makes use of mesh photomultipliers (Hamamatsu R3386) which perform well in high magnetic fields. This would considerably alleviate a severe problem with the LASS detector, namely the need to transport the light far away from the magnetic field, and heavily shield the photomultipliers. (This was particularly difficult for the lower segments because of interference with the floor.)

The CLEO-III prototype also used pressurized gas for a radiator, allowing some variability in the index of refraction and so the π and K thresholds. Another interesting possibility is silica aerogel, which has seen some dramatic improvements in quality and availability in recent years[155, 156, 157]. It remains to be seen, however, if aerogel with *low* enough index of refraction is available. This needs study.

5.6.3 Other techniques

The TOF and Čerenkov systems are implemented specifically for charged particle identification. However, other techniques are also available if we pay some attention to the relevant details of other parts of the detector. In some cases this requires a modest increase in cost to outfit channels with flash–ADCs (for some drift chamber channels) and TDCs (for the barrel calorimeter).

Constrained fitting

An important goal of the HALL D detector is the ability to identify exclusive events. That is, all outgoing particles will either be directly detected (four energy and momentum constraints) or a single particle is missing in which case one missing mass constraint fully characterizes the kinematics. Used in conjunction with other particle identification techniques, this is a powerful way to reject background from misidentification. For example, in reactions involving $K^{\pm}$ or K_S, we must conserve strangeness and if one kaon (or hyperon) is identified directly, the other is inferred and must satisfy the kinematic constraints.

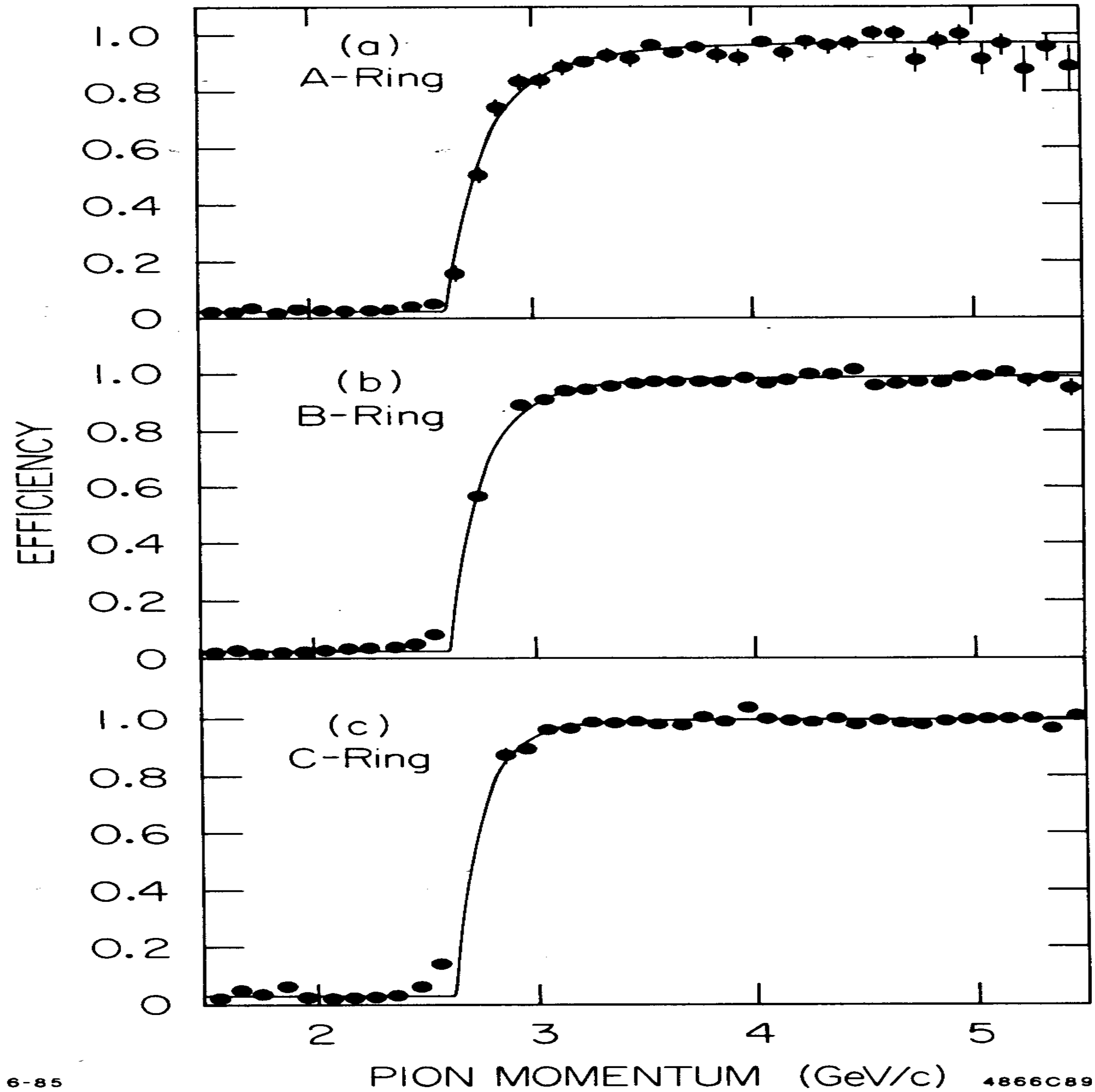

Figure 5.17: Performance of the LASS Čerenkov detector. The three "rings" correspond to the mirror and PMT configurations that encircle the beamline at three different radii. The detector is filled with Freon-114, for which the $\pi^{\pm}$ threshold is 2.5 GeV/c. The curves represent simultaneous fits through all three sets of data, for the expected Čerenkov efficiency curve plus a constant background. These fits yield asymptotic efficiencies of 0.971, 0.987, and 0.998 for rings A, B, and C respectively, and a yield of about five photoelectrons per meter of gas.

dE/dx from drift chambers

The differential energy loss dE/dx for a particle of charge q is roughly proportional to q^2/β^2 and therefore provides a handle on the particle velocity, and therefore PID, if the velocity is small. This will be useful in our detector for tracks emerging at large angles and which may not intersect the TOF system. The use of dE/dx in particle identification has in fact been recently reviewed [158, 159]. One key consideration (see Table 1 in [158]) is the number of samples along the track. Figure 5.18 shows the p/π^+ separation achieved in the E135/LASS detector using six concentric cylindrical proportional chambers [126] each with anode and two cathode readouts, for a total of up to 18 samples. The dE/dx resolution here is not well-determined (the chambers were operated in near-saturation mode), but it is roughly 10%. Depending on the final drift chamber configuration, we should do somewhat better, particularly if care is taken to ensure optimal dE/dx characteristics from the start.

Time-of-flight from the barrel calorimeter

The lead scintillating fiber structure of the barrel calorimeter provides a large number of samples as a particle traverses the individual fibers. This can be used to achieve a respectable timing resolution if care is taken with the readout. The KLOE collaboration at DAΦNE has demonstrated [160] RMS time resolutions of 252 ps (390 ps) for minimum ionizing particles traversing 19 (9) layers of lead and fiber. Improvements are possible.

5.6.4 Performance

We have studied the PID characteristics of the detector using a Monte Carlo simulation. We have only incorporated the forward detector region at this time, as we are mainly interested in the performance of the dedicated PID systems, namely the TOF hodoscope and Čerenkov detector.

Our initial design focuses mainly on K/π separation in the reaction $\gamma p \to K^\star \bar{K}^\star p \to K^+K^-\pi^+\pi^- p$. A key physics goal in HALL D will include reactions exciting various forms of strangeonium. These reactions will lead to multiparticle final states containing both $K^\pm$ and $\pi^\pm$. However, a large part of the cross section will lead to similar multiparticle states but with all pions, hence our present focus. We also consider identification of the recoil proton.

Events are generated by producing a state with mass 1.7 GeV/c^2 and width 0.250 GeV/c^2 decaying to $K^\star\bar{K}^\star$, and distributed in momentum transfer according to e^{bt} with b=5 $(GeV/c)^{-2}$. A number of different incident photon energies were considered, but for purposes of illustration here, we show the study with $E_\gamma = 10\ GeV$.

Figure 5.19 shows, for various assumed RMS time resolutions, the mass determined from the momentum and TOF hodoscope. (Only particles in the forward region are considered.) One sees clear peaks corresponding to pions, kaons, and protons. Of course, sharpest regions of the peaks are dominated by the slower particles and this, in itself, is not a sufficient measure of the PID capabilities of the TOF system. For the purposes of this study, we will assume an RMS time resolution of 100 ps.

If we somewhat arbitrarily define a kaon signal as a mass value measured in the range $0.40 \leq M_{\mathrm{TOF}} \leq 0.60\ GeV/c^2$, we determine the number of kaons identified correctly as kaons,

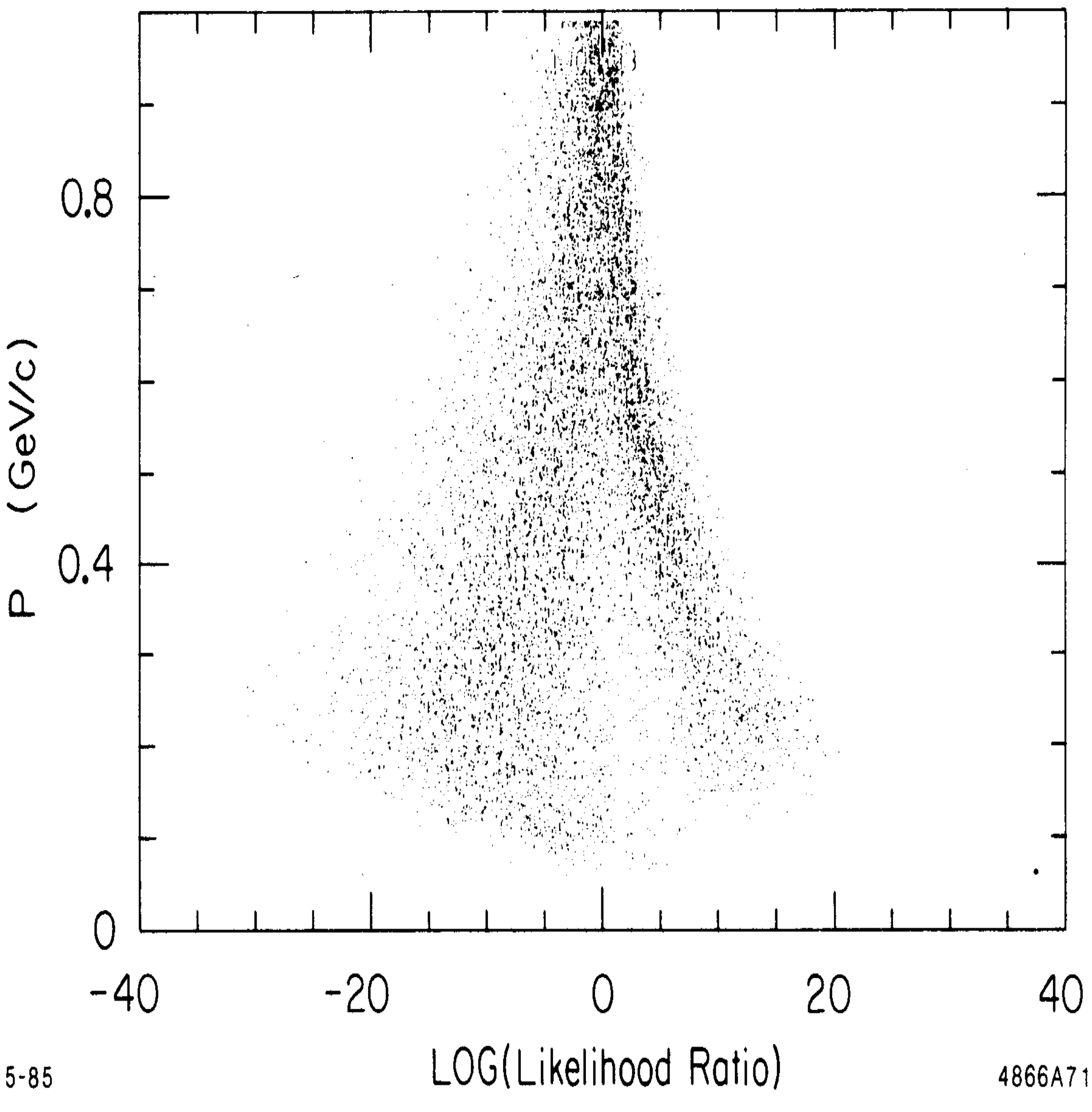

Figure 5.18: A scatterplot of the likelihood ratio P_p/P_π versus particle momentum for positively charged tracks in the E135 spectrometer. These data were taken with the cylindrical proportional wire chamber package, with up to 18 dE/dx samples per track. Clear separation is seen for momenta up to a few hundred MeV/c.

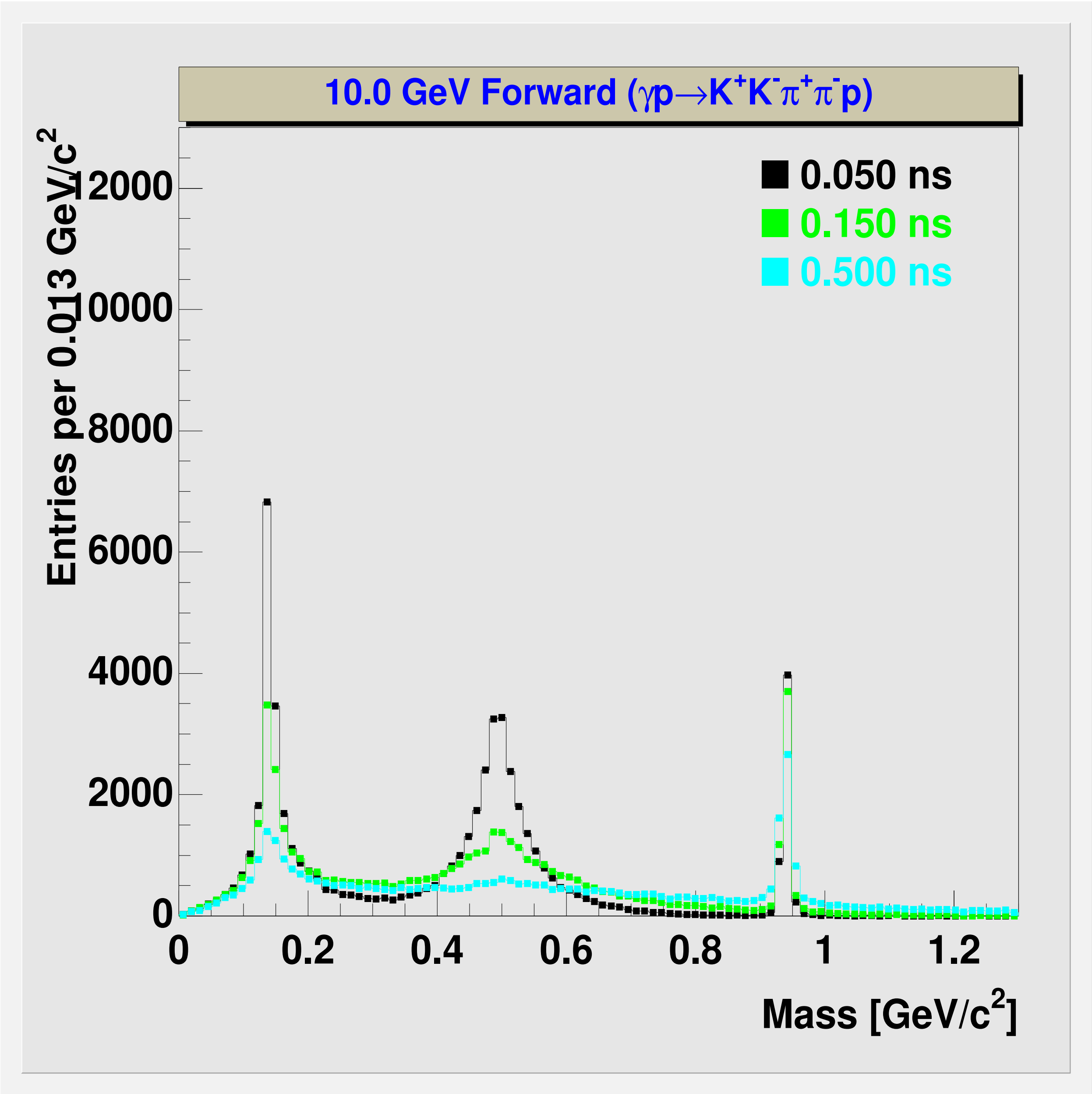

Figure 5.19: The reconstructed mass as a function of timing resolution in the forward region. The reaction used to generate these events is $\gamma p \rightarrow X p \rightarrow K^{\star} \bar{K}^{\star} p \rightarrow K^{+} K^{-} \pi^{+} \pi^{-} p$ with 10 GeV photons.

and the number of pions or protons misidentified as kaons. These fractions are shown as a function of particle momentum in left hand panel of Fig. 5.20, based on the data shown in Fig. 5.19. As expected, as the particle momentum increases, the fraction of correctly identified kaons decreases from unity, and a fair number of pions are misidentified in the same mass window. (The K/p separation is clearly very good over the entire momentum range.)

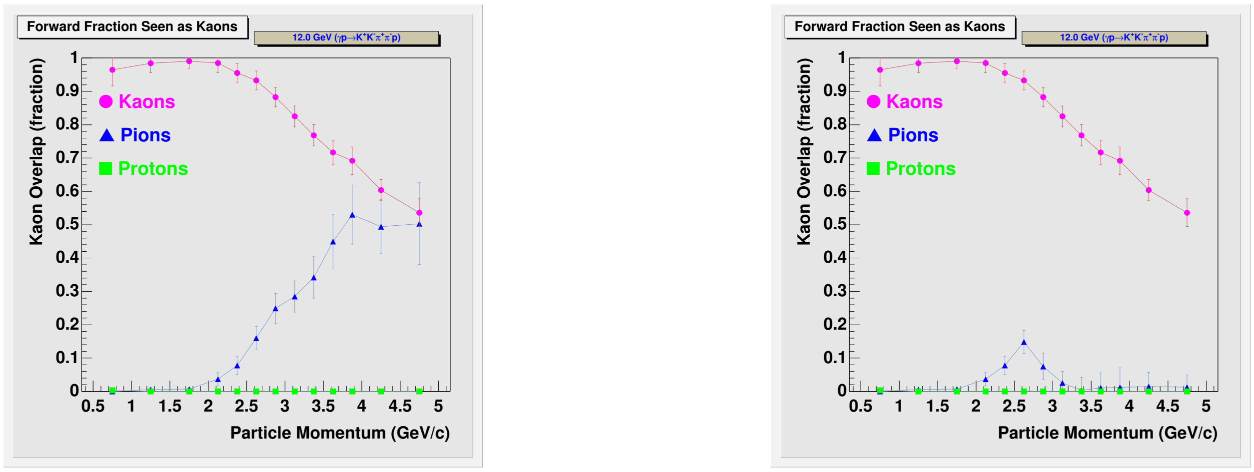

Figure 5.20: The fraction of π's, K's, and protons identified as K's as a function of particle momentum. A time of flight resolution of 100 ps RMS is assumed for the TOF hodoscope. On the left, K's are identified as particles whose mass is between 0.40 and 0.60 GeV/c^2 based on the TOF measurement. On the right, it is also required that the particle not register a signal in the Čerenkov detector.

The effect of the Čerenkov detector on PID is determined using a model based on the E135/LASS experiment. This is a ring shaped detector, 90 cm long, containing C_4F_{10} with $n - 1 = 1.4 \times 10^{-3}$. Following the Particle Data Group, an average number μ of detected photoelectrons is determined for each track according to

$$\mu = L \times 90 \times \left[1 - \frac{1}{\beta^2 n^2}\right]$$

where L (in cm) is the length of the track within the gas volume. (This result assumes a 90% light collection efficiency, and a 28% photocathode quantum efficiency.) An actual (integer) number of detected photoelectrons is then determined randomly based on Poisson statistics. We assume the particle registers a signal in the Čerenkov detector if at least one photoelectron is detected.

For K/π separation at high momentum, that is, where the separation becomes poor in the left panel of Fig. 5.20, we expect pions to start to trigger the Čerenkov detector. (An index of refraction $n - 1 = 1.4 \times 10^{-3}$ corresponds to a pion momentum threshold of 2.64 GeV/c and a kaon threshold of 9.34 GeV/c.) If we require, in addition to fitting within the kaon mass window from TOF, that the particle *not* fire the Čerenkov detector, then the resulting kaon identification fraction is as shown in the right hand panel of Fig. 5.20. Clearly, the pion detection efficiency is quite large and the separation is much cleaner.

5.7 Forward calorimetry

A circular lead glass array will serve as the forward electromagnetic calorimeter for the HALL D detector. An existing detector, The Brookhaven National Laboratory E852 lead glass calorimeter, will be salvaged and, with only minor modifications, will be configured for HALL D use. Figure 5.21 shows the configuration of the existing detector.

5.7.1 Modifications required for HALL D

Several modifications to optimize performance for HALL D are anticipated:

- The horizontal motion will be perpendicular to the existing configuration, that is, horizontal motion will be along the beam axis
- A platform behind the LGD darkroom will be added. This platform will carry the electronics associated with the LGD.
- The inner frame will be stretched vertically to allow a circular array of lead glass blocks. Shim structures will be built to support the stack in uninstrumented areas.

Figure 5.22 shows the E852 LGD as modified for HALL D. A large range of z-motion is required to allow removal and servicing of the solenoid region components. The addition of the platform makes the detector self-contained, all cables and electronics are contained on this platform and move with it. The circular stack matches the aperture of the solenoid and mimimizes the number of detector channels while maximizing the target to LGD distance.

5.7.2 Performance

The calorimeter on which the HALL D detector will be based was used as a detector and a trigger element in BNL E852 and has been described previously.[161] Good position and energy resolution allowed for the reconstruction of multi-photon final states. Figure 5.23 gives some examples. We anticipate similar performance in the HALL D environment.

A trigger processor[162] allowed the calorimeter to be used as a trigger device. The total energy deposited and the effective mass of the photon system were calculated by this trigger processor. This allowed selection of well contained events or the rejection of relatively uninteresting final states. When used in conjunction with a charged track counting trigger element, final state topologies like, for example, $\pi^+\pi^-\eta$ (with $\eta \to \gamma\gamma$) could be selected while the $\pi^+\pi^-\pi^0$ topology was reduced. Figure 5.24 shows the result when events are selected by such a trigger.

5.7.3 Radphi experience

Operating an electromagnetic calorimeter, like the LGD, near a photon beamline could be a concern given the backgrounds one might expect with a tagged bremsstrahlung photon beam. For this reason, the recent experience with the LGD used in the Radphi experiment during a recent test run in the Hall B photon beam is of particular relevance. Because of

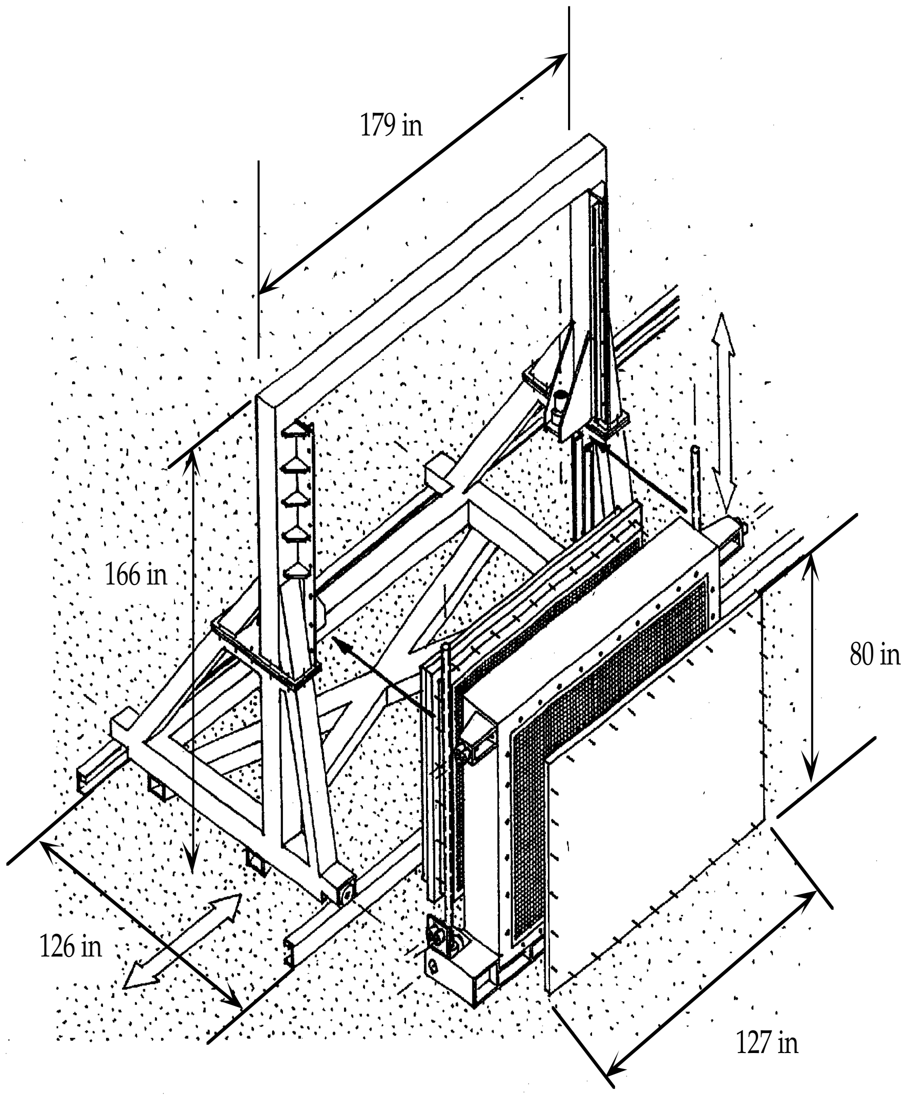

Figure 5.21: The E852 lead glass detector.

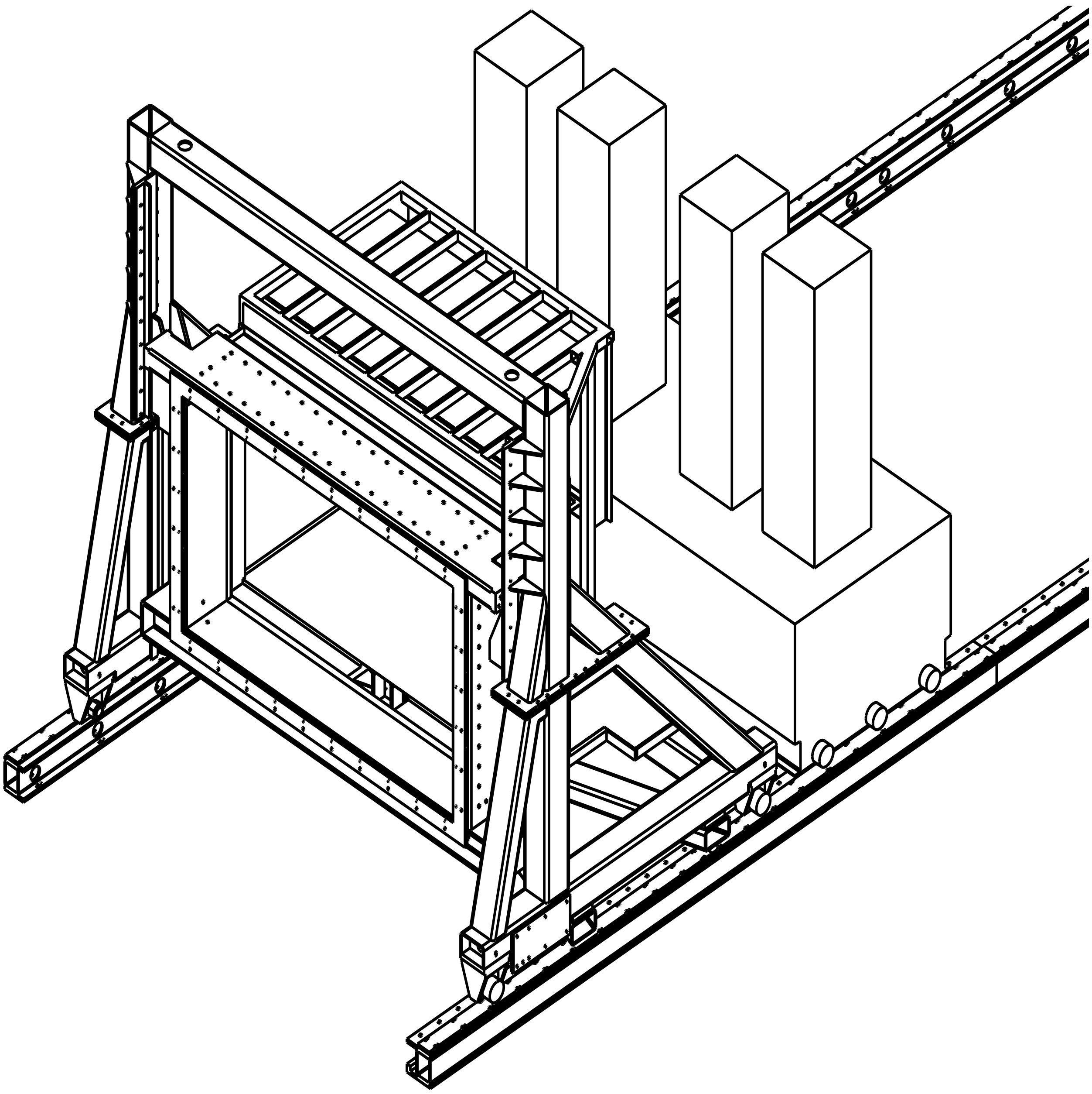

Figure 5.22: The E852 lead glass detector as modified for HALL D

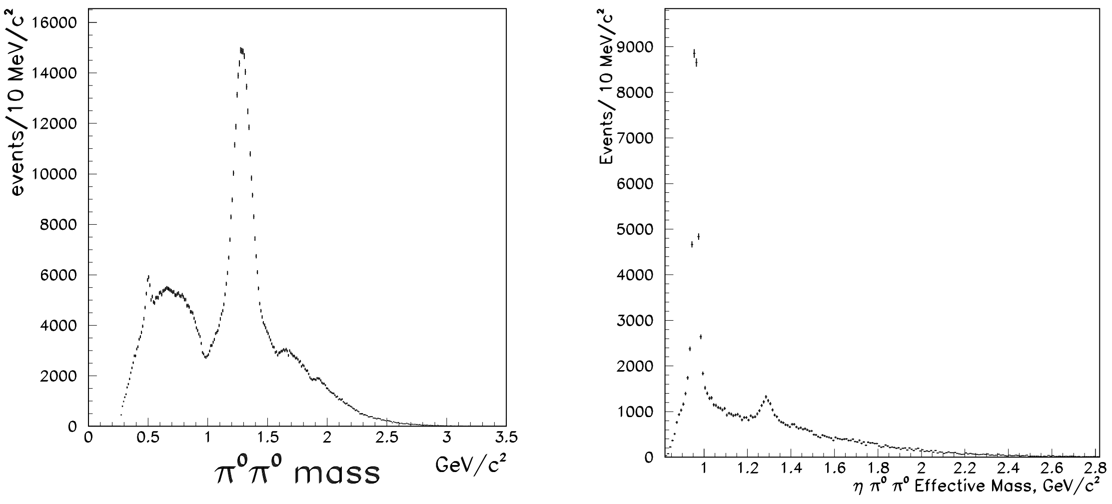

Figure 5.23: Left: The $\pi^0\pi^0$ effective mass as reconstructed from 4 photon events. Right: The $\eta\pi^0\pi^0$ effective mass as reconstructed from 6 photon events. Clear structures associated with the $\eta'(958)$ and $\eta(1295)$ are seen.

the high quality of the photon beam, beam-associated backgrounds were manageable, even when operating at an endpoint energy of 4 GeV. At higher energies the beam spot size will be even smaller and the LGD energy resolution will improve.

This goal of the Radphi experiment is the measurement of rare radiative decays of the ϕ meson. The Radphi experiment uses an LGD similar to that used in the E852 experiment with 700 similar lead glass blocks arranged in a roughly circular arrangement around the beam. A two block by two block hole allows for passage of the beam. The PMT bases are of the Cockcroft-Walton [163] type and the same ADCs and trigger processor used in the E852 experiment were used in this test run as well. The Radphi experiment is located in Hall B downstream of the CLAS detector. The tagged photon beam operated at an endpoint energy of 4 GeV and the photon beam passed through the CLAS target before reaching the Radphi experiment. For this run a cylindrical beryllium target was used (1 *inch* long and 1 *inch* diameter) placed about 1 m from the front face of the LGD wall.

The data shown here are from 10M triggers of the 15M collected in the test run. The events were passed through a cluster finder which looks for showers in the LGD array due to photons. Events with two clusters show clear presence of the π^0. The π^0 signal was used to calibrate the LGD by adjusting the gains of each of the modules to yield the nominal mass and to minimize the width of the π^0 seen in the 2γ mass distribution.

The 2γ effective mass spectrum from two cluster events in shown in Figure 5.25. Clear peaks at the π^0 and η are observed. The calibration procedure ensures that the centroid of the peak occurs at the nominal mass. The observed width of the peak is 0.014 GeV/c^2. A fit of the η peak, show in Figure 2, yields a mass of 0.547 ± 0.0044 GeV/c^2 and a width of 0.064 GeV/c^2.

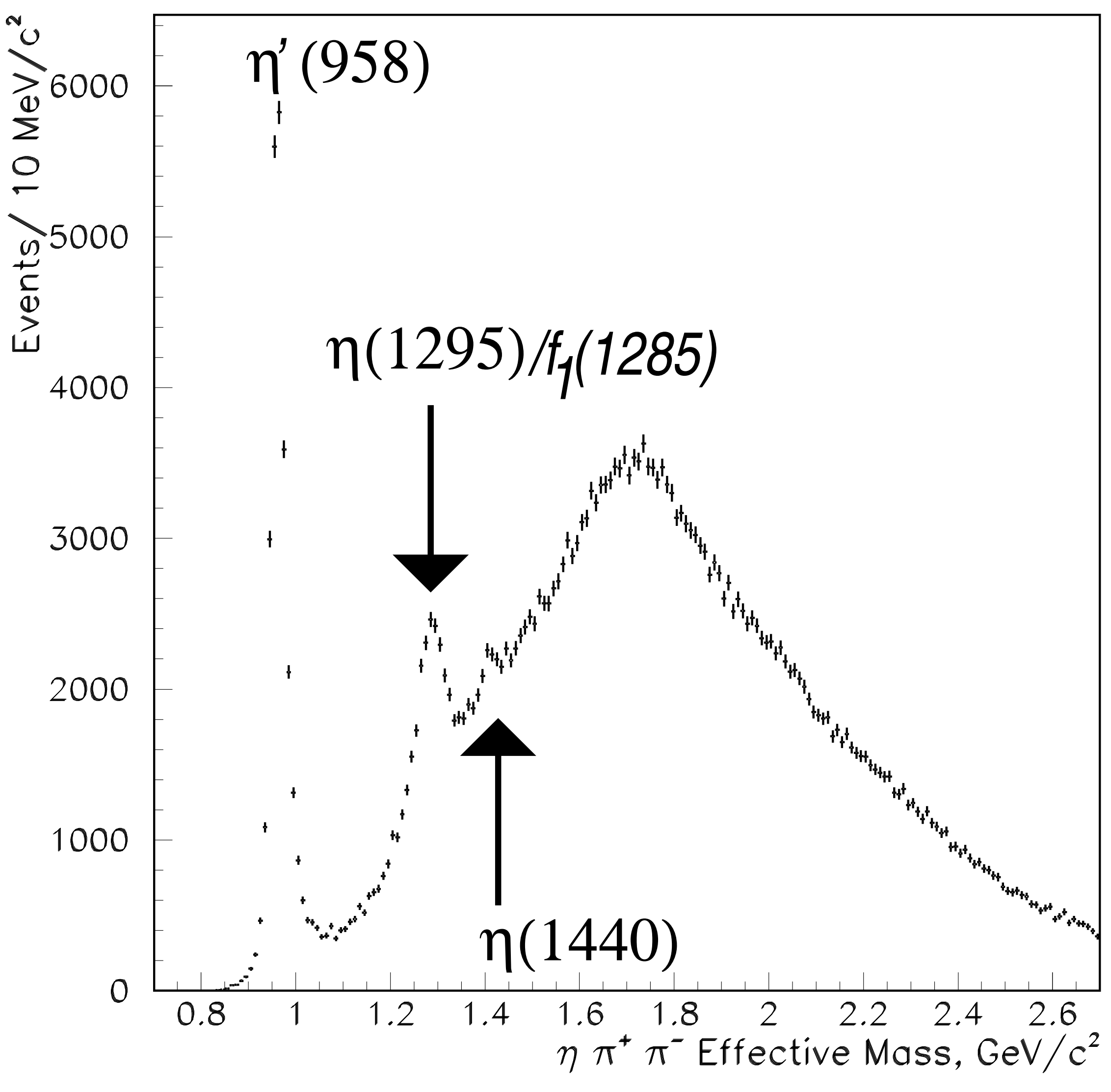

Figure 5.24: The $\eta\pi^+\pi^-$ effective mass distribution as reconstructed from "two charged tracks" plus $\eta \to \gamma\gamma$ events. Clear structures associated with the $\eta'(958), \eta(1295)$ and $\eta(1440)$ are seen.

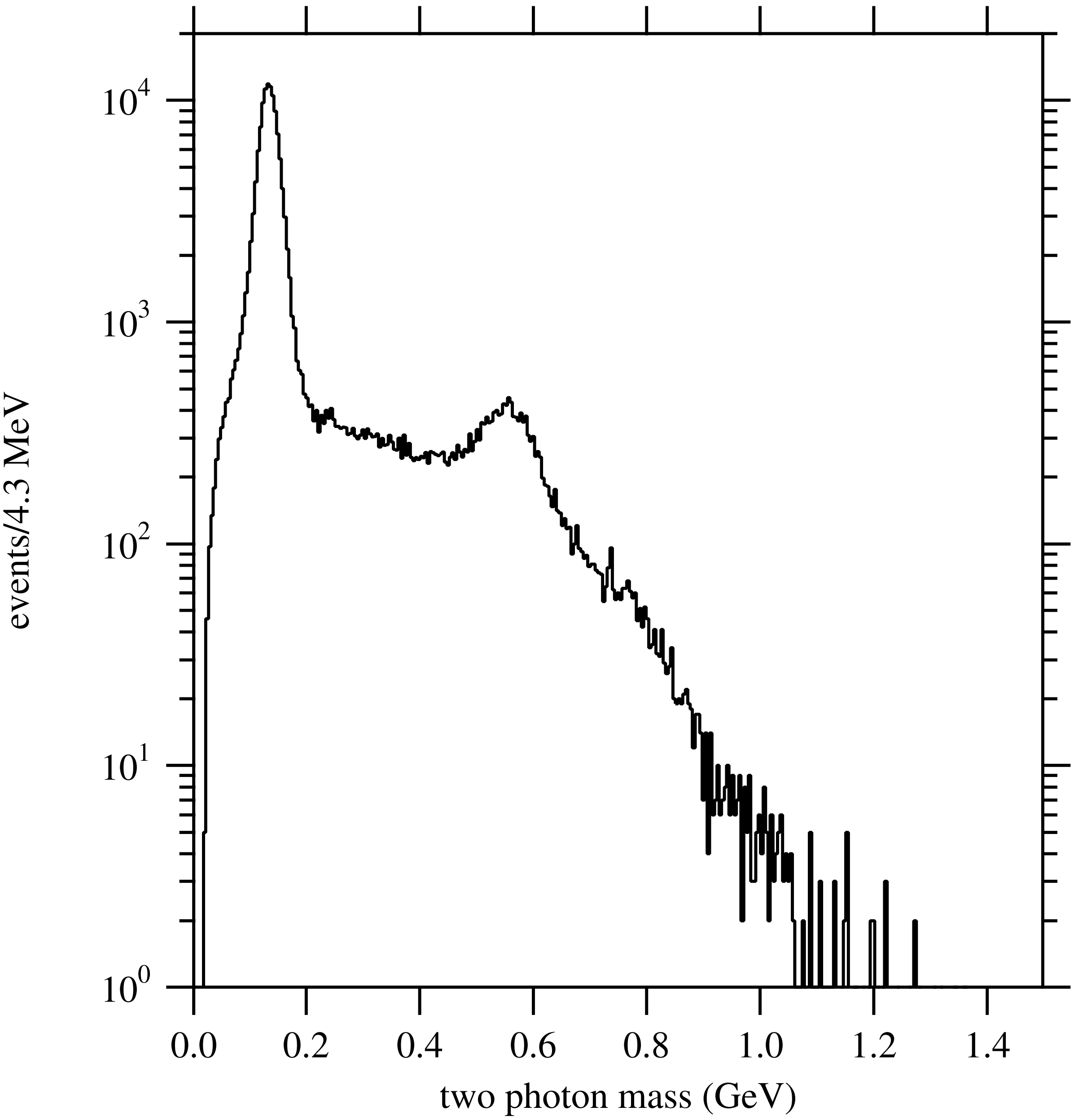

Figure 5.25: Two photon effective mass from two-cluster events from the Radphi experiment.

Chapter 6

Civil Construction

The meson spectrometer will be in a new experiment hall (HALL D) located at the end of a new beamline off the stub at the east end of the North Linac. Figure 6.1 shows an overview of the accelerator and proposed HALL D location.

Civil construction includes breaking through the stub, tunnel and beamline components to delivering beam above ground to the tagger, tagger building, HALL D building, beam dump, control room, roads, and parking area. Basic infrastructure for all utilities is also included.

We have had numerous meetings with JLab civil construction, accelerator, and RadCon staff, and conclude that there are no serious civil construction problems. The main problem is to minimize cost while satisfying HALL D requirements. In particular, the beamline and hall will fit on DOE/SURA land, building construction should straightforward, and RadCon problems can be handled by standard techniques.

Figure 6.1 shows the plan and elevation views for the HALL D beamline and associated buildings.[1] Figure 6.2 shows more detail of the tagger building and HALL D complex.

6.1 General requirements

Requirements and specifications assuming a maximum electron beam energy of 12 GeV are given in Table 6.1 and below:

- Single electron energy available for the D line
- HALL D is designed for a photon beam only (i.e. no primary electrons into HALL D)
- Civil construction compatible with 24 GeV beam (e.g. 80 m bend radius)
- Accelerator tangency point to radiator = 125 m
- Radiator to collimator distance = 80 m

[1]The elevation is for a beamline 1.5 m above grade. The option of a beamline which is 3.0 m below grade is also under consideration, but appears to be more expensive.

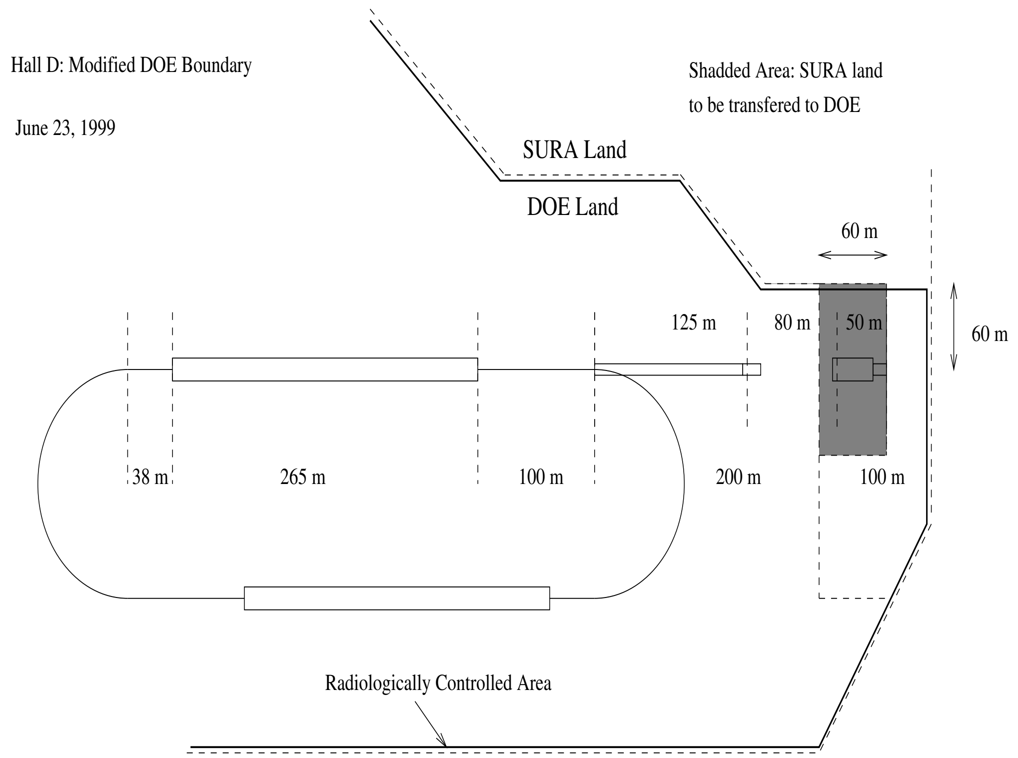

Figure 6.1: An overall view of the accelerator site and HALL D.

- Detector building = 17 m x 36 m (includes shielding and collimator) x 13 m (height) = 15 m x 30 m x 13 m
- Tagger building = 6 m x 15 m x 3.5 m (height)
- Dump house for sideways dump = 3 m x 3 m x 4 m (height)
- Nominal beam height above HALL D floor = 2.5 $\pm$ 0.3 m
- Nominal beam height above tagger floor = 1.5 m
- Permissible building settlements: 1 *inch* initial; 2 *inches* max over lifetime

Parameter	Operating Value	Design Max
Max Electron Current	3 μA	5 μA
Min Electron Current	$\sim$0.0001 μA	0.0001 μA
Electron Energy	12 GeV	12 GeV
Power	36 KW	60 KW
Photon Power (Collimator)	7 W	10 W
Photon Power (Detector)	1 W	1.5 W

Table 6.1: Beam parameters for a 12 GeV electron beam.

6.2 Environmental and radiation concerns

The civil construction includes shielding for all buildings which are obtained from preliminary, but conservative, estimates of expected radiation doses. They are based on original calculations by Lewis Keller, who has served as a consultant on this project. The Jlab RadCon group has reviewed his estimates, concluding that with one exception, they provide more than adequate protection. The entire HALL D building requires some shielding, as specified below.

6.2.1 Site dose limits

On–Site The design goal at Jefferson Lab is 250 mrem/year which may include occupancy as a factor and is based on the Jefferson Lab RadCon Manual. This implies an average dose rate of less than 0.1 mrem/hour. There is also an instantaneous accident dose rate limit which is identified in the Jefferson Lab Beam Containment Policy as 15 rem/hour based on maximum credible beam loss conditions.

Site Boundary The integrated dose limit at any point on the site boundary is 10 mrem/year.

6.2.2 Beam on radiator

The entire bend string that brings the beam from the accelerator must be in series on the same power supply. For the purpose of estimating dose rates, RadCon assumes that losses along the transport line are of order 0.1%. After the beam is horizontal, two burn-through monitors with small apertures preceding the radiator are needed. In addition there should be a 1-2 m steel wall downstream from the last vertical bend, as in the beam lines to the other halls.

JLab Personnel Protection rules further require that beam–loss protection systems use at least 3 independent devices using 2 or more independent technologies.

6.2.3 Tagger building

Jlab rules require that the instantaneous dose rate outside HALL D during a beam accident be less than 15 R/hr, assuming the beam will be turned off in less than 1 second. To shield photons and neutrons, 3.0 m of earth shielding is sufficient.

6.2.4 Tagger hodoscope

Assuming the dump is 20 m from the hodoscope elements and a 5 cm vacuum pipe leading to the dump, the neutron rate coming backward from the dump is 3×10^7/s, and the photon rate is 0.8×10^9/s for a 60 KW beam on the dump.

6.2.5 Beam on dump

The tagger magnet must be interlocked so that if its current falls below some level the beam is turned off. Two permanent–magnet dipoles located downstream from the tagger magnet, each with a small aperture burn-through monitor at its entrance, ensure that the 60 KW beam will not go down the photon channel. Sufficient shielding surrounds the upstream portion of the photon beamline to contain the mis-steered electron beam.

6.2.6 Beam dump building

JLab requires that the dose rate must be less than 0.1 mrem/hour outside the building. One m of steel and 5 to 6 m of earth on the top and sides of the building are required to contain the photons and neutrons resulting from the 60 KW beam.

6.2.7 Collimator enclosure

Assuming a limit of 0.1 mrem/hr outside the building and a 10 W photon beam, 1.2 m of steel is needed on the top and sides of the collimators for HEN's, and 1.7 m of earth or concrete is needed in the backward direction for the GRN's.

6.2.8 Detector building

Ten cm of concrete are required on the sides and roof of the detector building to shield against low energy neutrons.

6.2.9 Photon beam dump

About 10-12 m of Fe are required to absorb the 50 kHz of muons above 1 GeV/c produced by a 10 W photon beam in the collimator [164].

6.3 Costs

Preliminary designs, optimizations, and cost estimates have been performed and are summarized in the following subsections [165].

6.4 Schedule

Jlab engineers estimate that civil construction will take a minimum of 27 months (including design time) from project start until we can gain beneficial occupancy of the detector hall and control room.

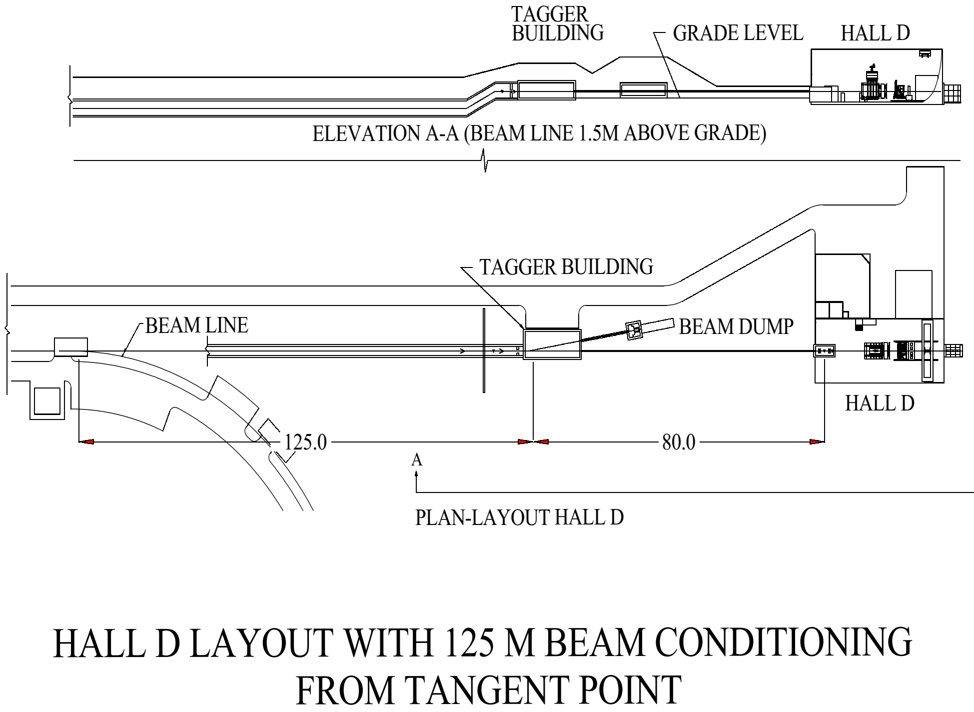

Figure 6.2: Elevation and plan view of the tagger and HALL D buildings.

Chapter 7

Rates, Trigger and Data Acquisition

7.1 Expected rates

7.1.1 Overview

We estimate trigger and background rates in HALL D using measurements of the hadronic cross section combined with the CLAS experience. The hadronic rate between any two photon energies E_1 and E_2 can be written as

$$R = \int_{E_1}^{E_2} n\sigma(E)\frac{dN}{dE}dE$$

where n is the number of target protons per unit area, $\sigma(E)$ is the hadronic cross section as a function of energy, and dN/dE is the photon energy spectrum. The photon flux is composed of a coherent and incoherent sum as detailed in Chapter 4. Background rates are dominated by the broad-band incoherent flux. The signal rates result from the photon flux in the coherent peak, which depend on the radiator crystal structure and its orientation. The coherent peak will be optimized to the specific physics program. For our rate estimates, we use the typical case for the flux computed on a diamond radiator with the coherent peak at $E_\gamma = 9\ GeV$ (See Table 4.5).

Both coherent and incoherent fluxes are proportional to the electron beam current and radiator thickness. Multiplying the number of electrons per second by the radiator thickness in radiation lengths gives the product N_0 which we will use in the following calculations. For conditions which we will refer to as “low intensity” (300 nA beam on a 10^{-4} radiator), $N_0 = 1.9\times 10^8$/s. For the coherent peak at 9 GeV the tagged photon flux between 8.4 and 9.0 GeV is $R_{tag} = 0.14\ N_0$. The average tagging efficiency over this interval is 0.375, so the tagged photon flux on target is 1.0×10^7/s. “High intensity” running, where the tagger becomes ineffective as part of the Level 1 trigger, nominally corresponds to $N_0 = 1.9\times 10^9$/s and yields 10^8/sec tagged photons on target.

The total hadronic γp cross section[1] is plotted in Fig. 7.1. For the experimental conditions defined above and a 30 cm liquid hydrogen target, the total hadronic rate in the detector is

$$R_0 = 2 \times 10^{-4} N_0 \tag{7.1}$$

[1]We use cross measured sections [166, 167] with actual data obtained from the Durham Data Base [168]

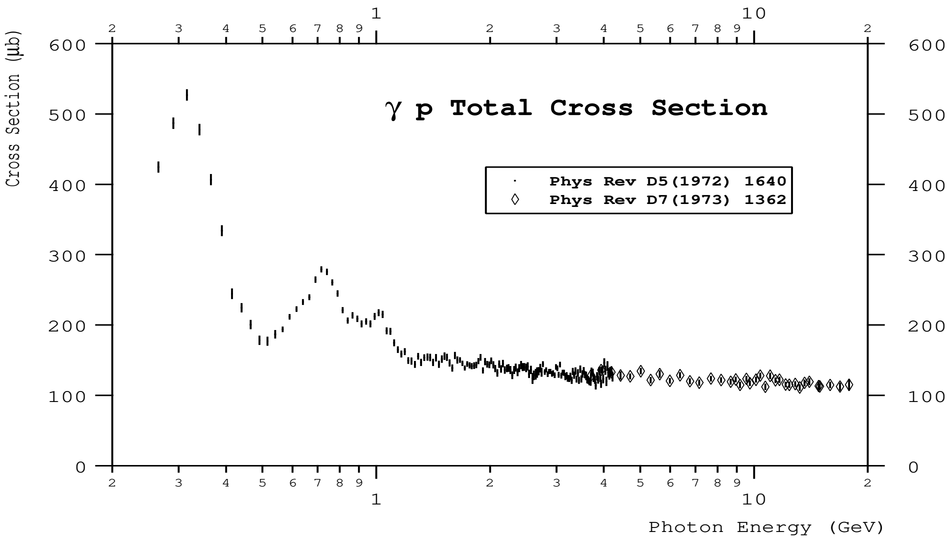

Figure 7.1: Total cross section for $\gamma p \rightarrow hadrons$ as a function of photon energy.

and a tagged hadronic rate

$$R_T = 7.4 \times 10^{-6} N_0 \tag{7.2}$$

For low intensity, the expected total hadronic rate is 37 kHz and the tagged hadronic rate is 1.4 kHz.

7.1.2 Trigger elements

We make some rudimentary assumptions about the trigger elements in order to estimate various rates. These assumptions are discussed further in the Trigger section of this document. Initial commissioning of the detector at low rates will use a level 1 trigger to select events of interest. At higher rates a sophisticated level 2 software trigger is required. We concentrate here on discussion of rates at lower photon beam fluxes.

The trigger consists of coincidences between several counter elements of the detector, and it must select the tagged hadronic rate in the presence of accidentally coincident backgrounds. The first trigger element is the **photon tagger**, essentially a segmented scintillation counter. The rate in this counter is determined by N_0, which is controllable (within limits) by the experiment.

The second trigger element is the **start counter**. A start counter similar in design to that used in CLAS would suffice for low intensity running, although modifications will likely be needed to handle high intensity conditions. One possible design might use several layers of scintillating fibers. Such a counter would also provide position information with sufficient resolution for track reconstruction. In comparing the demands of the HALL D start counter to the CLAS experience, it is useful to note that the HALL D target is inside a solenoidal magnetic field which will protect the start counter from the flux of low-energy Compton scattered electrons emerging from the target. The CLAS start counter does not enjoy this protection.

The tagger and start counters are small, and are therefore the best candidates for determining the precise event timing. For this discussion, we will assume that coincidences between them can be identified within a time window $\Delta T_1 = 15\,ns$.

Interesting events will have particles in the final state other than the one that satisfied the start counter requirement. These particles may be energetic, forward-going charged particles, forward or large angle photons, and/or charged particles with sufficient transverse momentum to reach the bore of the solenoid. Any particles of this type will be registered in other elements of the detector and these signals can be used as further requirements in the trigger. This refines the loose interaction definition given above. We refer to this collection of signals as the global level one trigger. As its elements are counters of extended size, we take a coincidence time window $\Delta T_2 = 100\,ns$ when the global level one trigger is required.

7.1.3 Accidental rates

The rate of interesting events given by Eq. 7.2 is $1.4\,kHz$ ($N_0 = 1.9\times\ 10^8$/s) and $14\,kHz$ ($N_0 = 1.9\times\ 10^9$/s) for low and high intensity beams respectively. However, various other processes will form accidental coincidences at the different trigger stages, and we need to recognize these. It is most important that these do not form the bottleneck for the data acquisition system, regardless of our ability to reject them offline.

We consider two sources of accidental background. They are not entirely mutually exclusive, but we consider them separately for ease of explanation. The first (A_1) of these comes from purely random time coincidences between the trigger elements, in which case we compute the time overlap based on the various counter singles rates. The second (A_2) is more "physical", considering hadronic photoproduction that is outside the tagging range, but in accidental coincidence with the tagging system.

First consider purely random coincidence events. A coincidence between the tagger and start counter loosely defines an interaction in the target. The rate A_0 of this coincidence is given by

$$A_0 = S R_{tag} \Delta T_1 \tag{7.3}$$

where S is the total rate in the start counter. Based on the experience in CLAS, we take $S = 0.03 N_0$, scaled using appropriate factors for collimation and beam intensity. This is most certainly an upper limit because of the solenoidal shielding effect. For $R_{tag} = 2.7 \times 10^7$/s we find $A_0 = 2.3 \times 10^6$/s, considerably larger than the tagged hadronic rate $R_T = 1400$/s. Further refinements are achieved by the global level one trigger.

The rate of the global level one trigger, $f_{L1} \times R_0$, is taken to be the total hadronic rate[2] reduced by the rate for single pion production for $E_\gamma\ \leq 0.5\ GeV$ ($f_{L1} = 0.5$). A loose trigger which uses a charged particle track count in the start counter and requires neutral energy in the barrel and/or forward calorimeter (see Section 7.2.2 below) should easily be able to eliminate these low energy events. The accidental rate using both the interaction and global level one triggers is

$$A_1 \;=\; A_0 f_{L1} R_0 \Delta T_2 = S f_{L1} (0.28 \times 10^{-4}) N_0^2 \Delta T_1 \Delta T_2 \tag{7.4}$$

[2]The cosmic-ray rate is small and has been neglected.

where we have substituted from Eqs. 7.1 and 7.3 and used $R_{tag} = 0.14 \times N_0$. The second accidental background comes from true hadronic events, and therefore would pass the global level one trigger. They are out of time with the precise RF signal, but that is much smaller than the online resolving time ΔT_1 of the interaction coincidence. Ignoring the "true" events that are part of this rate, one calculates

$$A_2 = f_{L1} R_0 R_{tag} \Delta T_1 = f_{L1}(0.28 \times 10^{-4}) N_0^2 \Delta T_1 \tag{7.5}$$

In order to evaluate the total accidental contribution numerically, correlations must be taken into account, which reduces the sum of the above estimates. For $N_0 = 1.9\times\ 10^8$/s, the accidental contribution to the trigger is $7.3\,kHz$, and the tagged hadronic rate is $R_T = 1.4\,kHz$. We note that as the photon flux increases, the start counter and tagger lose their effectiveness in reducing trigger rates, so the trigger rate asymptotically becomes proportional to the hadronic rate. At higher currents, a DAQ system with a software level 2 trigger is required. A summary of the rates is shown in Fig. 7.2 as a function of electron beam current.

7.2 HALL D Trigger

7.2.1 Overview

Figure 7.3 shows a schematic of the implementation of the HALL D trigger. An essential feature of the HALL D design is to build pipelining into the entire trigger, digitizer, and data acquisition systems at the outset. This has the virtue of allowing us to upgrade from initial photon fluxes of 10^7 photons/sec to eventual fluxes of 10^8 photons/sec.

A pipeline is basically a delay for which the timing resolution at the output is the same as the timing resolution at the input. An example is a clocked shift register. For each clock cycle, the data advance one step; the timing resolution is the same as the clock period, while the overall delay is the clock period times the number of stages.

Detectors which measure charge (calorimeters, dE/dX) are digitized by 8 bit, 250 *MHz* flash ADCs (FADC). Multiple channels are added together to form an energy sum. These adders are pipelined at the same 250 *MHz* rate, giving an energy measurement every 4 *ns* for use in the *Level 1 Trigger*. The energy sum then passes through a shift register thus making available a time window. Successive samples within this time window are added together. This is analogous to the gate width in a conventional charge sensitive ADC.

The level 1 trigger makes a decision based on detector elements which measure hadronic multiplicities (track counts) and energies. In the schematic shown, the start counter and barrel and forward TOF detectors provide the track count while the barrel and forward calorimeters determine the energy. A tight tagger OR/start counter coincidence also is used as input to the level 1 trigger for low photon fluxes of $\approx 10^7$ photons/sec.

For high photon fluxes ($\approx 10^8$ photons/sec), the tagger OR/start counter coincidence is not a useful requirement. It will be necessary to impose a software level 2 trigger which uses input from all detectors.

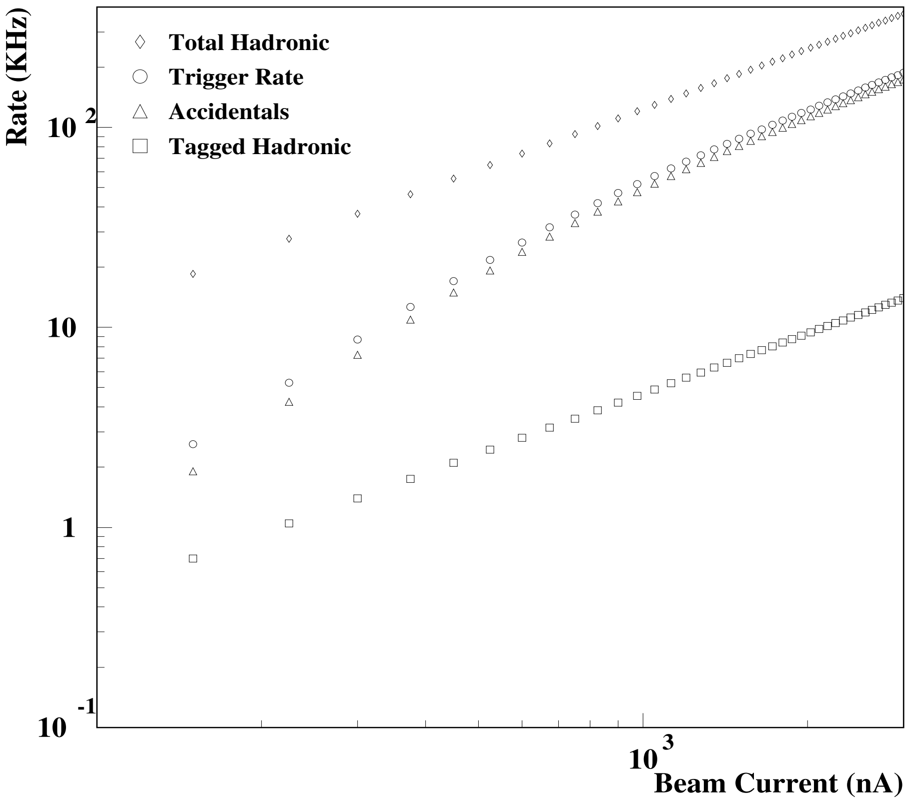

Figure 7.2: Estimated rates as a function of electron beam current. Plotted is the total hadronic rate, and the estimated trigger rate which is the sum of accidental coincidences and the tagged hadronic signal.

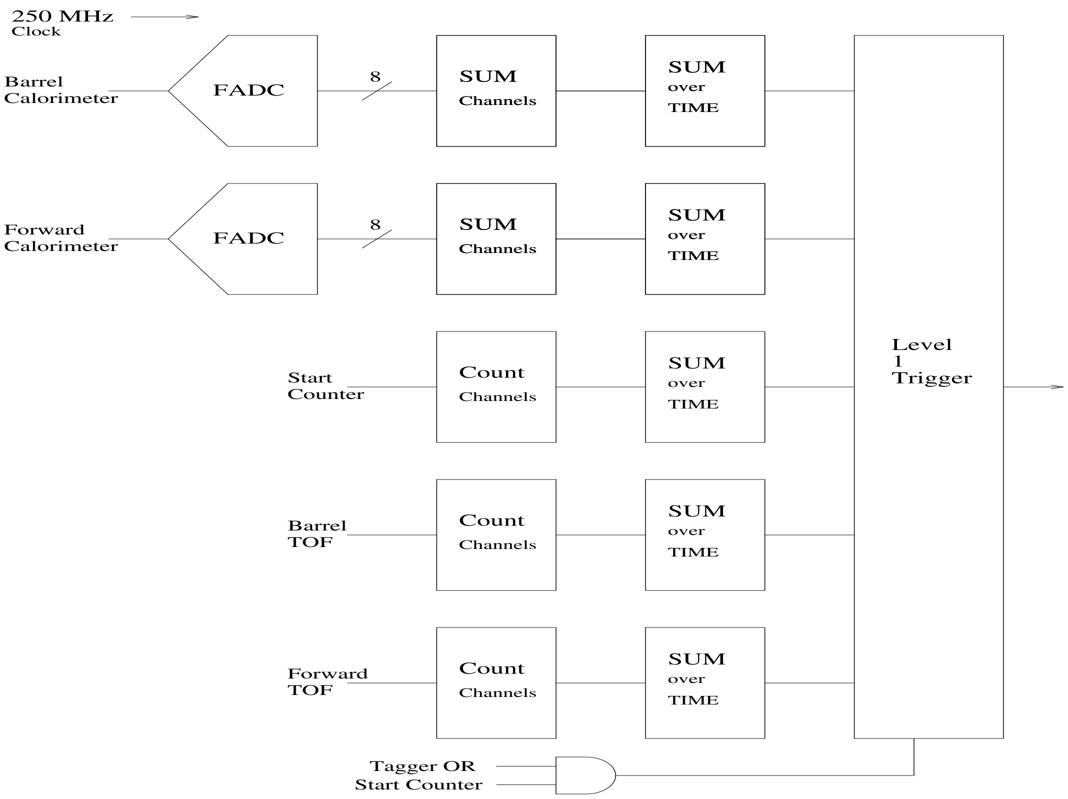

Figure 7.3: A schematic diagram of the HALL D trigger.

7.2.2 Level 1 Trigger

The level 1 trigger has the following 5 components:

1. **A track count** - obtained from the start counter. The start counter discriminator signals are used to create the prompt OR for coincidence with the tagger, but are also sent into a *track count pipeline* to determine the number of tracks. The sample rate for the pipeline would be $4\,ns$ ($250\,MHz$).

2. **A track count** - obtained from the barrel TOF. The discriminator signals from the central TOF are sent into another *track count pipeline* which determines the number of tracks. This pipeline runs synchronously with the start counter track count pipeline.

3. **An energy sum** - obtained from the barrel calorimeter. Continuous (in the same manner as in the CLAS detector) energy sums are computed for sections within the calorimeter. These sections will be complete azimuthal slices so that each sum will correspond to a fixed range in scattering angle. These sums are then sampled at the same $250\,MHz$ rate by a flash ADC, and selectively added together to form a global digital energy sum. The inclusion of the interesting regions of the calorimeter in the energy sum will be programmable. These energy sums may also be used in the level 2 trigger.

4. **A track count** - obtained from the forward TOF. Discriminator signals from the forward TOF are sent into a *track count pipeline* which determines the number of tracks. This pipeline runs synchronously with all the other level 1 pipelines.

5. **An energy sum** - obtained from the forward calorimeter. The sum is programmable in the same manner as for the central calorimeter. The precise definition of the regions to be included in the sum can be defined at a later stage. These also will be used in the level 2 trigger.

The level 1 Trigger runs at the same $250\,MHz$ rate, and has inputs from the 5 subsystems named above. Programming a single trigger means selection of

1. Either a minimum, maximum, or exact number of tracks in the start counter

2. A minimum, maximum, or exact number of tracks in the central TOF.

3. A minimum, maximum, or exact number of tracks in the forward TOF.

4. A minimum or maximum for the global energy in the barrel calorimeter. The global energy is obtained by programmed selection to include (or eliminate) interesting regions of the calorimeter.

5. A minimum or maximum for the global energy in the forward calorimeter. As above, certain areas might be programmed out of the sum.

Finally the boolean function of these five elements is programmed. The trigger would have the capability to have several simultaneously defined triggers. This trigger is very flexible and can be programmed to be very loose (say one track in the start counter) or very tight (specific track counts and energy thresholds in each detector). Examples of triggers which can be programmed in this scheme include:

1. at least two tracks in the start counter AND at least one track in the downstream TOF.
2. at least one track in the start counter AND a minimum energy in the downstream calorimeter.
3. at least two tracks in the start counter AND at least one track in the central TOF AND a minimum requirement of energy in the central calorimeter AND a minimum requirement in the downstream calorimeter.

All pipelines will run synchronously and will be timed so that the inputs from average momentum tracks ($\sim$ Ebeam/3) will hit the level 1 global processor at the same time. Higher and lower momentum tracks will be slightly out of time, but this effect should be less than 20 ns. The synchronous output of the level 1 trigger will then be ANDed with the coincidence of the tagger OR and the start counter OR. This allows the timing to be determined by the tagger and start counter, and removes the synchronous nature of the trigger.

The rate of the global level 1 trigger, $f_{L1} \times R_0$, is taken to be the total hadronic rate[3] reduced by the rate for single pion production for $E_\gamma \leq 0.5\ GeV$ ($f_{L1} = 0.5$). A loose trigger which uses a charged particle track count in the start counter and requires neutral energy in the barrel and/or forward calorimeter should easily be able to eliminate these low energy events. The resultant level 1 trigger rate is about 180 kHz. We note, however, that 80% of the hadronic rate comes from photons with energies below 2 GeV. This energy cut, which would require a more sophisticated trigger, would reduce the level 1 rate to 70 kHz.

7.3 Data Acquisition

7.3.1 Overview

The data acquisition goal for HALL D is to accept the level 1 trigger rate without incurring any DAQ system dead-time. The high rate of 70-180 kHz drives the design of the trigger, the front-end electronics, and the DAQ system. When the level 1 trigger is asserted, a time slice of each ring buffer will be copied, compressed and stored. Events will be buffered into groups of at least 10 on each electronics board and then transferred first across a backplane to be built into crate events fragments and then to a computer farm to be built into complete events. The farm will perform a quick analysis to reduce the event rate by approximately a factor of ten before recording to magnetic media. This design allows HALL D to start running with a modest tagged photon rate and then to scale-up by an order of magnitude.

[3] The cosmic-ray rate is small and has been neglected.

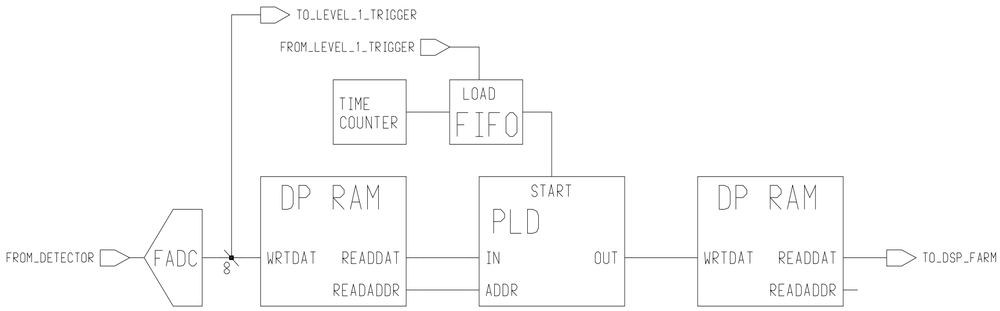

Figure 7.4: Block diagram of FADC board.

The DAQ system will be an important part of the whole HALL D data analysis system. The rates and complexity of the DAQ system for HALL D are challenging, nevertheless we will provide a flexible system that will allow different modes of read-out:

- production physics events,
- full FADC and TDC time window events, and
- several microseconds streams of raw FADC and TDC data for the whole detector.

Additionally, since demand for access to a DAQ system during accelerator down-time is very high, we propose that the system should allow independent trigger, control and read-out of sub-systems so that effective use of this time can be made. Each of the components of the data acquisition system will be discussed below.

7.3.2 Data flow

Two basic types of digitizing electronics will be used in HALL D. Channels which measure energy will be continuously sampled with flash ADCs. These boards would be designed by our collaboration. The data volume would require one or more on board processors to analyze and reduce the data stream. A conceptual design of these boards is shown in Fig. 7.4.

Channels which require precise time measurements will use a multi-hit TDC. We are evaluating a few sources of such boards. One company, "Acam Messelectonic Gmbh"[4]", has a prototype board based on the "F1" ASIC developed for the COMPASS experiment at CERN. This design can provide up to 60 ps resolution and is designed for high rate, low dead-time experiments.

Both the FADC and the TDC digitizing modules must store data for several microseconds so that the level 1 trigger can be processed. When the level 1 trigger is satisfied these devices must be read-out without dead-time. This will be achieved for the FADCs with a dual-port RAM running at the full FADC speed and for the multi-hit TDCs a multiple level buffering scheme is implemented. For the FADC, the level 1 trigger signal will cause a local programmable logic device (PLD) to copy a fixed delay, and fixed sized time window to an

[4]see www.acam.de for details on the "F1"

output queue. The TDCs can store hits for several microseconds and are equipped with a filter so that only times from a region of interest are read-out.

In HALL D there are approximately 20000 FADC and 7000 TDC channels. Each FADC produces a raw data stream of 250 MB/sec and the TDCs produce 32 bytes per level 1 trigger. If we assume a typical occupancy of 2%, a FADC time window of 100 nanoseconds, and that the full FADC time window is read-out, then the total FADC data rate would be 1 GB/second (20000 channels * 0.02 % occupancy * 25 bytes/channel * 100,000 events/second = 1 GB/sec) The 25 bytes/FADC channel is used to get an energy and a time signal. Previous work [169] indicates that one-fifth of a channel time resolution can be achieved by fitting the FADC waveform. Reduction of this data will be performed in real-time by digital signal processors. The result will be an energy, a time and perhaps 4-6 bytes leading edge digital trace. This would allow us to reduce the amount of data per hit to 10 bytes per FADC channel thereby lowering the total data rate to 400 MB/second. The computational resources required to achieve this reduced data rate are currently being studied. The data rate for the TDCs would be 448 MB/second. (7000 channels * 0.02 % occupancy * 32 bytes/channel * 100,000 events/second = 448 MB/sec)

Once the event fragments have been selected from a stream in each channel and reduced, they must be built into compete events and pass a filter that will reject accidentals and low energy events. Board level event fragments will be read out over a VME backplane and crate level event fragments will then be assembled and sent to the level 2 trigger farm. One important detail of the DAQ design is that the boards would have to buffer 10 (or more) events locally before transferring this group of event fragments to the crate computer. This is necessary because the tasks that the crate computer is required to do can't be done today at a 100 *kHz* interrupt rate with a commercial real-time operating system. At 10 events per buffer, we will have to transfer about 3.67 KB in less than 100 microseconds. This transfer speed (36.7 MB/sec) is achievable with current VME technology. Depending on the CPU power available, the crate CPU may reorganize the crate event fragments so all data from one event is contiguous.

Using current technology this data transfer rate could be handled using either gigabit ethernet or ATM OC-12 network links. Regardless of the network hardware, significant CPU resources will be require at the crate level to transmit the data. A fast switch with a backplane bandwidth greater than 672 MB/second and more than 40 ports will also be required. This switch technology is under development by many networking companies[5] and in a few years it should be common and less expensive.

The architecture of the CPU farm which preforms event building, filtering and recording is presented below. Event building and recording will be done in parallel on 10-20 computers. Each of these systems would send events to a sub-farm for filtering. The sub-farm nodes would send a pass/fail answer for each event received and the master node would record all events that passed the filter. It is possible that further information could be added to the event or that the events selected by the filter could even be reformatted before being sent to the recording computer(s).

[5]One product from Cisco is described at http://www.cisco.com/warp/public/146/1971.html

7.3.3 Level 2 Trigger

The goal of the level 2 trigger is to reduce the event rate given by the level 1 trigger to an acceptable on tape rate. In low intensity running (10^7 tagged photons/s) the level 1 trigger rate is expected to be $15\,kHz$. Since the DAQ system is being designed to handle this rate to tape, the level 2 trigger farm will not have to cut any events, although it may be used to reduce the event rate somewhat. In high intensity mode where the level 1 rate is approximately 100 kHz, the level 2 trigger must be able to reduce the event rate by a factor of ten.

Most of these unwanted events result from an untagged (mostly lower energy) photon interacting in coincidence with a tagged photon. Rejecting these events means that level 2 must be able to calculate, with reasonable accuracy, the energy of the photon which produced the event. This involves accurately reconstructing tracks, matching them with the calorimeters, and adding additional energy deposited by neutral particles in the calorimeters.

Because of the accuracy requirements and the demands of linking information from different detectors, we have decided to use a processor farm architecture for level 2 instead of building a dedicated hardware processor. All events passing the level 1 trigger will be read into the level 2 processor farm where they will be reconstructed; events passing the cuts applied will then be written to tape. This approach allows for algorithmic flexibility and improvements, and the ability to cost-effectively adjust to higher rates, but it does put pressure on the DAQ system.

An estimate of the processing power required can be made as follows. The Hall-B full event analysis, with momentum resolution of less than 1%, requires approximately 10 million instructions. We believe that HALL D events will be similar and require a similar amount of processing power. To do level 2 triggering we think that 1/10 the number of instructions will be adequate because unlike the 1% precision required in a full reconstruction, we are aiming for only 2-5% precision. In fact Hall-B has such a pattern recognition program in development; it is able to achieve 10% momentum resolution using only 300,000 instructions per event. Therefore, we believe that 1 million instructions per event is a good estimate of the processing power required. This means an aggregate processing power of 100,000 MIPS is required for the level 2 analysis. Allowing for 50% processor utilization (due to I/O overhead etc.) this means that a farm composed of 200 computers each capable of 1000 MIPS could handle the I/O and perform the level 2 analysis for the high intensity configuration.

Table 7.1 shows the rates, sizes, and processing requirements for the level 2 trigger.

7.3.4 Monitoring and control

Monitoring and control tasks include hardware configuration and control ("slow controls"), bookkeeping, online event monitoring, alarm systems,and messaging systems. These are less demanding tasks than data acquisition in HALL D, and should not present unusual challenges. We plan to follow some examples from Hall B, but to also make use of lessons learned there. In particular, we plan to integrate off-line data analysis tools with the online software at the outset to reduce the total cost of software development.

The number of events that can be processed online is largely determined by the number of processors available. In HALL D a monitoring component can be added to the main event

	Low Rate	High Rate
Event Size	5 KB	5 KB
Event Rate to Farm	10 kHz	100 kHz
Data Rate to Farm	50 Mbytes/s	500 Mbytes/s
Num Links to Farm	20	20
Data Rate per Link	2.5 Mbytes/s	25Mbytes/s
Link Technology	100 Megabit Ethernet	Gigabit Ethernet
Events/s per Link	500	5000
Num Inst/event for L2	1,000,000	1,000,000
Processing power/link	500 MIPS	5000 MIPS
Num 1000 MIPS processors/link	1	10
Total Num 1000 MIPS processors	20	200

Table 7.1: Rates, sizes, and processing requirements for the level 2 trigger.

filtering code to gather statistics about both the event that are being written to tape and those being discarded by the level 2 farm. The choice of the type and number of processors can wait until soon before the system is installed, when prices are lower and performance is better known.

The framework for slow controls should be uniform for all sub-systems in HALL D, but the choice is not obvious. VME-based EPICS works in Hall B, but does not mesh well with the online requirements and has proven to be manpower intensive. In fact, a number of Hall B systems do not use EPICS or VME, but instead resort to CAMAC or other options. Other software possibilities include message-based systems and hardware alternatives include PC or mixed hardware systems. We believe that an open, message-based system that implements a uniform interface to diverse hardware is probably best. Commercial products are currently available that implement this at moderate cost.

Bookkeeping tasks include all recordable activities of the experiment other than raw and calibration data. We expect this will be done using relational and/or object-oriented databases. Current commercial and public domain database technology should be adequate.

The alarm and messaging framework allows sub-systems to communicate their state to monitoring programs and operators. This system needs to be integrated across the entire online, DAQ, and database systems in a simple, uniform manner. The scale and performance requirements of this system are modest, and similar to other projects in progress or completed at Jefferson lab.

Chapter 8

Data handling plan

8.1 Overview

The overall strategy for handling the large volume of data produced by the HALL D detector is straightforward and similar to other large fixed target experiments. The amount of data generated by HALL D, essentially $15\,kHz$, is ambitious by todays standards but should be achievable at a reasonable cost in the near future. Current technology is exemplified by the CLAS detector at Jefferson lab, which can handle a sustained rate to tape of up to $2\,kHz$. The CLAS will be used in this chapter as a template for scaling up to the HALL D design rate of $15\,kHz$.

The movement of data from the DAQ to the computing center for HALL D will be identical to CLAS. On-line data is staged to disk in the counting house and moved to the computing center where it is written directly to tape. The off-line analysis will place a heavy reliance on automated tape silos to access the data for both track reconstruction and higher level analysis.

HALL D Software must be developed not only to orchestrate the movement of data but provide an integrated reconstruction and analysis environment. A design feature of this environment must include the ability to perform the same analysis of the data in the on-line and off-line environments, to allow for extensive data quality monitoring. This requires a common set of software tools to be used throughout the on-line and off-line software. From an organizational point of view this implies an integrated on-line and off-line software environment.

8.2 Hardware requirements

The off-line computing resource needs of an experiment can be broken down into three components, CPU, bandwidth, and data storage requirements for off-line data analysis. At Jefferson lab the CLAS detector places the greatest strain on computing resources and provides a good starting point for needs for a fixed target experiment capable of generating 10MB/sec using current technology. An extrapolation of existing technological trends for each of these core technologies will be done to estimate the scale of the HALL D computing effort.

Jefferson Lab routinely handles CLAS data rates of up to 10MB of data per second written to tape. To handle this flow of data, Jefferson Lab provides a dedicated fiber optic link between the experimental hall and the computing center capable of sustaining 25 MB/sec, with speeds of 100MB/sec anticipated by the end of the year. This implies that existing technology is already in place to handle the expected HALL D event rate. It is anticipated that networking speed will continue to improve over the next five years. Data transfer rates of 4 giga bit/sec are anticipated over existing fiber optic cable which would be provide ample bandwidth to handle the 75-150MB rates produced in the HALL D detector.

Data transfered by fiber to the computing center is written directly to tape. Two Redwood tape drives capable of writing 10 MB of data per second are located in the computing center to transcribe the CLAS data to tape. Next generation tape drives are anticipated to be capable writing data at 60 MB/sec, which is close to the estimated HALL D DAQ rate. Assuming a HALL D bandwidth of between 75-150 MB/sec it seems reasonable to assume 3-4 next generation tape drives should be able to accommodate the HALL D rate.

At a DAQ to tape rate of 100MB/sec one would expect to accumulate one to two thousand terabytes of data per year for the HALL D project. In addition, sufficient tape storage space will be needed to write processed data to the tape silo. It is estimated that the size of the processed data will be twice that of the raw data. Therefore the total tape storage requirement for HALL D are estimated to be three to six thousand terabytes.

Current tape storage technology allows for 50 GB of information to be stored per hundred dollar tape. Estimates for information density of tape storage media in the near future vary considerably, with values ranging from 200-600 GB per hundred dollar tape. Because tape storage technology may not progress as quickly as other technologies, one might expect as much as a factor of 2-3 more tapes per year will be required than are currently needed for the CLAS detector. With the increased data volume from the HALL D detector it is unclear where to physically locate a factor of two or three increase over existing computing resources, as the current space in the computing center in insufficient to house the additional capacity.

Events produced by the HALL D detector will be of comparable size and complexity (5KB/event, +30K channels) to the CLAS detector currently running at Jefferson Lab. The analysis of off-line data in CLAS is supported by a Pentium II based Linux farm with high bandwidth access to the redwood tape drives coupled to the tape silo. With the current CLAS reconstruction rate of 10-20 events/sec a 100 node Linux based computer farm is capable of keeping up with the DAQ rate. Estimating HALL D future computing needs is relatively straightforward. This can be done by using Moore's law, which estimates a doubling of computing power every 18 months for the same unit cost. Assuming this rapid progression in CPU technology we can anticipate that by 2005 computers will be 16 times as powerful as they are in 1999. Since the amount of data anticipated for HALL D is only an order of magnitude higher than CLAS, it is anticipated that computing requirements will not be a significant obstacle in data analysis for HALL D. This suggests that a computing farm of 200 PCs in 2005 should be more than sufficient to keep up with the data processing requirements for HALL D even if reconstruction speeds are a factor of two slower than in the CLAS.

Disk resource requirements for the analysis of off-line data are expected to be equivalent to 1-2% of the entire data set. For HALL D this translates into 30-60 TB of disk storage. With the current rapid progression of disk storage technology, analogous to advances in CPU power, it is not anticipated that disk resource costs in the future will be significantly greater than those currently for the CLAS detector.

With all these uncertainties in mind it is difficult to come up with an exact cost estimate for the data analysis in the year 2005. However it is anticipated that the costs will be on roughly the same scale as the computing infrastructure required for the CLAS detector.

Finally, it should be noted that the amount of data produced by the HALL D project is equivalent to what is anticipated in the next few years to be taken by RHIC, CERN and FNAL experiments. In addition, the LHC is expected to have a start date at the same time as HALL D and it anticipates rates to tape an order of magnitude larger than those expected for HALL D. These observations suggest that the technology needed for HALL D offline analysis will be in place well before 2005.

8.3 Software development

An often overlooked aspect of the design of an experiment is the software used in the reconstruction analysis and monitoring. Considerable human resources are expended in the development and maintenance of software, and as computing hardware costs decrease while their power increases a larger and larger portion of computing costs are associated with the development and maintenance of software. The HALL D collaboration recognizes that a well organized and coherent software infrastructure is essential to the success of the project.

Software cost estimates scale by the lines of code (loc) associated with a given project. For example the CLAS on-line and off-line software system consist of approximately 500K lines of code written mostly in FORTRAN and C. While productivity of individual programmers varies greatly, effective programmers can typically only produce 10-20K lines of useful code per year. Given these facts, it is clear that a strategy should be in place to reduce the amount of effort needed to develop and maintain the software.

The HALL D software strategy has several elements, first, HALL D will aggressively use modern languages and tools designed to minimize the number of loc and reduce maintenance costs. Coupled with this will be an integrated approach to software design, by treating all of the HALL D software as elements of a complete system. By treating the entire software (on-line, off-line, slow controls) as a complete system it allows one to used common libraries, programs, databases throughout the entire experiment. This approach reduces the number of redundant systems and allows one to use tools developed to solve one problem to solve novel problems in a different context. For example, in BNL experiment 852, no distinction was made in the software between the on-line and off-line processing of data. This allowed software tools developed to monitor the off-line data to be used to monitor data quality in the on-line and vice versa. Finally, existing software will be used when appropriate. For example, the modern, object oriented partial wave analysis code that has been developed for the analysis of CLAS data will be used in HALL D.

With this strategy in mind it seems clear that the HALL D experiment will require a core group of experienced programmers to write and organize the software effort. Previous experience with other collaborations and other software projects suggests that a group of 3 or 4 physicist/programmers familiar with modern programming techniques and tools be hired to work on the HALL D software. These individuals should be allowed three to four years to develop the system in advance of taking data.

8.4 Conclusions

HALL D computing requirements will be an order of magnitude greater than those for the CLAS, however, anticipated improvements in CPU power, bandwidth, and data storage make the data handling needs of the HALL D detector not unreasonable. Other approved experiments also anticipate handling equal to or larger data sets than HALL D without significant difficulty. Finally, modern software tools and techniques will be developed and encouraged by the HALL D collaboration to efficiently utilize limited human resources.

Chapter 9

Monte Carlo Simulations

9.1 Introduction

Prelminary Monte Carlo work has been done to study the expected resolution of the charged particle detectors proposed for HALL D. Since significant experience in calorimetry exists from BNL E852 and TJNAF RADPHI actual results from those experiments have been used for this report and Monte Carlo development in this area is not as complete. The emphesis in the work done to date is on creation of a useful and flexible system of programs that will allow design work to proceed quickly. Realistic models of detectors and materials are used so that expected resolutions can be estimated. An overview is presented below.

9.2 Monte Carlo framework

A Monte Carlo framework has been developed to understand the performance of key aspects of the HALL D detector systems. This framework is in general a collection of modules, each serving some particular function. These modules consist of individual programs and library routines which use common event I/O formats. Figure 9.1 illustrates this modular structure.

First, a Monte Carlo four-vector generator is used to create phase-space distributed events. Next is the detector simulation, *HDFast*, which is a fast and flexible simulation program based upon the MCFast framework developed by the simulation group at Fermilab. The Monte Carlo output includes (but is not limited to) the following data objects:

- generated event
- detector hits
- resolution modified (smeared) event
- time-of-flight information
- dE/dx information
- threshold Čerenkov information
- particle trajectory information

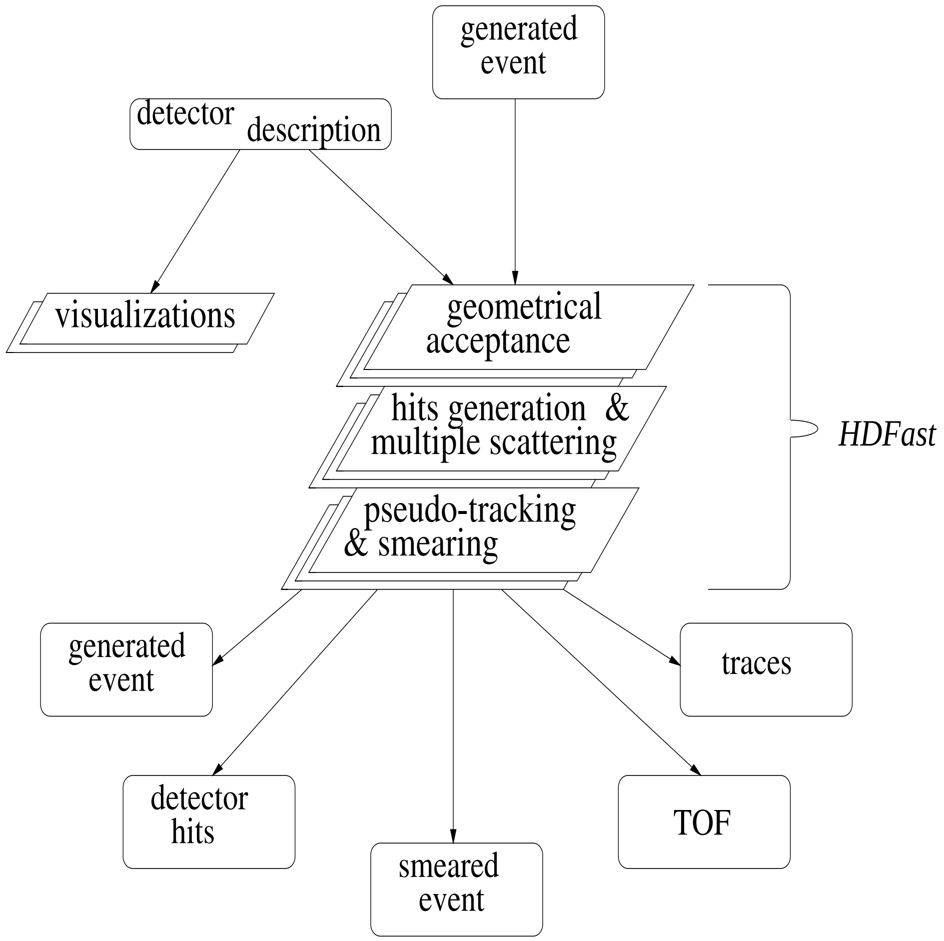

Figure 9.1: An illustration of the HALL D Monte Carlo modular pipelining

Monte Carlo events can be generated using the program *genr8*[170] or *cwrap*[171]. Both programs generate peripheral phase space Monte Carlo events where events can be produced which describe a complex decay chain of intermediate states. Both meson and baryon decay chains are allowed, but with a limiting assumption of a t-channel production process. The four-momentum transfer squared distribution follows that of

$$\frac{d\sigma}{dt} \propto e^{-b|t|}$$

where the user defines the t-channel slope or $d\sigma/dt$ can be specified by an input histogram.

HDFast is a fast and flexible simulation program based upon the MCFast framework developed by the simulation group at Fermilab[172]. MCFast consists of a set of modularized Monte Carlo library routines; it is designed to perform parameterized tracking by assembling a covariance matrix for each track that takes into account materials, efficiencies, and resolutions for all measurements planes, and use this matrix to smear the track parameters randomly. The covariance matrix is first diagonalized so as to properly account for effects due to correlations when parameters are smeared. In principle, the distribution of smeared tracks produced by this method would be similar to the distribution of real tracks that were measured by a real detector(with the same parameters) and analyzed with an idealized track fitting procedure[172].

HDFast is controlled via a set of user routines which act as an interface to the MCFast framework. They control the tracking and smearing of the four-vectors, in addition to the booking and filling of monitoring ntuples and histograms. The detector geometry is controlled by an ascii file which is read in during program execution. This allows the user to quickly create or modify the detector geometry without the need to recompile the executable. In addition, ROOT[173] was used to develop an event display which reads in the ascii geometry file and displays a two-dimensional visualization (see Figure 9.2 in next section) of the detector configuration and event track projections.

The motivation for using the MCFast framework is to facilitate the study of design changes and detector configurations. This does not exclude the use of a GEANT based simulation. MCFast provides routines for converting MCFast geometry to GEANT. Eventually, a GEANT4 based simulation will be incorporated into the HALL D Monte Carlo framework.

9.3 Acceptance studies

In order to better understand the effects of finite acceptance of a proposed detector configuration, a simple study of the acceptance as a function of total meson effective mass for various final states has been performed. In doing the Monte Carlo acceptance studies we considered the following reactions:

1. $\gamma p \to X^+ n$
   - $X^+ \to \pi^+\pi^+\pi^-$
2. $\gamma p \to X^+ n$
   - $X^+ \to \eta\pi^+\pi^+\pi^-$
     - $\eta \to \gamma\gamma$
3. $\gamma p \to X^+ n$
   - $X^+ \to \omega\pi^0\pi^+$

   - $\omega \to \pi^+\pi^-\pi^0$
   - $\pi^0 \to \gamma\gamma$

4. $\gamma p \to X^0 p$
   - $X^0 \to \pi^+\pi^-\pi^0$
     - $\pi^0 \to \gamma\gamma$

5. $\gamma p \to X^0 p$
   - $X^0 \to \eta\pi^0\pi^0$
     - $\eta \to \gamma\gamma$
     - $\pi^0 \to \gamma\gamma$

The acceptance studies were performed with a total effective meson masses ($Mass(X)$) of 1.4, 1.7, and 2.0 GeV/c^2. At each $Mass(X)$, events were distributed according to a Breit-Wigner of width $\Gamma = 0.250$ GeV/c^2. In generating the Monte Carlo events, the following assumptions were made:

- peripheral production where $\frac{d\sigma}{dt} \propto e^{-b|t|}$ and $b = 5.0$ $(GeV/c)^{-2}$;
- events distributed according to phase-space; and
- isotropic decay angles.

For each reaction, 30000 events (10000 for each $Mass(X)$) were generated for different photon beam energies of: 5, 6, 8, 10, and 12 GeV.

9.3.1 Detector geometry

The generated events were processed through *HDFast* with the assumed detector configuration displayed in Figure 9.2. This configuration is comprised of the following assumptions:

- 2.24 Tesla solenoid magnet –LASSmagnet,
- 5-layer Vertex Chamber (VTX),
- 22-layer Central Drift Chamber (CDC),
- 6 3-layer Forward Small Angle Chambers (BVT),
- 5 6-layer Forward Drift Chambers (FDC),
- Barrel Calorimeter which also acts as central TOF(BCAL),
- Cerenkov Detector,
- Forward time-of-flight (FTOF),
- Forward Lead Glass Detector (LGD) 172x172 cm with 8x8 cm beam hole,
- target-beam vertex distribution at $r = 0.0\,cm$, $z = 50\,cm$ with $\sigma_r = 0.3\,cm$, $\sigma_z = 15.0\,cm$ ($\hat{z}$ is along the magnet axis; the origin is located at the upstream face of the solenoid).

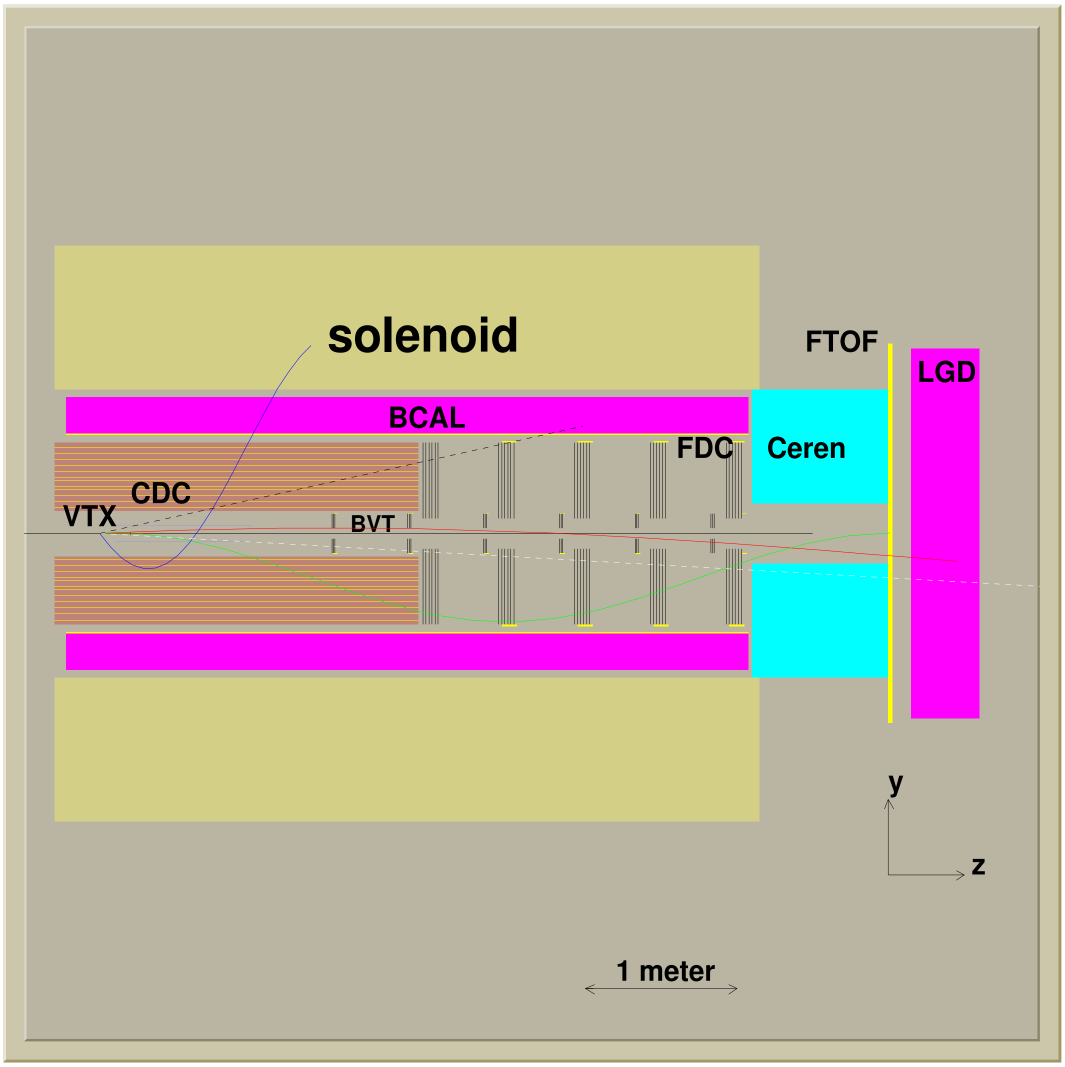

Figure 9.2: The HALL D Apparatus. The event shown contains both charged particles (line) and photons (dashed line).

9.3.2 Acceptance performance

In the simulation, an event was accepted if the following minimum conditions were met:

- all charged tracks were found with a minimum of four hits per track, and
- all gammas were detected in either the BCAL and/or LGD.

The acceptance as a function of total effective meson mass is shown in Figure 9.3. It is important to note that at higher beam energies the charged track momentum resolution degrades due to the forward increase of the track momentum, so even though the mass acceptance is seemingly good, the resolution of the tracks for this geometry at these higher energies is rather poor. See HALL D Note #7[174] for a more detailed discussion on tracking resolutions and the need to augment the detector with a forward tracker.

In Figure 9.4 through Figure 9.8, we show the acceptance for the Gottfried-Jackson decay angles. It is clear that the Gottfried-Jackson angular acceptance is quite good. The acceptnce for gammas is also quite well, but it suffers more from holes in the forward and backward regions. The hole in the backward region results from backward going gammas which is the dominant factor at lower beam energies. The forward hole, due to gammas hitting the beam hole in the LGD, becomes a factor (and effectively gets larger) for higher beam energies. Figure 9.9a displays a lost event for $\gamma p \to p\eta\pi^0\pi^0$ at $Mass(X) = 2.0\ GeV/c^2$ and beam of 5 GeV. For this channel 75% of the lost events were of this type. One the other hand, for a 12 GeV beam and the same final state about 50% of the lost events are due to the beam hole(See Figure 9.9b). While the beam hole is a necessity, the hole in the backward region suggests the need at the lower beam energies for a backward gamma veto. More importantly, the acceptance for the Gottfried-Jackson decay angles is flat and not strongly dependent on $Mass(X)$ or the beam energy. Even though the method of partial wave analysis can account for effects of finite detector acceptance, a small misunderstanding of the detector acceptance can be greatly amplified by the need for large acceptance corrections and thus produce false or misleading results. Work on acceptance studies for other more complicated final states and background channels, such as the affects of misidentified Δ's and $N^{\star}$'s, is in progress.

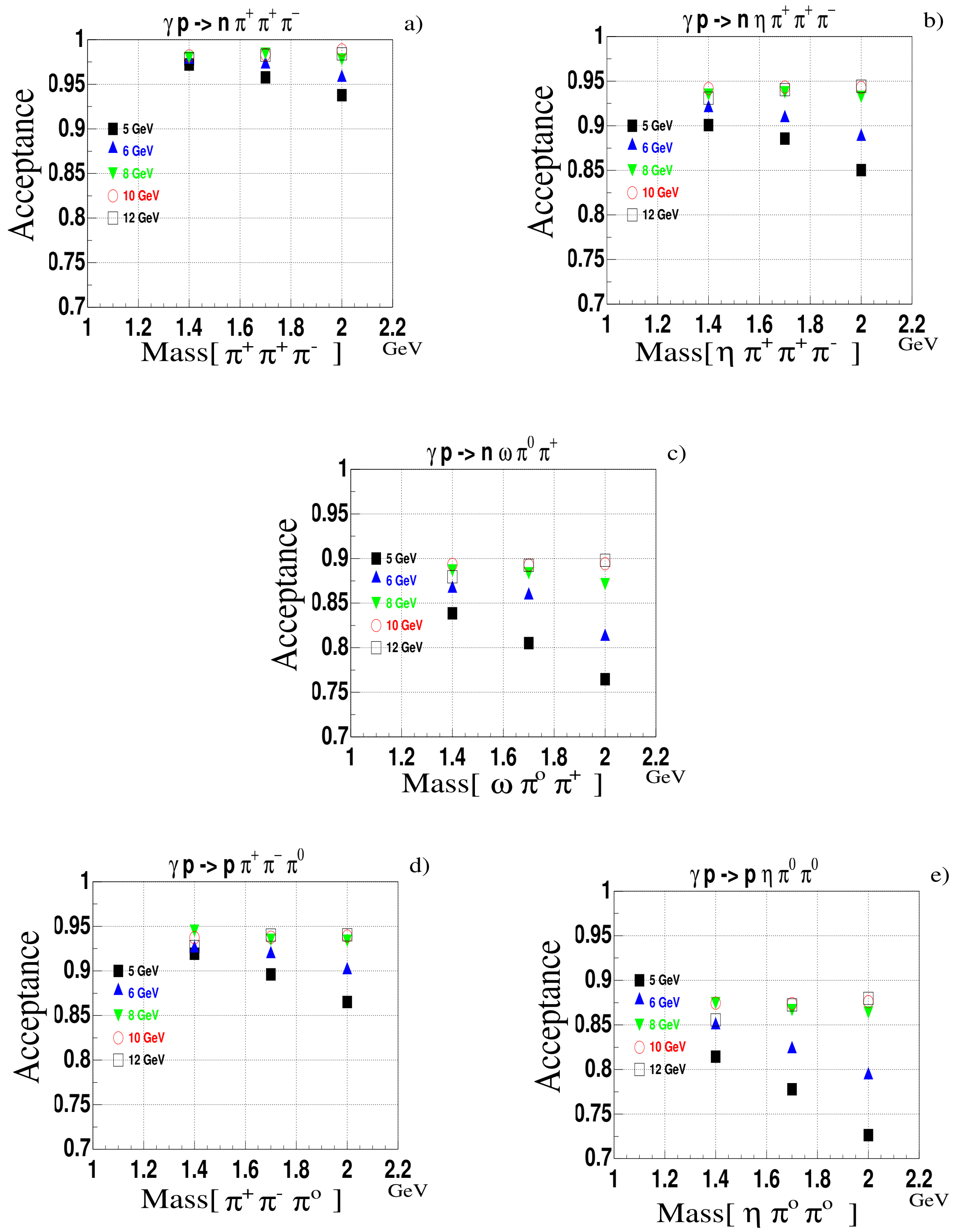

Figure 9.3: The acceptance as a function of total effective meson mass: a) $X^+ \to \pi^+\pi^+\pi^-$, b) $X^+ \to \eta\pi^+\pi^-\pi^+$, c) $X^+ \to \omega\pi^0\pi^+$, d) $X^0 \to \pi^+\pi^-\pi^0$, e) $X^0 \to \eta\pi^0\pi^0$.

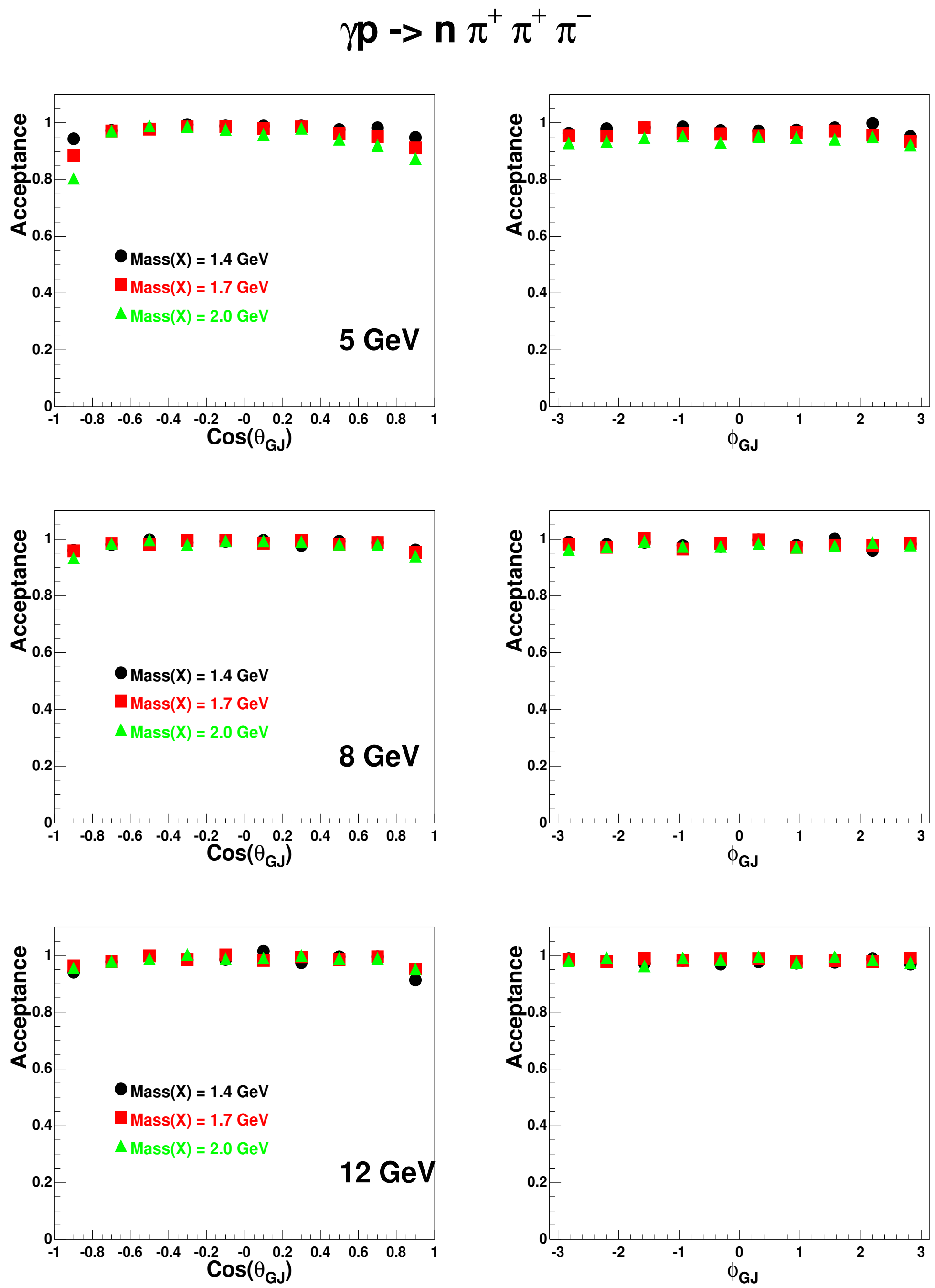

Figure 9.4: The acceptance in $cos(\theta_{GJ})$ and ϕ_{GJ} for $X^+ \to \pi^+\pi^+\pi^-$.

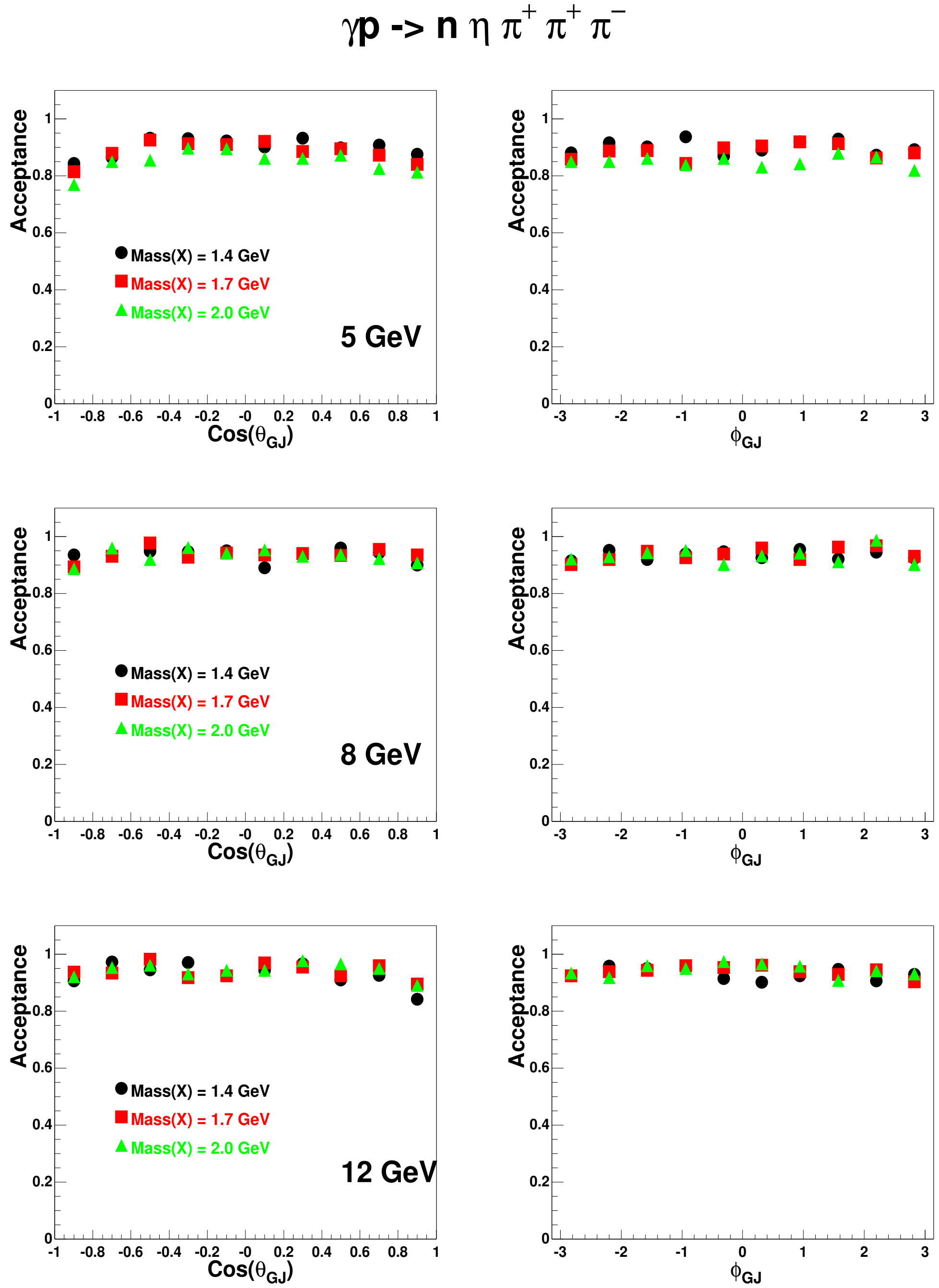

Figure 9.5: The acceptance in $cos(\theta_{GJ})$ and ϕ_{GJ} for $X^+ \to \eta\pi^+\pi^+\pi^-$.

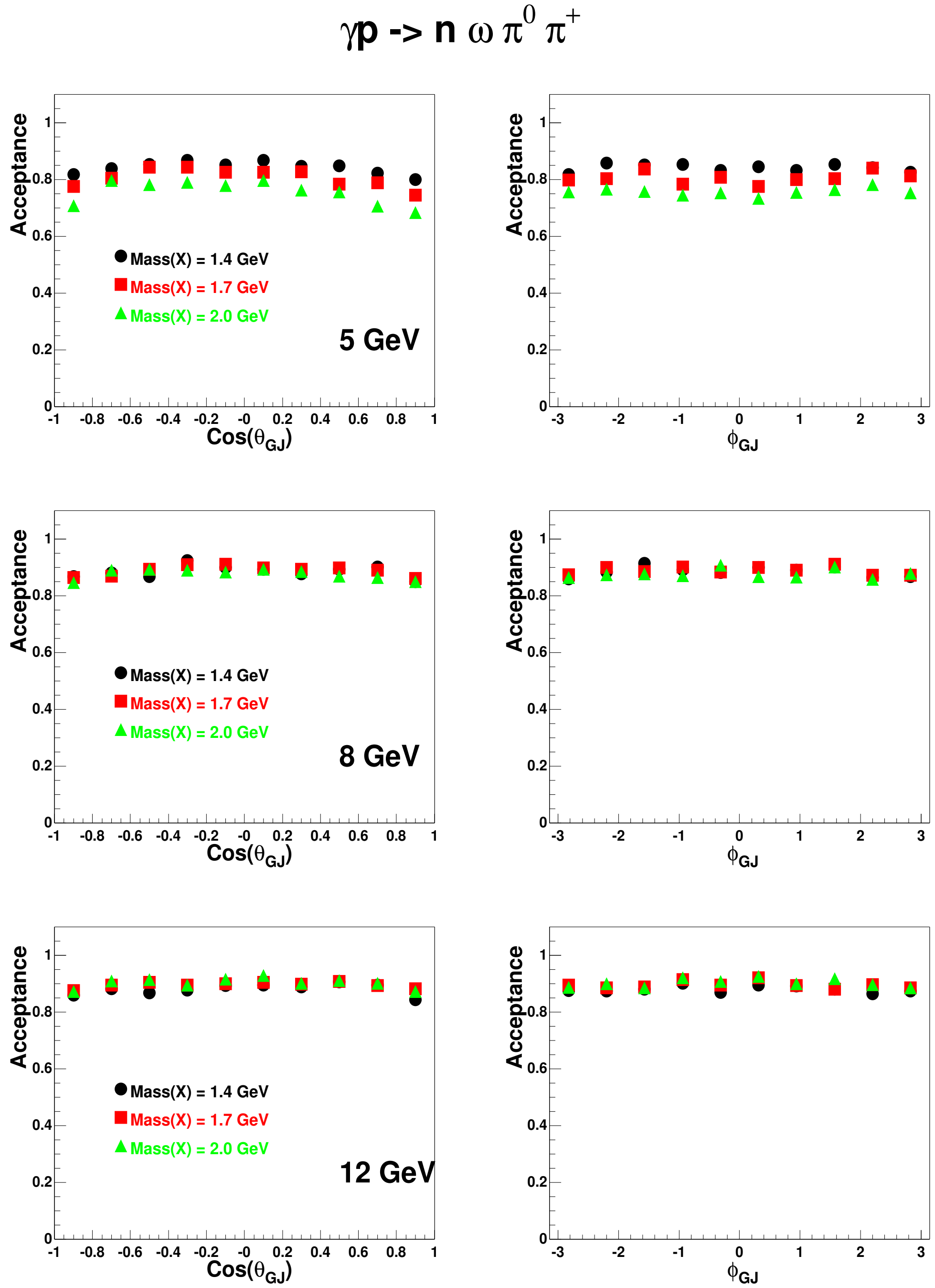

Figure 9.6: The acceptance in $cos(\theta_{GJ})$ and ϕ_{GJ} for $X^0 \to \omega\pi^0\pi^+$.

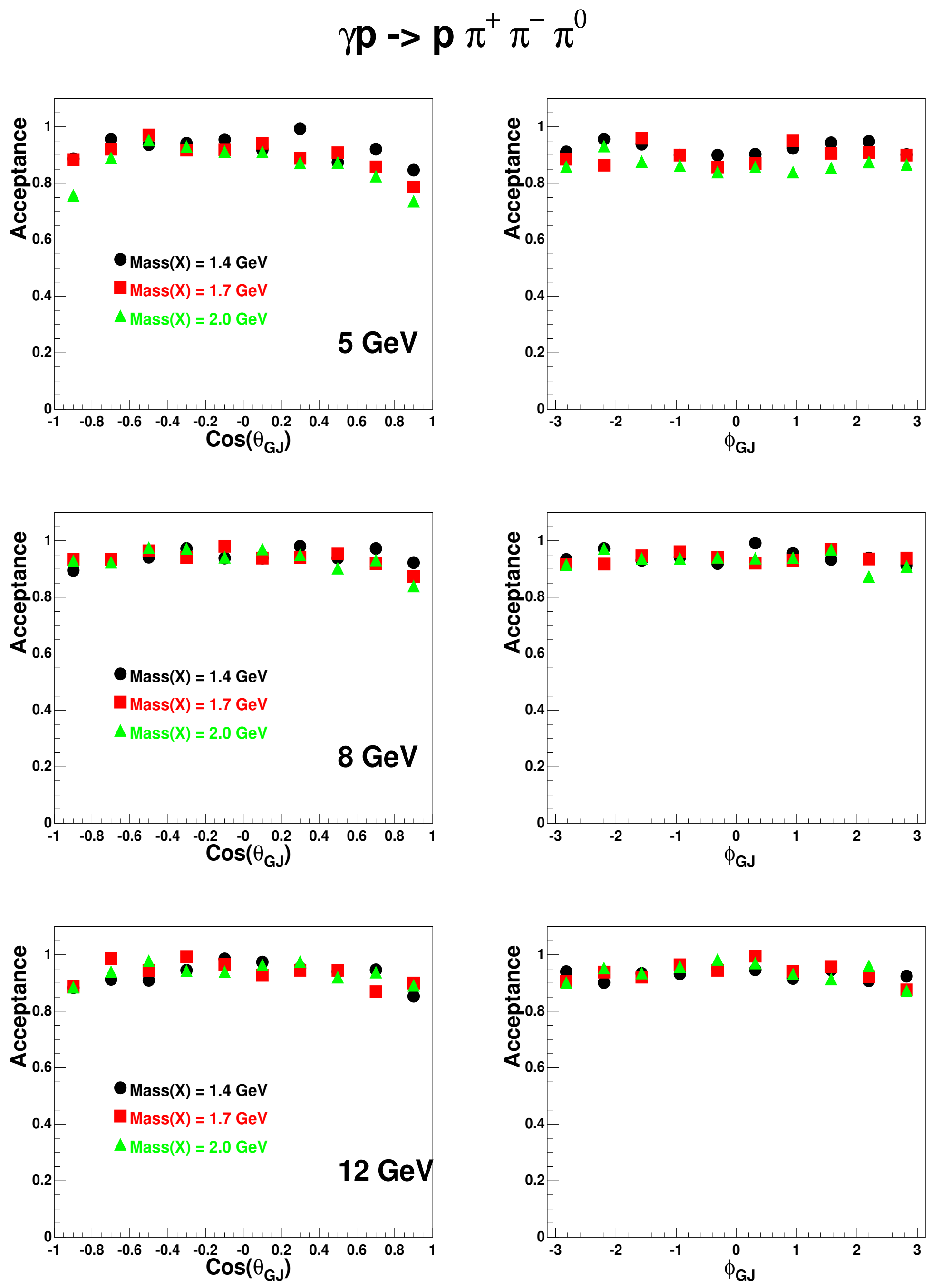

Figure 9.7: The acceptance in $cos(\theta_{GJ})$ and ϕ_{GJ} for $X^0 \rightarrow \pi^+\pi^-\pi^0$.

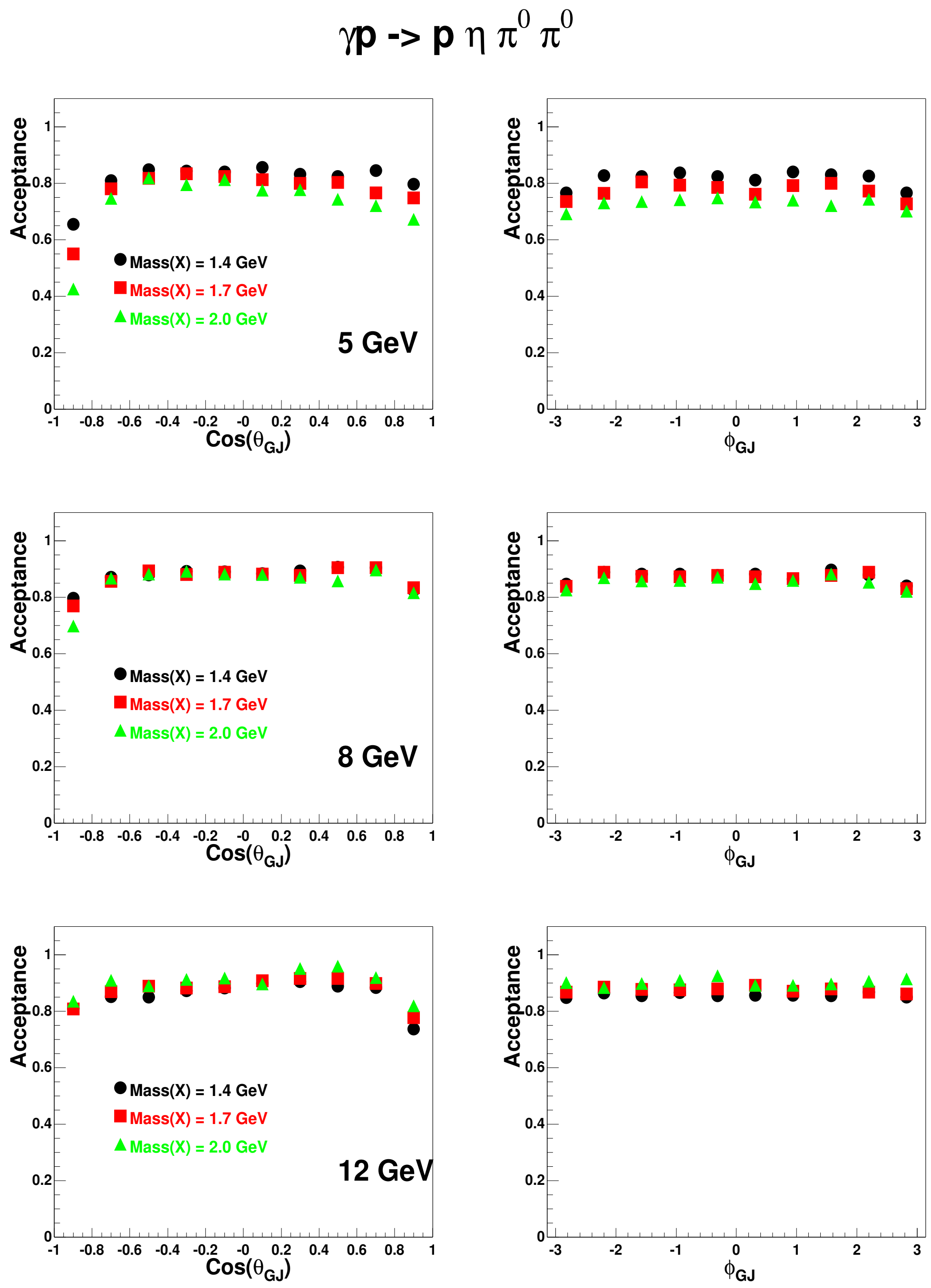

Figure 9.8: The acceptance in $cos(\theta_{GJ})$ and ϕ_{GJ} for $X^0 \rightarrow \eta\pi^0\pi^0$.

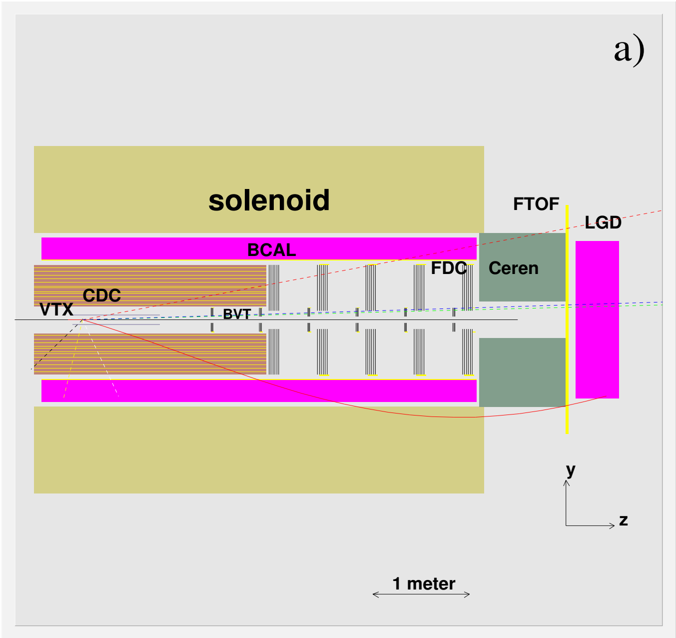

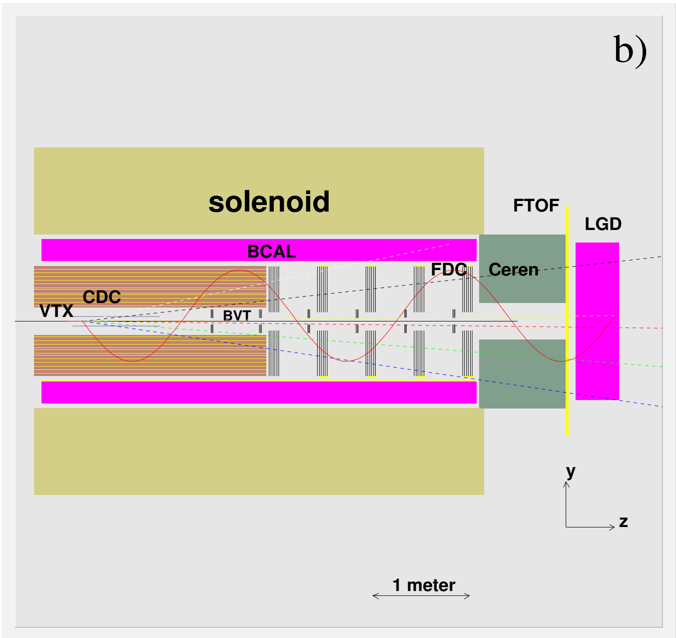

Figure 9.9: Event displays of lost events for $\gamma p \to p\eta\pi^0\pi^0$ for $Mass(X) = 2.0\ GeV/c^2$: a) backward missed gamma at beam= 5 GeV, and b) forward missed beam hole gamma at beam= 12 GeV.

Chapter 10

Data Analysis

10.1 Introduction

In order to identify the J^{PC} quantum numbers of a meson, it is necessary to perform a *partial wave analysis*. In the simplest terms, a partial wave analysis is an attempt to determine production amplitudes by fitting decay angular distributions. The fit may include information on the polarization of the beam and target, the spin and parity of the resonance, the spin and parity of any daughter resonances and any relative orbital angular momenta. The analysis seeks to establish both the production strengths and the relative phase motion between various production amplitudes. Phase motion is critical in determining if resoanance production is present.

While the implementation of a partial wave analysis is in principle straightforward, there are both empirical and intrinsic difficulties. Empirically, instrumentation effects, such as detector acceptance and resolution, can conspire to make one distribution look like another. These similar distributions lead to *leakage* in the partial wave analysis. Here, cropping, smearing, or incorrect acceptance corrections of two physically different distributions may lead to distributions which are apparently indistinguishable. These difficulties can be minimized by properly designing the experiment. Full angular coverage in the distributions can be achieved by using a nearly 4π detector with excellent resolution. In addition, high statistics are critical to be able to accurately separate these partial waves. A thorough partial wave analysis requires nearly 4π coverage, excellent resolution, high statistics and a very good understanding of the detector.

The PWA method is subject to intrinsic mathematical ambiguities for certain final states. Two or more different choices of amplitudes lead to identical observables. Here there are at least two approaches. The first assumes some a priori physics knowledge that allows one to choose one solution over another. The second, and cleaner approach is to simultaneously examine several final states to which the resonance can decay. While the distributions may be confused in one final state, such as $\eta\pi$, they are likely to be absent or different in a second such as $\rho\pi$. This latter approach assumes that the detector has been optimized for many different final states, and that relative normalizations between these are understood.

This latter approach of looking at multiple final states not only would allow one to separate different waves, but in itself yields key information about the relative decay rates of mesons. It is this latter information that is critical to understanding the underlying wave functions of the mesons — their content, and mixing with other states. This ability to accurately measure many final states, and perform a simultaneous partial wave analysis is a key feature of the Hall D spectrometer for doing excellent spectroscopy.

The use of photon polarization will also allow one to both simplify the analysis parameterization, as well as access additional information on the production of mesons. It will also provide key checks on the stability of the analysis itself. While circularly polarized light may yield some information in a few special cases, the true gain comes from linear polarization. Linear polarization defines a *new spatial direction* beyond the photon direction, while for circular polarization, the polarization and the momentum are in the same direction. Secondly, linearly polarized light is a coherent sum of circularly polarized light, which leads to new interference terms.

Finally, there is always a problem of background in a partial wave analysis. This limits one's ability to measure phase motion, and can be particularly severe in a region of dense overlapping resonances. Backgrounds involve a different final state accidently reconstructing as the channel under study. Either a particle is missed by the detector, or when putting the final state back together, multiple interpretations are possible. This can be minimized with a good 4π detector with high efficiency for detecting all final state particles with good resolution. One needs all particles to be reconstructed well enough to allow for a complete kinematical identificaiton of a specific final state.

10.2 Beam and final state normalizations

It will be necessary to show, in the first results from Hall D, that our experiment produces results that are consistent with previous investigations, albeit with much greater statistical precision. These will include total cross sections (at various photon energies) for various inclusive multi–particle photoproduction reactions [175], invariant mass distributions and differential cross sections for exclusive reactions [176, 7] and density matrix element determinations in processes for which polarized beams have been available [177].

Each of the measurements cited above have been carried out with relatively low flux photon beams (for which the beam normalization is rather straightforward) and using bubble chambers for particle detection (which therefore provide excellent, flat acceptance functions). Moving to high intensity beams and sophisticated electronic detectors, while leading to enormous gains in statistical precision, makes it more difficult to accurately determine normalizations. Since one of our main goals is to determine such things as relative branching ratios and production cross sections of new states, it is important to establish consistent connections with these previous measurements. Furthermore, it is likely that our experiment will run with different triggers for different running periods, and these data sets need to be merged as seamlessly as possible. All of these goals will need accurate controls of beam normalization and detector acceptance, as well as a clear determination of their inherent systematic uncertainty.

10.2.1 Photon beam flux

Beam normalization requires a two step process, each of which should be tied in with measurements in the detector itself. In the first step, a low flux photon beam is intercepted by a detector which absorbs the full beam. (It is not difficult to make a detector with essentially 100% detection efficiency for multi GeV photons, and whose losses can be accurately determined with well established simulation programs.) By measuring the fraction of tagged photons, as a function of energy, which are detected by the total absorption counter, we can determine the efficiency to transport these tagged photons through the various beam–line collimators and through the detector itself. This can be further correlated with the detection of real photoproduction reactions.

The second step requires a device which can live in the full beam flux, and which can be cross calibrated with the low flux measurement in the total absorption counter. The easiest way to accomplish this is with a device that uses some small radiation length foil to convert a tiny fraction of the beam to e^+e^- pairs. If these pairs are then detected, preferentially with some energy discrimination using a crude magnetic spectrometer system, then this rate will serve our purpose. In addition, such a pair spectrometer allows for a continuous online monitor of the beam flux during the course of a run. Such a monitor would be very sensitive to, for example, an inadvertent collimator adjustment which changes the overall beam by a small, but important, amount.

We emphasize that coherent bremsstrahlung, which will be necessary for polarized photons as well as for optimizing the photon beam energy, will make the flux normalization more difficult than what has been done so far at Jefferson Laboratory. The energy spectrum is no longer smooth, and the detailed shape is very sensitive to collimation. The collimation in turn is sensitive to the beam steering, which is likely to fluctuate over the course of a data set. All of these fold into our knowledge of the photon beam polarization itself, which we will be determined in large part on the basis of calculations.

Some techniques are also available for monitoring the high flux photon beam polarization directly, although they are not particularly useful for accurately determining the *degree* of polarization. It may be possible to use some techniques designed for low flux beams, but these need to be investigated further.

10.2.2 Particle detection efficiency and acceptance

Monte Carlo simulation will be our primary tool for evaluating detector acceptance and for applying it to data analysis techniques, in particular for the partial wave analysis. However, we need to calibrate, and otherwise confirm, the simulation against real data samples, under usual running conditions.

Some simple reactions have both large cross sections (which are already well–measured) but that also provide a redundant way to check other aspects of the detector. For example, $\gamma p \to \pi^+\pi^- p$ is fully dominated by $\gamma p \to \rho^0 p$ at our energies and its density matrix elements with polarized beam are known [178, 177, 4, 179]. Any two of the three charged particles in this final state can be identified and detected, and one can ask for the probability that the third is also seen. Using the enormous statistical power of our expected sample, we will be able to check details of the acceptance function as determined by the Monte Carlo, using very small and directed phase space bins. Measuring the cross section and density matrix elements in all four topologies (i.e., any one of the three particles missing and all three of them detected) must yield consistent results with each other and with existing data.

Another well known benchmark is $\gamma p \to \pi^+\pi^-\pi^0 p$ which will be dominated by $\gamma p \to \omega p$ [180]. Detection of the three charged particles allows us to determine the direction and energy of the π^0, and therefore to check its detection efficiency and resolution in the electromagnetic calorimeter. It is easy to see how one can extend these arguments to more complicated systems. For example, a measurement of $\gamma p \to \eta p$ using the same topology as for ω production must yield the same results as for $\eta \to \gamma\gamma$, using the well known relative branching ratios for η decay. Many other examples are obvious, and will be exploited.

We emphasize that all of these "calibration" measurements can be bootstrapped into new physics results, extending our present knowledge of some of the most basic photoproduction reactions. All of these new results will be important systematic checks on the more sophisticated analyses that will be possible given our increased statistical accuracy.

10.3 The Role of photon linear polarization

As discussed in section 3.1 the spin–1 nature of the photon allows one to probe helicity or spin structure of production amplitudes. The spin information has been crucial, for example in establishing the dominance of s–channel helicity conservation in ρ photoproduction, studies of violation thereof [178, 181], and in determining the importance of rescattering contribution, *i.e.* Drell–Söding processes [182, 183]. These latter rescattering contributions are important even at high energies [184, 185, 186] and through interference with the diffractive amplitude, they distort the mass distribution of the resonance from the Breit–Wigner shape and contribute to helicity–non–conservation [178, 181]. However, in order to take full advantage of the polarization information in the photon beam it is necessary to have access to linear polarization.

There are two main features that are enabled by linear polarization [13]. First, it allows one to access the largest set of spin–density matrix elements or partial wave amplitudes. This is important from the point of view of both, partial wave analysis, which as discussed earlier enables one to identify properties of the produced resonances, as well as for studies of production mechanisms of those resonances. Secondly, it allows one to identify naturality of the exchanged particle for t–channel dominated reactions. The former follows from considering transformation properties of the production amplitudes under parity. Symmetry under parity relates two production amplitudes with opposite helicities. If the production amplitude is dominated by a t–channel exchange, which at high energies is the case to leading order in t/s, then using parity one can further relate amplitudes with helicities flipped independently at the two, photon and nucleon vertices. With the intrinsic properties under parity, (determined by naturality) of all incoming and outgoing particles fixed, this relationship depends on the naturality of the exchanged particle. Thus by measuring appropriate spin–density matrix elements it is possible to discriminate between different exchanges. Conversely, if the properties of the t–channel are known, which might be the case at low t with one-pion-exchange dominance, then linear polarization enables one to fix the naturality of the produced resonance. As discussed in section 3.1 photons polarized perpendicular to the production plane under one-pion-exchange will yield (un)natural resonances produced with polarization (perpendicular)parallel to the production plane.

These features of linear polarization and its impact on partial wave analysis are best illustrated using vector meson production as an example [13]. Consider the reaction $\gamma p \to Vp$ on an unpolarized target with the subsequent decay of the vector mesons into two pseudoscalar mesons, $V \to PP$ as in $\rho^\circ \to \pi^+\pi^-$ or $\phi \to K^\circ \bar{K}^\circ (K^+K^-)$. There are typically three reference frames used to study such reactions, differing by the definition of the spin quantization axis: the *Gottfried–Jackson frame*, the *helicity system* and the *Adair system*. It is useful to study the angular distribution of the resonance's decay products in all three of these systems. Depending on the dynamics of the production process, production amplitudes, and in particular spin–density matrix elements the physics will appear in a characteristic form in one of the three systems. For example, if t–channel exchange dominates, the spin–density matrix is best analyzed in the Gottfried–Jackson frame. However, to study a dominantly s–channel helicity conserving reaction, one would use the helicity system.

In vector meson photoproduction, the angular dependence of the two pseudoscalars is fully determined in terms of 17, real spin density matrix elements, $\rho^\alpha_{m'_V,m_V}$, $\alpha = 0,\cdots 4$, $m'_V, m_V = \pm 1, 0$ which are defined as in equation 10.1.

$$\rho^\alpha_{m'_V,m_V} = \sum_{m'_N,m_N,m'_\gamma,m_\gamma} A^*(m'_N, m_N, m'_V, m'_\gamma)\sigma^\alpha_{m'_\gamma,m_\gamma} A(m'_N, m_N, m_V, m_\gamma) \tag{10.1}$$

Here m_N, m_V, m_γ refer to spin projections of the nucleon, vector meson and the photon respectively, and σ^α are the four Pauli matrices. Using the angular dependence of the vector meson decay products with unpolarized photons one only has access to ρ^0. Using circular polarization, one has access to ρ^0 and ρ^3, and finally with linear polarization to ρ^0, ρ^1 and ρ^2. It turns out that measurement of ρ^1 and ρ^2 simultaneously is necessary for identification of t–channel naturality thus implying the need for linear polarization. This can be inferred for example from the measurement of parity asymmetry, P_σ

$$P_\sigma \equiv 2\rho^1_{1,-1} - \rho^1_{0,0} = \frac{\sigma^N - \sigma^U}{\sigma^N + \sigma^U}, \tag{10.2}$$

where $\sigma^{(U)N}$ are the cross sections corresponding to the (un)natural parity t–channel exchanges. Another common observable is the Σ–asymmetry, defined in terms of the cross sections for a symmetric decay ($\theta = \frac{\pi}{2}, \phi = \frac{\pi}{2}$) with the two pseudoscalars emerging in the plane of the photon polarization, $\sigma_{||}$, and perpendicular to it $\sigma_\perp$,

$$\Sigma = \frac{\sigma_{||} - \sigma_\perp}{\sigma_{||} + \sigma_\perp} = \frac{\rho^1_{1,1} - \rho^1_{1,-1}}{\rho^0_{1,1} - \rho^0_{1,-1}}. \tag{10.3}$$

It turns out that the difference between P_σ and Σ asymmetries is also a measure of the helicity–non–conservation.

10.4 Description of the partial wave analysis

Parital Wave Analysis is the technique used in hadron spectroscopy to extract spin–parity and decay properties of resonances produced in high energy interactions. The general concept is to parameterize the observed angular distributions in terms of resonance production amplitudes which span the appropriate space. Although many such parameterizations are possible, we choose an expansion in terms of resonances and their appropriate decay couplings. This method also allows the direct assertion of relevant conservation laws, and also permits the direct interpretation of results in terms of resonance production and decay strengths.

The program which is currently being developed to analyze electroproduction and photoproduction data at CEBAF, was originally developed for the analysis of hadroproduction data at Brookhaven National Laboratory [187]. This program uses the extended maximum likelihood method [188] to fit the production amplitudes to the observed intensity distribution.

10.4.1 General description

The program is based on the partial wave formalism described above. The angular distribution is a squared sum of amplitudes taking in account initial and final state spin states as given in 10.4.

$$I(\tau) \propto \sum_{\alpha} \left| \sum_{\beta} {}^{\alpha}\psi_{\beta}(\tau) \right|^2 \tag{10.4}$$

The variable τ represents the set of variables necessary to define a configuration of the final state being investigated, and generally includes the angles of decay products in various reference frames, and the masses of decay products. For example, for the final state $\pi^+\pi^-\pi^0$, the system is described by a set of decay angles, θ and ϕ of the $\pi^+\pi^-$ system in the 3 π center–of–mass system, the decay angles, θ' and ϕ' of the π^+ in the $\pi^+\pi^-$ center–of–mass, and the mass of the $\pi^+\pi^-$ pair, for a given 3–π mass. The subscript β represents the definition of a specific partial wave, and α specifies parameters that do not interfere, for example any external spins that are not measured.

In a peripheral production experiment, the amplitudes of the reaction can be drawn as shown in Figure 10.1. A fundamental tenet of partial wave analysis is that the process factories, i.e. the resonance is produced, propagates for some time, and then decays. In general, an analysis is performed in bins of total meson effective mass and in bins of t so that a decay amplitude depends only on the resonance parameters, up to a constant, and is thus calculable. The total amplitude ${}^{\alpha}\psi_{\beta}$ can be written as the product of the production amplitude V and the decay amplitude A:

$${}^{\alpha}\psi_{\beta} = {}^{\alpha}V_{\beta}\, {}^{\alpha}A_{\beta}(\tau)\ . \tag{10.5}$$

As as way of illustration, consider our example of the photoproduction of 3 pions from an unpolarized photon beam on an unpolarized hydrogen target, Figure 10.1. In this case, the non–interfering components of the process come from the external spins in the process, i.e. the incident photon spin, the target proton spin, and the recoil proton spin. The description of the partial waves includes the J^P of the produced resonance, the mass of the $\pi^+\pi^-$ pair, the relative orbital angular momentum between the $\pi^+\pi^-$ pair and the bachelor π°, the orbital angular momentum between the π^+ and the π^-, and the J_z of the produced resonance. As the decay of the resonance is into only pseudo–scalar particles, the decay amplitude A

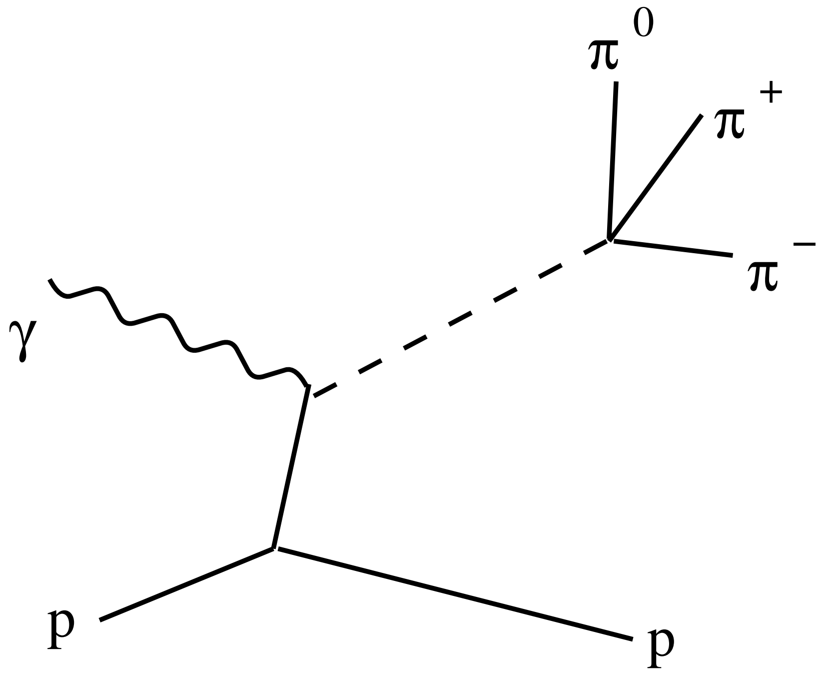

Figure 10.1: Photoproduction of a charged three pion system off a hydrogen target.

is not labelled by the spin index α. The angular distribution can thus be written as in equation 10.6.

$$I(\tau) \;=\; \sum_{\alpha} \left| \sum_{\beta} {}^{\alpha}V_{\beta}\; A_{\beta}(\tau) \right|^{2} \tag{10.6}$$

The likelihood function for finding 'n' events in a given bin with a finite acceptance $\eta(\tau)$ is given by a product of probabilities:

$$\mathcal{L} = \mathrm{e}^{-\bar{n}} \prod_{i}^{n} I(\tau_i) \tag{10.7}$$

where

$$\bar{n} = \int I(\tau)\eta(\tau)\; dLIPS$$

is the average number of events one would expect if the same experiment were repeated many times and $dLIPS$ is the differential lorentz invariant phase space element.

The $\ln(\mathcal{L})$ may be written as:

$$\ln(\mathcal{L}) \propto \sum_{i}^{n} \ln I(\tau_i) - \int I(\tau)\; \eta(\tau)\; d\text{LIPS}. \tag{10.8}$$

Since $I(\tau)$ is an expansion in terms of partial waves, the acceptance correction in the second term is done wave–by–wave *not* event–by–event. This allows the full statistics of the Monte–Carlo to used in the acceptance calculation, rather than just the events in a kinematic bin. In addition, the fit can be done even if there are holes in the acceptance, at the cost of possible ambiguities being introduced into the fit.

10.4.2 Decay amplitudes

The amplitude for the decay of a particle with spin J and $J_z = M$ into two particles with helicities λ_1 and λ_2 in the resonance center–of–mass system is given by [189]:

$$A = < \vec{p}\lambda_1; -\vec{p}\lambda_2 \mid \mathcal{M} \mid JM > = F^J_{\lambda_1\lambda_2} \mathcal{D}^{*J}_{M\ \lambda}(\phi, \theta, 0) \tag{10.9}$$

Calculation of the decay amplitudes for a resonance is done recursively within the isobar model, regarding the n–body final state as a result of a series of sequential, generally 2–body, decays through intermediate isobar states. The total decay amplitude is the amplitude for the resonance to decay into its intermediate children times the amplitude for each of its children to decay.

The initial decay of the resonance is calculated in the Gottfried–Jackson frame. This frame is a rest frame of the resonance with the z axis along the incident beam axis, and the y–axis is defined normal to the production plane. Each subsequent decay is calculated in the helicity frame, that is the rest frame of the decaying particle with the z–axis in the direction of the parent particle from the previous frame.

10.4.3 Initial state polarization

The intensity distribution, as written in 10.6, shows the familiar sum over final states and average over initial states as the sums over external spins. These sums can be handled explicitly as shown or as constraints on the structure of the spin density matrix of the intermediate state produced in the reaction. Imposing additional constraints that are known *a priori*, such as hermiticity and parity conservation, leads to a minimal number of independent fit parameters.

The spin density matrix of this state is written in terms of the production amplitudes as:

$$\rho_{\beta\beta'} = \sum_\alpha {}^\alpha V_\beta {}^\alpha V^*_{\beta'}. \tag{10.10}$$

When the physical constraints mentioned above are taken into account, ρ is block diagonal with 2 blocks.

The intensity distribution can then be written as

$$I(\tau) = \sum_{\beta\beta'} A_\beta(\tau)\ \rho_{\beta\beta'}\ A^*_{\beta'}(\tau)\,, \tag{10.11}$$

where the sums over spins have thus been absorbed into the density matrix. If none of the exterior spins are known, the density matrix must be symmetric in those spin indices. Polarization of the initial state spins, however, impose additional constraints on the structure of the density matrix and will allow us to take advantage of asymmetries produced.

10.4.4 Joint production of excited baryons and mesons

In the kinematic region of HALL D it is probable that baryon resonances will be produced in addition to the meson states we have been discussing. Processes such as the two shown

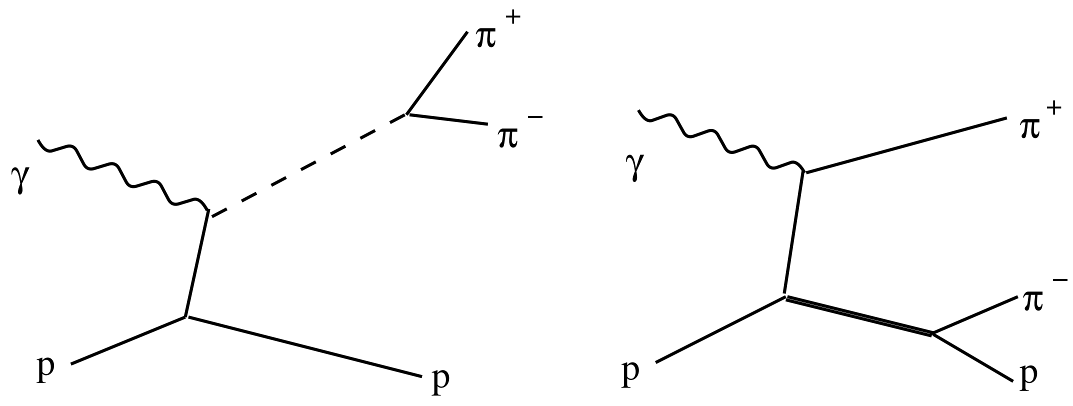

Figure 10.2: Example of interfering baryon and meson processes.

in Figure 10.2 will interfere wiht each other and they must be taken into account in the analysis.

In general this could lead to ambiguities, since the baryon states can be described as an infinite sum over meson states. In practice, however, the sum over meson states is truncated to a finite number of resonances, and will not well describe the distribution due to the baryon resonance. Hence, in order to get a good description of the intensity distribution, the baryon resonances must be included explicitly. Effects of ambiguities are mitigated at the cost of requiring an physically motivated *ansatz*, *i.e.* truncating the set of waves to the minimal set required by the fit. The impact of any ambiguities created will vary with the reaction being studied, but can be well determined using Monte–Carlo methods.

Chapter 11

Milestones

The HALL D Collaboration recognizes the need to develop milestones and these will be developed after consultation with and guidance from the Jefferson Lab management and PAC.

Chapter 12

Cost Estimates

The total cost for the HALL D project is $\approx$ \$30.9 M (not including contingencies) and the costs are summarized in Table 12.1. The cost of the dectector is $\approx$ \$18.4 M and is given in more detail in Table 12.2. The civil and beamline costs total $\approx$ \$10.9 M and include the tunnel from the accelerator to the HALL D tagger, beamline elements, the HALL D building, control room, parking and roads. The cost of the photon tagger is $\approx$ \$1.7 M. Further details of the costs for the various subsystems of the detector, the civil construction, beamline and tagger are given in Appendix A.

Not included in the HALL D cost estimate is the cost of the additional arc in the CEBAF accelerator which would allow 5.5 passes for the electron beam in HALL D. The cost of the extra arc is $\approx$ \$2.9 M and is assumed to be part of the overall accelerator upgrade. In Appendix A we also estimate costs for computer power needed to handle HALL D analysis ($\approx$ \$2.8 M). We envisage this as part of the lab upgrade of its computer facilities and therefore it is not included in the overall HALL D project cost.

The overall cost of Hall D is summarized in table 12.1.

Item	Cost (\$k)
Detector Package	18376.9
Civil and Beamline	10897.3
Photon Tagger	1670.0
Total Cost	30944.2

Table 12.1: HALL D cost estimate summary

A more detailed cost breakdown of all of the systems can be found in Appendix A.

Subsystem	Cost ($k)
Channels	6466.0
Tracking	2692.5
Barrel Calorimeter	2019.6
Cherenkov Detector	539.8
Forward Calorimeter	1594.6
Time of Flight Wall	643.9
Computing	2255.0
Start Counter	720.5
Trigger	595.0
Hydrogen Target	100.0
Solenoid	750.0
Detector Package	18376.9

Table 12.2: HALL D detector cost breakdown by system

Chapter 13

Management plan

The HALL D Collaboration recognizes the need to develop a management plan as part of a WBS. There are models for such plans and in the coming months the HALL D Collaboration will develop a management plan.

Appendix A

Detailed Cost Estimates

This appendix contains the detailed cost estimates for HALL D.

Item	Cost ($k)
Detector Package	18376.9
Civil and Beamline	10897.3
Photon Tagger	1670.0
Total Cost	30944.2

Table A.1: HALL D overall cost summary

Subsystem	Cost ($k)
Channels	6466.0
Tracking	2692.5
Barrel Calorimeter	2019.6
Cherenkov Detector	539.8
Forward Calorimeter	1594.6
Time of Flight Wall	643.9
Computing	2255.0
Start Counter	720.5
Trigger	595.0
Hydrogen Target	100.0
Solenoid	750.0
Detector Package	18376.9

Table A.2: HALL D detector cost summary

Signal Channels			
Detector	FADC	TDC	
Cherenkov	38		
Time of Flight	200	200	
Start	2510	10	
Barrel Calorimeter	576	576	
Tracking Detectors	13340	5984	
LGD (Forward Cal)	3000		
Tagger		250	
Total	19664	7020	
High Voltage			
	Number	Unit Cost	Cost ($k)
Tracking Detectors			250.0
PMTs (excluding LGD)	3324	$45k/256	585.0
Total			835.0
Electronics			
	Number	Unit Cost	Cost ($k)
8 Bit 250 *MHz* FADC	19664	200	3932.8
COMPASS F1 TDC	7020	75	526.5
VME Crates	54	10000	540.0
Racks for VME Crates	27	500	13.5
Cables	30910	20	618.2
High Voltage			835.0
Total Cost			6466.0

Table A.3: Channel count summary and readout cost

Channels			
Subsystem	Wires	Cathodes	
Central Drift Chamber (CDC)	5200	1000	
Forward Drift Chamber (FDC)	3570	7140	
Barrel Vertex Tracker (BVT)	414		
Materials			
Item	Number	Unit Cost	Cost ($k)
Straws (CDC)	5200	50	260.0
Wire (FDC/BVT)			40.0
Connectors			75.0
Cathode Strip Prints			150.0
Support Structure			50.0
Subtotal			575.0
Labor			
Item	Number	Unit Cost	Cost ($k)
Technician years	32	25000	800.0
Machinist weeks	104	1500	156.0
Student hours	25000	5	125.0
Shipping			100.0
Travel			25.0
Subtotal (Fringe)			1081.0
Fringe(%)		32	345.9
Subtotal (Overhead)			1551.9
Overhead(%)		30	465.6
Subtotal			2017.5
Other			
Calibration System			100.0
Total			2692.5

Table A.4: Cost, tracking detectors

Materials			
Item	Number	Unit Cost	Cost ($k)
Scintillator Fiber			750.0
Lead Sheet			65.0
Light Guides	576	150	86.4
PMTs	576	315	181.4
PMT Bases	576	160	92.2
Shields	576	50	28.8
Glue and Supplies			10.0
Support Structure			15.0
Subtotal			1228.8
Labor			
Item	Number	Unit Cost	Cost ($k)
Technician years (Weaving)	10	25000	250.0
Machinist weeks (Tooling)	70	1500	105.0
Student hours (Rolling)	8000	5	40.0
Shipping			5.0
Travel			5.0
Subtotal (Fringe)			395.0
Fringe(%)		32	126.4
Subtotal (Overhead)			531.4
Overhead(%)		30	159.4
Subtotal			690.8
Other			
Calibration System			100.0
Total			2019.5

Table A.5: Cost, barrel calorimeter

Materials			
Item	Number	Unit Cost	Cost ($k)
Mirrors	38		3
Tooling	3	500	1.5
Collectors	12	500	6
Cones	38	100	3.8
Lenses	12	250	3
PMTs	38	1971	74.9
Shields	38	300	11.4
Gas(m^3 C_4F_{10})	36	380	13.7
Support Structure			15.0
Subtotal			132.3
Labor			
Item	Number	Unit Cost	Cost ($k)
Technician Yrs	2	25000	50.0
Machinist weeks (mirrors)	3	1500	4.5
Machinist weeks (collec)	12	1500	18.0
Machinist weeks (struct)	40	1500	50.0
Student hours	4000	5	20.0
Shipping			5.0
Travel			5.0
Subtotal (Fringe)			142.5
Fringe(%)		32	45.6
Subtotal (Overhead)			198.1
Overhead(%)		30	59.4
Subtotal			257.5
Other			
Gas system			50.0
Calibration System			100.0
Total			2692.5

Table A.6: Cost, Cerenkov detector

Materials			
Item	Number	Unit Cost	Cost ($k)
PMTs	3000	0	0.0
PMT Bases	3000	100	300.0
Lead Glass Blocks	3000	0	0.0
Shields	3000	100	300.0
Support Structure			15.0
Subtotal			615.0
Labor			
Item	Number	Unit Cost	Cost ($k)
Technician years (Bases)	2	25000	50.0
Machinist weeks (Struct)	20	1500	30.0
Student hours (Assembly)	10000	5	50.0
Shipping			500.0
Travel			5.0
Subtotal (Fringe)			130.0
Fringe(%)		32	41.6
Subtotal (Overhead)			676.6
Overhead(%)		30	203.0
Subtotal			879.6
Other			
Calibration System			100.0
Total			1594.6

Table A.7: Cost, forward calorimeter

Materials			
Item	Number	Unit Cost	Cost ($k)
Scintillators	100	500	50.0
Light Guides	200	150	30.0
PMTs	200	1250	250.0
PMT Bases	200	100	20.0
Shields	200	100	20.0
Support Structure			15.0
Subtotal			385.0
Labor			
Item	Number	Unit Cost	Cost ($k)
Technician years	2	25000	50.0
Machinist weeks	20	1500	30.0
Student hours	1000	5	5.0
Shipping			5.0
Travel			5.0
Subtotal (Fringe)			85.0
Fringe(%)		32	27.2
Subtotal (Overhead)			122.2
Overhead(%)		30	36.7
Subtotal			158.9
Other			
Calibration System			100.0
Total			643.9

Table A.8: Cost, time of flight detector

Materials: Timing			
Item	Number	Unit Cost	Cost ($k)
Scintillators	10	500	5.0
Light Guides	10	100	1.0
PMTs	10	700	7.0
PMT Bases	10	160	1.6
Shields	10	100	1.0
Support Structure			3.0
Subtotal			18.6
Materials: Tracking			
Tracking Channels	2500	160	400.0
Cryostat			140.0
Support Structure			3.0
Subtotal			543.0
Labor			
Item	Number	Unit Cost	Cost ($k)
Technician years	2	25000	50.0
Machinist weeks	20	1500	30.0
Student hours	1000	5	5.0
Shipping			5.0
Travel			5.0
Subtotal (Fringe)			85.0
Fringe(%)		32	27.2
Subtotal (Overhead)			122.2
Overhead(%)		30	36.7
Subtotal			158.9
Total			720.5

Table A.9: Cost, start counter

Item	Number	Unit Cost	Cost ($k)
Crate sevel summation	35	10,000	350.0
Subsystem level summation	5	25,000	125.0
Lookup table	1	50,000	50.0
Clocks, synchronization, cables			50.0
VME Crates	2	10,000	20.0
Total			595.0

Table A.10: Cost, level 1 trigger

Data Acquisition Item	Number	Unit Cost	Cost ($k)
Single Board CPU	35	3,000	105
Main Switch	2	20,000	40
Sub-Farm Switch	10	4,000	40
DAQ Sun SMP	10	20,000	200
DAQ Field CPU	200	2,000	400
Miscellaneous PC/Sun	10	3,000	30
DAQ RAID	10	20,000	200
DAQ Tape Drive	6	100,000	600
CC Computer	2	20,000	40
Analysis Farm	250	2,000	500
Tape Media (TB/Year)	1000	200	200
Racks, Desks, Misc			100
DAQ Total			2255

Table A.11: Data handling, experiment side

Data Analysis Item	Number	Unit Cost	Cost ($k)
CC RAID	10	40,000	400
CC Tape Drive	10	100,000	1000
CC Tape Silo	2	300,000	600
Analysis Farm	100	2,000	200
Tape Media (TB/Year)	3000	200	600
Racks, Desks, Misc			30
Data Analysis Total			2830

Table A.12: Data handling, computer center side

Buildings (1.5m Below)	
Item	Cost ($k)
Construction	2727.0
Utilities	37.7
Crane	164.5
Access Control	42.5
Fire Protection	83.8
Mechanical	1538.2
Electrical	1023.6
Subtotal	5617.3
Profit at 15%	842.6
Subtotal	6459.9
A&E Design at 6%	387.6
Safety Training at 2%	129.2
Bond at 1.5%	96.9
Subtotal	7073.6
Contingency at 5%	353.7
Total	7427.3
Beamline	
Diagnostics	470
Service Building	110
Elements	1180
Labor	1710
Total	3470
Grand Total	10897.3

Table A.13: Civil construction cost

Spectrometer Magnet			Cost ($k)
Magnet Steel			200
Machining			200
Magnet Coils			200
Total			600
Power supply			140
Mechanical Const			Cost ($k)
Vacuum Chamber			150
Thin Exit Window			75
Magnet Support			50
Hodoscope Support			30
Total			305
Hodoscope			
Item	Number	Unit Cost	Cost ($k)
Scintillator/Light Guide	250	200	50
PMTs	250	300	75
Base and Shield	250	200	50
High Voltage	250	200	50
Total			225
Electronics			Cost ($k)
Discriminators			80
Logic			30
NIM Crates			35
Scalars/VME Crates			30
Total			175
Other			
Goniometer, etc...			225
Total			1670

Table A.14: Tagger cost

List of Figures

List of Tables

Bibliography

[1] S. Godfrey and J. Napolitano. Light meson spectroscopy. *Rev. Mod. Phys.*, **71**, 1999. Also available as hep-ph/981141.

[2] P. Minkowski and W. Ochs. Identification of the glueballs and the scalar meson nonet. hep-ph/9811518.

[3] A. Afanasev and P. R. Page. Photoproduction and electroproduction of $J^{PC} = 1^{-+}$ exotics. *Phys. Rev.*, D**57**:6771, 1998.

[4] J. Ballam *et al.* Vector-meson production by polarized photons from 2.8, 4.7, and 9.3 GeV. *Phys. Rev.*, D**7**:3150–3177, 1973.

[5] K. Abe *et al.* *Phys. Rev. Lett.*, **53**:751, 1984.

[6] Y. Eisenberg *et al.* *Phys. Rev.*, D**5**:15, 1972.

[7] G. Condo *et al.* *Phys. Rev.*, D**48**:3045, 1993.

[8] M. Atkinson *et al* (The Omega Collaboration). *Nucl. Phys.*, **B231**:15, 1984.

[9] M. Davier *et al.* The reaction $\gamma p \to \pi^+\pi^-\pi^+\pi^- p$ at high-energy and γ dissociation into 4π. *Nucl. Phys.*, **B58**:31, 1973.

[10] K. Abe *et al.* *Phys. Rev.*, D**32**:2288, 1985.

[11] M. Atkinson *et al* (The Omega Collaboration). *Nucl. Phys.*, **B243**:1, 1984.

[12] G. R. Blackett *et al.* The Photoproduction of the $b_1(1235)\pi$ System, hep-ex/9708032.

[13] K. Schilling, P. Seyboth, and G. Wolf. On the analysis of vector meson production. *Nucl. Phys.*, **B15**:398, 1970.

[14] A. Afanasev and A.P. Szczepaniak. in preparation.

[15] G.S. Adams *et al.* *Phys. Rev. Lett.*, **81**:5760, 1998.

[16] N. Isgur and J. Paton. *Phys. Rev.*, D**31**:2910, 1985.

[17] K.J. Juge, J. Kuti, and C.J. Morningstar. hep-lat/9809098.

[18] T. Barnes, F.E. Close, and E.S. Swanson. *Phys. Rev.*, D**52**:5242, 1995.

[19] C.Bernard *et al.* (MILC Collaboration). *Phys. Rev.*, D**56**:7039, 1997. hep-lat/9707008.

[20] K. Juge, J. Kuti, and C.J. Morningstar. *Nucl. Phys. Proc. Suppl.*, **63**:326. hep-lat/9709131.

[21] T. Schäfer and E. V. Shuryak. *Phys. Rev. Lett.*, **75**:1707, 1995.

[22] C. Roberts and A. Williams. *Prog. Part. Nucl. Phys.*, **33**:477, 1994.

[23] C. J. Burden and M. A. Pichowsky. J^{PC}-exotic mesons from the Bethe-Salpeter equation,in preparation.

[24] D. Horn and J. Mandula. *Phys. Rev.*, D **17**:898, 1978.

[25] S. Ishida, H. Sawazaki, M. Oda, and K. Yamada. *Phys. Rev.*, D**47**:179, 1992.

[26] E.S. Swanson and A.P. Szczepaniak. *Phys. Rev.*, D**59**:14035, 1999.

[27] A. Chodos. *Phys. Rev.*, D**9**:3471, 1974.

[28] T. Barnes. *Nucl. Phys.*, **B158**:171, 1979.

[29] T. Barnes and F.E. Close. *Phys. Lett.*, **B116**:365, 1982.

[30] M. Chanowitz and S. Sharpe. *Nucl. Phys.*, **B222**:211, 1983.

[31] M. Flensburg, C. Peterson, and L. Sköold. *Z. Phys.*, **C22**:293, 1984.

[32] P. Hasenfratz, R.R. Horgan, J. Kuti, and J.M. Richard. *Phys. Lett.*, **95B**:299, 1981.

[33] K.J. Juge, J. Kuti, and C.J. Morningstar. *Nucl. Phys. Proc. Suppl.*, **63**:543, 1998.

[34] V. A. Novikov, M. A. Shifman, A. I. Vainshtein, and V. .I. Zakharov. *Nucl. Phys.*, **B165**:67, 1979.

[35] J. I. Latorre, S. Narison, P. Pacual, and R. Tarrach. *Phys. Lett.*, **147B**:169, 1984.

[36] J. Govaerts. *Nucl. Phys.*, **B285**:674, 1987.

[37] J. Govaerts. *Phys. Rev. Lett.*, **53**:2207, 1984.

[38] I. I. Balitsky, D. I. Dyakanov, and A. V. Yung. *Z. Phys.*, **C33**:265, 1986.

[39] P.Lacock *et al.* (UKQCD Collaboration). *Phys. Lett.*, **401B**:308, 1997.

[40] S. Perantonis and C. Michael. *Nucl. Phys.*, **B347**:854, 1990.

[41] T. Manke *et al.* (UKQCD Collaboration). *Nucl. Phys. Proc. Suppl.*, **63**:332. hep-lat/9709001.

[42] C.J. Morningstar and M. Peardon. *Phys. Rev.*, D**56**:4043, 1997. hep-lat/9704011.

[43] G.S. Bali *et al.* *Phys. Lett.*, **309B**:378, 1993.

[44] J.Sexton *et al.* (IBM Collaboration). *Phys. Rev. Lett.*, **75**:4563, 1995.

[45] G. Bali *et al.* (SESAM Collaboration). *Nucl. Phys. Proc. Suppl.*, **63**:209. hep-lat/9710012.

[46] K.J. Juge, J. Kuti, and C.J. Morningstar. *Nucl. Phys. Proc. Suppl.*, **63**:513. hep-lat/9709132.

[47] T.J. Allen, M.G. Olsson, and S. Veseli. *Phys. Lett.*, **434B**:110, 1998. hep-ph/9804452.

[48] M. Tanimoto. *Phys. Lett.*, **116B**:198, 1982.

[49] A. Le Yaouanc, L. Oliver, O. Pene, J.-C. Raynal, and S. Ono. *Z. Phys.*, C **28**:309, 1985.

[50] F. Iddir, A. Le Yaouanc, L. Oliver, O. Pene, and J.-C. Raynal. *Phys. Lett.*, **207B**:325, 1988.

[51] N. Isgur, R. Kokoski, and J. Paton. *Phys. Rev. Lett.*, **54**:869, 1985.

[52] F.E. Close and P. Page. *Nucl. Phys.*, **B443**:233, 1995.

[53] E.S. Swanson and A.P. Szczepaniak. Decays of hybrid mesons. *Phys. Rev.*, D**56**:5692, 1997.

[54] P. Page, E.S. Swanson, and A.P. Szczepaniak. *Phys. Rev.*, D**59**:34016, 1999.

[55] Yu. S. Kalashnikova. *Z. Phys.*, C **62**:323, 1994.

[56] S. L. Zhu. hep-ph/9903537.

[57] S. Narison. QCD spectral sum rules. *Lecture Notes in Phys.*, Vol**26**:369, 1989.

[58] J. I. Latorre, S. Narison, and P. Pacual. *Z. Phys.*, C**34**:347, 1987.

[59] A. Le Yaouanc *et al.* *Phys. Lett.*, **205B**:564, 1988.

[60] H.G.Dosch and D.Gromes. *Phys. Rev.*, D**33**:1378, 1986.

[61] S.Godfrey and N.Isgur. *Phys. Rev.*, D**32**:189, 1985.

[62] D. V. Bugg. To be published in the proceedings of the World Hadron Symposium, March 1999, Frascati, Italy. T. Barnes, *ibid.*

[63] F. Iachello, N.C. Mukhopadhyay, and L. Zhang. Spectrum generating algebra for string-like hadrons: mass formula for mesons. *Phys. Lett.*, **256B**:295–300, 1991.

[64] F. Iachello, Nimai C. Mukhopadhyay, and L. Zhang. Spectrum generating algebra for string-like mesons. 1. mass formula for $q\bar{q}$ mesons. *Phys. Rev.*, D **44**:898–914, 1991.

[65] H.G.Blundell and S.Godfrey. *Phys. Rev.*, Dbf 53:3700, 1996.

[66] H.G.Blundell, S.Godfrey, and B.Phelps. *Phys. Rev.*, D**53**:3712, 1996.

[67] T.Barnes, F.E.Close, P.R.Page, and E.S.Swanson. *Phys. Rev.*, D**55**:4157, 1997.

[68] H.G.Blundell and S.Godfrey. *Phys. Rev.*, D**53**:3700, 1996.

[69] T.Barnes and N.Black. in preparation.

[70] D.Aston *et al.* *Phys. Lett.*, **215B**:199, 1988.

[71] A.Abele *et al.* (Crystal Barrel Collaboration). High-mass ρ-meson states from $\bar{p}d$-annihilation at rest into $\pi^-\pi^o\pi^o p_{\mathrm{spectator}}$. *Phys. Lett.*, **391B**:191, 1997.

[72] U.Thoma *et al.* (Crystal Barrel Collaboration). *AIP Conf. Proc.*, **432**:322, 1998.

[73] D.Weingarten. *Nucl. Phys.*, **B** (Proc. Suppl.) **34**:29, 1994.

[74] C.Michael. Liverpool report LTH 370, hep-ph/9605243 (May 1996).

[75] F.E.Close and M.J.Teper. On the lightest scalar glueball. RAL-96-040 / OUTP-96-35P (July 1996).

[76] C.Amsler and F.E.Close. *Phys. Lett.*, **353B**:385, 1995.

[77] C.Amsler and F.E.Close. *Phys. Rev.*, D**53**:295, 1996.

[78] J.Adomeit *et al.* (Crystal Barrel Collaboration). *Z. Phys.*, C **71**:227, 1996.

[79] P.Lacock *et al.* (UKQCD Collaboration). *Phys. Lett.*, **401B**:308, 1997. hep-lat/9611011.

[80] Carl E. Carlson and Nimai C. Mukhopadhyay. Perturbative QCD signatures of hybrid hadrons in electroproduction at high Q^2. *Phys. Rev. Lett.*, **67** :3745–3748, 1991.

[81] C. Amsler *et al.* High-statistics study of $f_0(1500)$ decay into $\pi^0\pi^0$. *Phys. Lett.*, **342B**:433–439, 1995.

[82] C. Amsler *et al.* Coupled channel analysis of $\bar{p}p$ annihilation into $\pi^0\pi^0\pi^0$, $\pi^0\eta\eta$, and $\pi^0\pi^0\eta$. *Phys. Lett.*, **355B**:425–432, 1995.

[83] J.Weinstein and N.Isgur. *Phys. Rev.*, D**27**:588, 1983.

[84] J.Weinstein and N.Isgur. *Phys. Rev.*, D**41**:2236, 1990.

[85] N.N.Achasov and V.Ivanchenko. *Nucl. Phys.*, **B315**:465, 1989.

[86] F.E. Close, N. Isgur, and S. Kumano. Scalar mesons in ϕ radiative decay: Their implications for spectroscopy and studies of CP violation at ϕ factories. *Nucl. Phys.*, **B389**:513, 1993.

[87] N. N. Achasov *et al.* (The SND Collaboration). 1998.

[88] T. Barnes. *Phys. Lett.*, **B165**:434, 1985.

[89] N.A.Törnqvist. *Phys. Rev. Lett.*, **67**:556, 1991.

[90] A. B. Wicklund *et al.* *Phys. Rev. Lett.*, **45**:1469, 1980.

[91] S. Wycech and A. M. Green. *Nucl. Phys.*, **A562**:446, 1993.

[92] R. J. Jaffe. *Phys. Rev.*, D**15**:267, 1997.

[93] N. N. Achasov, S. A. Devyanin, and G. N. Shestakov. *Usp. Fiz. Nauk*, **142**:361, 1984.

[94] R. Kaminski, L. Lesniak, and J. P. Maillet. *Phys. Rev.*, D**50**:3145, 1996.

[95] R. Kaminski and L. Lesniak. *Phys. Rev.*, D**51**:2264, 1995.

[96] G. Janssen, B.C. Pearce, K. Holinde, and J. Speth. *Phys. Rev.*, D**52**:2690, 1995.

[97] D. Cohen *et al.* *Phys. Rev.*, D**22**:2595, 1980.

[98] P. Estabrooks. *Phys. Rev.*, D**19**:2678, 1979.

[99] D.C. Fries *et al.* S-P wave interference in K^+K^- production near threshold. *Nucl. Phys.*, **B143**:408, 1978.

[100] D.P.Barber *et al.* A study of elastic photoproduciton of low mass K^+K^- pairs. *Z. Phys.*, **C12**:1, 1982.

[101] M. Pichowsky and H. Lee. *Phys. Rev.*, D **56**:1644, 1997.

[102] J.Lee-Franzini, W.Kim, and P.J.Franzini. *Phys. Lett.*, **287B**:259, 1992.

[103] R. R. Akhmetshin *et al.* Preprint BudkerINP 99-11, Novosibirsk, 1999.

[104] M. N. Achasov *et al.* Preprint BudkerINP 98-65, Novosibirsk, 1998.

[105] M. N. Achasov *et al.* hep-ex/9907005 and hep-ex/9907006.

[106] M. N. Achasov *et al.* *Phys. Lett.*, **438B**:441, 1998.

[107] M. N. Achasov *et al.* *Phys. Lett.*, **440B**:442, 1998.

[108] A. Gasparian. JLab Experiment E-99-014.

[109] M. Burkardt, J. Goity, V. Papavassiliou, and S. Pate, editors. *The structure of the η' meson.* World Scientific, 1998.

[110] A. Gasparian. Preliminary study on Primakoff η production.

[111] S. Scherrer. *Nucl. Phys.*, **A623**:215c, 1997. Also available as hep-ph/9612228.

[112] R. A. Miskiman *et al.* JLab Experiment PR-94-015.

[113] R. A. Miskiman. In A. Bernstein and B. Holstein, editors, *Proc. of the Chiral Dynamics: theory and experiment workshop*, page 122. World Scientific, 1994.

[114] V. Petrun'kin. *Sov. J. Part. Nucl.*, **12**:278, 1981.

[115] A. Nathan *et al.* *Phys. Rev. Lett.*, **80**:4382, 1998.

[116] V. Bernard *et al.* *Phys. Lett.*, **268B**:291, 1991.

[117] V. Bernard *et al.* *Nucl. Phys.*, **B383**:442, 1992.

[118] J. Bijnens, A. Bramon, and F. Cornet. *Phys. Lett.*, **237B**:488, 1990.

[119] G.D'Ambrosio, G. Ecker, G. Isidori, and H. Neufeld. In *The Second DAΦNE Physics Handbook*.

[120] C. Keppel. Development of a Compton-backscattered photon source for Hall B at Jefferson Lab. In *Physics with 8+ GeV Photons Workshop*. Workshop in Bloomington IN, July 14-16 1997, proceedings available from Jefferson lab.

[121] W. Kaune, G. Miller, W. Oliver, R.W. Williams, and K.K. Young. Inclusive cross sections for pion and proton production by photons using collimated coherent bremsstrahlung. *Phys. Rev.*, D **11**(3):478–494.

[122] H. Bilokon, G. Bologna, F. Celani, B. D'Ettorre Piazzoli, R. Falcioni, G. Mannocchi, and P. Picchi. Coherent bremsstrahlung in crystals as a tool for producing high energy photon beams to be used in photoproduction experiments at CERN SPS. *Nuclear Inst. and Meth.*, **204**:299–310.

[123] G. Diambrini-Palazzi. *Revs. Mod. Phys.*, **40**:611, 1968.

[124] U. Timm. *Fortschr. Phys.*, **17**:765, 1969.

[125] S.K. Matthews *et al.* *Nuclear Inst. and Meth.*, **A 421**:23, 1999.

[126] D. Aston *et al.* The LASS spectrometer. Technical report, 1987. SLAC-Report-298 Copies available from the SLAC publications office, at http://www.slac.stanford.edu/pubs/.

[127] J. S. Alcorn, H.O. Peterson, and S. St. Lorent. In *Applied Superconductivity Conference - 1972*, page 273.

[128] D.W. Hertzog *et al.* *Nuclear Inst. and Meth.*, **A294**:446, 1990.

[129] A. Antonelli *et al.* *Nuclear Inst. and Meth.*, **A370**:367, 1996.

[130] A. Antonelli *et al.* *Nuclear Inst. and Meth.*, **A354**:352, 1995.

[131] C. A. Meyer. Tracking resolution requirements in the meson spectroscopy facility at Jefferson Lab. HALL DNote **7**, linked from http://www.phys.cmu.edu/halld/notes_main.html, 1998.

[132] J. Mueller. A solenoidal tracking system for the stage 1 detector in hall. In S. Dytman, H. Fenker, and P. Roos, editors, *Proceedings of the Workshop on* Physics & Instrumentation with 6–12 GeV Beams, page 419. Jefferson Lab, 1998.

[133] C. Leonidopoulos and C. Lu. Development of a straw tube chamber with pickup-pad readout. hep-ex/9706007, 1999.

[134] S.R. Amendolia *et al.* *Nuclear Inst. and Meth.*, **A283**:573, 1989. http://scipp.ucsc.edu/groups/aleph/.

[135] C. Brand *et al.* *Nuclear Inst. and Meth.*, **A283**:567, 1989.

[136] The FELIX Collaboration. http://www.cern.ch/FELIX/Loi/HTML/C5/node4.html.

[137] The STAR Collaboration. http://www.rhic.bnl.gov/star/starlib/doc/www/star.html.

[138] D.R. Nygren. Internal Report, LBL, Berkeley, CA, February, 1974.

[139] Proceedings of the eighth international wire chamber conference, Vienna, Austria, Feb. 1997,. *Nuclear Inst. and Meth.*, **A419**:375–468, 1998.

[140] The ALICE Collaboration. http://consult.cern.ch/alice/Documents/1995/01/tech_prop.html.

[141] C. A. Meyer. A study of timing resolutions on particle identification in the HALL Ddectector at Jefferson Lab. HALL DNote **14**, linked from http://www.phys.cmu.edu/halld/notes_main.html, 1999.

[142] C. A. Meyer and P. Eugenio. A study of compined K–π separation using time–of–flight counters and a gas Čerenkov detector. HALL DNote **15**, linked from http://www.phys.cmu.edu/halld/notes_main.html, 1998.

[143] J. Baechler it et al. *Nuclear Inst. and Meth.*, **A419**:511, 1998.

[144] M. D. Petroff and M. Atac. *IEEE Trans. Nucl. Sci. NS-36*, page 163, 1989.

[145] M. R. Wayne. *Nuclear Inst. and Meth.*, **A386**:278, 1997.

[146] M. Ambrogiani *et al.* *Nucl. Phys. B* **B61**, page 384, 1998.

[147] B. Baumbaugh *et al.* *IEEE Trans. Nucl. Sci. 43*, page 1146 and references therein, 1996.

[148] T. Bienz. PhD thesis, Stanford University, 1990. SLAC Report 369.

[149] P. Rensing. PhD thesis, Stanford University, 1993. SLAC Report 421.

[150] M. Moszynski and B. Bengston. *Nuclear Inst. and Meth.*, **158**:1, 1979.

[151] B. Bengston and M. Moszynksi. *Nuclear Inst. and Meth.*, **204**:129, 1982.

[152] E. Chen, M. Saulnier, W. Sun, and H. Yamamoto. Tests of a high resolution time-of-flight system based on long and narrow scintillator. hep-ex/9606007.

[153] E. Cisbani *et al.* Proposal for a dual radiator rich for hermes. available through the HERMES home page at http://dxhra1.desy.de/.

[154] M. Sivertz *et al.* A compact gas Čerenkov detector with novel optics. *Nuclear Inst. and Meth.*, **A385**:37, 1997. hep-ex/9607013.

[155] A.K. Gougas *et al.* Behavior of hydrophobic aerogal used as a Čerenkov medium. *Nuclear Inst. and Meth.*, **A421**:249, 1999.

[156] Y. Asaoka *et al.* Development of a large area aerogel Čerenkov counter on board BESS. *Nuclear Inst. and Meth.*, **A416**:236, 1998. hep-ex/9805001.

[157] M. Yu Barnykov *et al.* Development of aerogel Çerenkov counters with wavelength shifters and phototubes. *Nuclear Inst. and Meth.*, **A419**:584, 1998.

[158] M. Hauschild. Progress in dE/dx techniques used for particle identification. *Nuclear Inst. and Meth.*, **A379**:436, 1996.

[159] A. Andryakov *et al.* dE/dx measurement in a he-based gas mixture. *Nuclear Inst. and Meth.*, **A409**:390, 1998.

[160] A. Antonelli *et al.* A Pb SciFi EM calorimeter for an experiment on CP violation at DAPHNE. LNF-91-073-P, 1991.

[161] R. R. Crittenden *et al.* *Nuclear Inst. and Meth.*, **387**:377, 1998.

[162] S. Teige. In Howard A. Gordon and Doris Rueger, editors, *Proceedings of the Fifth International Conference on Calorimetry in High Energy Physics*, pages 161–166. World Scientific, 1995.

[163] A. Brunner *et al.* *Nuclear Inst. and Meth.*, **A414**:466–476, 1998.

[164] SLAC-PUB-6385, Muon Background in a 1.0-TeV Linear Collider.

[165] Details of the preliminary civil design and cost can be obtained from Suresh Chandra, Jlab Engineering.

[166] Armstrong *et al.* *Phys. Rev.*, D**5**:1640, 1972.

[167] Caldwell *et al.* *Phys. Rev.*, D**7**:1362, 1973.

[168] The Durham online database is located on the WWW at http://durpdg.dur.ac.uk/HEPDATA.

[169] J. Va'Vra. *Nuclear Inst. and Meth.*, **A244**:391–415, 1986.

[170] P. Eugenio. *Genr8*: A general monte carlo event generator. Carnegie Mellon University, 1998.

[171] S. Teige. A monte-carlo user guide. Indiana University, 1998.

[172] Information on MCFast may be optained via the WWW at http://fnpspa.fnal.gov.

[173] Information on ROOT may be optained via the WWW at http://root.cern.ch.

[174] C. A. Meyer. Tracking resolution requirements in the meson spectroscopy facility at Jefferson Lab. HALL DNote **7**, linked from http://www.phys.cmu.edu/halld/notes_main.html, 1999.

[175] ABBHHM Collaboration. *Phys. Rev.*, **175**:1669, 1968.

[176] G. Condo *et al.* *Phys. Rev.*, D**41**:3317, 1990.

[177] J. Ballam *et al.* Bubble-chamber study of photoproduction by polarized photons. *Phys. Rev.*, D**6**:454, 1972.

[178] J. Ballam *et al.* Conservation of s-channel helicity conservation in ρ photoproduction. *Phys. Rev. Lett.*, **24**:960, 1970.

[179] J. Ballam *et al.* *Phys. Rev.*, D**5**:545–589, 1972.

[180] J. Ballam *et al.* Study of $\gamma p \to p\omega$ with linearly polarized photons. *Phys. Rev. Lett.*, **24**:1364, 1970.

[181] J. Ballam *et al.* A search for B and $\rho^-(1250)$ production in the reaction $\gamma p \to p\pi^+\pi^-+$ neutrals at 2.8, 4.7, and 9.3 gev. *Nucl. Phys.*, **B76**:375–399, 1974.

[182] S.D. Drell. *Rev. Mod. Phys.*, **33**:459, 1961.

[183] P. Söding. *Phys. Lett.*, **19B**:702, 1965.

[184] M. Derrick *et al.* (ZEUS Collaboration). *Z. Phys.*, **C69**:39, 1995.

[185] S. Aid *et al* (H1 Collaboration). *Nucl. Phys.*, **B463**:3, 1996.

[186] M.G. Ryskin and Yu.M. Shabelski. hep-ph/9712437.

[187] J.P. Cummings and D.P. Weygand. Brookhaven National Laboratory Report BNL-64637.

[188] Caso *et al.* (Particle Data Group). *Eur.Phys.*, **J3**:1, 1998.

[189] S.U. Chung. Spin formalisms. CERN Report 71-8, March 1971, Lectures given in the Academic Training Program of CERN 1969-1970.